Theory and Simulations of Charge Transfer in Engineered Chemical Systems

by

Jesús del Carmen Valdiviezo Mora

Department of Chemistry
Duke University

Date:_____
Approved:

_____
David N. Beratan, Advisor

_____
Michael J. Therien

_____
Peng Zhang

_____
David H. Waldeck

_____
Julio L. Palma

Dissertation submitted in partial fulfillment of
the requirements for the degree of Doctor
of Philosophy in the Department of
Chemistry in the Graduate School
of Duke University

2021

ABSTRACT

Theory and Simulations of Charge Transfer in Engineered Chemical Systems

by

Jesús del Carmen Valdiviezo Mora

Department of Chemistry
Duke University

Date:_____
Approved:

_____
David N. Beratan, Advisor

_____
Michael J. Therien

_____
Peng Zhang

_____
David H. Waldeck

_____
Julio L. Palma

An abstract of a dissertation submitted in partial
fulfillment of the requirements for the degree
of Doctor of Philosophy in the Department of
Chemistry in the Graduate School of
Duke University

2021

Copyright by
Jesús del Carmen Valdiviezo Mora
2021

Abstract

Electron transfer is an essential process for life to exist and is the working principle of electronics. Fundamental knowledge of electron transfer is crucial for understanding biological processes and developing future devices. Here, we present our theoretical and experimental efforts to design, synthesize and characterize the electronic properties of charge-transfer complexes and approaches to control their charge flow.

Computational methods, including wave function-based methods, density functional theory, quantum mechanics/molecular mechanics, and molecular dynamics, were combined with synthesis, ultrafast spectroscopy and conductance measurements to design and characterize engineered chemical systems for efficient charge and energy transfer.

Compelling foundational questions explored in this dissertation include: 1) Can we control the photoinduced electron transfer rate of molecules with chemically innocent vibrational excitations? 2) Can we create, sustain, and exploit chemical coherences to harvest and transmit energy and information? 3) What chemical modifications lead to enhancing intrinsic charge transport properties of molecular devices?

First, we discuss the photophysics of highly conjugated organic and organometallic systems consisting of electron donor and acceptor units. Electronic

structure calculations combined with ultrafast spectroscopy elucidated the excited-state dynamics of molecular candidates for controlling charge transfer with infrared pulses and directing energy transfer through nonthermal routes. Second, we introduce strategies to fabricate efficient DNA-based molecular wires and obtain abundant semiconducting carbon nanotubes. Molecular dynamics simulations and kinetic modeling revealed the chemical interactions relevant for engineering charge transport in nanostructures. The synergy between our theoretical calculations and experimental measurements provides guidelines to tailor the electronic properties of chemical systems and control charge flow in optically active charge-transfer complexes and nanostructures.

Dedication

For my brother, José Aristh, who asked for a younger brother.

For my parents, Aristeo and Carmen, who gave me life.

For my granny, Emerita, who loved me unconditionally.

A mi hermano, José Aristh, quien pidió un hermano menor.

A mis padres, Aristeo y Carmen, quienes me dieron la vida.

A mi abuelita, Emerita, quien me amó incondicionalmente.

Contents

Abstract iv

List of Tables xii

List of Figures xv

Acknowledgements xix

1. Introduction 1

1.1 Electron transfer rate theory 1

1.1.1 Adiabatic and non-adiabatic electron transfer 3

1.1.2 Charge transfer mechanisms 4

2. Excited state dynamics of molecular targets for IR-perturbed electron transfer 6

2.1 Significance of the study 6

2.2 Introduction 7

2.3 Ultrafast charge separation in unsymmetrical bis-alkynyl complexes based on CO(III)(cyclam) 8

2.3.1 Experimental details 10

2.3.2 Computational details 11

2.3.3 UV-Vis spectroscopic analysis 11

2.3.4 Fourier transform IR (FTIR) spectroscopy 15

2.3.5 Time-resolved spectroscopy in the visible and infrared regions 18

2.3.6 Summary 24

2.4 Symmetry controlled photo-selection and charge separation in butadiyne-bridged donor-bridge-acceptor compounds 25

2.4.1 Experimental details 31

2.4.2 Computational details 31

2.4.3 Steady-state absorption and emission spectra 32

2.4.4 Transient absorption spectroscopy in the mid-IR and visible spectral regions 37

2.4.5 Torsion angle distribution 41

2.4.6 Modeling of the spectral dynamics in m-IR 45

2.4.7 Symmetry origin of the S1-S2 oscillator strength variations with θ 48

2.4.8 S2-S1 electronic coupling varies with θ 50

2.4.9 Summary 52

2.5 Concluding remarks 54

3. Exploiting molecular coherences for directed energy flow 55

3.1 Significance of the study 55

3.2 Introduction 55

3.3 Quantum ratcheted photophysics of multi-chromophoric systems 57

3.3.1 Experimental details 59

3.3.2 Computational details 59

3.3.3 Design considerations 59

3.3.4 Photophysics of D_1-D_2-A and D_1'-D_2-A compounds 60

3.3.5 Summary 63

3.4 Engineering and sustaining excited-state coherences in cofacial porphyrin arrays 63

3.4.1 Experimental details 64

3.4.2 Computational details 64

3.4.3 Linear absorption spectra and TD-DFT analysis 65

3.4.4 Excited state dynamics 67

3.4.5 Summary 70

3.5 Concluding remarks 71

4. Delocalization-assisted transport through nucleic acids in molecular junctions 72

4.1 Significance of the study 72

4.2 Introduction 73

4.3 Methods 77

4.3.1 Conductance measurements 77

4.3.2 Computational details 77

4.3.2.1 Molecular dynamics 77

4.3.2.2 Electronic coupling and site energy analysis 78

4.4 Theoretical analysis of DNA and PNA structure and electronic properties 79

4.5 PNA vs DNA conductance 84

4.6 Molecular orbital interpretation of conductance oscillations 87

4.7 Summary and conclusions 93

5. Electron ratcheting in self-assembled soft matter 96

5.1 Significance of the study 96

5.2 Introduction 96

5.3 Electron ratcheting in nanostructures 99

5.3.1 A ratchet based on charge hopping 100

5.3.2 Simulation of charge carrier surfing 102
5.3.3 Kinetic modeling 103
5.3.4 Ratcheting in DNA 104
5.3.5 Proposed experimental tests of the ratcheting mechanism 109
5.4 Electron ratcheting in larger structures 110
5.4.1 Ratcheting driven by solution electrochemistry 111
5.4.2 Design considerations 112
5.4.3 Current estimates 115
5.4.4 Proposed experimental design 116
5.5 Conclusions 117
6. Enantiomeric separation of semiconducting nanotubes 119
6.1 Significance of the study 119
6.2 Introduction 119
6.3 Methods 122
6.3.1 Experimental methods 122
6.3.2 Computational methods 123
6.3.2.1 Molecular dynamics system preparation 123
6.3.2.2 Molecular dynamics simulation details 123
6.3.2.3 Solvation Free Energy calculations 124
6.3.2.4 Entropic and Enthalpic contributions to solvation 124
6.4 Results 125
6.5 Conclusions 127

7. Conclusions....128

7.1 Chapter 2: Excited-state dynamics of molecular targets for IR-perturbed electron transfer....128

7.2 Chapter 3: Exploiting molecular coherences for directed energy flow....129

7.3 Chapter 4: Delocalization-assisted transport through nucleic acids in molecular junctions....129

7.4 Chapter 5: Electron ratcheting in self-assembled soft matter....130

7.5 Chapter 6: Enantiomeric separation of semiconducting nanotubes....130

Appendix A....131

Appendix B....140

Appendix C....142

Appendix D....176

Appendix E....191

Appendix F....199

References....203

Biography....234

List of Tables

Table 1: Dipole moments (in Debyes) computed for compounds 1, 2a, and 2d in different electronic states in CH_3CN. 13

Table 2: Experimental and TDDFT computed vibrational frequencies and computed IR intensities (*I*) for 1, 2a, and 2d in different electronic states in CH_3CN. 17

Table 3: TD-DFT computed vibrational frequencies and IR intensities (*I*) for D-C4-NAP in toluene and DCM in the ground and excited states at $\theta = 0$. 37

Table 4: TD-DFT computed vibrational frequencies and IR intensities (*I*) for Si-C4-NAP in toluene and DCM in the ground and excited states at $\theta = 0$. 40

Table 5: TD-DFT computed vibrational frequencies and IR intensities (*I*) for D-C4-NAP with different dihedral angles in DCM in the ground and excited states. 44

Table 6: TD-DFT computed energy, dipole moment and oscillator strength at different dihedral angles for D-C4-NAP in DCM in the ground and excited states. 47

Table 7: Vertical excitation values of Dimer 1 with different levels of theory.....67

Table 8: Electronic couplings of cofacial porphyrin systems calculated using the Fragment-Excitation Difference (FED) method.....69

Table 9: Electronic couplings of cofacial porphyrin systems without the bridge unit calculated using the Fragment-Excitation Difference (FED) method 69

Table 10: HOMO energies (eV) and their standard deviations for the GC base pairs 81

Table 11: V_{RMS} values of GC-GC cross-strand (V_C), GC-GC intra-strand (V_I) and terminal AT-GC coupling (V_T).....82

Table 12: Enthalpic and Entropic contributions to the Solvation Free energies. 127

Table 13: Coordinates of ground state optimized structure of 1 in CH_3CN.....131

Table 14: Coordinates of ground state optimized structure of 2a in CH_3CN.....133

Table 15: Coordinates of ground state optimized structure of 2d in CH_3CN. 136

Table 16: TD-DFT computed vibrational frequencies and IR intensities (*I*) for Ph-C4-NAP in toluene and DCM in the ground and excited states at θ = 0. 140

Table 17: TD-DFT computed vibrational frequencies and IR intensities (*I*) for D-C4-NAP in toluene and DCM in the ground and excited states at θ = 0. 141

Table 18: Coordinates of the D_1-D_2-A optimized structure at the MN15/def2-SVP level of theory in toluene. 142

Table 19: Coordinates of the D_1-D_2-A optimized structure at the MN15/def2-SVP level of theory in toluene. 151

Table 20: Coordinates of the D_1'-D_2-A optimized structure at the MN15/def2-SVP level of theory in toluene. 160

Table 21: Coordinates of the D_1'-D_2-A optimized structure at the MN15/def2-SVP level of theory in dichloromethane. 168

Table 22: Electronic couplings of cofacial porphyrin systems calculated using the Edmiston-Ruedenbeg localization scheme. 176

Table 23: Electronic couplings of cofacial porphyrin systems without the bridge unit calculated using the Edmiston-Ruedenbeg localization scheme. 176

Table 24: Ground-state optimized geometry of monomer 8 at the CAM-B3LYP-D3BJ/def2-SVP level of theory in THF. 176

Table 25: Ground-state optimized geometry of monomer 9 at the CAM-B3LYP-D3BJ/def2-SVP level of theory in THF. 179

Table 26: Ground-state optimized geometry of dimer 1 at the CAM-B3LYP-D3BJ/def2-SVP level of theory in THF. 182

Table 27: Ground-state optimized geometry of dimer 3 at the CAM-B3LYP-D3BJ/def2-SVP level of theory in THF. 186

Table 28: HOMO energies and standard deviations (σ) in eV for each base pair of the n = 5 duplexes. 192

Table 29: V_{RMS} values of the electronic couplings in eV of the four nucleotides at the cross-strand section 194

Table 30: Best fit parameters for the data in Figure 36 using Equation 23. 196

Table 31: XYZ coordinates of the anionic surfactant in R configuration optimized in water at the wB97-XD/def2-SVP level of theory. 199

Table 32: XYZ coordinates of the anionic surfactant in S configuration optimized in water at the wB97-XD/def2-SVP level of theory. 201

List of Figures

Figure 1: Co^{III}(cyclam) based *D-B-A* systems studied and synthetic approach. 10

Figure 2: UV-Vis absorption spectra in CH_2Cl_2 vs. normalized emission spectra in CH_2Cl_2, taken at room temperature, for 1 and 2a-2d. 12

Figure 3: TD-DFT results showing the dominant orbital contribution to the bright state for compound 1. 14

Figure 4: TD-DFT analysis showing orbital transitions that contribute to the bright excited state prepared with a 400 nm pump (bright state) and the CS state for 2a. 14

Figure 5: TD-DFT results showing the dominant orbital contributions to the CSS and the bright state for 2d. 15

Figure 6: IR absorption spectra of 1, 2a, and 2d in CH_3CN. 17

Figure 7: Transient absorption spectra for 1, 2a and 2d in CH_3CN 18

Figure 8: Decay associated spectra for 2a (a) and 2d (b) constructed for the spectral dynamics within 60 ps window. 20

Figure 9: Transient kinetics for 2a (a) and 2d (b) at indicated frequencies (in cm^{-1}) 22

Figure 10: Summary of the excited-state dynamics in 1, 2a, and 2d. 23

Figure 11: TD-DFT results showing the dominant orbital contribution to the ^{T}NAP and ^{T}Co(cyclam) state for compound 1. 24

Figure 12: Coupled states for strong (a) and weak (b) coupling regimes 29

Figure 13: Structures of the butadiyne-bridged compounds studied. 31

Figure 14: Absorption (bright lines) and emission (light lines, λ_{exc} = 340 nm) spectra of (a) Si-C4-NAP, (b) Ph-C4-NAP, and (c) D-C4-NAP 34

Figure 15: TD-DFT results showing the dominant orbital contribution to the S_1 state for Si-C4-NAP in DCM. 34

Figure 16: TD-DFT results showing the dominant orbital contribution to the S_1 and S_3 state for D-C4-NAP in DCM. 35

Figure 17: Solvent subtracted FTIR absorption spectra of the three compounds amplitude normalized at the C=O as mode. 36

Figure 18: Transient spectra in the visible (left panel) and mid-IR (middle panel) regions for Si-C4-NAP (a), Ph-C4-NAP (b, c), and D-C4-NAP (d, e) compounds 39

Figure 19: Three characteristic energy diagrams involving the states relevant for transient absorption with 400 nm excitation. 41

Figure 20: Analysis of D-C4-NAP at different dihedral angles. 43

Figure 21: Analysis of $\nu_{CC,ss}$ and $\nu_{CC,as}$ mode frequencies. 47

Figure 22: Leading natural transition orbitals for $S_0 \rightarrow S_1$ and $S_0 \rightarrow S_2$ transitions of D-C4-NAP 48

Figure 23: Cartoon illustrating how symmetry affects the electronic coupling between the ground and S_1, S_2 excited states. 49

Figure 24: The TD-DFT computed S_2-S_1 coupling strength as a function of the dihedral angle. 50

Figure 25: Bend angle analysis of D-C4-NAP. 52

Figure 26: a) Structures of the light-harvesting complexes studied. b) Schematic depicting quantum ratcheted energy and electron transport dynamics. 58

Figure 27: Theoretical and experimental absorption spectra of (a) D_1-D_2-A and D_1'D_2-A in dichloromethane 61

Figure 28: Energetics and orbital transitions of (a) D_1-D_2-A and (b) D_1'-D_2-A calculated in implicit dichloromethane with TD-DFT at the MN15/def2-SVP level of theory 62

Figure 29: Emission spectra of (a) D_1-D_2-A and (b) D_1'-D_2-A and their corresponding benchmark structure. 62

Figure 30: Cofacial structures studied in this work 64

Figure 31: Linear absorption spectra of monomer 8 and 9, and Dimers 1 and 3 measured in 3:1 mixture of diethyl-ether and ethanol at 95K. 65

Figure 32: TD-DFT analysis of the four porphyrin-based structures analyzed. Energies, oscillator strengths (f) and natural transition orbitals are shown. 66

Figure 33: Kinetic decay trace of Monomer 8, Dimer 1 and Dimer 3 at 95K and 140K. Insets indicate the inter-exciton relaxation time (t_{dec}).....68

Figure 34: Proposed excited state dynamics of Dimers 70

Figure 35: PNA molecular junction and sequence.....76

Figure 36: Conductance measurements.....85

Figure 37: Molecular orbital energy picture of nucleic acid duplexes under a weak cross-strand coupling 88

Figure 38: Model describing the delocalized islands across two G-blocks 91

Figure 39: The energy landscapes for two kinds of electron-transfer ratchets 98

Figure 40: (a) The proposed flashing ratchet mechanism for vectorial charge transport101

Figure 41: Kinetics results and DFT analysis 105

Figure 42: Proposed structures and experimental setups for ratcheting at the nanoscale 110

Figure 43: Ratcheting mechanism based on electrochemical perturbation 112

Figure 44: Proposed architecture for electrochemical ratcheting at the mesoscale.....117

Figure 45: Structures of (a) chiral CNTs and (b) surfactants studied.....120

Figure 46: CD spectra of enantioenriched (+)(6,5)SWCNTs and (-)(6,5)SWCNTs using chiral surfactants.....122

Figure 47: Procedure to obtain single-chirality, enantioenriched SWCNT samples.....122

Figure 48: Final snapshots of solvated carbon nanotubes simulated for 3 ns using the CHARMM36 force field 126

Figure 49: TD-DFT results showing all sizable contributions for the lowest energy triplet state of compound 1. 131

Figure 50: Computed S2-S1 energy gap and the H_{DA} (H_{12}) coupling dependences on torsional angle θ. 141

Figure 51: RMSD maps for the MD production simulations of the nucleic acid duplexes. 191

Figure 52: Comparisons between the standard deviations of several parameters between duplexes 192

Figure 53: Average structures from the 3000 MD snapshots. The intra-strand and cross-strand G-G overlaps are shown for each duplex. 193

Figure 54: Average structures from the 3000 MD snapshots for the four nucleobases at the cross-strand section. 193

Figure 55: RMSDs (excluding H atoms) from its average structure along the MD production runs for the four nucleobases at the cross-strand section. 194

Figure 56: Nucleobase labeling for the calculation of the superexchange contribution to the coupling 194

Figure 57: Contour plots of fitting parameters R_0 and T_{GG}. B and C are fixed at the values given in Table 30. 198

Acknowledgements

I am very grateful for having shared this journey with fantastic people throughout my graduate school education. Each of them deserves a personal letter with more words of gratitude that I can write here. I hope one day I could send them.

I'll always be thankful to the admissions committee of the Duke Department of Chemistry and the Duke Graduate School, who gave me the opportunity to join the amazing Duke community, wherein I found the perfect fit to continue my scientific training and personal development.

I want to thank my advisor, Prof. David Beratan, who has always supported me in all aspects of my career with a smile. His enthusiasm and passion for science have been contagious and have increased my excitement for research. I could not have asked for a better mentor. It has been a true honor working with him during my Ph.D. studies.

Special thanks to Prof. Peng Zhang, who was always available to offer his guidance. I really admire his approach to our scientific questions and his tennis strokes during our matches after working hours.

Many thanks to my additional committee members, Prof. Michael Therien, Prof. David Waldeck, and Prof. Julio Palma, who have also been my teachers and collaborators. It has been a privilege to discuss science with them. I am particularly grateful to Julio for introducing me to the field of Theoretical and Computational Chemistry back in 2012 and encouraging me to pursue a Ph.D.

Thanks to the Beratan and Yang lab members for sharing more than office spaces.

I also want to thank my other collaborators and friends in the Therien and Brown groups at Duke, the Rubtsov group at Tulane, the Ren group at Purdue, the Waldeck group at Pitt, the Achim group at CMU, the Palma group at Penn State, the Makri group at UIUC, the Wasielewski group at Northwestern and the Fleming group at Berkeley. All of them have made my scientific journey more fun.

I thank the fellowships from the Fulbright Program, the Duke Chemistry Department, and the Duke Graduate School for generously supporting my studies.

Many thanks to all my students and friends during my time as an instructor at Clubes de Ciencia and Duke for giving me the opportunity to share my passion for science and reminding me why I love what I do so much.

My sincere thanks to my Dukie friends who made my graduate school experience an unforgettable adventure. They cheered me up during challenging times and shared my excitement when good news arrived.

I am also very grateful to my friends from my pre-graduate school time for their support. They showed me how true friendship becomes stronger as the years roll on.

Lastly, I want to express my deepest gratitude to my brother, Aristh Valdiviezo, my parents, Aristeo Valdiviezo and Carmen Mora, and my grandma, Emerita Aguilar, who have always believed in me and given me unconditional love. This milestone is theirs. I love them.

1. Introduction

This chapter contains an introductory description of the theory involved in the following chapters. The background described in this section is based on the content from a book in preparation co-authored by Jesús Valdiviezo, Jonathon Yuly, Peng Zhang, and David Beratan.

1.1 Electron transfer rate theory

Electron transfer (ET) can be seen as the spatial relocation of an electron from a donor (D) to an acceptor (A) moiety, and it is considered the simplest chemical reaction ($D + A \rightarrow D^{+} + A^{-}$). It is essential for life to exist and is the working principle of many modern technologies.

A proper description of the electron transfer rate (k_{ET}) is crucial for the understanding of biological processes and for the development of electronic devices. We can associate the electron transfer rate with the reaction free energy barrier, described by the Arrhenius equation in the classical transition state theory:

$$k_{ET} = A \exp\left[-\frac{E_a}{k_B T}\right] \tag{1}$$

where E_a is the activation energy, k_B is the Boltzmann constant, T is the temperature and A is a pre-exponential factor. The activation energy $E_a = (\Delta G^{\circ} + \lambda)^2/4\lambda$ and is expressed in terms of the Gibbs free energy ΔG°, and the reorganization energy λ. Therefore, the rate of an electron transfer reaction equals:

$$k_{ET} = A \exp\left[-\frac{(\Delta G^\circ + \lambda)^2}{4\lambda k_B T}\right] \tag{2}$$

The relationship between ΔG° and λ determines the type of electron transfer reaction:

- Normal: $> -\Delta G^\circ > 0$
- Barrierless: $-\Delta G^\circ = \lambda$
- Inverted: $< -\Delta G^\circ < 0$

The reorganization energy can be separated in two terms, the inner-sphere reorganization energy λ_i and the outer-sphere reorganization energy λ_o:

$$\lambda = \lambda_i + \lambda_o \tag{3}$$

The inner-sphere reorganization energy is the free-energy change associated with changes in the bond lengths and angles of the reactant and is described as follows:

$$\lambda_i = n\left(\frac{1}{2}\sum_j f_j (d_p - d_r)^2\right) \tag{4}$$

Here, n is the number of bonds involved in the reaction, f_j is the force constant of a particular bond j, d_p is the product equilibrium bond and is the reactant equilibrium bond.

The outer-sphere reorganization energy describes the response of the solvent to the electron distribution of the product:

$$\lambda_o = \frac{e^2}{4\pi\epsilon_o}\left(\frac{1}{2r_D} - \frac{1}{2r_A} + \frac{1}{R}\right)\left(\frac{1}{\epsilon_{op}} - \frac{1}{\epsilon_s}\right) \tag{5}$$

where e is the elementary charge, ϵ_o is the vacuum permittivity, r_D is the donor radius, r_A is the acceptor radius, R is the donor-acceptor distance, ϵ_{op} is the solvent optical constant and ϵ_s is the solvent dielectric constant. Commonly $\lambda_i \ll \lambda_o$. Therefore, $\lambda \approx \lambda_o$.

1.1.1 Adiabatic and non-adiabatic electron transfer

The pre-exponential factor in the electron transfer rate depends on the donor-acceptor electronic coupling strength V_{DA}. This coupling can be interpreted as the interaction of the donor and acceptor orbitals that changed their electron occupancy during the electron transfer process. In the strong coupling regime, the electron transfer is described by the adiabatic expression:

$$k_{ET}^{ad} = \nu_n \exp\left[-\frac{(\Delta G^\circ + \lambda)^2}{4\lambda k_B T}\right] \tag{6}$$

where ν_n is a nuclear frequency prefactor, typically on the scale of 10^{13} s^{-1}. In the weak coupling regime, where electron transfer in chemical systems typically occurs, the prefactor is described in terms of the reduced Planck constant $\hbar$, the donor-acceptor electronic coupling V_{DA}^2, the reorganization energy and the temperature. The expression is known as the non-adiabatic Marcus theory expression:

$$k_{ET}^{nonad} = \frac{2\pi}{\hbar}\frac{V_{DA}^2}{\sqrt{4\pi\lambda k_B T}}\exp\left[-\frac{(\Delta G^\circ + \lambda)^2}{4\lambda k_B T}\right] \tag{7}$$

In situations where weak coupling exists between donor and acceptor vibronic energy levels, the electron transfer is described as:

$$k_{ET}^{nonad} = \frac{2\pi}{\hbar} \frac{V_{DA}^2}{\sqrt{4\pi\lambda k_B T}} \sum_{w=0}^{\infty} \frac{e^{-S} S^w}{w!} \exp\left[-\frac{(\Delta G^\circ + \lambda_i + wh\nu)^2}{4\lambda k_B T}\right] \tag{8}$$

Here, $S = \lambda_i / h\nu$ and w represents a vibrational mode.

1.1.2 Charge transfer mechanisms

The donor and acceptor moieties are typically connected through one or several bridge units (B) that determine the donor-acceptor distance. In the nonadiabatic regime, the donor wavefunction can tunnel through the bridge if there exist sufficient overlap with the acceptor wavefunction and the energy levels of D and A moieties match. This mechanism is known as coherent superexchange and is dominant at short donor-acceptor distances. The effective electronic coupling is expressed as follows:

$$V_{DA}^{SE} = \frac{V_{DB} V_{BA}}{E_B - E_{D/A}} \tag{9}$$

For a system with N bridge units, the effective coupling $\tilde{V}_{DA}$ takes the form:

$$\tilde{V}_{DA} = \frac{V_{DB_1} V_{B_N A}}{V_{BB}} \left(\frac{V_{BB}}{E_B - E_{D/A}}\right)^N \tag{10}$$

This superexchange coupling follows an exponential decay with the donor-acceptor distance (i.e. molecular length L). Therefore, the electron transfer rate is approximated as:

$$k_{ET}^{SE} \approx \exp(-\beta \mathrm{L}) \tag{11}$$

where $\beta = {}^{2}/_{b} \ln \left| {}^{V_{BB}}/_{E_B - E_{D/A}} \right|$ and depends on the distance between nearest neighbor bridge units b.

At long donor-acceptor distances, the superexchange mechanism is disfavored and the electron transfer proceeds mainly through incoherent hopping. In this mechanism, thermal fluctuations bring the bridge energy levels closer to resonance with the donor/acceptor site and the charge can populate the bridge sites. The electron transfer rate expression becomes approximately:

$$k_{ET}^{HOP} = \frac{\exp\left(-\Delta E_{DB}/k_B T\right)}{\frac{1}{k_{B_N A}} + \frac{1}{k_{B_1 D}} + \frac{(N-1)}{k}} \tag{12}$$

Note that $k = k_{B_n B_{n+1}}$ and $n = 1, 2, 3, \ldots, N-1$. When the number of bridge sites N, increases, the electron transfer rate has a weak dependence on molecular length ($k_{ET}^{HOP} \sim 1/N$).

2. Excited state dynamics of molecular targets for IR-perturbed electron transfer

This chapter is excerpted from:

Bazinger, S. D.; Li, X.; Valdiviezo, J.; Zeller, M.; Zhang, P.; Beratan, D. N.; Rubtsov, I. V.; Ren, T., Unsymmetrical Bis-Alkynyl Complexes Based on Co(III)(cyclam): Synthesis, Ultrafast Charge Separation and Analysis. *Inorg. Chem.* **2019,** 58 (22), 15487-15497.

Li, X.; Valdiviezo, J.; Bazinger, S. D.; Zhang, P.; Ren, T.; Beratan, D. N.; Rubtsov, I. V., Symmetry Controlled Photoselection and Charge Separation in Butadiyne-Bridged Donor-Bridge-Acceptor Compounds. *Phys. Chem. Chem. Phys.* **2020,** 22 (17), 9664-9676.

Part of this research has been generously supported by the National Science Foundation (grant no. CHE-1955138).

2.1 Significance of the study

The efficiency of opto-electronic devices strongly depends on the photoinduced charge separation and charge recombination rates. Current strategies to control electron transfer kinetics have reported to be chemically invasive or irreversible. The possibility to use infrared excitations to control electron transfer is of substantial interest, since it is a nondestructive method (the energy absorbed ranges between 2.5-8.5 kcal/mol), spatially selective (specific bonds can be excited) and infrared active functional groups can be easily incorporated into molecular architectures. In recent years, UV-IR-Vis-3-

pulse experiments showed that IR perturbations of a specific molecular vibrational mode could influence photoinduced electron transfer rates in donor-bridge acceptor (D-B-A) assemblies. We combined synthesis, computational methods, and ultrafast spectroscopy techniques to investigate the excited state dynamics of organic and organometallic D-B-A complexes. With strong donors, the optical excitation of the acceptor leads to the ultrafast formation of charge-separated states. These fast dynamics make them excellent candidates for electron transfer rate modulation by infrared excitation without rare-earth metals.

2.2 Introduction

Molecular donor-bridge-acceptor (*D-B-A*) structures have received intense interest as electron-transfer (ET) model systems.[1, 2] A topic of recent notice is the modulation of ET dynamics through vibrational excitation. Studies of this kind require ultrafast ET that proceeds more rapidly than intramolecular vibrational energy redistribution. As such, strongly coupled *D-B-A* structures with infra-red (IR) active bridge modes are a key synthetic target.

Rubtsov, Beratan, Sessler and coworkers demonstrated CS rate retardation by mid-IR excitation in a *D-B-A* ensemble formed by nucleobase pairing (GC),[3] and charge recombination (CR) rate acceleration upon mid-IR excitation.[4] They related the rate modulations to the changes in the density of states in the Marcus curve-crossing region.[4] Rubtsov, Schmehl, Beratan and coworkers also reported a *ca.* 30% enhancement of

intramolecular ligand-to-ligand charge transfer rate in a Re(I) compound via selective excitation of the acceptor ligand 4,4'-(dicarboxyethyl)-2,2-bipyridine at 1540 cm^{-1} (⊗(bpy)).[5] Weinstein and coworkers studied a series of *D-B-A* compounds with a *trans*-Pt(II)-bis-alkynyl bridge and found that the photoinduced electron transfer (PET) between phenothiazine (*D*) and naphthalimide (*A*) can be attenuated by vibrational excitation of the Pt-bound C≡C bonds.[6-9]

Here, in collaboration with experimental groups, we study the excited state dynamics of oganometallic and organic *D-B-A* structures using ultrafast spectroscopy techniques and electron transfer methods. The fast dynamics and presence of IR-active functional groups makes them promising candidates for electron transfer modulation with 3-pulse spectroscopy.

2.3 Ultrafast charge separation in unsymmetrical bis-alkynyl complexes based on CO(III)(cyclam)

Transition metal alkynyl compounds are appealing targets from the standpoints of synthetic and structural chemistry, as well as materials applications, and could provide access to species with rapid intramolecular ET rates that may be susceptible to IR-induced rate modulation.[10-13] Materials applications of transition metal alkynyl compounds include molecular wires,[14-17] molecular memory devices,[18, 19] and high performance opto-electronic materials.[20-23] Recently, metal alkynyl compounds based on 3*d* metal cyclams have been investigated by Ren and coworkers.[24, 25] The Co(III)(cyclam) motif is especially attractive because of the feasibility of stepwise alkynylation under

mild reaction conditions. This was first demonstrated by Shores and coworkers through the preparation of $[Co(cyclam)(C_2Ph)Cl]^+$,[26] and was explored by the Ren group to attain the dicobalt complexes bridged by oligoyn-diyls (μ-C_{2m}).[27, 28] The general preparations of the unsymmetric *trans*-$[Co(cyclam)(C_2Ar)(C_2Ar')]^+$ compounds were developed either through an intermediate *trans*-$[Co(cyclam)(C_2Ar)(NCCH_3)]^{+2}$,[29, 30] or *via* lithiation to install the second alkyne.[31] Such Co(III) bis-alkynyls are attractive alternatives to the aforementioned Pt species since the Co species also provide a rigid framework for *D-B-A* dyads and the structures possess vibrationally active Co-C≡C bonds based on an earth abundant metal.

The transient absorption studies of Co(III)-containing complexes are scarce, and studies of cobalamin species focused on the effects Co-C bonds are noteworthy.[32, 33] Transient absorption studies of electronically excited Co complexes show complexity in the dynamics, with characteristic times ranging from a few picoseconds to a few nanoseconds.[34, 35] The ligand-field (LF) excited states in octahedral Co(III) complexes were found to occur at energies below 12,000 cm^{-1}.[34] Nevertheless, the lifetime of the lowest electronic excited state (ES) in some species, such as $[Co(en)_3](ClO_4)_3$ (en = ethylenediamine), $[Co(tpen)](ClO_4)_3$ (tpen = tetrakis(2pyridylmethyl)ethylenediamine), $[Co(tppn)](ClO_4)_3$ (tppn = tetrakis(2-pyridylmethyl)-1,2-propylenediamine), $[Co(NH_3)_5Cl]^{2+}$, and $[Co(en)_2(NO_2)_2Cl]^{2+}$, were found to be rather short, not exceeding 500 ps.[34, 36]

Here, we report the spectroscopic and electronic structure properties of *trans*-[Co(cyclam)(C_2D)(C_2A)]$^+$ complexes, where *D* and *A* are C_6H_4-4-Y (Y = H, NMe_2 or N(4-MeOPh)$_2$) and *N*-isopropyl-1,8-napthalimide (NAP^{iPr}), respectively, (Figure 1). The excited-state dynamics of compounds **1**, **2a** and **2d** were examined using femtosecond transient absorption spectroscopy with 400 nm excitation and detection both in the visible and mid-IR spectral regions. The dynamics reveal the ultrafast formation of charge separated states (CS state) in compounds **2a** and **2d**, and their fast conversion to a Co(III) centered triplet state ($^3T_1$). Our study also finds that the MN15 density functional, a functional optimized using databases that included transition metals, describes the excited state properties of Co(III) complexes, especially the charge transfer excitation energies, a task that is challenging for most functionals.

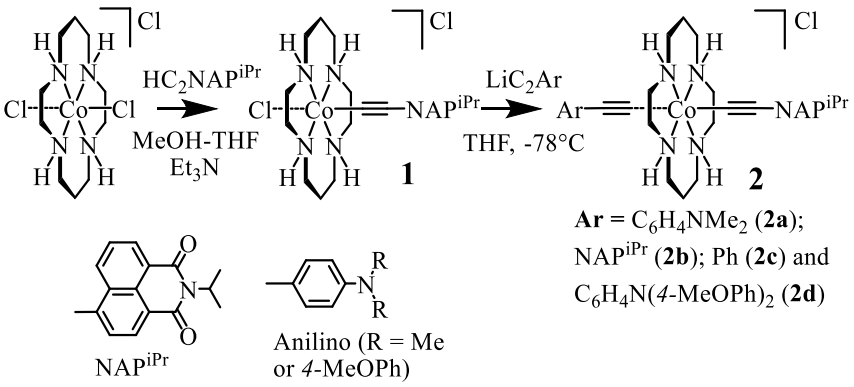

Figure 1: Co^{III}(cyclam) based *D-B-A* systems studied and synthetic approach.

2.3.1 Experimental details

Experimental details can be found elsewhere.[37] Major experimental results are presented here to facilitate the interpretation of the computational results.

2.3.2 Computational details

DFT and TD-DFT calculations for the cations in 1, 2a, and 2d were performed using the MN15 functional[38] and the Def2-SVP basis set[39] for all atoms as implemented in Gaussian 16.[40] The Polarizable Continuum Model (PCM)[41] was used to simulate the solvent effects of acetonitrile in the ground-state and excited-state calculations. The B3LYP,[42] CAM-B3LYP,[43] wB97X-D,[44] M06,[45] and M06-2X[45] functionals were also tested by comparing the character of the excited states and the vertical excitation energies with experiments. A better agreement with the experimental vibrational frequencies and electronic spectra was found with the MN15 functional. Coordinates of the optimized geometries in the ground state are listed in Appendix A.

2.3.3 UV-Vis spectroscopic analysis

Absorption spectra for complexes **1** and **2a** - **2d** are shown in Figure 2. For all the complexes, the visible window is dominated by a broad and intense peak at *ca.* 400 nm. The free ligand $Me_3SiC_2NAP^{iPr}$ displays an intense peak at *ca.* 370 nm, which is assigned as a π–π^* transition localized on NAP^{iPr}. The strong resemblance of the spectral shapes and extinction coeffcients for complexes **1** and **2** and $Me_3SiC_2NAP^{iPr}$ suggests that the transition at 400 nm is primarily a π–π^* transition localized on NAP^{iPr}. This assignment is supported by TD-DFT analysis (*vide infra*). The 30 nm red shift of the transition from $Me_3SiC_2NAP^{iPr}$ to the values in complexes **1** and **2** is apparently due to the replacement of Me_3Si with a Co(III) center. The broad nature of the 400 nm peak obscures the

expected *d-d* ($^1A_1 \rightarrow {}^1T_1$) transition, except in the case of **1**, where a weak shoulder peak is observed around 480 nm, consistent with values reported for other Co(cyclam) bisalkynyls.[46] The *D-B-A* species, **2a** and **2d**, display UV bands attributed to the donor ligands. Compound **2a** displays a sharp peak at 290 nm which can be assigned to a π-π* transition localized on C_6H_4-4-NMe_2, and compound **2d** has a broad band centered at 330 nm assigned to a π-π* transitions localized on TPA (Figure 2). This is consistent with the absorption spectrum of the free donor ligands, which exhibit a strong absorption *ca.* 300 nm. It should be noted that no such peak is present for **2b** or **2c**, due to the absense of an *N*-donor aryl substituent.

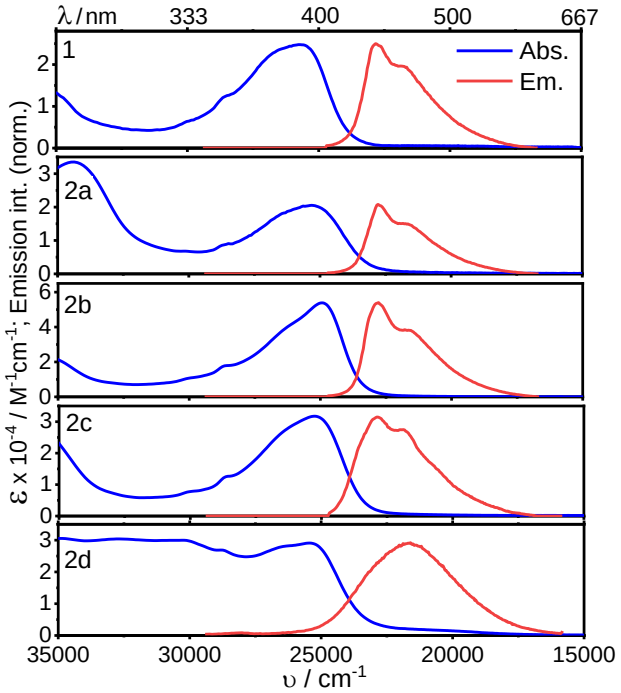

Figure 2: UV-Vis absorption spectra in CH_2Cl_2 vs. normalized emission spectra in CH_2Cl_2, taken at room temperature, for 1 and 2a-2d.

To understand the nature of the transition with high oscillator strength at ca. 400 nm, TD-DFT calculations of compounds **1**, **2a**, **2d** compounds were performed. The analysis indicates that the bright state involves only NAP^{iPr} orbitals in **1** (Figure 3), but that the states are partially polarized in **2a** and **2d**, involving *ca.* 8.4% contribution of the orbitals responsible for CS (i.e., the HOMO of the donor (*D*(HOMO)) and the LUMO of the acceptor (*A*(LUMO) as shown in Figure 4 and Figure 5). The percentages reflect the normalized squared excitation coefficients. To evaluate the amount of CT character in the transition, the dipole moments were evaluated for both the ground and excited states. The ground states are found to be polarized, with the NAP^{iPr} acceptor having a slight negative charge (Table 1). The dipole moments are further increased in the excited states by *ca.* 5.6, 25.2 and 10.5 D for **1**, **2a**, and **2d**, respectively.

Table 1: Dipole moments (in Debyes) computed for compounds 1, 2a, and 2d in different electronic states in CH_3CN.

	μ (GS)	μ (ES)	μ (CSS)	μ (^{T}Co(cyclam))
1d	19.0	24.6	-	15.5
2a	17.6	42.8	55.4	17.3
2d	4.9	15.4	68.2	4.8

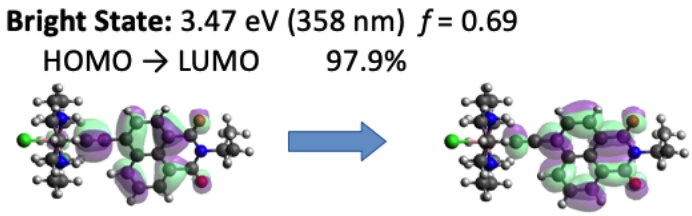

Figure 3: TD-DFT results showing the dominant orbital contribution to the bright state for compound 1. The transition energy, wavelength, and oscillator strength (*f*) are shown.

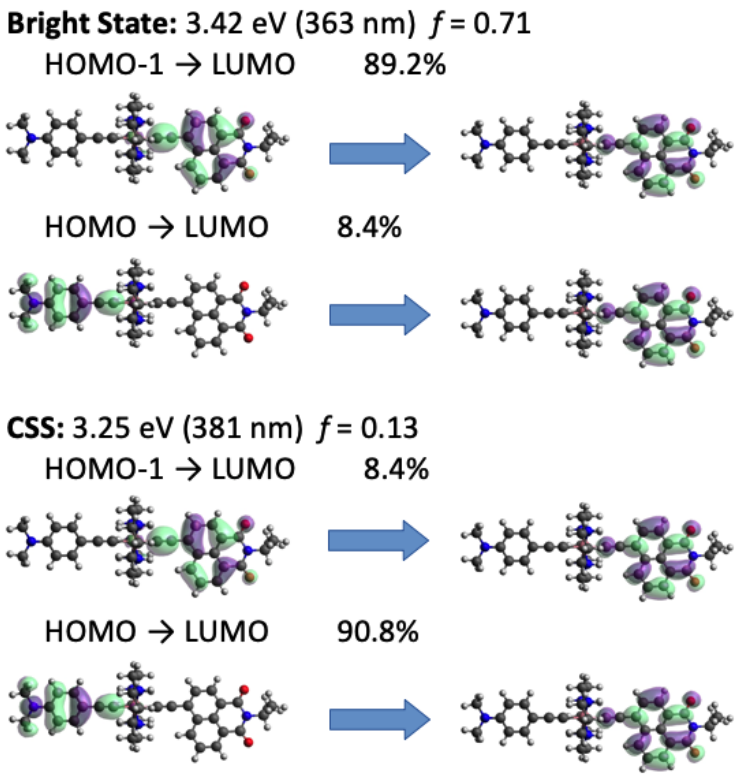

Figure 4: TD-DFT analysis showing orbital transitions that contribute to the bright excited state prepared with a 400 nm pump (bright state) and the CS state for 2a. A mixing between the HOMO-1→LUMO and HOMO→LUMO transition is present in both states. The high oscillator-strength transition is mainly a π–π* transition localized on NAP^{iPr} (89.2%) and the CS state is mostly *D*(HOMO)→*A*(LUMO) (90.8%). The transition energies and wavelengths of these states are blue-shifted with respect to the experimental values (ca. 30 nm), which is generally found in TD-DFT analysis. The oscillator strength (*f*) values, which indicate the probability of absorbing a photon, are also indicated.

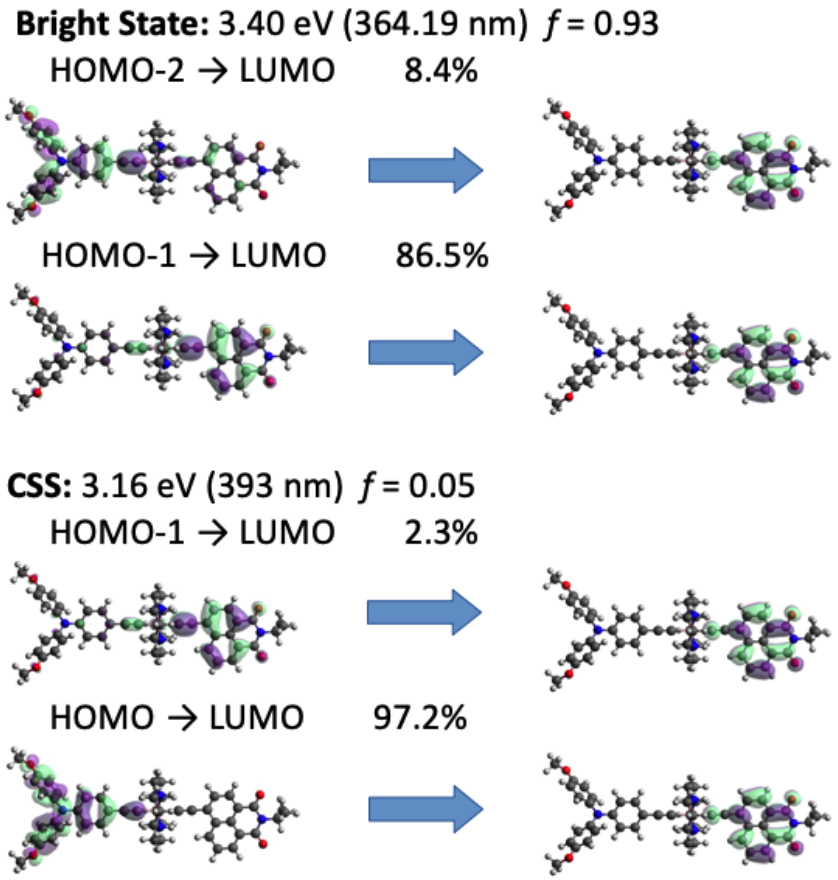

Figure 5: TD-DFT results showing the dominant orbital contributions to the CSS and the bright state for 2d. The transition energy, wavelength, and oscillator strength (*f*) are shown.

2.3.4 Fourier transform IR (FTIR) spectroscopy

The IR absorption spectra of **1, 2a** and **2d** are dominated by the antisymmetric ($\nu_{C=O,as}$) and symmetric ($\nu_{C=O,ss}$) C=O stretching modes of NAP^{iPr} at 1658 and 1698 cm^{-1} in **1** and 1656 and 1697 cm^{-1} in **2a** and **2d** (Figure 6). The C≡C stretching frequencies in **2a** and **2d** (2092 cm^{-1}) are significantly red-shifted compared to compound **1** (2110 cm^{-1}), indicating the influence of the donor moieties.

DFT-based normal-mode analysis finds that the two C≡C vibrations in the ground states of **2a** and **2d** are coupled weakly with an interaction energy of a few wavenumbers, while the frequencies of the normal modes are separated by ca. 18 cm^{-1} with the low-frequency peak originating predominantly from the donor acetylide and the high-frequency peak from the acceptor acetylide. Essentially, a single peak is observed experimentally with a weak tail on the high-frequency side, in approximate agreement with the DFT analysis, which predicts that the lower-frequency peak carries ca. 4-fold larger IR intensity (Table 2). The extinction coefficients of the C=O and C≡C modes in the three compounds are similar but grow with increasing donor strength, with $\varepsilon_{C=O,ss}$ of 1230, 1360, and 1475 $M^{-1}cm^{-1}$ for **1**, **2a**, and **2d**, respectively. The transition dipoles of the C=O and C≡C modes grow concomitantly in the three compounds, which is apparent from the essentially unchanged extinction coefficient ratio of $\nu_{C=O,ss}$ and $\nu_{C\equiv C}$ of ca. 2.4 (Figure 6).

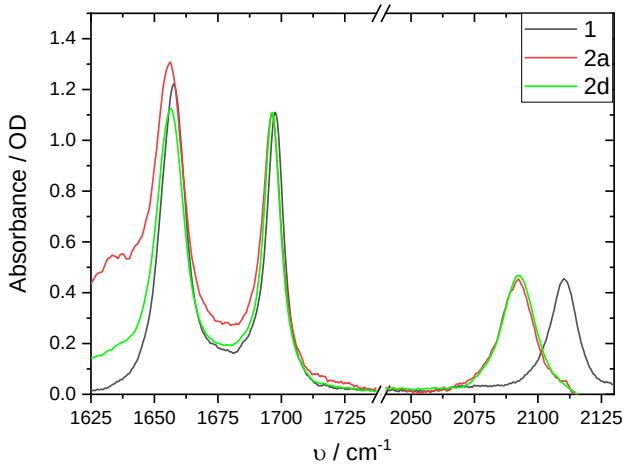

Figure 6: IR absorption spectra of 1, 2a, and 2d in CH_3CN.

Table 2: Experimental and TDDFT computed vibrational frequencies and computed IR intensities (*I*) for 1, 2a, and 2d in different electronic states in CH_3CN.

	$\nu_{C=O,as}$ / cm^{-1} (*I* / km/mol)	$\nu_{C=O,ss}$ / cm^{-1} (*I* / km/mol)	$\nu_{C\equiv C,as}$ / cm^{-1} (*I* / km/mol)	$\nu_{C\equiv C,ss}$ / cm^{-1} (*I* / km/mol)
		1		
GS DFT	1657.0	1698.7	2110.7	-
	(916)	(577)	(190)	
GS exper.	1657.5	1697.5	2110	-
		2a		
GS DFT	1655.3	1696.7	2091.5	2097.2
	(919)	(609)	(254)	(50)
GS exper.	1656.3	1696.5	2092	
^{S}CSS DFT	1593.1	1675.0	2026.6	2112.9$^{\#}$
	(11020)	(35741)	(435)	(180353)
^{S}CSS exper.	1580	1625	2035	
		2d		
GS DFT	1655.8	1697.3	2092.0	2099.9
	(919)	(609)	(287)	(7)
GS exper.	1656	1696.5	2092	
^{S}CSS DFT	1576.0	1641.7	2053.0	2070.4$^{\#}$
	(1648)	(10916)	(875)	(51988)
^{S}CSS exper.	1570	1610		2060

2.3.5 Time-resolved spectroscopy in the visible and infrared regions

TD-DFT analysis indicates that the CS state in **2d** (Figure 5) is essentially a pure charge transfer transition, involving 97.2% *D*(HOMO)→*A*(LUMO) orbitals, while in **2a** (Figure 4) it is only 91% charge transfer in character with 8.4% NAP-based transition (the same transition that dominates the NAP-based bright state). The stronger mixing in **2a** is due to a closer energy match between the pure NAP-based bright state and the pure CS state. These calculations support the observations that $\nu_{C\equiv C}$ (CS state) and $\nu_{C=O}$(NAP$^-$) peaks are much stronger in **2d** than in **2a** (Table 2) The larger extent of CS state formation in **2d** compared to **2a** explains the larger red shift of its $\nu_{C\equiv C}$ band (Figure 7b). The $\nu_{C=O}$(NAP$^-$) peaks of **2d** are also more red-shifted than those of **2a** (Figure 7a).

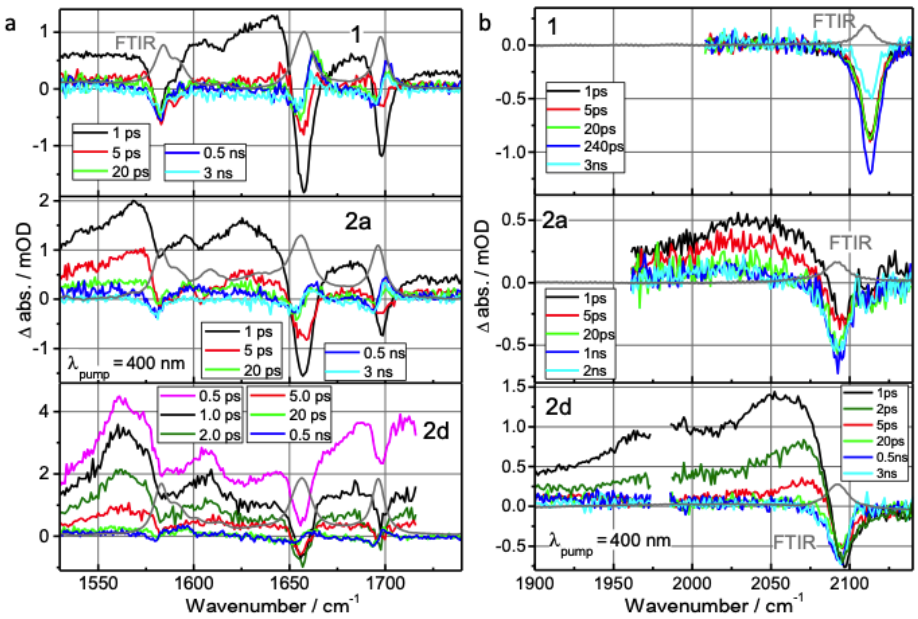

Figure 7: Transient absorption spectra for 1, 2a and 2d in CH_3CN in the (a) 1500 – 1740 cm^{-1} and (b) 1900 – 2130 cm^{-1} mid-IR regions. The time delays are indicated as insets.

The spectral dynamics are different for **2a** and **2d**. For **2d**, formation of the CS state is time resolved in the visible and IR regions, manifesting as rising components with different spectral shapes compared to those of the bright excited state prepared with a 400 nm pump. The rising components are most pronounced in the visible region (Figure 8b) and for the 1570 cm^{-1} peak (Figure 9b). The decay-associated spectral (DAS) analysis allows identification of the principle decay components common for kinetics at all wavelength.[47, 48] The DAS analysis of the early-time dynamics for **2d** resulted in three sizable principal components, one rising and two decaying (Figure 8b). The DAS spectrum of the rising (0.25 ± 0.05 ps) and first decaying (0.83 ± 0.1 ps) components are similar, suggesting rapid formation of a new state with dominating absorbance followed by its decay. The DAS spectrum of the slower decay component (3.6 ± 0.4 ps) is broad, resulting in a red shift of the spectrum. The two decay times are similar to the decay times of the C=O bleach peak decays and are associated with formation of a LLS (Figure 9c), suggesting that no other electronic excited states are formed.

In **2a** the visible decay-associated spectra for early-time dynamics resulted in two principal decay components (Figure 8a); the two components, 0.68 and 7.7 ps, with similar DAS spectra indicate that both belong to the same species, while the state dynamics is not single exponential. It is conceivable, that the formation of the CS state in **2a** occurs faster than the instrumental time resolution (<100 fs). This hypothesis is supported by TD-DFT analysis that shows mixing of the CS state and pure bright states in **2a**, which is expected to facilitate the electronic transition (Figure 4).

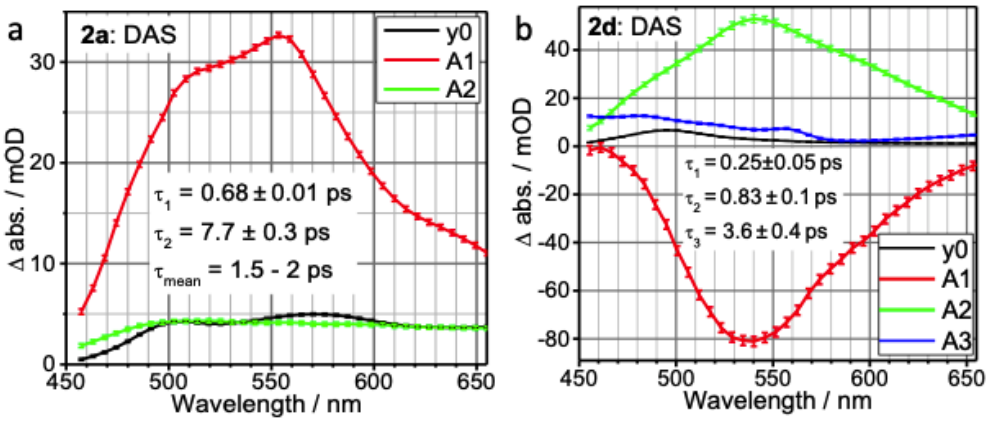

Figure 8: Decay associated spectra for 2a (a) and 2d (b) constructed for the spectral dynamics within 60 ps window.

The vibronic dynamics in the mid-IR region is masked by a broad featureless absorbance across the fingerprint region, observed in all three compounds (Figure 7 bottom). Such broad absorbance, reported previously for Pt-bis-alkynyl-NAP compounds, was attributed to transitions between closely spaced electronic states.[49-54] In **1** and **2a,** the broad absorption decays rapidly (0.1-0.2 ps, Fig. S8), not preventing the assignment of the vibrational peaks. However, in **2d** the broad absorption (BA), in addition to a fast component of ca. 0.2 ps, features a relatively slow component of ca. 1.0 ps (Figure 9b), which significantly masks the dynamics on this same time scale (0.8 and 4 ps, Figure 8b). The broad featureless spectrum has a uniform amplitude across the 1680 – 2120 cm^{-1} region, which permits its subtraction from the signals at frequencies of characteristic vibrational transitions (C=O GSB, 1670 cm^{-1}, and at 2000-2100 cm^{-1}, Figure 9b). A global fit of the resulting kinetics produces the 0.25 ± 0.1 ps rise, 0.9 ± 0.2 ps and 4.1 ± 0.2 ps

decay time constants (Figure 9b), which are similar to those obtained in the DAS analysis in the visible region (Figure 8b).

The spectral dynamics for **2a** in the mid-IR is much simpler than that for **2d** featuring only a broad ultrafast component with an 8 ps decay (Figure 9a). Because of the time constant separation, no broad background subtraction was necessary for **2a**.

The C≡C peaks of the CS state in **2a** and **2d** are extremely broad likely because of the wide distribution of dihedral angles between the donor and acceptor planes (θ) in the ground electronic state, which affects the *D-A* coupling strength and the extent of mixing. It is expected that the coupling is stronger for more planar *D-A* conformations (small θ angle), resulting in a larger dipole moment for the CS state. The decay times for **2d** (with dominant components between 0.9 and 4 ps, Figs. 9b, 10b) are attributed to the process leading to a non-polarized bridge – a charge recombination (CR) process. It is apparent that the CR process is faster in the more planar conformations (Figure 7b), but the difference is not large. Note that the spectral diffusion associated with the θ angle change in the CS state is not expected to contribute at the time window of 5 ps in **2d** due to the relatively larger size of its donor moiety.

The C≡C peak in the CS state of **2a** decays slower than that for **2d** with the dominant component of ca. 8 ps, which matches its C=O GSB recovery time (Figure 9a). The C≡C peak shifts to slightly lower frequencies with time (Figure 7b). The shift can be associated with the solvation dynamics further stabilizing the CS state. The red shift may also be influenced by differences in the CR rates at different θ angles, such that the decay

is slower for conformations with smaller θ angles having red-shifted peaks, but the contributions of different relaxation processes are difficult to specify.

As noted earlier, the antisymmetric C≡C stretching mode dominates the spectrum in the GS, as the two ethynyl arms are exposed to a similar charge environment with the unit positive charge at the Co center and close to zero charges at the donor and acceptor moieties. However, in the CS state, the ethynyl mode at the acceptor side dominates the spectrum as the mixing of the two CC modes is reduced. Our population DFT analysis indicates that the Co center still carries about a unit charge in the CS state, while the electron is transferred from the donor to the acceptor moieties making the ethynyl group at the acceptor side polarized much stronger than that at the donor side and resulting in its dominant contribution to the C≡C IR intensity (Table 2).

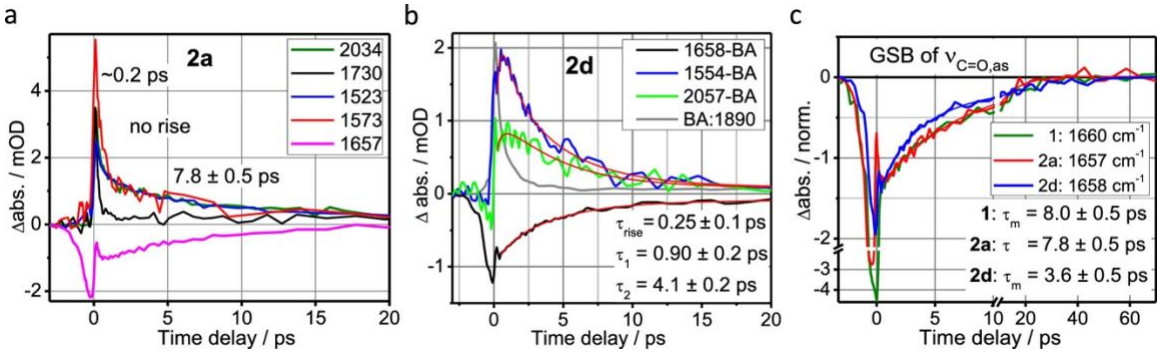

Figure 9: Transient kinetics for 2a (a) and 2d (b) at indicated frequencies (in cm^{-1}), normalized in (a) to show a match in characteristic decay times. The decay times of characteristic components are indicated on the graphs. Global fit results are shown in panel b with red lines. (c) Normalized transient $\nu_{C=O,as}$ kinetics for 1, 2a, and 2d at indicated frequencies (thick lines) and their fits with two-exponential functions (thin lines of matching colors). Mean decay times are shown as inset while the fit parameters are: 1: 3.6±1.5 ps (40%) and 10.9±2.4 ps (60%); 2a: 7.8±0.5 ps; 2d: 0.9±0.2 ps (17%) 4.1 ± 0.2 ps (83%).

Solvation, vibrational relaxation, and structural relaxation each complicate the dynamics, producing variations in kinetics at individual wavelengths. Figure 10 is consistent with all major spectroscopic observations.

$$\mathbf{1}: \quad \mathrm{GS} \xrightarrow{400\ \mathrm{nm}} {}^{1}\mathrm{NAP} \xrightarrow{8\ \mathrm{ps}} {}^{3}\mathrm{Co(cyclam)}$$

$$\mathbf{2a}: \quad \mathrm{GS} \xrightarrow{400\ \mathrm{nm}} {}^{1}\mathrm{NAP}^{\&} \underset{\mathrm{CS}}{\overset{<0.1\ \mathrm{ps}}{\longleftrightarrow}} {}^{1}\mathrm{CSS} \underset{\mathrm{CR}}{\overset{8\ \mathrm{ps}}{\longrightarrow}} {}^{3}\mathrm{Co(cyclam)}$$

$$\mathbf{2d}: \quad \mathrm{GS} \xrightarrow{400\ \mathrm{nm}} {}^{1}\mathrm{NAP}^{\&} \underset{\mathrm{CS}}{\overset{0.25\ \mathrm{ps}}{\longrightarrow}} {}^{1}\mathrm{CSS} \underset{\mathrm{CR}}{\overset{4\ \mathrm{ps}}{\longrightarrow}} {}^{3}\mathrm{Co(cyclam)}$$

Figure 10: Summary of the excited-state dynamics in 1, 2a, and 2d. ^{1}NAP$^{\&}$ denotes the NAP bright state with partial *D*(HOMO)→*A*(LUMO) contribution.

The long-lived state can be assigned to ^{3}Co(cyclam) or ^{3}NAP. TD-DFT analysis shows that the Co-based triplet state is lower in energy than the ^{3}NAP state (Figure 10). The vibrational frequencies of the NAP carbonyl modes were computed in both states. In the ^{3}Co(cyclam) state these frequencies differ from those in the GS by only a few wavenumbers, as observed experimentally. The C=O frequencies in a ^{3}NAP state were assessed in a fully organic compound, Ph-C_4-NAP, showing formation of the ^{3}NAP state. The C=O frequencies in the ^{3}NAP state are found to be ca. 50 cm^{-1} lower than the respective GS frequencies. Characteristic C=O frequencies for the ^{3}NAP state were reported at 1590, 1640 and 1950 cm^{-1} by Weinstein and co-workers.[8, 49, 55, 56] The absence of significant peaks at these frequencies in the transient IR absorption spectra of **2a** and **2d** (Fig. 7) eliminates the possibility of the ^{3}NAP state being the LLS and corroborates the assignment of ^{3}Co(cyclam). The presence of low lying Co-based triplet and quintet states were found previously.[32] The Co-based quintet ($^{5}T_1$) state in $[Co(III)(en)_3](ClO_4)_3$ (en =

ethylenediamine) was reported at energies below 900 nm.[34] Therefore, the LLS was assigned as the ^{3}Co(cyclam) state.

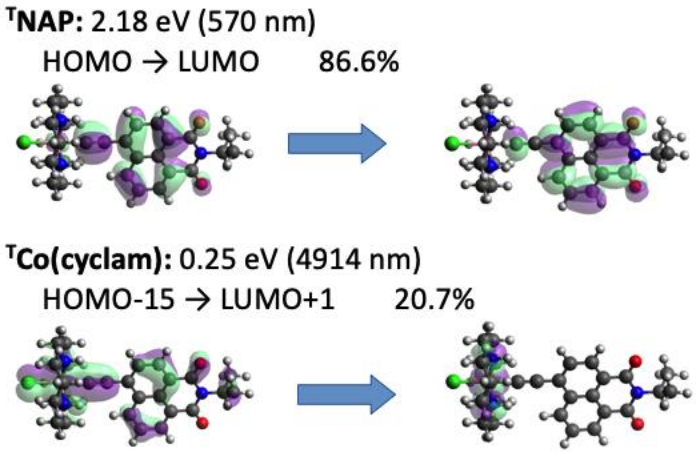

Figure 11: TD-DFT results showing the dominant orbital contribution to the ^{T}NAP and ^{T}Co(cyclam) state for compound 1. The transition energy and wavelength are shown.

2.3.6 Summary

Through stepwise addition of alkynyls, dissymmetric Co(III) *D-B-A* complexes were obtained in respectable yields, enabling the probe of excited-state CS dynamics. Despite the presence of Co-based triplet states at lower energies, efficient CS occurs in compounds **2a** and **2d**. The fast CS is enabled by strong communication between the donor and acceptor mediated by the Co(cyclam) bis-alkynyl bridge. The low-lying Co-based states eventually serve as energy sinks, resulting in CR. The Co-centered excited state is very long-lived, relaxing to the GS with a characteristic time of 2 - 4 ns. The CS to CR rate ratios are 16 fold for **2d** (0.25 ps / 4 ps)$^{-1}$ and 80 fold for **2a** (0.1 ps / 8 ps)$^{-1}$. Further

CS studies involving more complex donors and/or acceptors are ongoing. If the CS in such systems remains efficient, the overall ET yield will remain high.

The *D-B-A* structures synthesized and studied here are appealing for future studies of IR induced rate modulation. When the ET reaction is slower than the lifetime of the vibrational mode targeted for ET rate modulation, the relaxation of the vibrational mode during the ET reaction makes it difficult to ascertain the origin of the ET modulation, to either the excited vibrational mode or the daughter modes of its relaxation. When the ET reaction is fast, limited vibrational relaxation occurs during the ET reaction. The CS rate in **2d** is expected to be faster than the vibrational relaxation, making **2d** an attractive target for the ET modulation studies. The CR reaction, although slower than the vibrational relaxation, is still fast enough to include only a few daughter modes into analysis. The alkyne bridges offer substantial interactions among the *D*, *B* and *A* moieties, suggesting that IR excitation of the bridge modes could strongly influence interactions among the subunits and thus perturb the ET kinetics. This hypothesis will be explored in future studies.

2.4 Symmetry controlled photo-selection and charge separation in butadiyne-bridged donor-bridge-acceptor compounds

Compounds featuring conjugated bridging motifs attract strong interest because these bridges enable significant coupling of the localized electronic states. Compounds of this kind enjoy applications as light harvesting chromophores,[57-59] nonlinear absorbers

and optical limiters,[60-62] as well as generators of application for photoinduced charge separation (CS).[63, 64]

A range of conjugated bridge structures appears in donor-bridge-acceptor (DBA) compounds, including alkenes,[65-70] phenylenes,[71-73] stilbenes,[74] and alkynes,[75-80] as well as motifs with more extended or mixed π structures.[11, 81-86] Alkyne bridges are particularly attractive as they offer compact, linear structures that supports conjugation. While rather rigid with respect to bending, alkyne bridges feature small barriers to torsional rotation of the D and A moieties, producing a wide distribution of dihedral angles in the ground state (GS).[87]

Compounds with butadiyne bridges that link weakly reducing donor and weakly oxidizing acceptor moieties were developed as chromophores and broad-band white-light fluorophores.[88] The large emission frequency width in these compounds originates from contributions of locally excited and partially charge-separated states.[88-90] The high emission quantum yields in these systems suggests that their extent of charge separation is low.

Here, we explored the excited state and electron transfer properties of compounds where D and A are linked by a butadiyne (C4) bridge. A strong electron acceptor (NAP) was used with donors of various oxidation potentials, including a rather strongly reducing electron donor. Compounds of this kind have the potential to serve as

"smart" chromophores responding to the environment, where photoinduced electron transfer (ET) rates may be modulated by external stimuli.

The torsion angle distribution in butadiyne bridged compounds is expected to depend on the nature of the bridging moieties. The Albinsson and Anderson groups measured and computed the rotation free energy barriers in butadiyne bridged metal porphyrins,[87, 91] finding the rotational barriers to be less than $k_B T$ and that the planar conformations are favored. They also found that porphyrin-to-porphyrin coupling produces excited states that are fully delocalized on the porphyrins in the planar geometries, while orthogonal conformations of the porphyrins are electronically decoupled.[92, 93] The noted sensitivity of the electronic coupling to the torsion angle influences the absorption spectra, allowing selective excitation of either planar or orthogonal conformation in the Q or Soret band of the porphyrin (P).[92, 93] Planarization in P-C4-P chromophores was achieved by axial ligation with a specially designed ligand that chelates both porphyrins. This butadiyne linked porphyrin dimer was also used as a bridge linking a ferrocene donor with a C_{60} acceptor.[92] Both CS and charge recombination (CR) rates were found to be significantly slower in the structures with orthogonal porphyrins.[92]

A large number of studies has examined the dihedral angle dependence of the electronic couplings in poly-phenylene bridged DBA structures.[94-98] For example, studies of Harriman and coworkers[99] used an elegant tethered strap approach to study

how the torsion angle between two phenyl moieties in C_2-Ph-Ph-C_2 bridges influences electronic couplings. Connecting a $Ru^{II}(tpy)_2$ / $Os^{II}(tpy)_2$ donor-acceptor pair with this bridge, they found a dramatic decrease in the electronic coupling for the species with a 90° torsion angle between the two phenyl rings.[99]

The ET rate between a donor and acceptor is influenced by the electronic coupling (in the non-adiabatic or weak coupling regime), the reorganization energy, and the reaction free energy.[100] The bridge electronic structure and DA separation distance determine the electronic coupling.[101-103] The torsion angle between the D and A has a particularly strong influence on the bridge-mediated DA coupling, and extensive theoretical and experimental studies have characterized the bridge-mediated coupling.[93, 104-106]

A particularly useful feature of the alkyne bridges is that they can support DBA conformations with a symmetry plane (C_s) for the D and A moieties being either coplanar and orthogonal. As a result, the interactions among the D and A localized frontier orbitals may be tuned, and the nature of the optical excitation, charge separation, and recombination can be controlled. Here, we demonstrate a unique feature of the alkyne bridged DBA compounds where symmetry defines the excited state and ET properties, making this class of DBA species attractive targets for ET rate modulation through conformational control via external stimuli.[4, 5, 107, 108]

Alkyne bridges can support strong bridge-mediated coupling of D and A electronic states. If the CS state in these species is coupled strongly to a D- or A-localized state, the coupling produces eigenstates, that are an equal mixture of the two diabatic state wavefunctions.[109] This mixing can reduce dramatically the CS character of the two eigenstates, limiting it to only 50% (Figure 12a). To increase the CS state character with a fixed coupling strength, the energy gap between the diabatic CS and D- or A-localized state(s) has to be increased to become larger than the coupling energy, thus eliminating the strong coupling condition (Figure 12b). This can be achieved, for example, by using a more strongly reducing electron donor, thus lowering the diabatic CS state energy (Figure 12b), or by selecting a more polar solvent which will stabilize the radical cation / radical anion charge separated state. The dihedral angle between D and A, θ, is a key determinant of the electron coupling strength and the non-adiabatic ET rate.

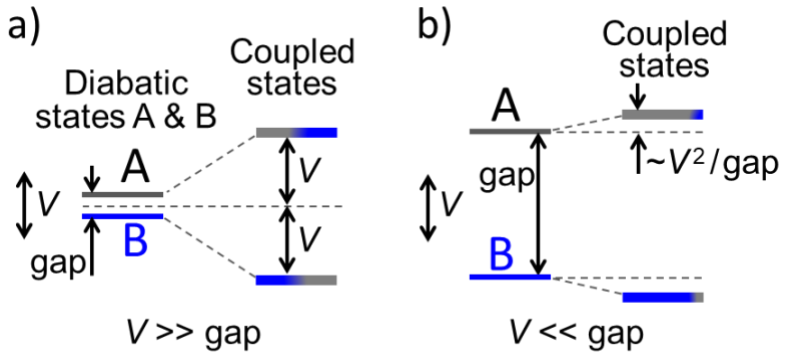

Figure 12: Coupled states for strong (a) and weak (b) coupling regimes, defined by the relation between the diabatic state (A, B) interaction energy, *V*, and their energy gap.[110]

The novel butadiyne (C4) bridged DBA structures studied here have an *N*-isopropyl-1,8-napthalimide (NAP) acceptor and various donors (Figure 13). Femtosecond-nanosecond transient absorption measurements in the visible and mid-IR regions following 400 nm excitation were performed for Si-C4-NAP, Ph-C4-NAP and D-C4-NAP in dichloromethane (DCM) and toluene solvents. Transient mid-IR spectra of the C≡C bridge stretching modes were found to be critical for understanding the excited state electronic dynamics. Formation of a highly polarized state, namely the charge separated state (CSS), was observed in D-C4-NAP. Vibronic relaxation, charge separation, dihedral angle (θ) equilibration, charge recombination, and triplet state formation were tracked in the excited electronic states. TD-DFT analysis of the excited electronic states and normal mode analysis enabled the assignment of the observed dynamics to specific electronic transitions. We have shown that the torsional barrier to rotation in the ground state is less than $k_B T$, providing access to a wide range of dihedral D-A angles. Excited state dynamics, including CS, is strongly influenced by the dihedral angle. The observations are rationalized, as well, based on frontier orbital symmetry. Interestingly, the torsional motion, and the associated spectroscopic changes, allows interrogation of the ET dynamics associated with molecular sub-populations.

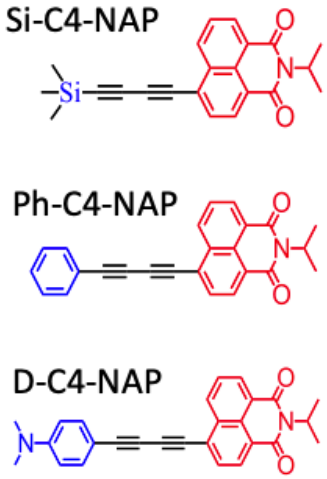

Figure 13: Structures of the butadiyne-bridged compounds studied.

2.4.1 Experimental details

Experimental details can be found elsewhere.[111] Major experimental results are included to facilitate the interpretation of the computational results.

2.4.2 Computational details

DFT and TD-DFT calculations for Si-C4-NAP, Ph-C4-NAP and D-C4-NAP were performed using the MN15 functional[38] and the Def2-SVP basis set[39] as implemented in Gaussian 16.[40] The MN15 functional was chosen based on its close agreement with the experimental vibrational frequencies and electronic spectra. The CAM-B3LYP functional[43] was also tested and showed similar results. The polarizable continuum model (PCM)[41] was used to simulate the solvent effects of toluene and dichloromethane in the DFT and TD-DFT analysis. Torsion angles of 0, 15, 30, 60, 75, and 90° between D and A moieties were fixed to evaluate the influence of torsion angle on the vibrational

spectra and electronic couplings. For cases where torsional conformations do not correspond to energy minima, projected frequencies were calculated.[112]

Electronic couplings between the S_1 and S_2 states (H_{ab}) were calculated using the generalized Mulliken-Hush (GMH) method:[113]

$$H_{ab} = \frac{\mu_{12}\Delta E_{12}}{\sqrt{(\mu_1 - \mu_2)^2 + 4{\mu_{12}}^2}} \tag{13}$$

Here, μ_{12} is the transition dipole moment between the S_1 and S_2 state, ΔE_{12} is the energy difference between the S_1 and S_2 states, μ_1 is the S_1 dipole moment, and μ_2 is the S_2 dipole moment. The transition dipole moments between excited states were computed in Dalton 2018[114] using quadratic response theory with the CAM-B3LYP functional, and the same basis set was used as in the TD-DFT analysis. Dipole moments and energy differences were obtained from TD-DFT calculations with the MN15 functional.

2.4.3 Steady-state absorption and emission spectra

The absorption and normalized emission spectra of the three compounds studied are shown in Figure 14. A clear mirror image of the emission spectra with preserved vibrational structure is found for the Si-C4-NAP and Ph-C4-NAP emission and absorption spectra in both toluene and DCM solutions. The Stokes shift is small (~1000 cm^{-1}) and essentially solvent independent for Si-C4-NAP (Fig. 2a), indicating that both the ground and relaxed excited states are only weakly polarized. For Ph-C4-NAP, the absorption spectrum changes weakly with solvent polarity, indicating small polarization of the ground state. However, both the emission spectrum and the Stokes shift for Ph-

C4-NAP depend strongly on the solvent polarity (Figure 14b), indicating significant solvent reorganization to accommodate a polarized excited state. With an increase of the donor strength in D-C4-NAP, a new absorption peak appears at lower frequencies, red-shifted by ca. 5000 cm^{-1}. The absorption peak width is sensitive to the solvent polarity, indicating a larger polarization of the Frank-Condon excited state, compared to that for Ph-C4-NAP. The Stokes shift for D-C4-NAP is extremely large and solvent dependent, reaching 7000 cm^{-1} in DCM. This shift indicates very high polarization of the excited state (Figure 14c) and suggests that the charge-separated state is observed directly in the linear absorption and emission spectra. The TD-DFT calculations confirm that the CSS in D-C4-NAP is indeed a bright state, deriving its oscillator strength from a higher-energy electronic state, S_3. Interestingly, this electronic state (S_3) is similar to the lowest energy NAP-based excited state observed for Si-C4-NAP (Figure 15 and Figure 16).

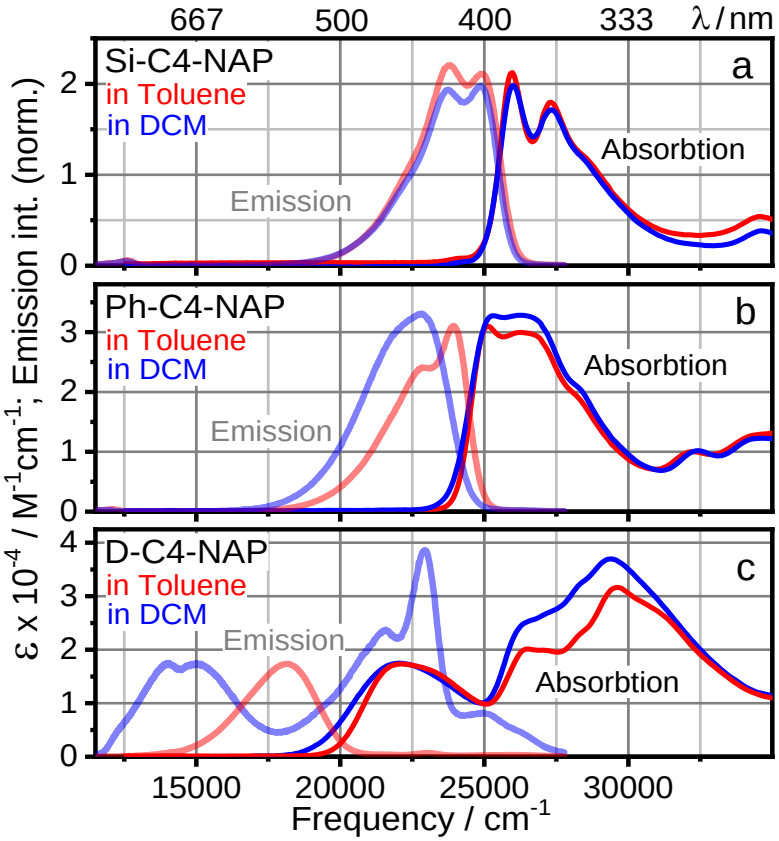

Figure 14: Absorption (bright lines) and emission (light lines, λ_{exc} = 340 nm) spectra of (a) Si-C4-NAP, (b) Ph-C4-NAP, and (c) D-C4-NAP in toluene (red lines) and DCM (blue lines).

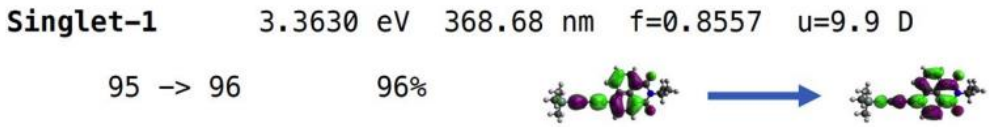

Figure 15: TD-DFT results showing the dominant orbital contribution to the S_1 state for Si-C4-NAP in DCM. The transition energy, wavelength, oscillator strength (*f*) and dipole moment are shown.

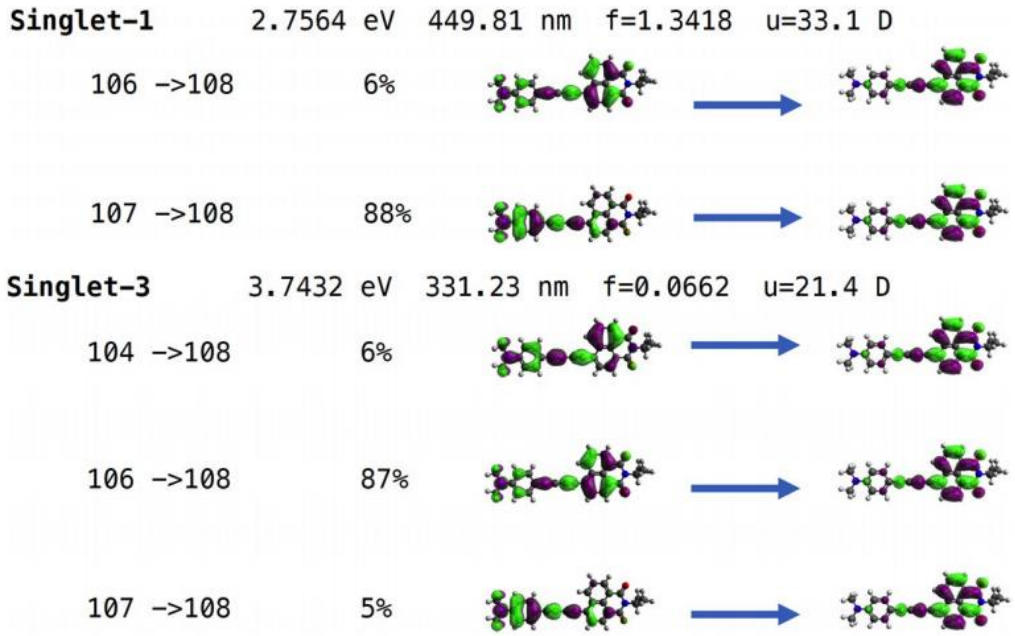

Figure 16: TD-DFT results showing the dominant orbital contribution to the S_1 and S_3 state for D-C4-NAP in DCM. The transition energy, wavelength, oscillator strength (*f*) and dipole moment are shown.

The vibrational absorption spectra (FTIR) of the three compounds studied here feature several strong vibrational transitions (Figure 17), including symmetric and asymmetric carbonyl stretching modes of NAP (ν_{ss}(C=O), ν_{as}(C=O), see labels in Figure 17c) and two strong phenyl (donor) and naphthyl (NAP) ring deformation modes around 1600 cm^{-1}, involving CC stretching and CH in-plane bending at the two moieties. The lower frequency peak of the two (~1589 cm^{-1}) belongs mostly to NAP and is present for all three compounds. The higher frequency peak (1604 cm^{-1}) is mostly located at the donor moiety and is strong only in D-C4-NAP. Despite large distance between the phenyl and naphthyl moieties of ca. 6.7 Å, the DFT calculations revealed a partial (10-

20%) mixing of the donor and acceptor vibrational modes, suggesting that their conjugation-facilitated coupling is ca. 3 cm^{-1}.

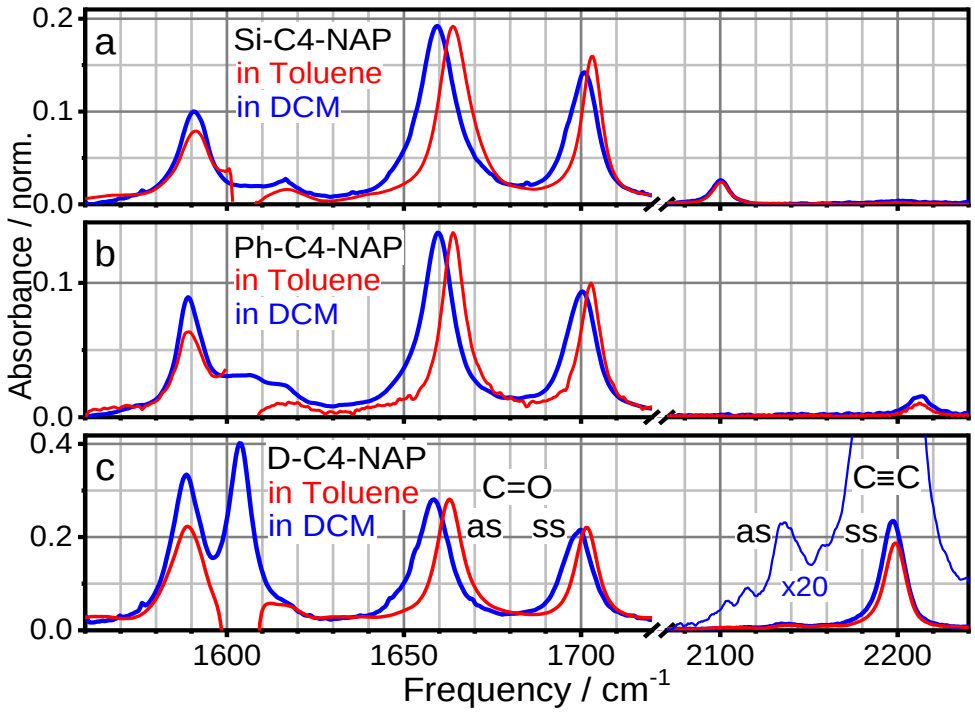

Figure 17: Solvent subtracted FTIR absorption spectra of the three compounds amplitude normalized at the C=O as mode. Strong toluene absorption at ca. 1605 cm^{-1} prevented accurate measurements in this region.

The butadiyne (C4) bridge features two strongly delocalized $\nu_{C\equiv C}$ stretching normal modes – symmetric ($\nu_{C\equiv C,ss}$) and antisymmetric ($\nu_{C\equiv C,as}$). However, a single vibrational absorption peak dominates the spectrum for each compound, typically arising from a symmetric stretching mode. For example, for D-C4-NAP, the peak at 2198 cm^{-1} arises from $\nu_{C\equiv C,ss}$, while the $\nu_{C\equiv C,as}$ peak is seen at 2136 cm^{-1} (computed at ~2254 cm^{-1} wihout a scaling factor) with ca. 20-fold weaker IR intensity (Figure 17c, thin blue line, Table 3 for DFT).

Table 3: TD-DFT computed vibrational frequencies and IR intensities (*I*) for D-C4-NAP in toluene and DCM in the ground and excited states at θ = 0.

States	$\nu_{C=O,as}$ / cm^{-1} (*I* / km/mol)	$\nu_{C=O,ss}$ / cm^{-1} (*I* / km/mol)	$\nu_{C\equiv C,as}$ / cm^{-1} (*I* / km/mol)	$\nu_{C\equiv C,ss}$ / cm^{-1} (*I* / km/mol)
		In toluene		
S_0	1793.6 (594)	1831.5 (571)	2257.7 (45)	2328.4 (1602)
		In DCM		
S_0	1781.2 (812)	1823.5 (693)	2254.1 (101)	2322.3 (2152)

For the Ph-C4-NAP species, the peak at ca. 2212 cm^{-1} arises from a symmetric stretching mode; it is much weaker than the corresponding mode for the D-C4-NAP species (Figure 17b). A similarly weak single $\nu_{C\equiv C}$ peak is found for Si-C4-NAP at ~2100 cm^{-1}; it arises from an antisymmetric stretching mode (Figure 17a). The IR intensity of $\nu_{C\equiv C,ss}$ for Ph-C4-NAP and D-C4-NAP derives from light-induced polarization of the molecule across the bridge in the GS. This polarization is indicated from the shift in the C≡C peak frequency for D-C4-NAP in the more polar DCM solvent (Figure 17c). Transient absorption spectroscopy in the mid-IR and visible spectral regions, and DFT calculations, were employed to understand the charge distributions in these compounds and the excited state dynamics.

2.4.4 Transient absorption spectroscopy in the mid-IR and visible spectral regions

Figure 18 shows transient absorption spectra of the three compounds in the visible (left) and mid-IR spectral regions (middle) at selected delay times (see insets)

following excitation at 400 nm. The spectral changes are measured over a time window ranging from sub-picoseconds to ca. 3.5 ns. The spectral changes in the visible range are large in all compounds. Except for D-C4-NAP in DCM, these transient features do not decay to zero at large pump - probe delay times, revealing the formation of a long-lived state and the absence of the GS recovery. This long-lived state is assigned to a NAP localized triplet state (^{T}NAP), based on the similarity of the transient features in all three compounds, including the Si-C4-NAP species that lacks a donor group, the long lifetime of the state that exceeds 10 ns, and the characteristic changes of the NAP C=O frequencies that both experience a ca. 50 cm^{-1} red shift compared to the GS frequencies. These observations are consistent with the DFT-computed $\nu_{C=O}$ changes for the ^{T}NAP state (Table 4).

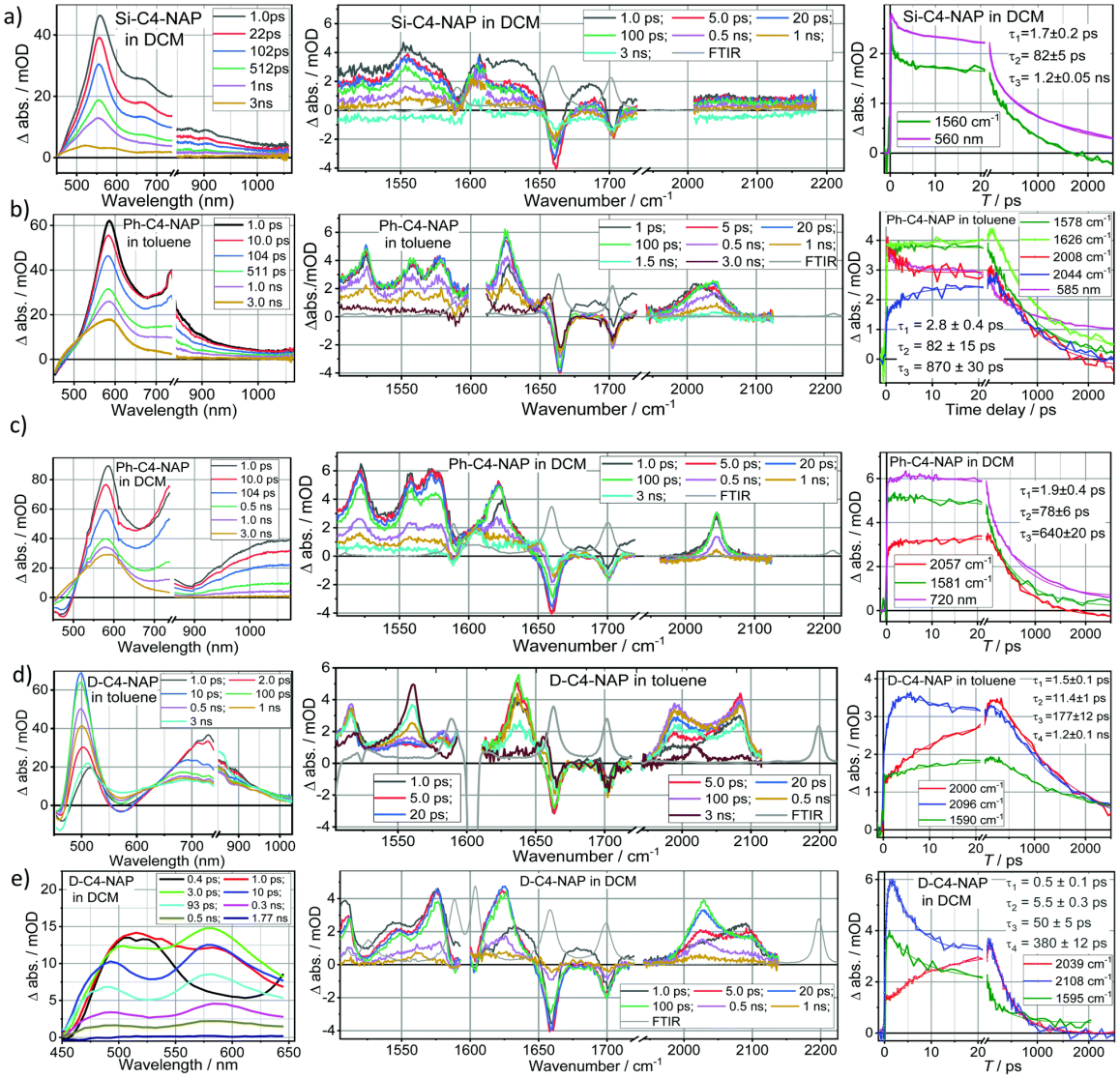

Figure 18: Transient spectra in the visible (left panel) and mid-IR (middle panel) regions for Si-C4-NAP (a), Ph-C4-NAP (b, c), and D-C4-NAP (d, e) compounds in toluene and DCM (indicated) measured at indicated time delays following 400 nm excitation. The mid-IR transient spectra also show scaled linear absorption spectra (FTIR, grey line). Right panels show selected characteristic kinetics and the results of a global fitting with multi-exponential function (thin lines of matching colors); the resulting time constants are shown as insets.

Table 4: TD-DFT computed vibrational frequencies and IR intensities (*I*) for Si-C4-NAP in toluene and DCM in the ground and excited states at θ = 0.

States	$\nu_{C=O,as}$ / cm^{-1} (*I* / km/mol)	$\nu_{C=O,ss}$ / cm^{-1} (*I* / km/mol)	$\nu_{C\equiv C,as}$ / cm^{-1} (*I* / km/mol)	$\nu_{C\equiv C,ss}$ / cm^{-1} (*I* / km/mol)
		In toluene		
S_0	1795.7 (591)	1834.0 (456)	2224.3 (113)	2344.0 (2)
S_1(TD-DFT)	1745.2 (729)	1783.4 (960)	2104.2 (57)	2126.4 (0.5)
T_1 (variational)	1731.5 (497)	1790.0 (596)	1997.7 (363)	2152.1 (15)
		In DCM		
S_0	1783.3 (805)	1826.0 (566)	2221.9 (114)	2343.1 (2)
S_1(TD-DFT)	1728.5 (1056)	1771.9 (1422)	2107.9 (184)	2128.8 (4)
T_1 (variational)	1722.3 (723)	1780.7 (817)	1997.4 (519)	2150.7 (7)

The extent of the GS recovery in these compounds can be judged from the ground state bleaching (GSB) signals of the C=O stretching modes of NAP. Except for D-C4-NAP in DCM, where the GS recovery is complete within a nanosecond, only a partial GS recovery is observed for other compounds, apparent from the presence of the GSB peaks at ca. 1705 and 1665 cm^{-1} at large delay times of 1-3 ns. Therefore, the large changes in the transient visible spectra (Fig. 4a-d) in the ns time scale are associated with the formation of the ^{T}NAP state.

The observed transient spectral dynamics for Ph-C4-NAP and D-C4-NAP are consistent with the involvement of two singlet excited states featuring different polarization extents: for D-C4-NAP in both solvents the polarization extent in the S_1 state

is much larger than that in the S_2 state suggesting that the S_1 state is essentially the CS state (Figure 19b,c); the situation is reversed for Ph-C4-NAP in toluene whereas for Ph-C4-NAP in DCM the polarization extents of S_1 and S_2 are similar.

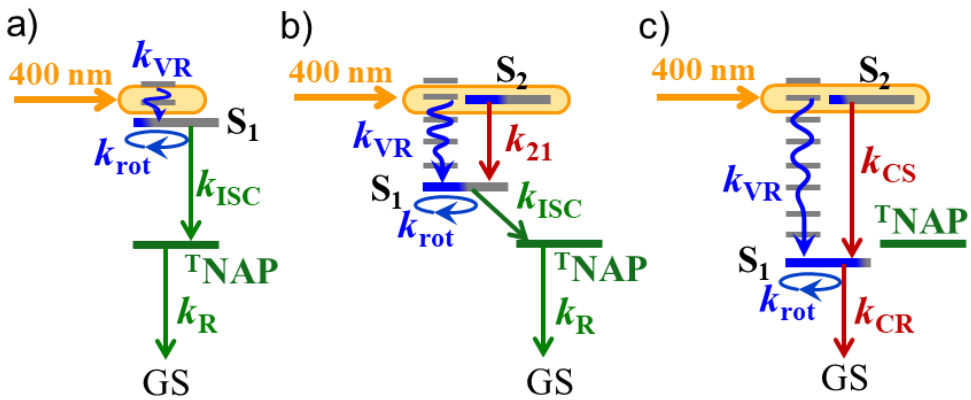

Figure 19: Three characteristic energy diagrams involving the states relevant for transient absorption with 400 nm excitation. Diagram a) is describes behavior of Si-C4-NAP in both toluene and DCM solvents involving a single singlet excited state, S_1. Diagram b) is characteristic for Ph-C4-NAP in both solvents and for D-C4-NAP in toluene, although the polarization extent for the states S_2 and S_1 varies for different systems. 400 nm radiation excites S_2 and vibrationally hot S_1 states. The triplet state is the lowest energy excited state for a) and b) panels. Diagram c) describes D-C4-NAP in DCM where the S_1 state, which is essentially the CSS, is the lowest energy state. The charge separation, k_{CS} = (5.5 ps)$^{-1}$ occurs much faster than charge recombination, k_{CR} = (0.38 ns)$^{-1}$; accumulation of the ^{T}NAP state is not observed.

2.4.5 Torsion angle distribution

DFT and TD-DFT computations were performed to characterize the excited states. The computations showed that in the GS, the planar conformation is the most energetically favorable, but the energy barrier to achieve 90° conformation is only ca. 25 meV (~200 cm^{-1}) for D-C4-NAP (Figure 20a); a similar barrier of ca. 170 cm^{-1} was recently measured for torsional motion of butadiyne-linked porphyrin dimers.[115] The low barrier

results in a broad distribution of θ conformations in the GS. Excited state computations showed that the oscillator strength for both S_1 and S_2 states depends strongly on θ and that the two dependences are complementary: for small θ angles the GS→S_1 transition is bright while the GS→S_2 transition is dark; opposite is observed for large θ angles: the GS→S_1 transition is dark while the GS→S_2 transition is bright (Figure 20b). As a result, the 400 nm pulses excite an S_1 state in compounds with small θ angles, producing a hot S_1 state with ca. 5000 cm^{-1} excess of vibrational energy, and an S_2 state in compounds with large θ angles. Note that 400 nm excitation wavelength is at the tail of the S_1 absorption peak, centered at 460 nm (Figure 14), so the S_2 state excitation at 400 nm is more efficient than the S_1 excitation. Normal modes were computed for the S_1 and S_2 states as a function of θ (Figure 20c). In the highly polar S_1 state, the frequencies of both C≡C modes decrease with an increase of the dihedral angle: the $\nu_{CC,ss}$ changes by ca. 150 cm^{-1} (Figure 20c), in agreement with the experimental observations. Very high IR intensities, exceeding 20000 km/mol, were found for the $\nu_{CC,ss}$ in the S_1 state, shown in Figure 20c with circles having diameters proportional to the IR intensity. The IR intensities of $\nu_{CC,as}$ in S_1 and of both $\nu_{CC,ss}$ and $\nu_{CC,as}$ in S_2 are about ten-fold smaller (Figure 20c, Table 5).

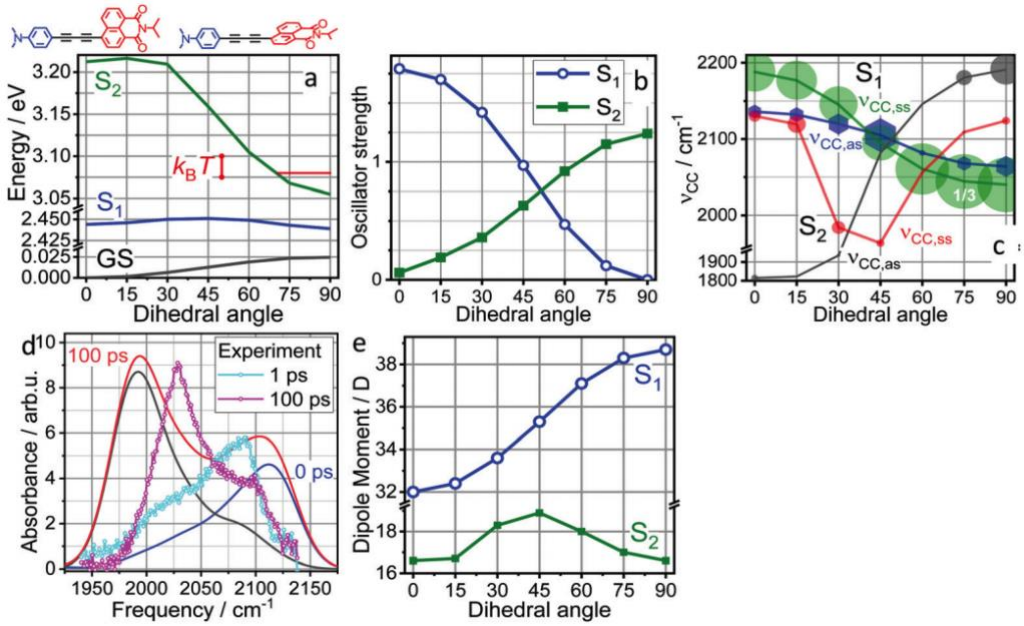

Figure 20: Analysis of D-C4-NAP at different dihedral angles. Energies (a) of the ground state (GS) and S_1 and S_2 singlet excited states and the S_1, S_2 oscillator strengths (b) as a function of the dihedral angle, θ, for D-C4-NAP in DCM. (c) Dihedral angle dependence of the $\nu_{CC,as}$ and $\nu_{CC,ss}$ frequencies for the S_1 (green and blue) and S_2 states (red and grey). The symbol sizes are proportional to the IR intensity of the mode (the IR intensities for the $\nu_{CC,ss}$ mode in the S_1 state were scaled by 1/3 factor not to overwhelm the graph. (d) Modeling of the absorption spectrum for the ν_{CC} modes at zero time (blue line) and at 100 ps (red line). The black line shows the contribution due to the $S_2 \rightarrow S_1$ relaxation. The experimental transient absorption spectra at indicated time delays are also shown. (e) Dipole moment of D-C4-NAP in DCM computed for the S_1 and S_2 states vs. the dihedral angle.

Table 5: TD-DFT computed vibrational frequencies and IR intensities (*I*) for D-C4-NAP with different dihedral angles in DCM in the ground and excited states.

Dihedral angle / degrees	$\nu_{C=O,as}$ / cm^{-1} (*I* / km/mol)	$\nu_{C=O,ss}$ / cm^{-1} (*I* / km/mol)	$\nu_{C\equiv C,as}$ / cm^{-1} (*I* / km/mol)	$\nu_{C\equiv C,ss}$ / cm^{-1} (*I* / km/mol)
Ground state				
0	1781.2 (812)	1823.5 (693)	2254.1 (101)	2322.3 (2152)
90	1782.4 (806)	1825.0 (597)	2255.6 (105)	2339.7 (854)
Excited state S_1				
0	1731.2 (1309)	1771.0 (3690)	2136.1 (1744)	2188.3 (16317)
15	1731.5 (1322)	1771.2 (3706)	2132.1 (1865)	2177.1 (15966)
30	1732.2 (1385)	1771.8 (3711)	2119.8 (2650)	2145.3 (15044)
45	1733.1 (1500)	1772.5 (3702)	2105.1 (4275)	2094.9 (14620)
60	1734.3 (1609)	1773.4 (3667)	2081.7 (803)	2060.8 (21051)
75	1735.2 (1654)	1773.8 (3617)	2068.0 (1850)	2044.3 (22509)
90	1735.3 (1671)	1773.9 (3573)	2063.9 (2661)	2040.0 (22483)
Excited state S_2				
0	1768.7 (962)	1794.2 (944)	1814.9 (869)	2130.3 (1557)
15	1765.0 (1041)	1797.0 (1986)	1822.4 (179)	2119.5 (2379)
30	1747.0 (1140)	1784.6 (2694)	1935.0 (463)	1984.0 (1749)
45	1732.2 (1089)	1772.4 (2212)	2081.8 (3)	1963.4 (1041)
60	1727.2 (1085)	1769.7 (1744)	2146.0 (178)	2056.0 (136)
75	1725.2 (1104)	1769.1 (1432)	2180.9 (2065)	2109.2 (430)
90	1724.2 (1110)	1768.8 (1327)	2191.4 (4112)	2124.2 (1051)

The C≡C absorption spectrum in the excited states was modeled at zero time and at 10 ps following excitation using the computed C≡C frequencies in the S_1 and S_2 states and their IR intensities, angular Boltzmann (θ) distribution of the ground-state conformations, and oscillator strengths of the S_2 and S_1 transitions. The relative population of the S_1 and S_2 states after 400 nm excitation was the only free parameter in the modelling (Figure 20d, solid lines). The modelling predicts double-peak shapes for both early time and 10 ps spectra with the red-shifted peak growing with time. The overall peak shifts are larger than those observed in the experiment, but the overall similarity between of the observed and simulated transients is impressive. While simple analysis of the experimental transient C≡C spectra may suggest that the two observed peaks originate from different excited states, mostly S_2 for the high frequency peak and mostly S_1 for the low frequency peak, the modeling indicates that both peaks originate predominantly from the S_1 state, just from different θ conformations.

2.4.6 Modeling of the spectral dynamics in m-IR

The initial C≡C peak found at small delays predominantly at 2090 cm^{-1} is mostly due to directly excited S_1 states, thus representing compounds with small θ angles. The $\nu_{CC,ss}$ frequency in S_1 for $\theta = 0 - 30^o$ is centered at ca. 2160 cm^{-1} (Figure 20c). The compounds featuring $\theta > 50^o$ are excited to the S_2 state; their relaxation occurs with a characteristic time of ca. 5.5 ps and results in formation of the S_1 states with the same θ angles. The red-shifted $\nu_{CC,ss}$ peak that appears at later time delays arises mostly from the

$\nu_{CC,ss}$ mode in the S_1 state for $\theta > 50^o$; it is centered at ca. 2055 cm^{-1} (Figure 20c). The calculations confirm that the observed C≡C peak alternation is caused by $S_2 \rightarrow S_1$ relaxation. There is a significant contribution to the blue C≡C peak from the $\nu_{CC,as}$ in the S_2 state with $\theta \sim 90^o$ (Figure 20c, gray line and circles). $S_2 \rightarrow S_1$ relaxation for such conformations produces a slight decrease in the high-frequency C≡C peak amplitude, as observed in the experiment.

To evaluate the extent of charge separation in the S_1 state, the dipole moment of the compound in the S_1 state was computed for various θ angles (Figure 20e). The dipole moment increases as θ approaches ca. 39 D, which corresponds to a separation distance of 8.1 Å for a full electron charge. Note that the bridge length is about 6.7 Å, indicating that the S_1 state for D-C4-NAP manifests complete charge separation. Figure 20e confirms that, for the CS state, the C≡C frequencies report the extent of charge separation: larger θ angles feature smaller $\nu_{CC,ss}$ frequencies and larger charge separation (Figure 21). Note however, that such correlation is not observed for acceptor-localized excited states featuring a small charge separation extent, as apparent for the S_2 state where strongly varying C≡C mode frequencies correspond to essentially the same dipole moment of the molecule (Figure 20, Table 6).

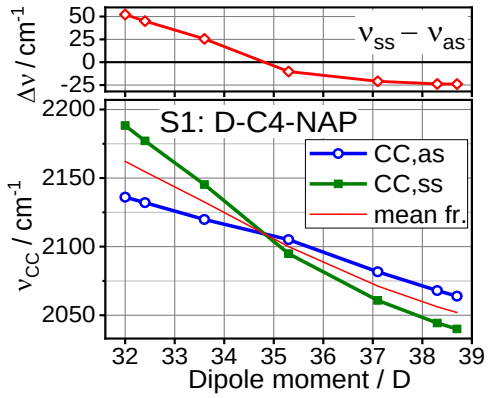

Figure 21: Analysis of $\nu_{CC,ss}$ and $\nu_{CC,as}$ mode frequencies. (Top) The frequency difference between $\nu_{CC,ss}$ and $\nu_{CC,as}$ as a function of the dipole moment of the D-C4-NAP compound in S_1 state, DFT computed in DCM. (Bottom) A correlation of the $\nu_{CC,ss}$ and $\nu_{CC,as}$ mode frequencies with the dipole moment of the compound.

Table 6: TD-DFT computed energy, dipole moment and oscillator strength at different dihedral angles for D-C4-NAP in DCM in the ground and excited states.

Dihedral angle / degrees	Energy / eV	μ / D	*f*
Ground state			
0	0.000	11.6	-
90	0.025	10.7	-
Excited state S_1			
0	2.444	32.0	1.79
15	2.446	32.4	1.70
30	2.450	33.6	1.42
45	2.451	35.3	0.97
60	2.449	37.1	0.47
75	2.443	38.3	0.12
90	2.439	38.7	0.00
Excited state S_2			
0	3.212	16.6	0.00
15	3.216	16.7	0.10
30	3.209	18.3	0.36
45	3.159	18.9	0.63
60	3.105	18.0	0.92
75	3.068	17.0	1.15
90	3.055	16.6	1.24

2.4.7 Symmetry origin of the S1-S2 oscillator strength variations with θ

To explore the reasons that the S_1 and S_2 oscillator strength alternates as a function of θ, we performed natural transition orbitals analysis.[116] The natural orbitals for $S_0 \rightarrow S_1$ and $S_0 \rightarrow S_2$ transitions at θ = 0° (left) and θ = 90° (right) are shown in Figure 22. The symmetry of the natural orbitals with respect to the plane perpendicular to the acceptor plane passing through the C4 bridge is indicated for each orbital. For θ = 0°, the $S_0 \rightarrow S_1$ transition is symmetry allowed involving symmetric orbitals, whereas the $S_0 \rightarrow S_2$ transition is symmetry forbidden, involving antisymmetric→symmetric and symmetric→antisymmetric orbitals (Figure 22) The principle is illustrated schematically in Figure 23. At θ = 90° the $S_0 \rightarrow S_1$ transition is forbidden (antisymmetric→symmetric), while the $S_0 \rightarrow S_2$ transition is allowed (symmetric→symmetric, Fig. 21). This analysis points to symmetry as the main reason behind the alternation of the oscillator strength in the S_1 and S_2 states (Figure 22).

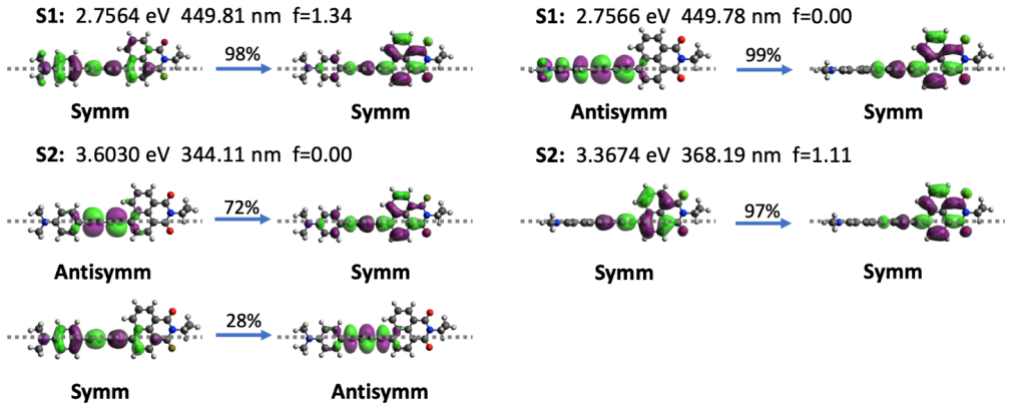

Figure 22: Leading natural transition orbitals for $S_0 \rightarrow S_1$ and $S_0 \rightarrow S_2$ transitions of D-C4-NAP with their contributions in % above the arrow. The transition energy (in eV), transition wavelength, and the oscillator strength (*f*) values are shown. The

symmetry of the orbitals with respect to the plane shown with dots is indicated. Note that the acceptor as a whole is not symmetric with respect to the plane; therefore, only the symmetry of the acceptor motif attached to the bridge is considered.

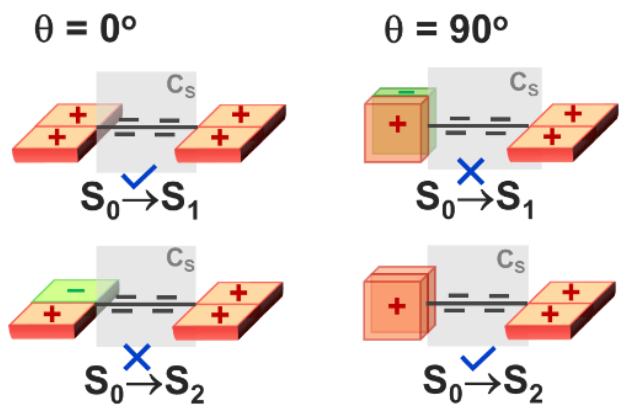

Figure 23: Cartoon illustrating how symmetry affects the electronic coupling between the ground and S_1, S_2 excited states.

Interestingly, the S_2 energy surface has a minimum at 90°, which is sufficiently deep (~$8k_BT$) to significantly alter the torsion angle distribution that existed in the GS (Fig. 7a). If the S_2 lifetime is comparable or longer than the internal rotational time, dynamic population of DBA conformations with larger θ angle will occur. Such orthogonalization may change the relaxation rate to S_1, depending on the angular dependence of the S_2 - S_1 coupling strength. The calculations, using the GMH approach,[113] revealed that the S_2 - S_1 coupling is the largest at θ ~ 30° and decreases monotonically towards both 0° and 90° (Figure 24). Therefore, the dynamic orthogonalization is capable of dramatically reducing k_{CS} for the D-C4-NAP compound. Under the conditions studied, however, the mean S_2 lifetime is shorter than the θ rotational time, preventing a clear observation of this effect.

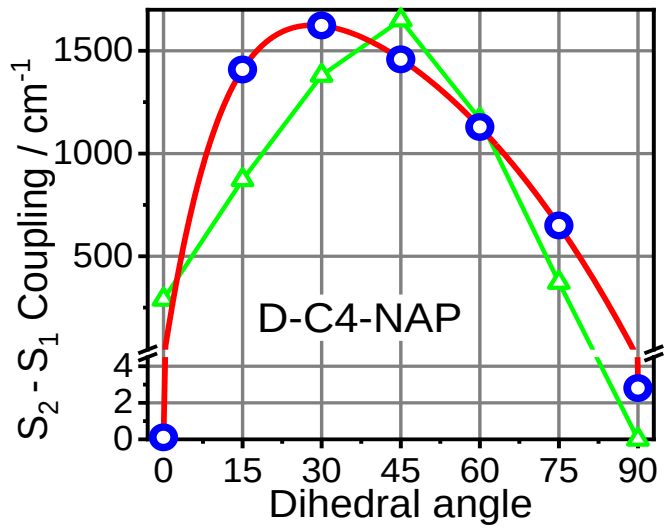

Figure 24: The TD-DFT computed S_2-S_1 coupling strength as a function of the dihedral angle, θ (blue circles and red line for eye guidance) for D-C4-NAP and the product of f_1 and f_2, the oscillator strengths of the S_1 and S_2 states, respectively (green).

2.4.8 S2-S1 electronic coupling varies with θ

The computed electronic $S_2 - S_1$ coupling is small at 0 and 90°, peaking at ca. 30° (Figure 24). The dependence of the coupling strength on θ originates with the orbital overlap between the donor and acceptor fragments as a function of angle. The small coupling strength at 0 and 90° can be understood in the context of the symmetries associated with the $S_0 \rightarrow S_1$ and $S_0 \rightarrow S_2$ transitions. At both 0 and 90°, S_1 and S_2 states feature opposite symmetries (Figure 20b), which result in near zero $S_2 - S_1$ couplings at these angles. The maximal coupling is realized at ca. 30°, where the symmetry is low and both transitions from the ground state are allowed. As a result, the S_2-S_1 coupling θ-dependence tracks the product of the f_1 and f_2 oscillator strengths (Figure 24, green, normalized).

Large values of the coupling strength at $\theta = 15\text{-}60^{o}$ suggest that the S_1 and S_2 states are mixed to a significant extent at these angles. A signature of this mixing is seen in the increase of the dipole moment of the S_2 state (Figure 20e). Adiabatic ET likely takes place at angles in this range. The ET process at smaller coupling strength ($\theta < 10^{o}$ and $>75^{o}$) is likely nonadiabatic. The Marcus theory ET rate with $G^{o} = -0.5$ eV and $\lambda_{total} = 1$ eV, $(k_{CS})^{-1}$ was computed at 4.6 ps for a coupling strength of 100 cm^{-1}, which corresponds to the angle of ca. 88°. It is surprising to see that the experimentally measured CS rates correspond to such a narrow window of torsion angles ($>83^{o}$).

To test the extent the butadiyne bridge can bend we performed DFT energy calculations at different bend angles for two torsion angles, 0° and 60° (Fig. S10). We found that the range of bend angles thermally accessible at room temperature is rather narrow ($165 – 180^{o}$). Moreover, the state energies and transition dipole moments are found to be weakly dependent on the bend angle (Figure 25). The results suggest that the analysis performed with the linear bridge structures is robust with respect to the bend angle deviations.

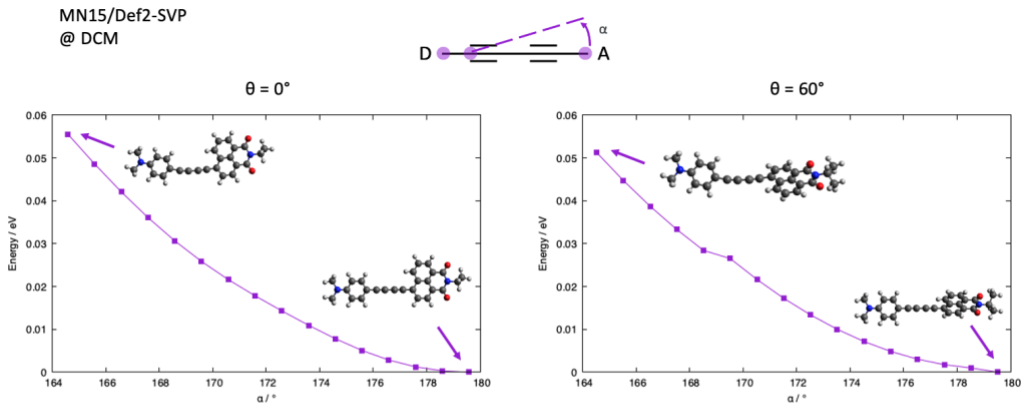

State	α = 165° Energy / eV	α = 165° f	α = 180° Energy / eV	α = 180° f
S1	2.75	1.27	2.76	1.34
S2	3.59	0.00	3.60	0.00
S3	3.74	0.09	3.74	0.07
S4	3.85	0.00	3.88	0.00

State	α = 165° Energy / eV	α = 165° f	α = 180° Energy / eV	α = 180° f
S1	2.75	0.47	2.76	0.39
S2	3.41	0.76	3.40	0.83
S3	3.81	0.38	3.84	0.49
S4	3.96	0.24	3.97	0.23

Figure 25: Bend angle analysis of D-C4-NAP. (Top) Ground state energies as a function of the bend angle α at two torsion angles θ of 0° (left) and 60° (right) for D-C4-NAP in DCM. (Bottom) The energies and oscillator strengths for S_1 - S_4 singlet excited states for two bend angles: α = 165° and α = 180°.

2.4.9 Summary

In summary, we characterized the excited state dynamics for a set of novel DBA compounds featuring a butadiyne bridge using transient absorption spectroscopy in the visible and mid-IR regions and electronic structure calculations. While the bridge, in general, enables strong state coupling and conjugation, we found that it is the symmetry of the frontier orbitals that plays the major role in identifying the coupling pattern among the electronic states. This symmetry is affected greatly by the dihedral angle. For the D-C4-NAP species, the symmetry dictates that the S_1 state is bright only for conformations with small dihedral angles, while the S_2 state is bright for conformations with large dihedral angles. This finding offers the opportunity to utilize photo-selection

upon excitation, such that while both S_1 and S_2 states became excited at specific excitation wavelength, the dihedral angles in the S_1 and S_2 states are very different. For example, with 400 nm excitation of D-C4-NAP the S_1 state will possess small dihedral angles, while S_2 electronic excited states will possess large dihedral angles close to 90°. Note that this photoselection is different from an ability of selecting particular geometries by exciting at different frequencies. We have shown that the S_1 state in D-C4-NAP is predominantly the CSS, characterized by a θ-dependent dipole moment of 32 – 39 D, with the largest value at θ = 90°. Moreover, the frontier orbital symmetry affects greatly the coupling of the S_2 and S_1 states; the coupling at θ = 90° was computed to be ca. 500-fold smaller than that at θ = 30°. The $S_2 \rightarrow S_1$ relaxation, which constitutes a CS reaction, occurs with different rates for different dihedral angles. An indication of the rate distribution was observed in variations of the CS rates obtained from fitting of kinetics at different observation wavelengths. The mean values for k_{CS} were measured at ca. 5.5 and 11.4 ps for D-C4-NAP in DCM and toluene, respectively. An additional component of 50 – 180 ps was observed from the global fit of the transient data. This time component is assigned to the rotational motion resulting in the changes of the dihedral angle, θ. Because of at least an order of magnitude difference between k_{CS} and k_{rot}, the influence of the rotation onto the CS process has not been observed clearly. The decay process of CSS (k_{CR} or k_{ISC}) is at least several fold slower than k_{rot}. Therefore, the rotational process may affect the recombination in a significant way, but the current

measurements did not permit a clear separation of such processes. We found that the polarization of the charge separated state correlates with the frequency of the C≡C stretching modes of the bridge, supported by the TD-DFT modeling.

Interestingly, the S_1 (CS) state for D-C4-NAP in DCM became lower in energy than the NAP-localized triplet state, preventing formation of the latter and resulting in a ca. 0.4 ns lifetime for the charge separated state. For the Ph-C4-NAP species, the diabatic CS state occurs at higher energies where a larger number of D- and A-localized diabatic states are found; stronger mixing of these states produces a much lower extent of polarization in the eigenstates. The D-C4-NAP compound offers exciting opportunities for ET-rate modulation by exciting vibrational modes on the bridge,[4, 5, 108, 117-119] which will be reported elsewhere.

2.5 Concluding remarks

Through a collaborative effort between experiment and theory, we combined synthesis, computational methods, and ultrafast spectroscopy methods to investigate the evolution of excited states in organic and organometallic D-B-A complexes. Under the presence of strong donors, the optical excitation of the acceptor leads to ultrafast formation of charge separated states (CSS). These fast dynamics makes them excellent candidates for electron transfer rate modulation by infra-red excitation in compounds without rare-earth metals.

3. Exploiting molecular coherences for directed energy flow

In collaboration with members of the Beratan and Therien group at Duke, the Makri group at UIUC, the Wasielewski group at Northwestern and the Fleming group at Berkeley. Manuscripts in preparation.

This research has been generously supported by the National Science Foundation (grant no. CHE-1925690).

3.1 Significance of the study

The wave-like properties of matter at the nanoscale allows electronic and vibrational states to remain quantum coherent when a fixed phase and amplitude is present between different states. However, random fluctuation of the environment causes coherence to be short-lived. Sustaining coherence could enhance function in chemical systems, allowing them to harvest and transmit energy and information. Here, I discuss the collaborative efforts of the NSF Center for Synthesizing Quantum Coherence (CSQC) to construct covalently linked, strongly coupled light-harvesting complexes based on porphyrin arrays that exhibit efficient energy transfer assisted by coherent, non-thermal processes.

3.2 Introduction

Coherence phenomena pervade modern science, including the fields of optics, non-linear classical dynamics, quantum computing and quantum information science,

signal processing and communications, metrology, and applied mathematics and mathematical optimization. Coherence phenomena permeate chemistry. The Heitler-London theory of the valence bond, the Woodward-Hoffmann rules of electrocyclic reactions, and the tunneling mechanisms that underpin molecular bioenergetics are all manifestations of coherent quantum phenomena. Broadly speaking, coherence refers to fixed temporal and/or spatial correlations between signals or parameters of a system, especially correlations resulting from interference patterns. More specifically, the fixed correlations often refer to specific phase relationships between values of periodic or quasi-periodic signals or physical parameters.

Understanding the coherences intrinsic to strongly coupled electronic, vibrational, and spin states in molecular and nanoscale structures, promises to enable chemists to direct the flow of electronic excitation energy, charge, and spin in profound new ways. First, the fundamental knowledge gained in these studies will provide access to a new kind of chemical reactivity that does not rely on thermalized populations. The experimental tools needed to probe coherent electronic states (excitons, polarons, and trions, in particular), and the theoretical tools to simulate them, have only emerged over the last decade. Second, the development of fundamental principles underpinning coherent molecular phenomena will enable innovation in wide ranging areas of chemistry that span energy conversion to molecular sensing to quantum computing

arising from the coherent flow of energy, charges, and spin at the molecular and nanoscale.

This chapter presents our collaborative efforts to study coherence phenomena present in electron and energy transfer processes in donor-bridge-acceptor systems. First, we introduce the exploration of a quantum ratchet[120] that produces efficient electron transfer assisted by a non-thermal energy transfer process. Second, we analyze the exciton dynamics of cofacial porphyrin structures reported by Fletcher and Therien.[121] A combination of ultrafast spectroscopy techniques and TD-DFT analysis reveals the excited state dynamics of the strongly coupled light-harvesting complexes.

3.3 Quantum ratcheted photophysics of multi-chromophoric systems

We designed light-harvesting artificial complexes with the aim of producing efficient electron transfer assisted by a non-thermal energy transfer process known as quantum ratcheted energy transport. The complex consists of meso-to-meso ethyne-bridged (porphinato)zinc(II) oligomers (D_1 or D_1'), strongly coupled to a (porphinato)zinc(II) monomer (D_2), which is covalently bonded to a naphthalenediimide acceptor (A) (Figure 26a). Light excitation of D_1 generates a hot exciton. Vibronic coherence enables exciton transfer from D_1* to D_2*, followed by an ultrafast electron transfer step that defeats vibrational relaxation (Figure 26b). The electronic structure and photophysical properties of the compounds were studied using time-dependent density functional theory (TD-DFT). Contrary to the ratchet mechanisms presented in Chapter 5,

which are based on incoherent hopping, the quantum ratchet presented here exploits coherence effects such as electronic and vibronic coherences. Directionality is determined by the intrinsic energy landscape of the molecular system.

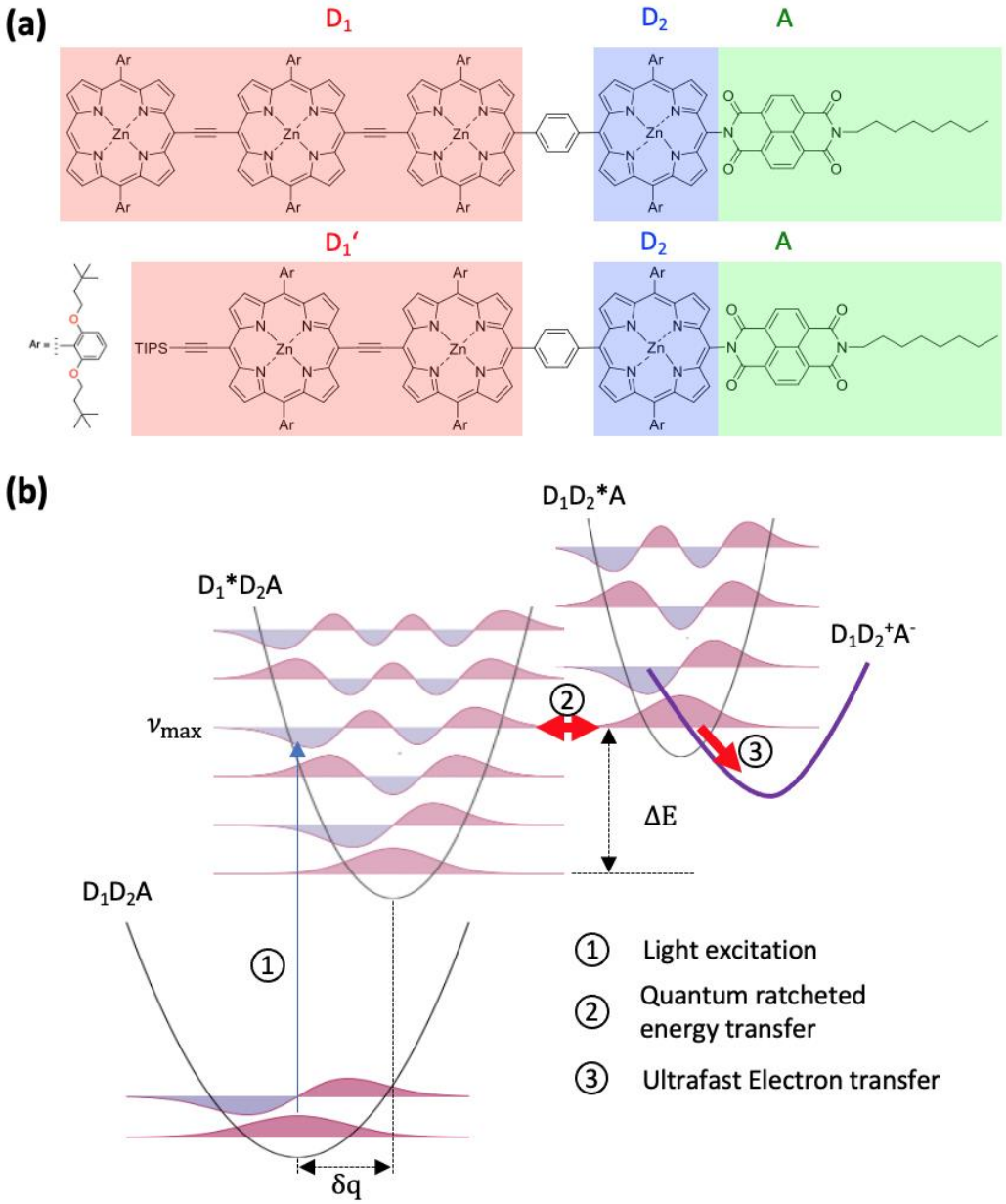

Figure 26: a) Structures of the light-harvesting complexes studied. b) Schematic depicting quantum ratcheted energy and electron transport dynamics.

3.3.1 Experimental details

The procedure followed for obtaining the spectra will be provided elsewhere. We present experimental results in Section 3.3.4 to accompany the theoretical calculations.

3.3.2 Computational details

DFT and TD-DFT calculations for D_1-D_2-A (PZn_3-Ph-PZn-NDI), D_1'-D2-A (TIPS-PZn_2-Ph-PZn-NDI) and subsystems (D_1-A, D_1'-A, D_2-A, D_1-D_2 and D_1'-D_2) were performed in Gaussian 16[40] at the MN15/def2-SVP level of theory.[38, 39] Aliphatic chains where truncated to methyl groups to reduce the computational cost. The CC2 method[122] with the same basis set as implemented in Turbomole[123, 124] was used to benchmark the DFT functional chosen. Solvation effects of toluene and dichloromethane were simulated in TD-DFT calculations using the polarizable continuum model (PCM).[41] Coordinates of the optimized structures in both solvents can be found in Appendix C.

3.3.3 Design considerations

This system leverages resonant energy transfer (EnT) to produce D_2*, and ultrafast $D_2 \rightarrow A$ electron transfer to irreversibly generate a charge-separated state. This ratcheted ET process requires charge separation (CS) to occur on a timescale much faster than that for thermalization; CS trapping on A through a Marcus inverted behavior should be on a similar time scale or faster than the D_1*/D_2* Rabi oscillation that would eventually drive relaxation of the coherent excited state to D_1*.

3.3.4 Photophysics of D_1-D_2-A and D_1'-D_2-A compounds

The electronic structure and photophysical properties of the compound were studied using time-dependent density functional theory (TD-DFT). Calculated absorption spectra of D_1-D_2-A and D_1'-D2-A (Figure 27) demonstrate qualitative agreement between calculations and experiments.

Computed TD-DFT analysis of the locally excited ($D_1^*D_2A$ and $D_1D_2^*A$) and charge-transfer ($D_1D_2^+A^-$) excited states of the two compounds in implicit dichloromethane solvent are shown in Figure 27. The energetics of the states present the proper energy level ordering required for quantum ratcheting (Figure 26). Both compounds present similar predicted energetics for the $D_1D_2^*A$ and $D_1D_2^+A^-$states but different $D_1^*D_2A$ state energetics, as expected from the conjugation reduction when substituting D_1 for D_1'.

Emission measurements of D_1-D_2-A and D_1'-D2-A were carried out to examine any fluorescence quenching that could suggest the existence of an energy transfer or charge transfer process. The two compounds presented marked differences in their emission spectra. No fluorescence quenching was observed for D_1-D_2-A when compared to D_1 alone (Figure 29A). The steady-state emission of D_1'-D_2-A compound show excitation energy dependent emission quenching relative to the D_1' benchmark (Figure 29A). The presence of emission quenching relative to the D_1 benchmark (as shown), and the D_1-D_2 reference species, strongly suggest the occurrence of charge transfer.

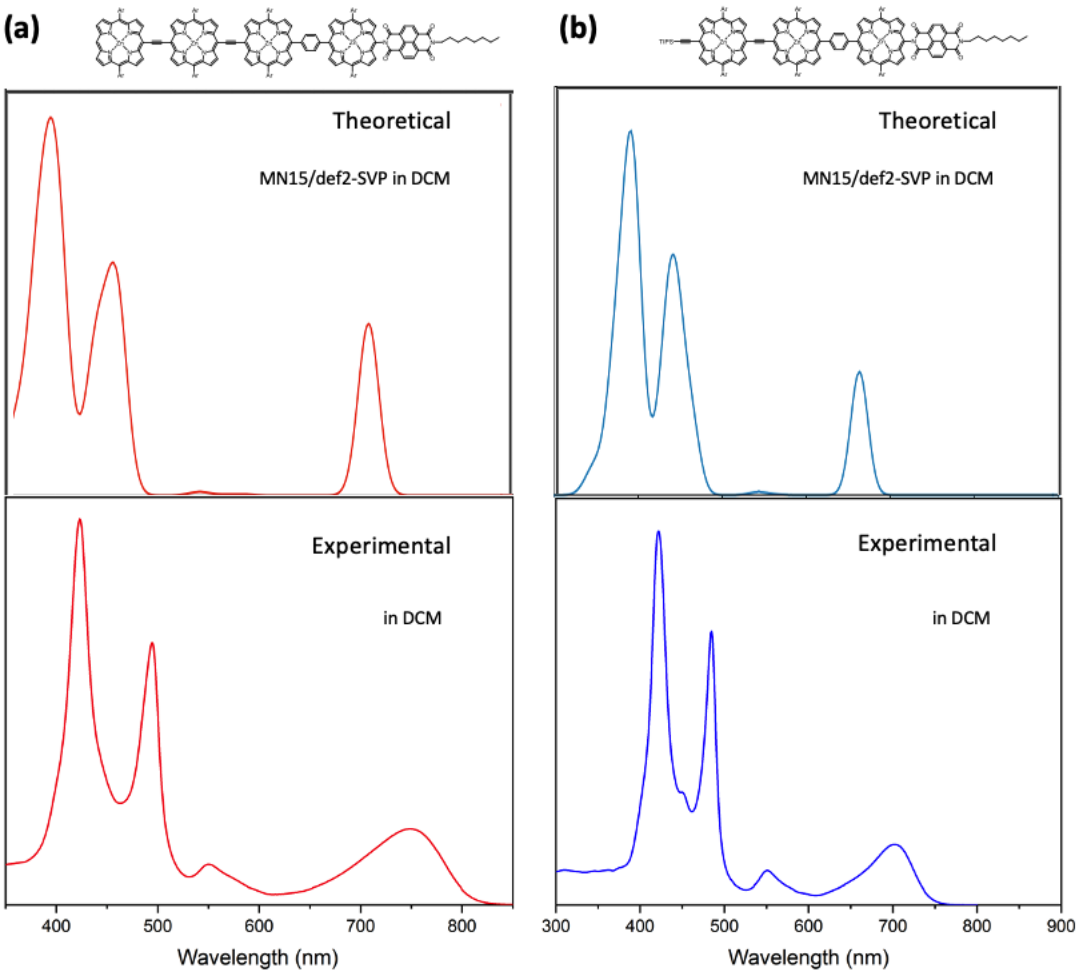

Figure 27: Theoretical and experimental absorption spectra of (a) D_1-D_2-A and $D_1'D_2$-A in dichloromethane

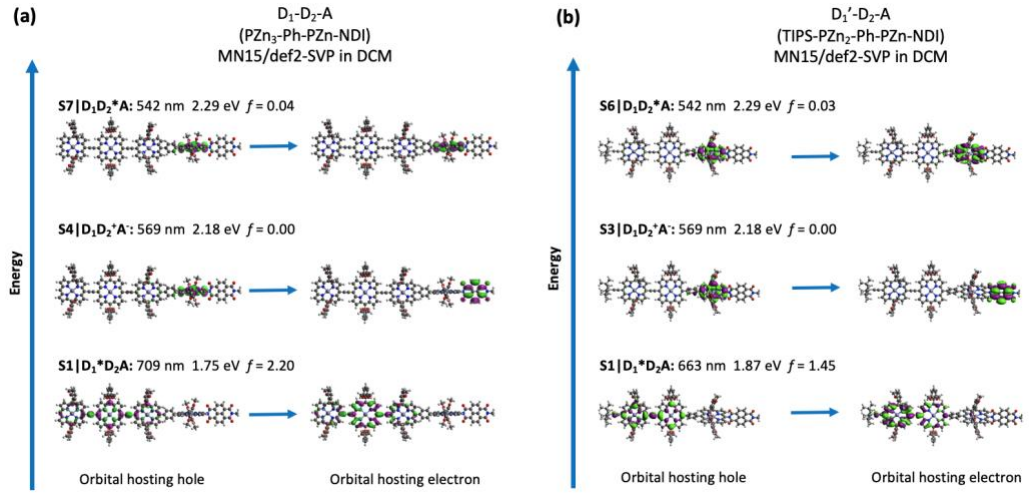

Figure 28: Energetics and orbital transitions of (a) D_1-D_2-A and (b) D_1'-D_2-A calculated in implicit dichloromethane with TD-DFT at the MN15/def2-SVP level of theory. The oscillator strength(f) values, which indicate the probability of absorbing a photon are also included.

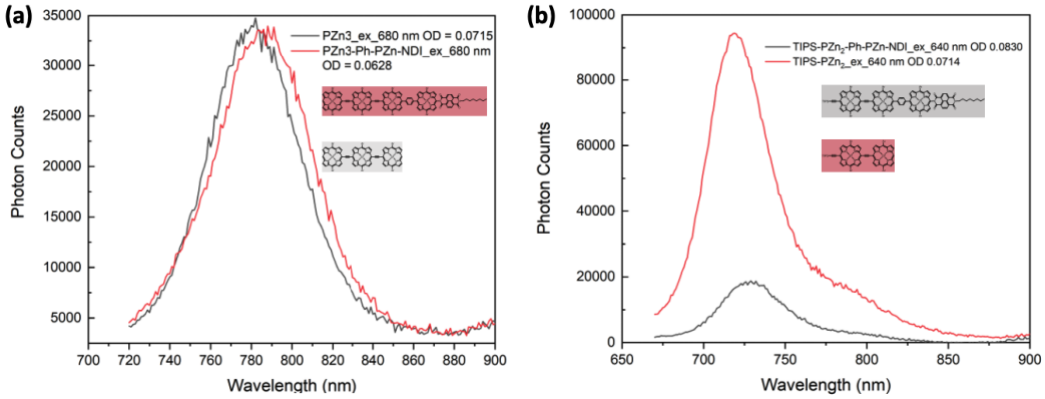

Figure 29: Emission spectra of (a) D_1-D_2-A and (b) D_1'-D_2-A and their corresponding benchmark structure.

To conclusively identify the mechanism through which charge transfer reactions occur, excitation energy dependent transient absorption spectroscopic experiments in a range of solvents are needed. 2DEV experiments to interrogate the vibrational modes that control coherence and drive energy ratcheting would also be incisive.

3.3.5 Summary

We have studied the photophysics of two multichromophoric systems engineered for ratcheted energy transfer. The systems consist of two different donors separated by a decoupling bridge unit and an acceptor covalently attached to one of the donors. TD-DFT analysis supported by steady-state emission measurements suggest the presence of ratcheted electron and energy transfer.

3.4 Engineering and sustaining excited-state coherences in cofacial porphyrin arrays

Covalently linked chromophores offer the possibility of producing strong chemical interactions that may generate coherent electronic or vibronic dynamics (Figure 30). We examine how symmetry in these multi-chromophoric structures may influence electronic and vibronic coherences using experiment and theory. This study aims to unmask the origins of the coherent dynamics in cofacial porphyrin structures.

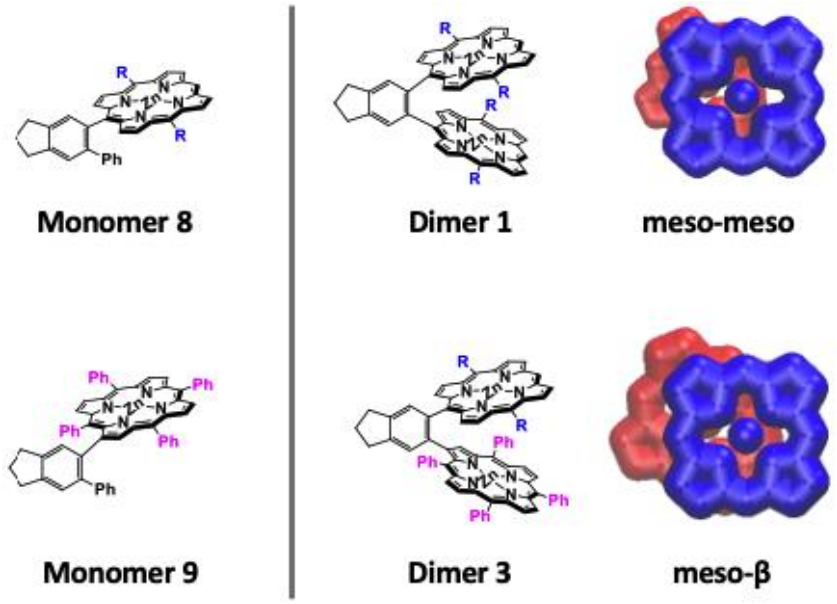

Figure 30: Cofacial structures studied in this work. The numbers correspond to the label used by Fletcher and Therien.[121] The optimized structures of Dimer 1 (meso-meso bridged) and Dimer 3 (meso-β bridged) at the CAM-B3LYP-D3BJ/def2-SVP level of theory are also shown.

3.4.1 Experimental details

Details of the experimental measurements will be provided elsewhere. In sections 3.4.3 and 3.4.4 we present experimental results that are supported by theoretical calculations.

3.4.2 Computational details

Geometry optimizations, frequency calculations and vertical excitations in the ground and excited state geometries performed using the CAM-B3LYP-D3BJ/def2-SVP[39, 43, 125] level of theory as implemented in Gaussian 16. [40] Similar results were found with the MN15 functional.[38] PCM was used to simulate the solvent effects. Tetrahydrofuran (THF) was chosen as the solvent since it has a similar dielectric constant as the 3:1

mixture of diethyl-ether and ethanol used in experiments. The coordinates of the optimized structures can be found in Appendix D.

Electronic couplings between the S1, S2, S3 and S4 states where calculated in Q-Chem 5.3.2[126] using the Edmiston-Ruedenberg localization scheme[127] and the Fragment-Excitation Difference (FED) method[128] in the presence of an implicit solvent (THF). The electronic couplings calculated with the Edmiston-Ruedenberg localization scheme are shown in Appendix D.

3.4.3 Linear absorption spectra and TD-DFT analysis

Figure 31 shows the linear absorption spectra of the two monomers and two dimers. The peaks less than 17000 cm^{-1} are treated as vibronic replicas of the Q-bands.[129] Interestingly, the absorption spectra of Dimer 1 presents two peaks which might correspond to the higher exciton and lower exciton manifolds.

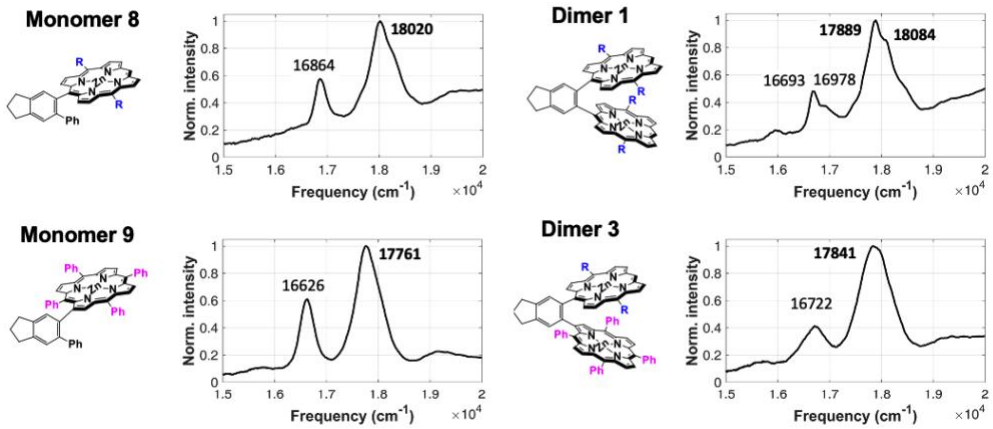

Figure 31: Linear absorption spectra of monomer 8 and 9, and Dimers 1 and 3 measured in 3:1 mixture of diethyl-ether and ethanol at 95K.

TD-DFT analysis of the four compounds is summarized in Figure 32. In Dimer 1 orbital distribution is highly delocalized whereas in Dimer 3 the electron density is localized on one of the two porphyrin motifs. The S1 and S2 states are mainly localized on the phenyl-substituted unit. S3 and S4 are localized on the complementary unit.

The absorption frequency of the monomers and Dimer 3 is overestimated (c.a. 400 cm^{-1}). Interestingly, for Dimer 1 the low frequency and the high frequency absorption peaks are underestimated and overestimated, respectively, with DFT. However, the excitonic gap predicted with the CAM-B3LYP functional is consistent with the MN15 functional and the CC2 approach (Table 7).

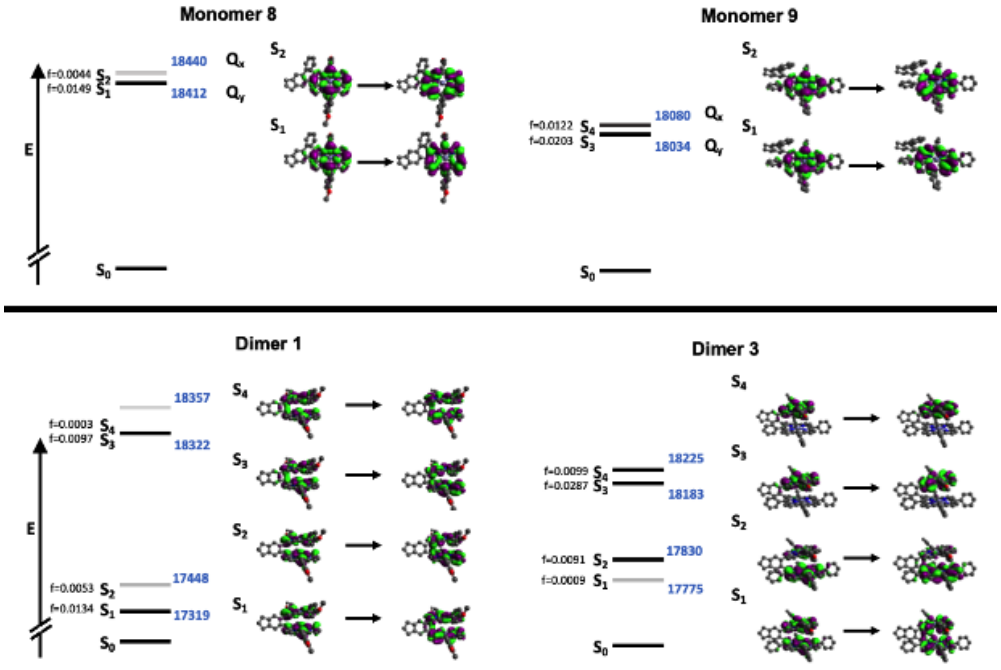

Figure 32: TD-DFT analysis of the four porphyrin-based structures analyzed. Energies, oscillator strengths (f) and natural transition orbitals are shown.

Table 7: Vertical excitation values of Dimer 1 with different levels of theory. The def2-SVP basis set was used for all methods. The DFT values were calculated in implicit THF solvent.

State	CAM-B3LYP-B3DJ / cm^{-1}	MN15 / cm^{-1}	CC2 / cm^{-1}
S1	17319	16967	18631
S2	17448	17143	18760
S3	18322	18293	19769
S4	18357	18363	19793

3.4.4 Excited state dynamics

Two-dimensional electronic spectroscopy (2DES) measurements provided evidence of inter-excitonic population transfer in Dimers 1 and 3 (not shown). Figure 33 shows the pump-probe study conducted to detect the inter-exciton relaxation time. There is no sub-ps decay for Monomer 8. Dimer 1 has an order of magnitude acceleration when compared to Dimer 3. Additionally, both compounds exhibit rapid ground state recovery, which competes with the inter-excitonic relaxation. The kinetics of both dimers was shown to be temperature-dependent, suggesting the presence of a thermally activated process.

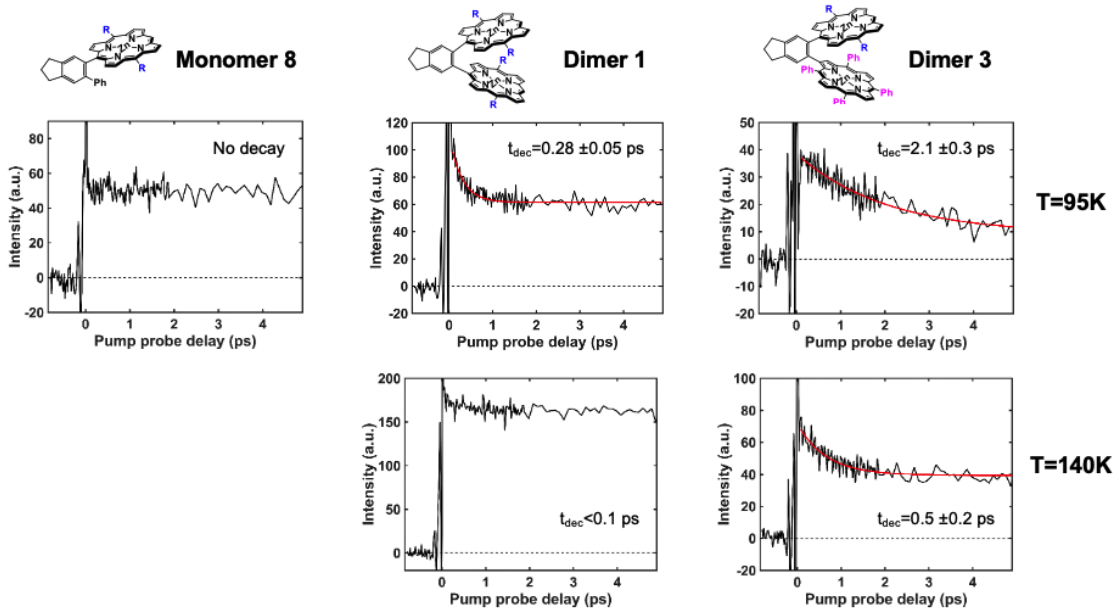

Figure 33: Kinetic decay trace of Monomer 8, Dimer 1 and Dimer 3 at 95K and 140K. Insets indicate the inter-exciton relaxation time (t_{dec}).

The faster relaxation time in Dimer 1 and high orbital delocalization was attributed to a higher electronic coupling between the porphyrin units. Electronic coupling calculations using the fragment excitation difference method[128] (Table 8) indicated that Dimer 1 has an electronic coupling at least three times stronger (0.064 eV) than Dimer 3 (0.022 eV). The Dimer 1 highest electronic coupling value is close to a beat map at 0.042 eV found in experimental measurements.

To probe if the increase in coupling was due to topology (meso-meso vs meso-β) or symmetry (homo vs hetero-dimer) effects, we calculated the electronic couplings of the meso-β bridged homodimer (Dimer 1 meso-β, Table 8). This change in connectivity led to similar electronic couplings as in Dimer 3. Therefore, the increase in coupling was

attributed to topology effects, presumably due to a stronger π-stacking between porphyrin units (Figure 30).

Table 8: Electronic couplings of cofacial porphyrin systems calculated using the Fragment-Excitation Difference (FED) method. The geometry used corresponds to the ground state minimum.

States		Dimer 3 coupling/eV	Dimer 1 coupling/eV	Dimer 1 meso-*β* coupling/eV
1	2	0.001	0.008	0.006
1	3	0.022	0.049	0.027
1	4	0.006	0.064	0.012
2	2	0.005	0.054	0.007
2	3	0.016	0.047	0.026
3	4	0.000	0.002	0.003

To analyze if the electronic interaction proceeds through-bond or through-space, we calculated the dimer structures without the bridge subunits (dangling bonds were capped with hydrogens). The similar electronic couplings reported in Table 8 and Table 9 indicate that the interaction occurs mainly through-space.

Table 9: Electronic couplings of cofacial porphyrin systems without the bridge unit calculated using the Fragment-Excitation Difference (FED) method. The geometry used corresponds to the ground state minimum.

States		Dimer 3 coupling/eV	Dimer 1 coupling/eV	Dimer 1 meso-*β* coupling/eV
1	2	0.001	0.015	0.004
1	3	0.030	0.012	0.037
1	4	0.008	0.093	0.032
2	2	0.010	0.077	0.025
2	3	0.029	0.015	0.038
3	4	0.001	0.002	0.001

Figure 34 shows a proposed scheme that reflects the competition between the fast ground state recovery and the inter-excitonic relaxation channels. The ground state recovery is attributed to a conformational relaxation that leads to a conical intersection (CI). Computational calculations such as minimum-energy crossing point (MECP)[130] could test the hypothesized dynamics by finding conformations closer to the conical intersection.

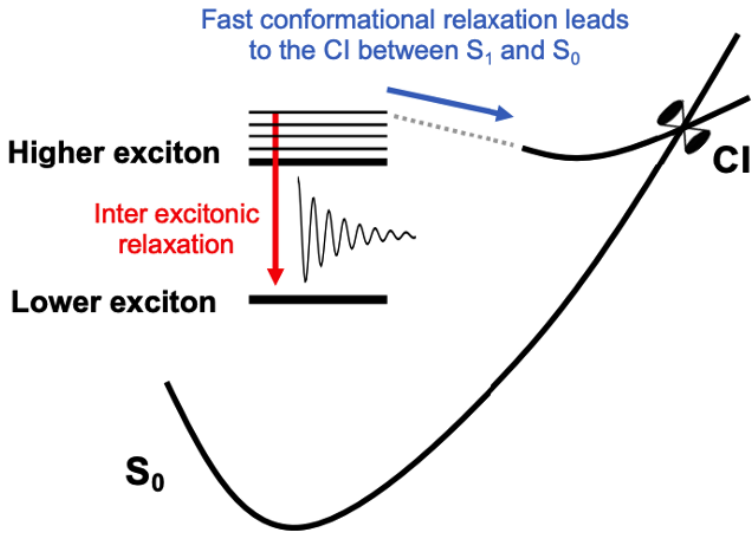

Figure 34: Proposed excited state dynamics of Dimers. After absorbing light, the inter-excitonic relaxation pathway competes with a conformational relaxation that leads to a conical intersecion (CI).

3.4.5 Summary

We have studied coupled chromophore arrays to examine how symmetry breaking impacts the nature and persistence of vibronic coherence. The differences in connectivity between Dimer 1 (meso-meso) and Dimer 3 (meso-β) lead to significantly different excited state dynamics. The inter-exciton relaxation measured with pump-

probe spectroscopy is about an order of magnitude faster in Dimer 1 (0.28 ±0.05 ps) than in Dimer 3 (2.1 ±0.3 ps). TD-DFT analysis found that the frontier orbitals are highly localized on one of the two porphyrin units in Dimer 3, while they are delocalized in Dimer 1. The differences in inter-exciton relaxation and electron density distribution between the dimers is qualitatively consistent with the calculated electronic couplings. The results indicate that upon excitation, there exists a competition between fast ground state recovery, attributed to the presence of a conical intersection, and inter-excitonic relaxation. This study points toward a strategy for the synthetic control of the electronic coupling in cofacial porphyrin dimer structures, and points to schemes to influence their coherent dynamics.

3.5 Concluding remarks

We have combined ultrafast spectroscopy with TD-DFT calculations to elucidate the excited state dynamics of covalently linked, strongly coupled light-harvesting complexes. Current experiments suggests that vibronic coherence plays a role in the energy transport process in quantum ratchets and cofacial porphyrins. Additional experimental and theoretical analysis would be valuable to unmask the normal modes relevant for the coherent energy transfer processes.

4. Delocalization-assisted transport through nucleic acids in molecular junctions

This chapter is excerpted from:

Valdiviezo, J.; Clever, C.; Beall, E.; Pearse, A.; Bae, Y.; Zhang, P.; Achim, C.; Beratan, D. N.; Waldeck, D. H., Delocalization-Assisted Transport through Nucleic Acids in Molecular Junctions. *Biochemistry* **2021,** 60 (17), 1368-1378.

Part of this research has been generously supported by the National Science Foundation (grant no. CHE-1925690).

4.1 Significance of the study

DNA duplexes are promising structures to build functional nanodevices given their ability to transport current over long distances efficiently. In these systems, coherent tunneling dominates over short distances, and incoherent charge hopping is mainly present over long distances. Recent works reported the existence of an intermediate coherent-incoherent regime in DNA sequences with stacked guanine-cytosine (GC) base pairs supported by charge delocalization over several base pairs. We have studied the single-molecule conductance of peptide nucleic acid (PNA) duplexes with stacked GC base pairs and compared our values with previous studies on DNA. Our results show that PNA has higher conductance than DNA and incoherent transport is the dominant mechanism. Theoretical simulations suggest that the peptide backbone

enhances the electrode-molecule coupling and the base pair coupling, reducing the coherent contribution to the total conductance.

4.2 Introduction

Charge transport through nucleic acids[102, 131-141] can proceed by tunneling, resonant, near-resonant, or incoherent pathways that are sensitive to the macromolecular structure and its environment.[142-145] Until recently, charge transport through nucleic acids was believed to proceed by coherent tunneling at shorter distances and incoherent (multi-step) hopping at longer distances.[141, 146-148] However, recent studies found that neither the coherent nor the incoherent pictures are adequate to describe the transport at short to intermediate distances.[149-151] For example, the single-molecule conductances measured for deoxyribonucleic acid (DNA) duplexes with alternating cytosine (C) and guanine (G) bases, namely -$(GC)_n$- with n ranging from 3 to 8, were compared to those for duplexes of the same length with the G and C bases separated into blocks, i.e., -G_nC_n-.[150] The -$(GC)_n$- duplex conductance decreases linearly with n, while the -G_nC_n- (G-block) duplex conductance oscillates with n. The linear decrease of the conductance in -G_nC_n- is consistent with an incoherent charge-transport mechanism. The G-block conductance oscillations suggest extended carrier delocalization (coherence) over strongly-coupled, adjacent G-blocks.[152]

The strong sequence dependence conductance found for DNA[137] and charge transfer[153-157] indicate sequence-dependent delocalization characteristics. Indeed, the more

rapid exponential decrease of electrical conductance in AT duplexes compared to GC duplexes is well documented.[158] Less well understood is the influence of cross-strand couplings on the strength and mechanism of nucleic acid charge transfer and transport.[159] For example, positioning the molecule-electrode linker groups and the G-blocks on the 3′ termini of the DNA duplexes causes an order of magnitude increase in the single molecule conductance compared to duplexes with the electrode-molecule linkers and G-blocks on the 5′ termini. This enhancement of the 3′-anchored G-block duplexes was explained by the larger cross-strand G-to-G coupling between G-blocks accessed in the middle of the 3′-3′structure, compared to the corresponding cross-strand coupling in the 5′-5′ chains.[159] Because the G-blocks mediate the charge flow,[153] the cross-strand block-to-block coupling is critical.[160] Indeed, the G-to-G cross-strand coupling is estimated to be two to three times larger in the 3′-anchored duplexes than in the 5′-anchored species.[161] The amplitude of the even-odd conductance oscillations in the 5′-anchored G-block systems are larger, as a percentage of the total conductance, because the cross-strand coupling is weaker.

Comparing the molecular conductance through aminoethylglycine peptide nucleic acid (PNA) and DNA duplexes with the same base sequences can help to reveal the structural origins of the molecular conductances.[162-165] PNA and DNA duplexes that have the same number of bases and the same sequence, but a different backbone structure, can display conductances that differ by 10- to 20-fold.[165] These conductance differences were explained as arising from differences in the populations of strongly coupled

nucleobases, as well as by differences of energy level broadenings. Indeed, energy level broadening can produce mechanisms that are neither purely coherent nor incoherent. The 'flickering resonance' mechanism,[166] relies on accessing conformations through molecular fluctuations that can support coherent transport during the persistence time of the quasi-degenerate energy configurations. The studies reported here describe the single-molecule conductance of G-block PNA duplexes for five different lengths ($n = 3 - 7$), and compare the conductances to those measured in G-block DNA duplexes reported previously.[159] This study explores how changes in backbone chemistry influence the conductance values and the relative contributions of coherent and incoherent transport mechanisms.

The structure of N-linked PNA is shown in Figure 35. An amine-modified thymine nucleobase is positioned at the N-terminus of the self-complementary G-block PNA oligomer; Watson-Crick hybridization of the PNA oligomer leads to a PNA duplex that has a palindromic sequence with amine-modified thymines on both ends of the duplex. Electronic coupling occurs between the electrode and the amine-modified thymine at the N-terminus of one strand of the duplex; the modified thymine at the N-terminus of the complementary strand interacts with the STM break junction tip (N-to-N transport). The N-terminus of PNA is analogous to the 5′ terminus of DNA.[167] The conductance measured for the G-block PNA duplexes is as much as 20 times larger than is measured for the analogous G-block DNA duplexes, and the even-odd conductance oscillations are found to be less pronounced in PNA.

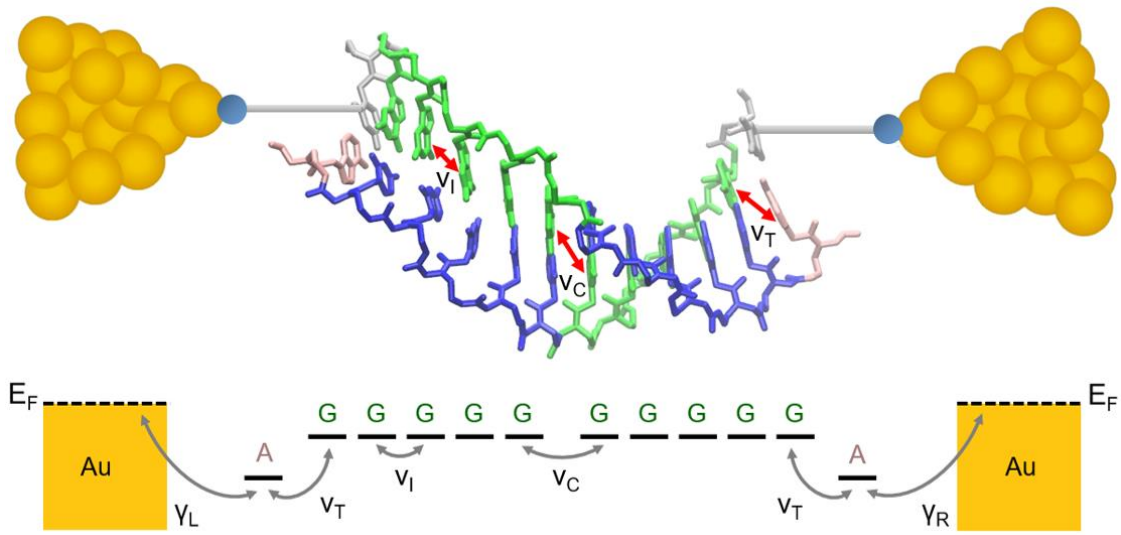

Figure 35: PNA molecular junction and sequence. The opposing termini orientations are shown for the N-linked PNA for n = 5 (top). The sequence shown is TG_5C_5A and each color represents a different nucleotide. The duplexes are anchored to gold electrodes via amine modifications on the terminal thymine nucleobase. The arrows indicate the nucleobases considered for the GC-GC intra-strand (V_I), GC-GC cross-strand (V_C), and terminal AT-GC (V_T) electronic coupling calculations. One-dimensional model used in this work (bottom). E_F is the Fermi level of the gold electrode, γ_L and γ_R are the molecule-lead electronic couplings, and V_I, V_C and V_T are the nucleobase electronic couplings described above.

The enhanced conductance of PNA duplexes, found in earlier comparisons between DNA and PNA homoduplexes, was attributed to the greater backbone structural flexibility in PNA.[165] The current study shows that the conductance of G-block PNA is larger than in G-block DNA, however the G-block duplexes of DNA and PNA appear to have similar structural flexibility (*vide infra*). Nevertheless, the theoretical analysis suggests that the structural changes associated with the different nucleic acid backbones affect the electronic couplings through the π-stack and the nucleic acid-electrode interactions, producing stronger electrode-molecule coupling for PNA compared to DNA.

That is, the electronic coupling interactions near the chain ends (γ_L , γ_R, and V_T, indicated in the bottom panel of Figure 35), are much larger for PNA duplexes than for DNA duplexes. The measured conductance value trends for the three duplex types, and the magnitude of the even-odd conductance oscillations are rationalized using an orbital model to describe the mediating state (*vide infra*).

4.3 Methods

4.3.1 Conductance measurements

Information about the conductance measurements can be found elsewhere.[168]

4.3.2 Computational details

4.3.2.1 Molecular dynamics

The nucleic acid duplexes were solvated in a TIP3P water box[169] that extended at least 15.0 Å from each atom. DNA duplexes were neutralized with Na^+ ions. CHARMM36 force field[170] parameters for DNA[171] and PNA[172] were used. The scaling factor for 1-4 electrostatic interactions was set to 1.00. A distance of 12 Å was selected for truncating van der Waals interactions. The maximum non-bonded interaction distance for the periodic calculation of the interaction energy was set to 14 Å. The Particle Mesh Ewald method[173] with a grid spacing of 1 Å was used to compute the electrostatic interactions. Full electrostatic interaction energies were evaluated every 2 time steps. The lengths of all chemical bonds between hydrogens and heavy atoms were

constrained. The unit cell vectors were (in Å): (74, 54, 54) for DNA 5′, (74, 54, 54) for DNA 3′, and (62, 80, 58) for PNA N-end.

The NAMD 2.11 software[174] was used to run the MD simulations. First the duplexes were optimized with 8×10^4 energy minimization steps. The minimization was followed by 225 ps of solvent equilibration (fixed nucleic acid duplex) at 300 K to allow water molecules and ions to adjust. Next, the constraints were removed, and a Langevin thermostat and piston[175, 176] were used to equilibrate the systems at constant temperature and pressure for 1.5 ns (temperature = 300 K, pressure = 1 bar, barostat period = 100 fs, characteristic damping time = 50 fs, damping coefficient = 2.0 ps^{-1}). The final MD production run lasted 100 ns. Snapshots were saved for each system every 33 ps (3000 coordinate frames in total).

4.3.2.2 Electronic coupling and site energy analysis

For each MD snapshot, the nucleobase HOMO energies and nearest-neighbor cross-strand (V_C), intra-strand (V_I), and terminal AT-GC (V_T) couplings (Figure 1) were computed from the Fock matrix using the block diagonalization method;[177] the Fock matrix was obtained at the INDO/S level[178] from the CNDO program.[179] The INDO/S method gives a good description of charge transfer parameters in organic π-stacks at a reasonable computational time.[180] Electronic couplings were computed in the two-state approximation. Only the nucleobases were included in the computation of orbital energies and electronic couplings, denoted as *in vacuo* (solvent and backbone atoms were

removed, and dangling bonds were capped with hydrogens). The explicit treatment of backbone and solvent as classical point charges (QM/MM scheme) has been reported to have a small influence on the HOMO energy mean values,[181] and in sequences with longer bridges, as in this study, the rate constant for hole transfer calculated using a QM/MM formalism and *in vacuo* approaches are similar.[182] It has also been shown that QM/MM calculated electronic couplings are similar to the *in vacuo* results,[181, 182] so we used the *in vacuo* results in the analysis described here. The methods used here were shown to provide reliable estimates of the electronic couplings in DNA.[161, 162]

A cross-strand coupling via the superexchange guanine-cytosine-guanine pathway was also calculated for snapshots taken every 5 ns, using only the four nucleobases in the cross-strand region. A density functional theory approach was selected to describe the hydrogen bonding interactions between nucleobases,[183] which are relevant for the superexchange pathway. The Kohn-Sham matrix obtained with the M11 functional[184] and the ma-def2-TZVPP basis set[185] as implemented in Gaussian 16[40] was used to compute the associated electronic couplings.

4.4 Theoretical analysis of DNA and PNA structure and electronic properties

Molecular dynamics simulations of PNA and DNA duplexes –(G_5C_5) – were run for 100 ns. This time range allows sampling of the inter-nucleobase fluctuations and a subset of duplex conformational changes.[162] Analysis of these structural data indicates that the root-mean square deviations (RMSD) for the structural fluctuations of PNA duplexes

are comparable to those of the DNA duplexes. The duplex RMSD value from its average structure calculated with VMD[186] is 1.3 ± 0.3 Å for N-linked PNA, 1.4 ± 0.4 Å for 3′-linked DNA, and 1.5 ± 0.4 Å for 5′-linked DNA. The small difference in RMSD values suggests that the PNA duplexes are slightly more rigid than the corresponding DNA structures (Figure 51 and Figure 52). This result is the opposite of results that were found earlier for PNA and DNA duplexes with a *mixed* nucleobases sequence. (For mixed sequences, the PNA duplexes were found to be more flexible than the DNA duplexes.[162]) This finding indicates that the relative structural flexibility of the nucleic acids is sequence dependent. The larger overlap between nucleobases in the PNA G-blocks leads to stronger π-π interactions and decreased flexibility as compared to the earlier mixed nucleobase sequence studies of PNA duplexes.[187]

MD snapshots were used to calculate HOMO energy fluctuations for each base pair in the duplexes (at the INDO/S level). The HOMO energy fluctuations and standard deviations of each base pair are shown in Table 10 for the $n = 5$ length, which is illustrated in Figure 35, for the case of PNA. The similar HOMO energies, and their standard deviations suggest that the energy fluctuations are similar for PNA and DNA duplexes. These HOMO energies, calculated *in vacuo*, are 1.5 eV to 2 eV below the Au work function. However, the influence of a metal electrode on the electronic state energies of adsorbed species can be substantial (circa 1 eV[188]), and we expect the energy offset between the

Fermi level and the effective HOMO orbital energies to be significantly less than 1.5 – 2 eV.

Table 10: HOMO energies (eV) and their standard deviations for the GC base pairs examined in the cross-strand, intra-strand, and terminal electronic coupling calculations. These values are computed for $n = 5$ chains.

	DNA 5′		DNA 3′		PNA N-end	
	E_{HOMO}	σ	E_{HOMO}	σ	E_{HOMO}	σ
Cross	-6.51	0.22	-6.55	0.21	-6.97	0.19
Intra	-6.41	0.22	-6.37	0.21	-6.47	0.19
Term	-6.68	0.21	-6.71	0.22	-6.56	0.18

We calculated the nearest-neighbor root mean square electronic couplings (V_{RMS}) between base pairs (INDO/S, block diagonalization method, capped bases),[161] where $V_{RMS} = \sqrt{\langle V^2 \rangle} = (1/n)\sqrt{\sum_{i=1}^{n} V_i^2}$, $V_{RMS}^2 = \langle V \rangle^2 + \sigma^2$, σ is the standard deviation of V, and n is the number of MD snapshots used for averaging. Table 11 shows the calculated V_{RMS} values. Table 11 reports the calculated electronic couplings of the terminal AT base pairs with their nearest GC pair (V_T) for each of the three duplex types. These calculations indicate a nearly three-fold increase in V_T for N-terminal PNA compared to the corresponding couplings in the DNA duplexes. Table 11 also shows that the N-linker PNA duplex intra-strand couplings (V_I) are larger than the values found for the DNA counterpart. The increase in the couplings, V_I and V_T, for PNA versus DNA are consistent with the larger molecular conductances that are observed experimentally. The cross-strand coupling (V_C) also affects the conductance and earlier work[159] showed that it affects

the even-odd oscillations and they are discussed next. A description of how these computed electronic coupling values are linked to the conductance measurements follows this subsection.

Table 11: V_{RMS} values of GC-GC cross-strand (V_C), GC-GC intra-strand (V_I) and terminal AT-GC coupling (V_T) in eV. The cross-strand GC-GC couplings for the superexchange pathway (V_C^{SE}) are also shown.

	DNA 5′	DNA 3′	PNA N-end
V_T	0.011	0.017	0.047
V_I	0.087	0.071	0.120
V_C	0.006	0.012	0.002
V_C^{SE}	0.001	0.005	0.017

The direct cross-strand couplings V_C of the N-linked PNA and 5′-linked DNA are both small compared to the other couplings, presumably because of the small overlaps between the G-bases on the two strands (Figure 53). Thus, we examined how these values compared with coupling obtained from a superexchange pathway involving three nucleobases, V_C^{SE} (Table 11). MD simulations show that the geometrical parameters of PNA produce larger G-C π overlaps in the cross-strand region and, as a consequence, stronger π couplings compared to the case in DNA (Figure 54). The strong π interaction between the stacked GC nucleobases in PNA provides a superexchange pathway for charge transfer. The cross-strand coupling, V_C^{SE} for the guanine-cytosine-guanine superexchange pathway was calculated for selected snapshots taken every 5 ns with density functional theory to describe hydrogen bonding interactions (M11/ma-def2-

TZVPP, block diagonalization, capped bases).[183, 189] $V_C^{SE} = {V_{G5-C6}V_{G6-C6}}/{\Delta E}$, where the subscripts indicate the nucleobase and the position in the $n = 5$ duplex (see Appendix E). and ΔE is the energy difference between guanine and cytosine localized states, which is close to 0.7 eV.[190, 191] V_C^{SE}, which are the RMS couplings, are included in Table 11. V_C^{SE} is larger than the RMS V_C values only for PNA, suggesting that the superexchange contribution to the cross-strand coupling is more relevant to the transport mechanism in PNA than in DNA, and we will address the implications for the charge transport below.

In addition to differences in coupling pathways for PNA and DNA, the MD simulations reveal structural differences among the duplexes that can affect the electrode-molecule electronic couplings (γ_L and γ_R). Recall that V_T as well as γ_L and γ_R determine the electronic coupling interactions near the chain ends. The orientation of the terminal AT base pair, which contains the amine groups that bind to the Au electrodes, with respect to the first GC base pair of the G-block (Figure 35) appears to be different in the PNA junctions than in the DNA duplexes. In particular, the DNA terminal base pairs exhibit larger structural fluctuations than in PNA, which leads to 'fraying' of the duplex in the absence of the distance constraint described above. In addition, the increased rigidity of the PNA nucleobases, which correlates with enhanced π-π stacking interactions, likely contributes to establishing strong contacts with the leads and increasing the conductance.

4.5 PNA vs DNA conductance

The average experimentally measured single-molecule length-dependent conductance for the high-conductance mode of each duplex is shown in Figure 4. For the N-to-N linked PNA, the average conductance of the highest conductance mode is ~ $3 \times 10^{-2}\ G/G_0$ (where G_0 is the quantum of conductance). The average conductances for the PNA duplexes are an order of magnitude larger (or more) than for DNA duplexes of the same length. Figure 4b shows the mean conductance value obtained from the PNA conductance histograms, which are 3-5 times larger than the literature conductance values reported for 3′ DNA. In addition to the PNA conductances, the conductances for the first few ($n = 3, 4,$ and 5) 3′- and 5′-linked G-block DNA duplexes were measured in this study and are plotted as filled symbols in Figure 36. The measurements performed here are in good agreement with those reported by Tao and coworkers (unfilled symbols) and also display the even-odd oscillation.[159] Note that the increased conductance in PNA compared to DNA is consistent with earlier findings for mixed PNA sequences,[158, 165] although the details of the mechanism for the large PNA conductance may be different.

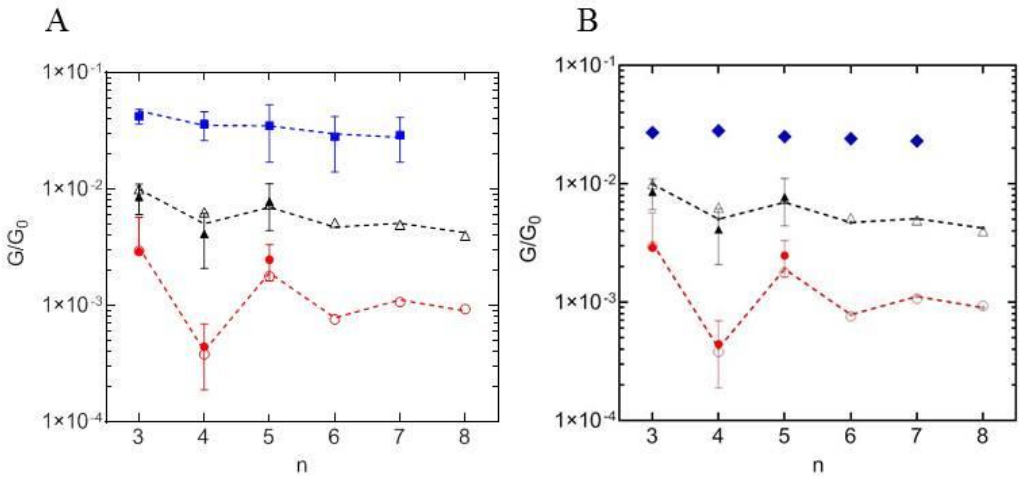

Figure 36: Conductance measurements. Panel A shows the results for the N linker PNA (blue squares) with data for 3′-linker DNA (black triangles) and 5′-linker DNA (red circles); the open symbols are from a previous study[159] and the filled symbols are from this study. Error bars are shown for the duplexes studied here representing a single standard deviation of the fitted Gaussian function for the highest observable mode. The negative component of the error for the 5′-linker DNA $n = 3$ data point has been excluded for clarity. The lines in the plot connect the best fit conductances found using the Büttiker double barrier model (see Supporting Information). Panel B shows an alternate analysis in which the PNA conductance values were assigned to the mean conductance value of the histogram, in order to show the increased PNA conduction in a model-independent manner.

The G-block PNA molecules show a significantly higher conductance (2 to 4 percent of G_0) than is typically found for molecules of comparable length, ~ 3 to 5 nm.[192] For example, molecules that display conductances on the order of a few percent of G_0 are typically the size of a single aromatic ring, e.g., benzenedithiol and benzenediamine. Two key factors influencing the molecular conductance in a junction are the electrode-molecule linker group and the molecule's electronic structure. The linker group can have an order(s) of magnitude effects on the measured conductance.[192, 193] The amine linkers for the PNA and DNA duplexes used in this study couple the aromatic stack of the duplex more

strongly to the electrode than do the backbone-based thiol linkers used in earlier studies.[194] The electronic structure of the mediating molecule, e.g., saturated versus unsaturated, is known to have a large influence on the molecular conductance as well.[68] However, molecules with highly conjugated electronic structures, such as oligo(phenylene-vinylenes) and oligophenylethynylenes, show conductances in the range of 10^{-3} G_0 or lower if they are a few nanometers in length.[192, 195] The length dependence of the molecular conductance through a homologous series of molecules is often characterized using an exponential decay as a function of length L; i.e., $exp(-\beta L)$.[196] Conjugated molecules show a much weaker decay with distance (smaller β value) than do saturated systems. Both the shallow dependence of the PNA conductances on length and the high conductance values are consistent with transport mediated by extended π systems.

The observation that the molecular conductance of G-block PNA duplexes are 10 to 20 times higher than the corresponding 5′-DNA duplexes with the π-stacked linkers is consistent with previous observations. Bruot et al.[194] compared the molecular conductance through 5′-A$(CG)_n$T-3′ ($n = 2-12$) DNA duplexes consisting of thiol linker groups connecting to the nucleic acid backbone with duplexes of the identical nucleobase sequence that have amine linkers bonded directly to the base stack. They found that the conductance was 10-20 times higher for the π-stack linker than the backbone linker for otherwise identical DNA duplexes. In earlier studies, we compared the molecular conductance of PNA duplexes to DNA duplexes with thiol linker groups on the nucleic

acid backbone. In those cases, the PNA displayed a molecular conductance that was about 20 times higher than that of the DNA.[158, 165] The high conductances measured for the PNA duplexes in this study is consistent with these earlier findings. The combined effects of the amine/thymine-based linker group and the high electronic coupling through the G-block stack are responsible for the high conductances reported here (vide infra).

4.6 Molecular orbital interpretation of conductance oscillations

The N-to-N linked PNA duplexes show a one- to two-order of magnitude increase in the molecular conductance compared to the values for the corresponding 5′-linked DNAs. This increase in conductance is consistent with the findings for mixed sequence DNA and PNA duplexes reported earlier.[158, 165] Conductance oscillations observed previously in the 5′-linked and 3′-linked DNA systems are barely evident for the PNA duplexes. The decreased amplitude of the even-odd oscillations with G-block length is explained by the larger cross-strand coupling and electrode-molecule couplings in PNA. We first discuss the cross-strand coupling effect and then examine the influence of the electrode-molecule coupling on the conductance oscillations.

In earlier studies, conductance oscillations as a function of length in G-block DNA duplexes (Figure 36) were explained by an electronic energy effect that arises in finite length periodic structures.[159, 197, 198] Odd-length G-blocks possess a "mid band" localized orbital with an energy near the Fermi level of the gold electrode, approximately equal to the energy of a G monomer.[159] This length-independent near degeneracy was proposed to

strengthen coherent charge transport for odd-length chains by providing a flickering resonance coupling pathway across the entire duplex.[159] In contrast, the orbital energies for even length G-blocks are offset from the "mid-band" position (Figure 37) and are unlikely to form flickering resonance coupling pathways across the structures. This picture accounts for the conductance oscillations with length, as shown in Figure 36.

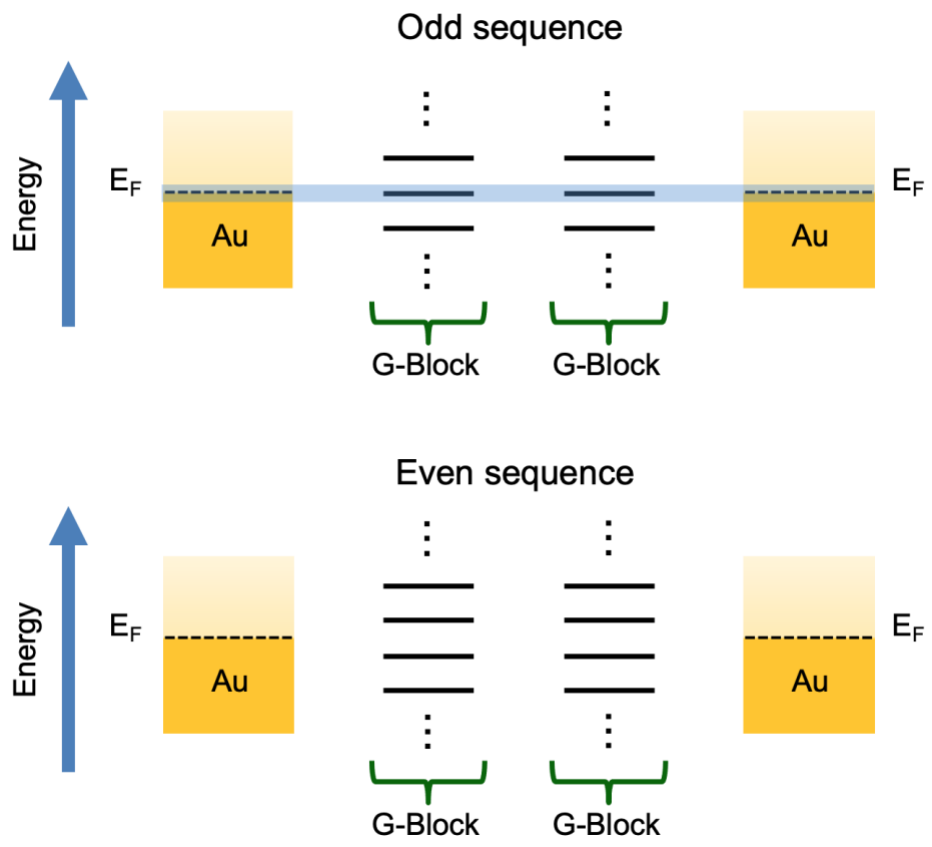

Figure 37: Molecular orbital energy picture of nucleic acid duplexes under a weak cross-strand coupling. Top: Flickering resonance energy level alignment for odd-length sequences. Each G-block possess a mid-band orbital in resonance with the Fermi level of the electrodes. Bottom: Energy level alignment for even sequences. A mid-band state in resonance with the Fermi level of the electrodes is absent.

Figure 36 shows that the conductance oscillations diminish in amplitude through the three duplex types as the overall conductance of the duplex increases. For example, the conductance oscillations are substantially less pronounced when the molecular linkers are positioned at the 3′ termini of DNA, as compared to the 5′ termini, and the corresponding molecular conductance of the 3′ species is observed to be larger. The decrease in the amplitude of the conductance oscillations, and the overall increase in the conductance in DNA, was attributed to geometric differences of the base pairs at the cross-stand position in the two cases (Figure 53 and Figure 54), which causes a change in the cross-strand coupling.[159] Intriguingly, a large cross-strand GC-GC coupling at the molecule's center reduces the likelihood of forming a fully delocalized (resonant) state across the G-blocks and the electrodes (vide infra).[199]

As a rule of thumb, the number of G bases over which the hole can delocalize at room temperature is up to about five.[159, 200] When the cross-strand coupling is weak, as in DNA 5′, the dominant position for the delocalized hole is across the n guanines that form each of the separate G-blocks, forming two domains. Thermal fluctuations can bring these two domains into resonance, i.e., flickering resonance, and form a fully delocalized state across the entire duplex[166] (Figure 38). Because the odd length G-blocks have resonant states near the Fermi level, and the even length G-blocks do not, a strong modulation of the conductance with the G-block length is predicted to manifest. As the cross-strand coupling increases, delocalization can occur among G nucleobases of the two blocks, and

this leads to a lower statistical weight for configurations that have the hole delocalized over each of the G-blocks. The growth in the number of configurations with delocalized domains leads to a higher overall conductance. The decreased statistical importance of the configuration with the extended G-block delocalization manifests as a decrease in the amplitude of the even-odd length conductance oscillations. Overall, the conductance is limited by the squared coupling between these domains and by the molecule-lead interaction strengths. The observation that the conductance increases from DNA 5′, to DNA 3′ - and increases further as the backbone is switched to PNA - is consistent with growth in the number and size of the cross-strand delocalization domains and their importance for the charge transport (switching from 5′ to 3′ increases the cross-strand coupling 3-4 fold, and switching to PNA increases the coupling by almost another 2 fold).

Figure 38 illustrates this mechanistic explanation for the change in conductance and in the even-odd effect for 5′-DNA and PNA. The bottom panel illustrates the mechanistic picture described in our prior analysis of the even/odd effects on the 5′-linked DNA conductance.[159] In this structure, the weaker cross-strand coupling in the 5′ structure (compared to 3′) leads to delocalization of orbitals on each of the two separated G blocks. Formation of a transient structure with extended delocalization only requires bringing these two blocks into resonance with each other and with the electrodes. The figure illustrates the case of odd length ($n = 3$) and even length ($n = 4$) chains to underscore how the energy of the G-block states are offset from the Fermi level of the electrodes. The

dependence of the energy mismatch on whether n is even or n is odd, and the promotion of delocalization across each G-block by the weak cross-strand coupling, leads to a strong even-odd conductance effect.

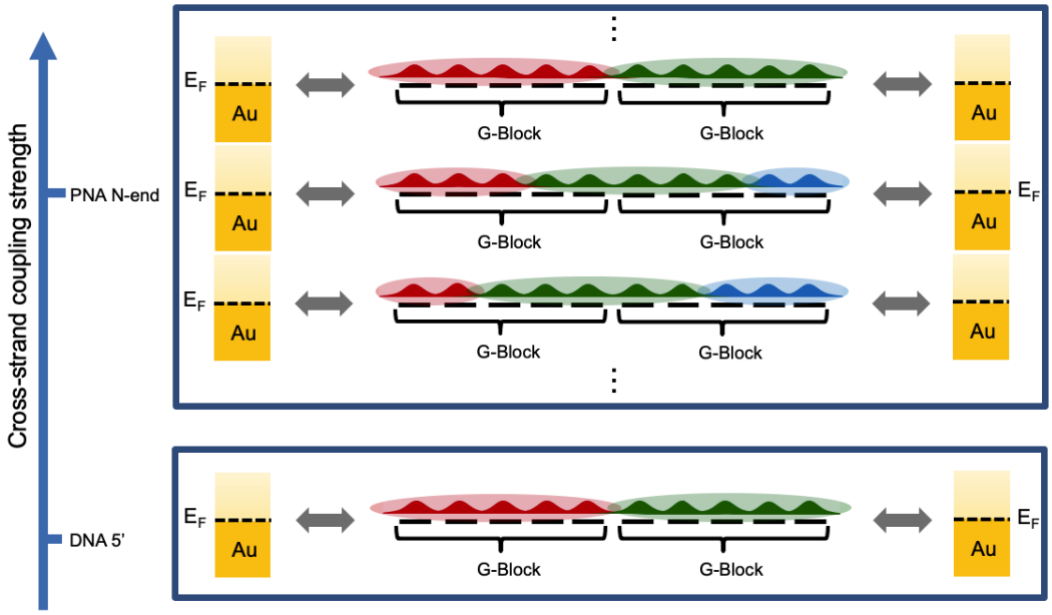

Figure 38: Model describing the delocalized islands across two G-blocks, each with $n = 5$. The maximum number of Gs over which the hole can delocalize is up to five (each color represents a delocalized block of orbitals).[159, 200] Top: Regime with a strong cross-strand coupling. The strong cross-strand coupling allows the five base pair delocalization to occur anywhere across the entire ten-base sequence of the G-blocks (e.g., the green block can be delocalized across the two strands). Therefore, the carrier position in PNA is less constrained than in DNA. For the sake of illustration, three possible configurations that support delocalization are shown (many others are possible). Bottom: Regime where the coherent channel with the hole delocalized over each G-block contributes significantly to the conductance. This coherent channel is absent in even-length sequences (see Figure 5).[159, 197] The weak cross-strand coupling pins the carrier delocalization on one of the G-blocks. The odd length G-block sequences are near resonant with the Fermi level of the leads and create a delocalized state for coherent transport.

The top panel in Figure 38 explains the mechanistic picture for the case where the cross-strand coupling is large (comparable to the intra-strand GC-GC couplings). In this

case, many possible delocalized islands of about five or fewer Gs may form in the structure. Indeed, in this regime, the likelihood of forming a delocalized state spread over the entire length of each G-block is diminished because of the increase in the overall number of other possible configurations that support delocalization, as illustrated by the additional two configurations shown in the top panel of Figure 38. Although this effect creates delocalized islands with more than one energy mismatch (so that multiple level matchings are required to delocalize over the entire molecule), many more configurations which display these delocalized islands manifest and provide many more flickering resonance conductance pathways in PNA, which leads to an overall increase in its conductance.

Our theoretical analysis (Table 11 and discussion) suggests that the electrode-molecule couplings for the PNA duplexes are stronger than in the 3′-linked and 5′-linked DNA. This feature is not included in the diagrams of Figure 38 for simplicity. A stronger electrode-molecule coupling is expected to produce a stronger mixing between the gold and the G-blocks of PNA compared to DNA. The stronger molecule-lead coupling expected to further enhance the conductance of PNA. This prediction is consistent with the observed higher conductance in PNA and softer even-odd effect compared to DNA. We note that strong molecule-lead interactions can perturb the "band structure" for each G-block, and will shift the energy of the mid-band state that appears for odd-length chains. The effect of the strong molecule-lead coupling can break the degeneracy between

delocalized hole states in each G-block and dampen the conductance oscillations in PNA compared to the case in 5′-DNA. This scenario was explored in detail by Segal et al., who showed that strong molecule-lead hybridization can indeed cause the even-odd effects to vanish.[197]

4.7 Summary and conclusions

Charge transport through nucleic acids can access coherent, incoherent, and flickering resonance mechanisms. The experimental and theoretical studies reported here find that structural differences in the duplex backbone with the same base sequences can produce order-of-magnitude changes in molecular conductances and can strongly influence how coherence manifests for single-molecule PNA and DNA junctions. For PNA duplexes, a conductance value of 0.03 G_0 was found with fourteen base pairs (~50 Å). PNA also has a high-mode conductance that is up to 30 times larger than that of DNA, and the conductance decreases monotonically with duplex length. The corresponding DNA structures show a striking conductance oscillation. The nearly monotonic and weak (< 2 -fold for distances from ~ 2 to 5 nm) change in conductance with duplex length that is found in PNA indicates an extremely low molecular resistance, in strong contrast with that for the 5′-linked DNA duplexes. The overall conductance in 5′ DNA changes by only two-fold between the $n = 3$ and $n = 8$ G-block pairs. The even-odd conductance oscillations in 5′ DNA with G-block length can be up to four-fold, and the average conductance in 5′ DNA is one to two orders of magnitude lower than in PNA. Despite

these dramatic differences in the experimental conductances and their length dependences, the flickering resonance transport mechanism provides a consistent explanation for the observed behavior.

Theoretical analysis finds that the PNA and DNA G-block structures studied here have similar structural flexibility, base-energy fluctuations, and base-to-base electronic interactions. The main differences between the PNA and DNA duplexes appear to be rooted in 1) differences in the molecule-electrode interaction strength and 2) differences in the base-to-base interactions in the cross-strand region, which arises from geometry differences between duplex PNA and DNA. The stronger cross-strand and molecule-lead couplings in PNA lead to higher conductance than in DNA. As such, the characteristics of cross-strand, intra-strand, and molecule-lead couplings collectively influence the contribution of competing coupling pathways to the conductance. The mechanistic origin of the even-odd conductance effect found in the DNA is consistent with that reported earlier,[159] which found that cross-strand interactions in the center of the duplex tips the balance among mechanisms. In contrast to earlier studies, the findings reported here indicate that the conductance mechanism is also influenced by the strength of the nucleic acid-electrode interactions. Growing the electrode-molecule or the block-to-block couplings is expected to reduce the statistical importance of delocalized states spread across just one G-block, leads to a decrease in the even-odd length conductance oscillations with length, and produce an overall increase in the molecular conductance.

Future work should explore effects of the molecule-lead coupling strength on conductance; for example, one can vary the aliphatic chain length of the amine linkers or modify the electrode's Fermi level in order to realize this goal. Detailed theoretical studies to assess the molecule-lead interactions[201] would also be incisive.

5. Electron ratcheting in self-assembled soft matter

This chapter is excerpted from:

Valdiviezo, J.; Zhang, P.; Beratan, D. N., Electron Ratcheting in Self-Assembled Soft Matter. *J. Chem. Phys.*, **2021**, DOI: 10.1063/5.0044420.

This research has been generously supported by the Air Force Office of Scientific Research under award no. FA9550-19-1-0331.

5.1 Significance of the study

Electron ratchets rectify electric current over long distances using energy sources different from a net applied bias along the transport direction. Experimental demonstrations have been reported using solid-state electronics, such as 2D electron gas and organic field transistors, inviting the exploration of ratcheting in chemical systems. We have examined ratcheting mechanisms to establish a directional charge flow in organic polymers. We propose experimental setups to build DNA-based electron ratchet devices.

5.2 Introduction

Molecular walkers, motors, and transporters all exploit ratcheting mechanisms in their function.[202-206] Biological ratcheting is accomplished by repeatedly switching free energy landscapes.[207-209] It is remarkable (and notable from the standpoint of very long range charge transport) that ratcheting accomplishes directional motion without the application of chemical or electrochemical biases across the entire structure from the

electron source to the electron drain. This intriguing feature of ratcheting could be of particular utility if it could be used to control and drive the flow of electrons through soft matter, as moving charge over micrometer and longer distance via multi-step hopping through bioinspired structures has proven to be challenging to realize.[210] "Bacterial nanowires" based on multi-heme proteins enable micrometer scale charge transport, presumably by unbiased diffusion to an irreversible electron sink.[211] Ratcheting processes dissipate free energy on the nanoscale to produce transport on the micrometer scale. Ratcheted systems offer the possibility of manipulating the direction and the kinetics of charge flow through molecular networks with novel connectivity.

Directional charge transport over long distances (≥ 30 nm) has been achieved in single molecule molecular wires,[212-215] but the structures require a source-drain voltage bias of 1-5 V, and the electrical currents typically amount to 1-5 nanoamperes. For distances beyond ~ 100 nm, the current is predicted to be essentially zero at similar source-drain voltage.[215] Realizing higher currents on the micrometer and larger length scales remains challenging because of molecular breakdown induced by high source-drain voltages. Electron transport ratchets (referred to here as ratchets) may be able to increase the functional length scale of prior charge transport devices.[216] Thus, our aim here is to simulate long range directional transport using the kinds of ratcheting mechanisms shown in Figure 39.

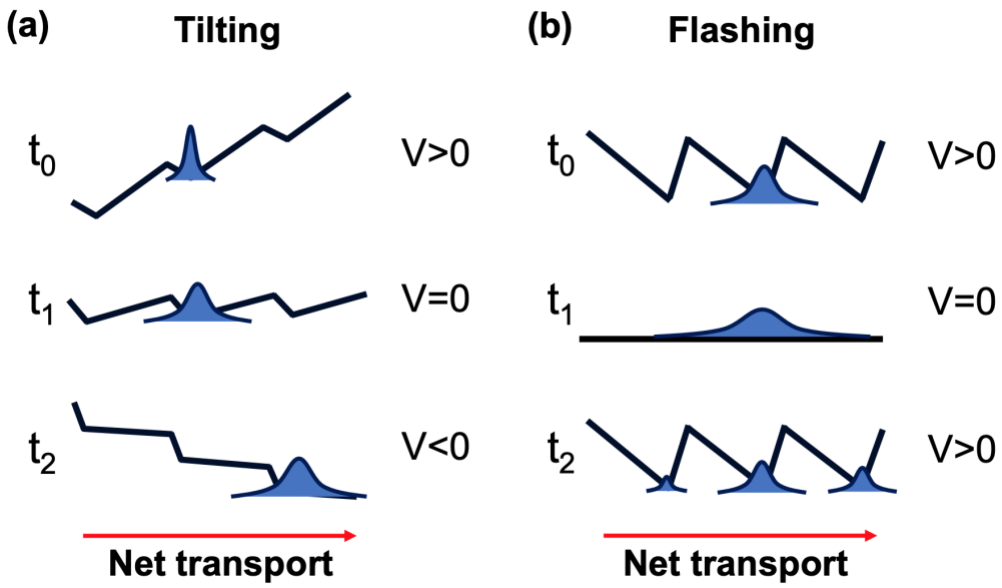

Figure 39: The energy landscapes for two kinds of electron-transfer ratchets are shown. (a) Tilting ratchet. The potential profile remains constant, but the entire profile is tilted up and down over time. The sawtooth structure biases the overall directionality of the transport. (b) Flashing ratchet. The potential energy landscape switches between flat and saw-toothed shape over time. When the potential is flat, electrons diffuse in both directions. When the sawtooth potential is turned on, the electrons drift preferentially to the right.

Electron ratcheting has been demonstrated in solid-state electronics. Ratcheting can produce charge rectification[217] and reduce the voltage bias required for device operation.[218-228] However, ratcheting is less well explored in the context of bioinspired, self-assembling molecules. For example, one would like to direct current flow through redox species appended to self-assembled structures, including DNA origami or brick motifs.[229, 230] Many DNA structures that convey charge (typically holes) suffer from slow transport over nanometer scales, because the charge transfer dynamics is limited by hopping among specific DNA nucleobases or nucleobase "islands" (typically purines for

hole transport).[231, 232] Achieving ratcheted charge transport in nucleic acids or other macromolecules may create novel opportunities to realize molecule-based circuitry in self-assembling matter.[233, 234] In contrast to prior studies, which focused mainly on solid-state electronics, the ratchets explored here are based on a bottom-up approach based on self-assembling soft matter. We use nucleic acid structures to illustrate our design principles, and we explore their ratcheting performance at the micro- and nanoscales.

We will describe two different ratcheting mechanisms in Sections 5.3 and 5.4 Section 5.3 describes ratcheting in molecular assemblies based on an electric Stark effect. Ratcheting transport efficiency is simulated and evaluated using kinetic models, and we propose experimental designs to test the directional charge flow. Section 5.4 analyzes electrochemically driven ratcheting that targets mesoscale structures in solutions, and we propose an architecture that would enable productive ratcheting over multiple micrometers. These theoretical studies aim to motivate future experimental realizations and tests of these molecular designs and predictions.

5.3 Electron ratcheting in nanostructures

In this section, we describe ratcheting mechanism based on a Stark effect that is induced orthogonal to the electron transport direction. This mechanism is aimed to realize transport at the nanoscale through polymers. The transport exploits the position-dependent orientation of electric dipole moments for the constituent monomers in a helical polymer.

5.3.1 A ratchet based on charge hopping

The ratcheting mechanisms described here are illustrated through simulations on double-stranded DNA structures with Watson-Crick base pairing. The base pairs have molecular dipole moments in the base pair (xy) plane (Figure 40(a)), and these dipoles form a helix along the molecular (z) axis (the pitch angle in DNA is about 34° per base pair).[235] An external electric field that rotates in the x-y plane will thus shift the molecular base pair electronic energies by approximately $\vec{\mu} \cdot \vec{E}$. This dependence of this electronic energy on the applied field may be used to generate a ratcheting potential and to drive current along the helical (z) axis. Thus, the time-varying electric field in the xy plane will produce a flashing ratchet for hole transport. In a homopolymer of DNA, our simulations indicate that a hole can be driven unidirectionally through the structure, due to the helical orientation of the base pair dipoles in the double helix,[236] if the time scale for the electric field rotation is synchronized with the hole hopping rates.

A rotating electric field orthogonal to the DNA helix (z) axis is illustrated in Figure 40. Holes "float" to minimize their free energy, so current will be driven directionally along the helix axis (Figure 40). We refer to this ratcheting mechanism as "surfing," since a hole is predicted to follow the stabilized HOMO, whose spatial localization will move linearly along the helix axis as a function of time.

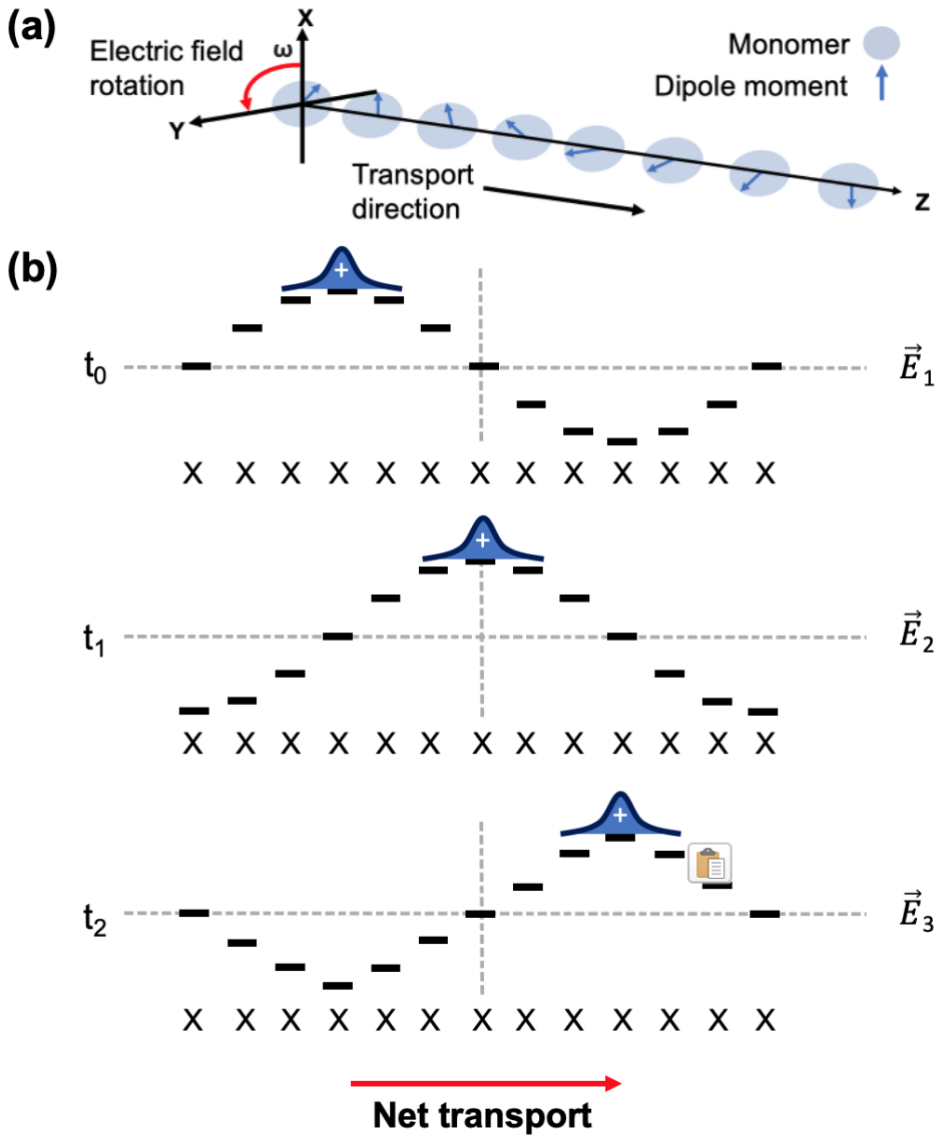

Figure 40: (a) The proposed flashing ratchet mechanism for vectorial charge transport is shown schematically. A rotating external field normal to the helix axis, with frequency ω, generates directional transport along the helix axis (z). (b) Surfing Mechanism. The applied electric field produces a ratcheting potential that drives carries along the helix axis. As the electric field rotates, the orbital energy maximum (energy minimum for a hole) is displaced in a unidirectional manner along the z axis.

5.3.2 Simulation of charge carrier surfing

Charge surfing transport is now described in the context of a multi-step charge hopping model.[237 238-241 242 243, 244] Although charge carriers are somewhat delocalized among neighboring bases in nucleic acids,[200] long-distance transport through DNA is believed to occur through multi-step hopping.[245]

The charge transfer rate is approximated by:[100, 246]

$$k_{CT} = \nu \exp\left[-\frac{(\Delta G^0 + \lambda)^2}{4\lambda k_B T}\right] \tag{14}$$

where λ is the reorganization energy, k_B is Boltzmann's constant, T is the temperature ΔG^0 is the standard Gibbs free energy of the electron or hole transfer reaction, and ν is a prefactor with frequency units. The prefactor depends on the adiabaticity of the reaction. For an adiabatic electron transfer mechanism, ν is a nuclear frequency factor, typically on the scale of 10^{13} s^{-1}. For nonadiabatic electron transfer, ν depends on both electron tunneling and nuclear frequency factors.[247]

In the ratcheting mechanism described above, the time-varying external field modifies the free energy landscape by shifting the energies of the charge localizing sites. Linear response theory, which underpins Equation 14, describes the reorganization energy as being largely unaffected by the external field,[248] and no explicit molecular deformations are included in the model. Therefore, the influence of the field is to introduce a time-dependent energy shift, $\Delta\varepsilon(t)$, the electron hopping free energy. As such, the field dependent hopping rate is:

$$k_{CT}(t) = \nu \exp\left[-\frac{(\Delta G + \Delta\varepsilon(\mathrm{t}) + \lambda)^2}{4\lambda k_B T}\right] \tag{15}$$

The $\Delta\varepsilon(\mathrm{t})$ term is approximated by:[249]

$$\Delta\varepsilon(\mathrm{t}) = -\vec{\mu} \cdot \vec{E}(t) \tag{16}$$

where $\vec{\mu}$ is the dipole moment for each redox species and $\vec{E}(t)$ is the rotating applied field, $\vec{E}(t) = E_0\,\hat{\imath}\cos\omega t + E_0\,\hat{\jmath}\,\sin\omega t$. The value of $\Delta\varepsilon(\mathrm{t})$ needs to be larger than thermal energies ($k_B T$) to induce directional charge ratcheting (e.g., $\Delta\varepsilon$ values of ~ 10 $k_B T$ will suffice). Electric fields of the order 10^9 V/m and typical molecular dipole moments (5-15 D) will induce the required energy shifts.[250, 251] Electron transfer reorganization energies (λ values) of 1.1 eV were assumed. This value is typical of estimated DNA reorganization energies.[252]

5.3.3 Kinetic modeling

A scheme that describes multi-step charge hopping kinetics among redox multiple redox active species, X_n, is indicated in Equation 17. X represents a hole on site n in the helical structure. The time-dependent hole hopping rates is given by Equation 15 when a slowly rotating electric field is applied.

$$X_1 \underset{k_{-1}}{\overset{k_1}{\rightleftharpoons}} X_2 \underset{k_{-2}}{\overset{k_2}{\rightleftharpoons}} X_3 \cdots \underset{k_{-n_{-1}}}{\overset{k_{n_{-1}}}{\rightleftharpoons}} X_n \tag{17}$$

The kinetics equations are:

$$
\begin{aligned}
\frac{d[X_1]}{dt} &= -k_{-1}[X_1] + k_1[X_2] \\
\frac{d[X_2]}{dt} &= k_1[X_1] - k_{-1}[X_2] - k_2[X_2] + k_{-2}[X_3] \\
\frac{d[X_3]}{dt} &= k_2[X_2] - k_{-2}[X_3] - k_3[X_3] + k_{-3}[X_4] \\
&\vdots \\
\frac{d[X_n]}{dt} &= k_{n_{-1}}[X_{n-1}] - k_{-n_{-1}}[X_n]
\end{aligned}
\tag{18}
$$

These equations were solved using *Mathematica* 12[253] using the Gear implicit backward differentiation strategy (BDF method)[254, 255] to describe the motion of a hole that is located initially on site 1.

5.3.4 Ratcheting in DNA

We studied a guanine-cytosine (GC) DNA structure.[212, 213,256] Hole hopping in DNA is believed to occur between purine bases. Lewis and co-workers found that hole transfer rates between neighboring GC base pairs are of 4.3 x 10^9 s^{-1}.[257] Assuming that λ = 1.1 eV,[258] a prefactor of ν equal to 1.9 x 10^{14} s^{-1} produces the experimental rate at $\Delta G^0 = 0$. These values are consistent with values in the broader literature.[150, 231, 259, 260] The kinetic modeling of hole flow through a 15-mer G-block induced by a rotating electric field is shown in Fig. 3(c). We chose a G-block structure to illustrate our mechanism, since G-rich sequences are predicted to be excellent hopping conductors.[142]

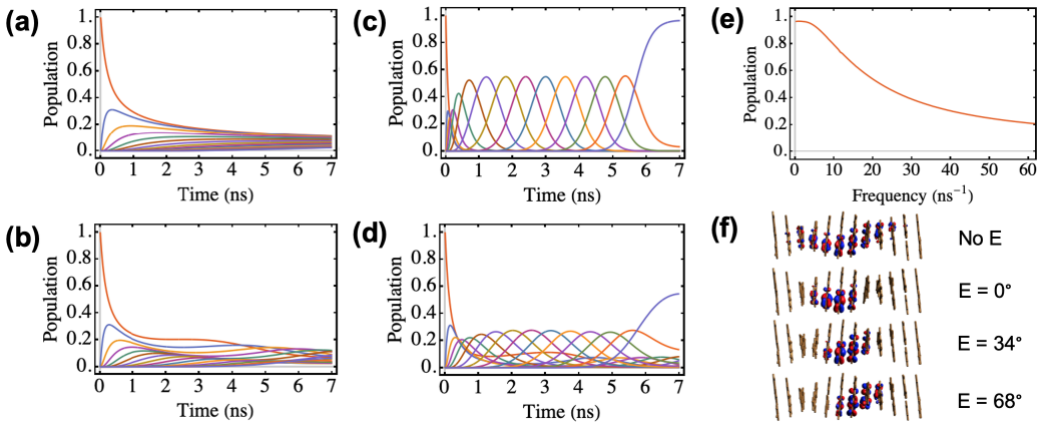

Figure 41: Kinetics results and DFT analysis. (a) Kinetics of GC15 with no applied electric field. (b) Kinetics of GC15 when an electric field of 1 x 10^8 V/m is applied with a rotation frequency of 1 ns^{-1}. (c) Kinetics of GC15 when an electric field of 1 x 10^9 V/m is applied with a rotation frequency of 1 ns^{-1}. (d) Kinetics of AT15 with an electric field of 1 x 10^9 V/m and a rotation frequency of 1 ns^{-1}. (e) Maximum population transfer to the terminal GC site as a function of the field frequency. (f) HOMOs of a GC homopolymer obtained at the M06-2X/6-311+G(d,p) level of theory[45, 261, 262] in the presence of a 1.54 x 10^9 V/m field orthogonal to the helix axis (bases only in the analysis). The geometry used is based on a canonical B-DNA structure.[263] Water solvent effects were included using the PCM model.[41]

We computed the ratcheting efficiency in our kinetic model for a guanine (G) dipole moment of 7.2 D and a 34° pitch angle between nearest-neighbor bases in the GC15 DNA.[264, 265] Charge transfer will not have time to respond to the rotating applied field if the field rotation frequency is much larger than the hoping rate. In the opposite regime of slow field rotation, particles would diffuse along the entire chain (with peaks and dips as indicated in Figure 40), equally favoring forward and reverse transport. The electric field rotation therefore needs to match approximately the scale of the hole transfer rates to realize efficient charge ratcheting.

The applied field strength is also critical. When a rotating electric field of 1×10^8 V/m was modeled (Figure 41(b)) with a rotation frequency of 1 ns^{-1}, no significant ratcheting was predicted from the kinetic analysis. However, when the magnitude of the electric field strength was increased to 1×10^9 V/m with a rotation frequency of 1 ns^{-1}, productive charge surfing was found in the kinetic modeling (Figure 41 (c)). With a 1×10^9 V/m field and 1 ns^{-1} rotation frequency (on the same scale as the electron hopping frequency (Figure 41 (e)), nearly 100% of the initial population is transferred over 15 sites when a hole is released on the first guanine at t = 0. Extending the number of GC units to 100, we computed a transport efficiency in GC100 near 100% after 34 ns. This simulation corresponds to hole transfer over 34 nm, thus showing that surfing-based transport may be used to advance charge over long distances if appropriate transverse fields can be generated.[212] Varying the electronic coupling and reorganization energy influences the hole transfer time scale, but the high efficiency ratcheting persists, since it is defined by $\Delta\varepsilon$ (Eq. (3)) and the time scale matching condition described above. Decreasing the monomer dipole moment to 3 D, which would correspond to that of adenine (A),[265] reduces the ratcheting efficiency to 58% (Figure 41 (d)). However, the ratcheting yield would increase if a stronger electric field were applied. Since large fields may ionize the molecular structures, monomers with large dipole moments are preferred candidates for realizing ratcheting.

A rotating electric field lowers the molecular symmetry and produces spatially localized HOMOs. We analyzed the frontier molecular orbitals in a system with twelve GC base pairs (without explicitly including the sugar phosphate backbone) in a rotating applied field of 1.54 x 10^9 V/m orthogonal to the helical axis. At zero field, the DNA HOMO is delocalized (this is an overestimate of the expected delocalization, as thermal and vibronic relaxation around the hole were not included). With the field on, the DNA HOMO becomes spatially localized, and further localization is expected as noted. The location of the HOMO depends on the orientation of the applied field at a given time. Single point density functional analysis of the electronic structure for a GC12 sequence was performed using Gaussian 16[40] at the M06-2X/6-311+G(d,p) level.[45, 261, 262] The polarizable continuum model (PCM)[41] was used to simulate the effects of water on the electronic structure. We used the Avogadro DNA building tool[266] to construct canonical GC12 B-DNA structure.[263] The phosphate backbone atoms were removed in the electronic structure analysis, and the dangling bonds were capped with hydrogens. A field of 1.54 x 10^9 V/m was applied normal to the helix axis. The results shown in Figure 41 (f), which correspond to adiabatic states,[105] indicate that the orientation of the electric field determines the spatial localization of the HOMO. These results show that the HOMO localization in a particular region of the DNA strand depends on the orientation of the applied field. Orbital localization in DNA base pairs persists in simulations with an explicit phosphate backbone.[200] Indeed, the backbone's negative charges are predicted

to have a minor effect on the structure of the HOMOs, since their charge is screened by the counterions and water molecules that surround the DNA duplex.[181]

Although the ratcheting fields required are large, molecules in the biological milieu are exposed to strong fields.[267, 268] Electric fields of 3 x 10^9 V/m can cause DNA damage,[269] but DNA is predicted to preserve its structure in the presence of weaker fields. Computational results indicate that some DNA assemblies, such as G-quadruplexes, are particularly stable.[270] Therefore, supramolecular architectures based on DNA (e.g., DNA origami and brick structures) or foldamer structures may be sufficiently stable to support ratcheting transport mechanisms.

A recent study found that B-DNA with 102 nucleotides (~ 30 nm) and fullerene anchoring groups, subjected to a 1 V source-drain bias, produces currents in the nanoampere range.[215] The predicted conductance for one base pair is close to 50 nS. In the hopping regime, the conductance decays with a rate of ~ 0.5 nS/nm. Assuming ohmic behavior, the conductance at 100 nm would decay essentially to zero. The ratcheting mechanism described above would reduce the distance dependence of the conductance, increasing the length scales over which self-assembled soft matter structures could transport charge in the absence of a source-drain bias. Analyzing hopping transport using a steady-state flux approach,[271, 272] the conductance is found to depend linearly on the charge transfer rate. Ratcheting increases the forward hole hopping rate by at least two-fold (Equation 15). Therefore, the conductance decay would be reduced by about a

half. If the decay of conductance with distance in a ratcheted mechanism is 0.25 nS/nm, a 1 V bias would produce nanoampere currents at 100 nm.

5.3.5 Proposed experimental tests of the ratcheting mechanism

The field-induced ratcheting mechanism described above is not limited to DNA structures and may be applied to other chiral structures, such as those shown in Figure 42(a). PNA, helical peptides, DNA-wrapped carbon nanotubes and Janus nanoparticles with chiral linkers are chiral structures that seem suitable to realize ratcheted charge transfer over long distances.[165, 273-275] To further explore electron-transfer ratcheting, we propose three designs. The first uses four electrodes to produce a rotating electric field (i.e., a 90° advancing phase, as is used in electrorotation, Figure 42 (b)).[276] The relative phase of the four electrodes would create a rotating electric field.[277] The fabrication of nanoscale electrodes might represent a major fabrication challenge, but the existence of technologies such as solid-state nanopore-based DNA sequencing encourage this kind of design.[278, 279] The second scheme describes the attachment of chromophores to DNA that would generate transient fields upon photoexcitation (Figure 42 (c)), through changes in the charge state or dipole orientation of the excited states. The time varying electric fields are expected to shift the orbital energies of the base pairs near the chromophores, creating a ratcheted potential that would favor directional hole transfer. The architecture in Figure 42 (c) uses the substitution of several DNA bases with redox active species, such as anthraquinone, which can be reversibly oxidized electrochemically with a gate

voltage[280] (Figure 42 (d)). Ratcheting in this structure would be driven by transient oxidation/reduction of the redox groups, caused by electrochemical gating.

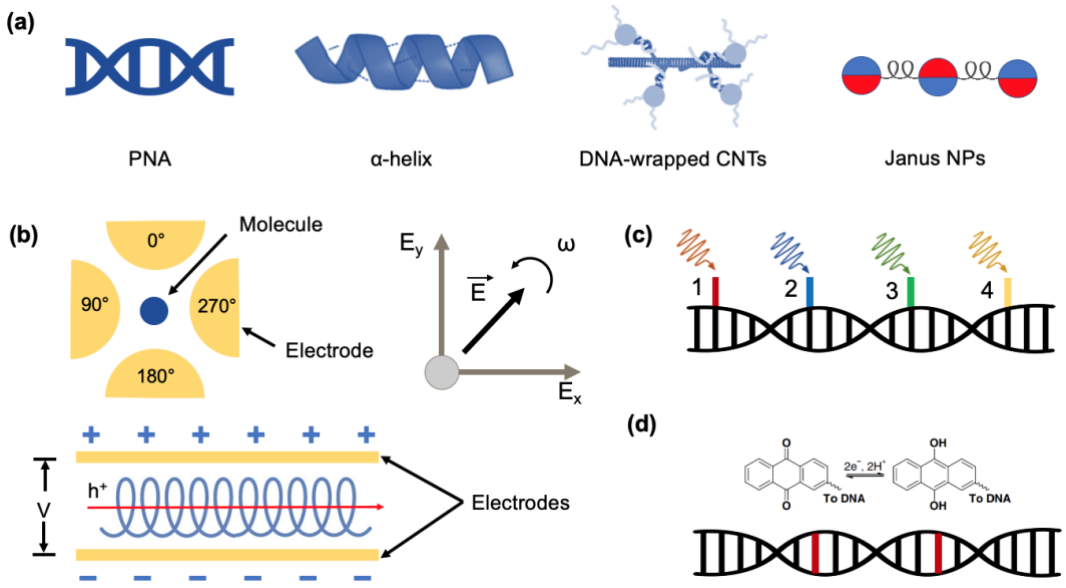

Figure 42: Proposed structures and experimental setups for ratcheting at the nanoscale. (a) Candidate architectures to support charge ratcheting. (b) Experimental designs to test the ratchet mechanism. Top left: Schematic representation of a molecule suspended in a rotating electric field that is generated by four electrodes with 90° advancing phase. Top right: Rotating electric field generated by four electrodes with frequency ω. Bottom: Schematic representation of the experimental setup with two electrodes removed for visualization. (c) Sequential photoexcitation of light absorbing groups. (d) Replacement of DNA base with other redox active species, such as anthraquinones. The locations of the redox groups are indicated in red. Electrochemical gating switches the redox group between the oxidized and reduced states.

5.4 Electron ratcheting in larger structures

In this section, we describe a ratcheting mechanism on length scales beyond nanometers. In contrast to the mechanism in Section 5.3, the mechanisms described here do not require spatial control of a single monomer's properties.

5.4.1 Ratcheting driven by solution electrochemistry

Figure 43 illustrates charge ratcheting driving by a polarized electrode near the DNA. Gate electrode polarization is expected to induce an energy shift of the guanines' HOMOs in DNA, creating a potential with a maximum in the area near the polarized electrode that stabilizes DNA holes. Molecular polarization induced by the electrodes is expected to produce a corresponding shift in the location of the potential energy minimum for a hole in the molecular chain. Since holes float to the HOMO, current will be driven unidirectionally along the chain as the electrode potential is modulated with time. Experimental architectures similar to those shown in Figure 43 were used to shift molecular frontier orbital energies.[281, 282] In contrast to the rotating field-induced ratcheting described in Figure 40, which considers the interaction of an external field with the dipole moment of each monomer, the mechanism described here uses electrochemical gating of the electrostatic interaction that is weakly dependent on the dipole orientation of specific monomers: the effect depends primarily on the potential generated by the electrode. With this mechanism, the external electric field translates in time, retaining its orientation. An ionic solution for the DNA will interact with the hole. The potential generated with the polarized electrode has a peak that is not periodic along the helix axis (in contrast to the prior example).

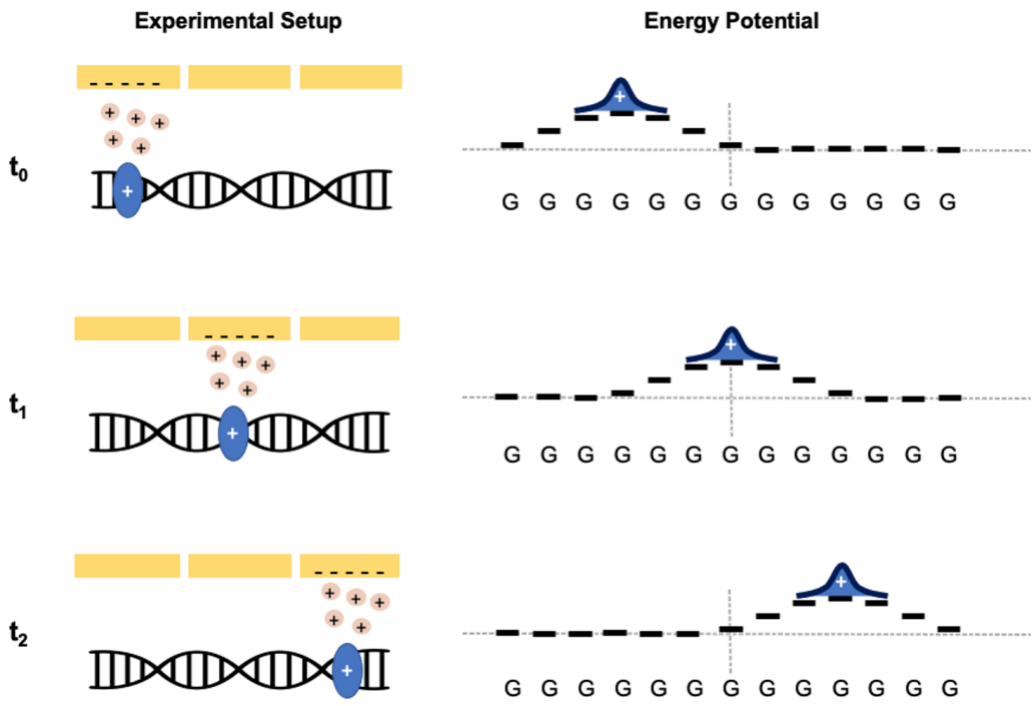

Figure 43: Ratcheting mechanism based on electrochemical perturbation. Left: An electrode is polarized in a specific region. The electrostatic interaction induces localization of a hole along the molecular chain (figure not to scale). Right: When the electrode polarization shifts to a different position, the hole follows it, producing unidirectional charge transport.

5.4.2 Design considerations

For DNA to retain its structural integrity, it is believed to be essential that DNA extend more than 2 nm above the electrode surface. Experiments have placed DNA 2.4-2.6 nm above electrode surfaces using chemical linkers.[215] We consider DNA self-assembled monolayers (SAMs) where the orientation of DNA duplexes can be controlled by electrochemical methods.[283] We now estimate the potential experienced by DNA using Debye-Hückel theory, which has been used to describe highly charged surfaces, including cell membranes,[284, 285] and provides a qualitative description for

metallic electrode surfaces.[286] Charges at the electrode surface are screened by the ions present in solution. The Debye screening length of the electrolyte must be longer than the distance between the gate electrodes and the DNA for the electrode potential to influence the DNA energetics. For water at room temperature, the Debye length, λ_D, is:[287]

$$\lambda_D(nm) = \frac{0.304}{\sqrt{I(M)}} \tag{19}$$

where I is the ionic strength in molar units. For a monovalent electrolyte concentration of 0.001 M, such as NaCl, $\lambda_D \approx 10$ nm, which is larger than the electrode-DNA separation considered in our example (2.4–2.6 nm). This distance would allow DNA bases to respond to the electrode's potential to produce ratcheting. The concentration of 0.001 M considered here would produce a longer Debye length than typical DNA ionic strength values (~ 0.1M), and the DNA duplex is predicted to be stable at room temperature.[288] The presence of transition metal ions might further stabilize DNA structures[289] but we do not consider these effects in our model.

Debye-Hückel theory[284] estimates the potential, $V(x)$, that DNA nucleobases would experience near the charged electrode as:

$$V(x) = \frac{\sigma\lambda_D}{\epsilon_s\epsilon_0} e^{-x/\lambda_D} \tag{20}$$

σ is the charge per unit area of the electrode, ϵ_s is the dielectric constant of the solvent, ϵ_0 is the vacuum permittivity, and x *is* the distance from the electrode surface. The parameter $\sigma = {}^{CV}/_{A}$, where C is the electrode capacitance, V is the voltage and A is the

area. Considering an electrode with σ = 0.4 C/m^2,[290, 291] λ_D = 10 nm, ϵ_s = 80, ϵ_0 = 9x10^{-12} F/m and x = 2.4 nm, the potential at the DNA is 4.4 V. An alternative to using aqueous electrolyte solutions is to use mesitylene solvent (ϵ_s = 2.3), as in recent break junction experiments on DNA, in order to increase the potential that the DNA would experience.[165]

The electric field (the gradient of the potential in Equation 20) that the base pairs would experience from this potential at a 2.4 nm separation distance is 4x10^8 V/m, and a localized charge on the DNA at 2.4 nm from the electrode would experience an energy shift two orders of magnitude larger than k_BT. This shift would produce a strong ratcheting potential. Indeed, our description assumes that the gate electrodes can generate a charged surface with a strong electric field as illustrated in Figure 43. This analysis assumes electrodes with well-defined geometries and DNA SAMs with linear DNA strands, and a density of molecules that can range from 10^{10} to 10^{13} molecules/cm^2.[283]

If the gate electrode width and the separation between each gate electrode is one micrometer, there would be about 3,000 DNA base pairs (or more) with an energy shift determined by the electrode. This energy shift is orders of magnitude larger (≥ 1 eV) than the energy difference among the four DNA bases (A,T,C,G), so holes in the DNA would be driven to reach the segment that is near a negatively charged (low potential) electrode, assuming that all of the other electrodes are uncharged.[292] The diffusion

constant for holes to move through DNA is given approximately by the hopping rate (this depends on sequence) between nearest bases and the inter-base separation distance. Assuming a hopping rate of ~10^9 s^{-1}, the carrier diffusion coefficient, D, for holes in DNA is ~10^{10} $Å^2/s$. Using a one-dimensional random walk diffusion model, $\langle d^2 \rangle = 2Dt$ as a lower limit, we estimate that a hold time for the electrode potential of 10 ms would be needed for the carriers to diffuse to the adjacent electrode region a distance, d, of 1 μm, which corresponds to the distance separation between gate electrodes. This simple diffusion model does not consider the bias that would be present due to the potential generated in regions close to the adjacent electrode.

5.4.3 Current estimates

30 ms is required for a hole to diffuse 3 μm, as described above. Since the ratcheting potentials favor directional charge flow (left to right), reverse hole-transfer (right to left) would be very slow ($k_{back} \leq 10^7$ s^{-1}) and may be neglected.

The current will depend on the DNA length and on the number of DNA strands along the transport direction. In one DNA molecule of 3 μm, there are about 10,000 base pairs. Assuming a lower limit of one hole per 100 base pairs, we have 100 holes per strand. Since it takes 30 ms for a hole to diffuse the entire length of the DNA, the current will equal ca. 0.1 pA for a DNA SAM with at least 100 duplexes, a value considered to be high for DNA assemblies at the micrometer scale. In fact, the current predicted to result from the proposed ratcheting mechanism is comparable to values observed in G-

quadruplex DNA molecules shorter than 100 nm with a source-drain voltage less than 5 V,[213] and this current would be at least an order or magnitude larger than was measured in DNA double-crossover junctions (up to 20 nm).[210] Importantly, these currents could be induced over micrometer distances. The mechanism proposed is expected to produce picoampere currents over distances longer than nanometers at gate electrode voltages less than 5 V. We emphasize that the reduced conductance decay realized in the proposed ratcheting mechanism is achieved by gate electrode enabled biased hole diffusion. The resistance is determined largely by the electrode width and the distance separation between adjacent gate electrodes; the resistance does not grow linearly with the overall polymer length (as would be found in simpler source-drain biased configurations).

5.4.4 Proposed experimental design

The proposed electrochemical ratcheting in DNA requires the use of gates near the nucleobases. An array of gate electrodes can control the spatial distribution of nearby ions. To realize electron ratcheting at the mesoscale, we propose the architecture described in Figure 44. The gate electrodes will have widths and separations on the order of micrometers and will be polarized sequentially to displace negative ions from the region. A source electrode will inject holes initially, and the drain electrode will detect the net current of the ratcheting device. No source-drain bias is required. The proposed experimental architecture is similar to that of the electron ratchet devices

reported recently by Weiss et al.[225] The structures considered here utilize self-assembled soft matter, rather than amorphous organic films and symmetric electrodes. As well, peptide nucleic acids can be used in place of DNA to eliminate the counter-ions and thus minimize electrostatic screening.[162, 168]

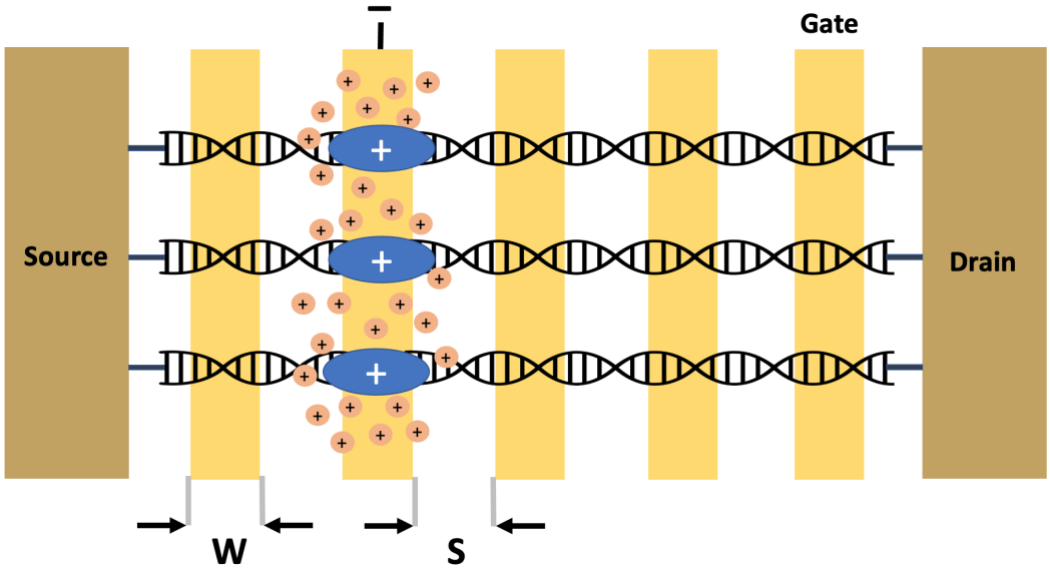

Figure 44: Proposed architecture for electrochemical ratcheting at the mesoscale. The width (W) and separation (S) of the gate electrodes are on the scale of μm. A positively polarized gate electrode will increase the concentrations of anions, attracting the holes present in the DNA strands. Polarization of sequential gate electrodes along the transport direction generates a net current that can be detected by the drain electrode.

5.5 Conclusions

We have described and simulated two charge ratcheting schemes at the nano- and mesoscales, and we described molecular architectures that promise to realize each mechanism. The schemes exploit electric fields to tune the free energies of hopping electron transfer steps. In Section 5.3, we described a ratcheting mechanism for

nanoscale structures. It requires electric fields that rotate in a plane that is orthogonal to the transport direction. The corresponding kinetic models predict that an end-to-end population transfer above 50% will occur with molecular motifs having dipole moments around 3 D with driving fields of ~ 10^9 V/m. Larger molecular dipole moments are predicted to increase the ratcheting efficiency to nearly 100%.

In Section 5.4, we introduced a second mechanism for transport length scales beyond nanometers. The required ratcheting potentials may be produced electrochemically and are expected to generate unidirectional charge transport through DNA at the micrometer scale, increasing the maximum distance over which current may be driven.[213, 215] The results described here offer the promise of using self-assembled soft matter to fabricate electron ratchets, with ratcheting function programmed into the molecular building blocks. Ratcheting was demonstrated previously in organic field effect transistors.[225] In contrast, the ratcheting mechanism proposed here is derived from the intrinsic structure and properties programmed into the molecular building blocks. In a similar spirit, fully quantum ratcheting was proposed to direct excitation energy transfer in molecules.[120, 293] The theoretical designs described in this study aim to motivate the exploration of soft matter charge ratcheting assemblies that may function over many length scales. If successful, one can imagine exploiting these charge transport structures to enable the function of self-assembled supramolecular machines.

6. Enantiomeric separation of semiconducting nanotubes

This chapter is excerpted from:

Mastrocinque, F.; Valdiviezo, J.; Meikle, H.; Bullard, G.; Nayak, A.; Zhang, P.; Beratan, D. N.; Therien, M.J., Enantiomeric Separation of Single-Chirality, Single-Walled Carbon Nanotubes Using Axially Chiral, Molecular Surfactants. *Manuscript in preparation*.

6.1 Significance of the study

Applications of chiral carbon nanotubes in spintronics have been limited due to the absence of scalable handedness separation methods. Here, we report the enantiomeric separation of semiconducting carbon nanotubes using binaphtylene-based surfactants. This study provides a cost-effective strategy to produce enantioenriched carbon nanotube samples. Theoretical analysis reveals design guidelines for selective chiral dispersants.

6.2 Introduction

A major factor that has impeded the broad utilization of single-walled carbon nanotubes (SWCNTs) in electro-optic, spintronic, and nonlinear optic applications has been the inability to obtain SWCNT samples having structural, morphological, and electronic structural homogeneity. Commercially-available SWCNT samples contain

heterogeneous distributions of SWCNT chiralities and lengths, along with impurities that include multi-walled tubes and amorphous carbon.[294]

Each SWCNT structure is indexed by two integers (n, m) that define the diameter and helicity of that tube's roll-up vector on a graphene sheet. While (n, 0) and (n, n) SWNTs, commonly referred as zigzag and armchair structures, are achiral, all the other SWNTs possess chemical chirality, meaning that they exist as non-superimposable mirror images; such enantiomers lattice structures having opposite helical handedness (Figure 45a).

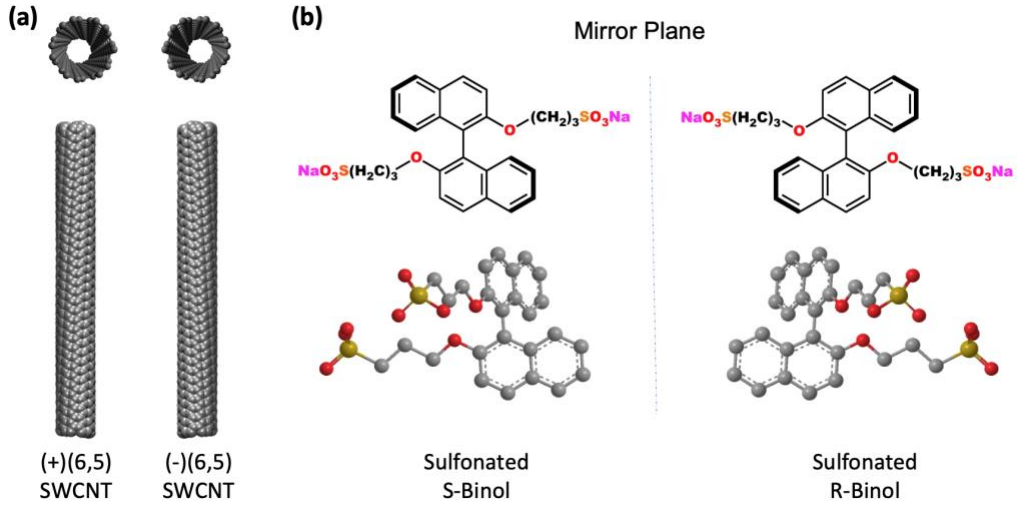

Figure 45: Structures of (a) chiral CNTs and (b) surfactants studied.

Current post-synthetic protocols for the separation of carbon nanotubes have enabled the isolation of individualized, single-diameter SWCNTs, and include gel chromatography,[295] density gradient ultracentrifugation (DGU),[296, 297] polymer-facilitated selective dispersion,[298, 299] and aqueous two-phase (ATP) separation.[300] Modified SWCNT

sorting procedures have been demonstrated to achieve simultaneous chirality and handedness control, but only for a small number of SWCNT chiralities with limited degree of enantioenrichment. Here, ATP has been successfully employed to isolate chirality-enriched SWCNTs, providing a rapid, facile, low-cost, and scalable method for isolating chirality-enriched SWCNT samples, and a route to obtain specific SWCNT chiralities that were previously inaccessible.[294]

We aimed to realize a scalable technique that provides diameter-sorted SWNTs of a single helical handedness; towards this goal, we have developed a simple, robust, two-step, enantioselective ATP-like protocol that has allowed the isolation of single-diameter SWCNT enantiomers. This process utilizes a chiral, binaphthylene-based surfactant (Figure 45 b) that discriminates SWCNT helical handedness by selectively dispersing one nanotube enantiomer into an aqueous solution. The resulting supernatant and sediment can be separately subjected to ATP protocols to obtain enantioenriched, single-diameter SWCNTs.

We have been able to isolate (6,5) and (5,6)SWCNTs (Figure 46) using this two-step technique and interpreted the observations in terms of solvation free energy differences using molecular dynamics. The ability to isolate these and other single-diameter SWNT enantiomers will open entirely new opportunities to generate and propagate spin currents in polymer-wrapped/SWCNT assemblies[301] that take advantage of the chirality-induced spin selectivity (CISS) effect.[302]

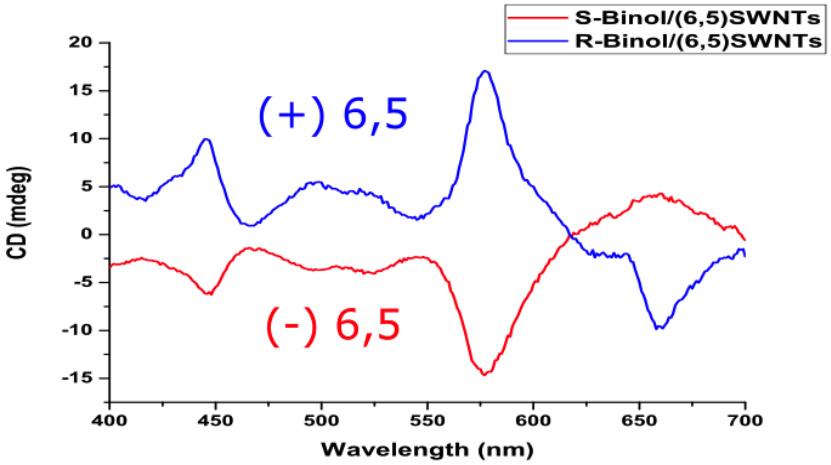

Figure 46: CD spectra of enantioenriched (+)(6,5)SWCNTs and (-)(6,5)SWCNTs using chiral surfactants.

6.3 Methods

6.3.1 Experimental methods

Detailed experimental methods will be provided elsewhere. A summary of the procedure is shown in Figure 47.

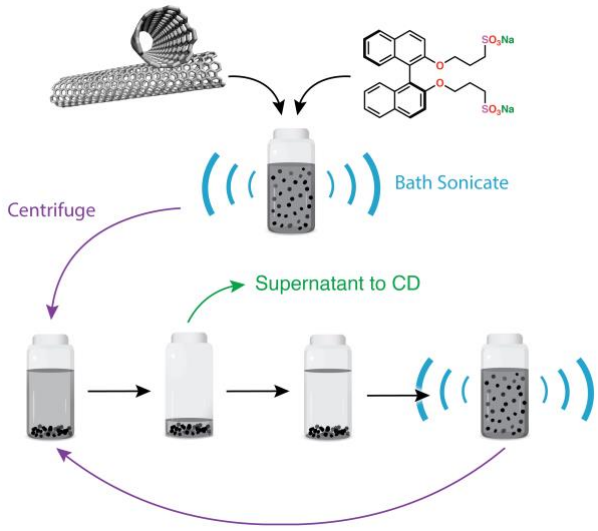

Figure 47: Procedure to obtain single-chirality, enantioenriched SWCNT samples.

6.3.2 Computational methods

6.3.2.1 Molecular dynamics system preparation

Single unit cells of the (+) (6,5) and (-) (6,5) single-walled carbon nanotubes (364 atoms) were built using the nanotube builder tool in Avogadro 1.2.0.[266] Initial geometries of the anionic surfactants in the R and S configuration correspond to optimized structures at the wB97-XD[44]/def2-SVP[39] level of theory under a polarizable continuum model for water,[41] as implemented in Gaussian 16.[40]

Four simulation boxes corresponding to each carbon nanotube with different chiral surfactants were built in PACKMOL.[303, 304] For each box, the carbon nanotube was positioned at the center of the box and aligned to the z-axis. The tube was solvated with 30 surfactant molecules, 3000 water molecules and 60 sodium ions. The unit cell vector for the z-axis was set to the nanotube length (≈ 4.1 nm) to assure connectivity with its periodic image. The remaining vectors were set to 5.2 nm.

6.3.2.2 Molecular dynamics simulation details

The GROMACS code[305-312] version 2019.1 was used to run the molecular dynamics (MD) simulations and predict the solvation free energy of the carbon nanotubes. We used the CHARMM36 force field parameters[170] and the SPC/E model for water.[313] Carbon nanotubes and surfactant topologies were constructed using CHARMM-GUI.[314] The carbon atoms were treated as aromatic sp^2 carbons with no partial charges.[315]

We followed an approach similar to Hinkle and Phelan Jr.[316] for the MD simulations. All the systems were energy minimized, thermalized (200 ps), and equilibrated (200 ps) at standard conditions ($T = 300$ K and $P = 1$ bar) using the leap-frog stochastic dynamics integrator,[317] a semi-isotropic Parrinello-Rahman barostat[318] (the system compressibility for the z-axis was set to 0), PME electrostatics,[173] and periodic boundary conditions. The cutoff distance for truncating van der Waals and Coulomb interactions was 12 Å. Hydrogen bonds were constrained by the LINCS algorithm.[319] The final MD production in the NPT ensemble covered 3 ns, with a time step of 2 fs. Analysis of trajectories was made in VMD (version 1.9.4a).[186]

6.3.2.3 Solvation Free Energy calculations

The solvation free energy ΔG_{solv} was estimated via the Bennett's Acceptance Ratio method[320, 321] using the GROMACS tool gmx bar. This free energy perturbation approach couples the solute-solvent interactions to a parameter λ.[322-325] We used an equidistant λ spacing of 0.05 to gradually transform an initial state without solute-solvent wan der Walls interactions ($\lambda = 0$) to a final state with normal solute-solvent van der Waals interactions ($\lambda = 1$).

6.3.2.4 Entropic and Enthalpic contributions to solvation

The change in entropy ΔS_{solv} as estimated using a finite difference approximation[326] as follows:

$$\Delta S_{solv}(T) = -\frac{\partial \Delta G_{solv}}{\partial T} \approx= -\frac{\Delta G_{solv}(T + \Delta T) - \Delta G_{solv}(T - \Delta T)}{2\Delta T} \tag{21}$$

The value of ΔT was set to 20 K. entropy ΔG_{solv} and ΔS_{solv} were used to calculate the enthalpic contribution:

$$\Delta H = \Delta G + T\Delta S \tag{22}$$

6.4 Results

The selective dispersion of (+)/(-)(6,5) SWNTs facilitated by the chiral surfactants was rationalized in terms of Solvation Free Energies. Molecular dynamics simulations corroborate experimental evidence of a given binaphthol-based surfactant's preference for a given (+) or (-) (6,5)SWCNT. The chirality combination of the CNT and the surfactant determines their interaction strength. $\Delta\Delta G_{[(+)/R]\rightarrow[(+)/S]} = -15.7$ kcal/mol and $\Delta\Delta G_{[(-)/S]\rightarrow[(-)/R]} = -15.5$ kcal/mol. The differences in Solvation Free energies between R and S is caused by the surfactant geometry on the CNT. Figure 48 shows that the surface coverage is higher for the (+)(6,5) SWCNT with the S surfactant and the (-)(6,5) SWCNT with the R surfactant.

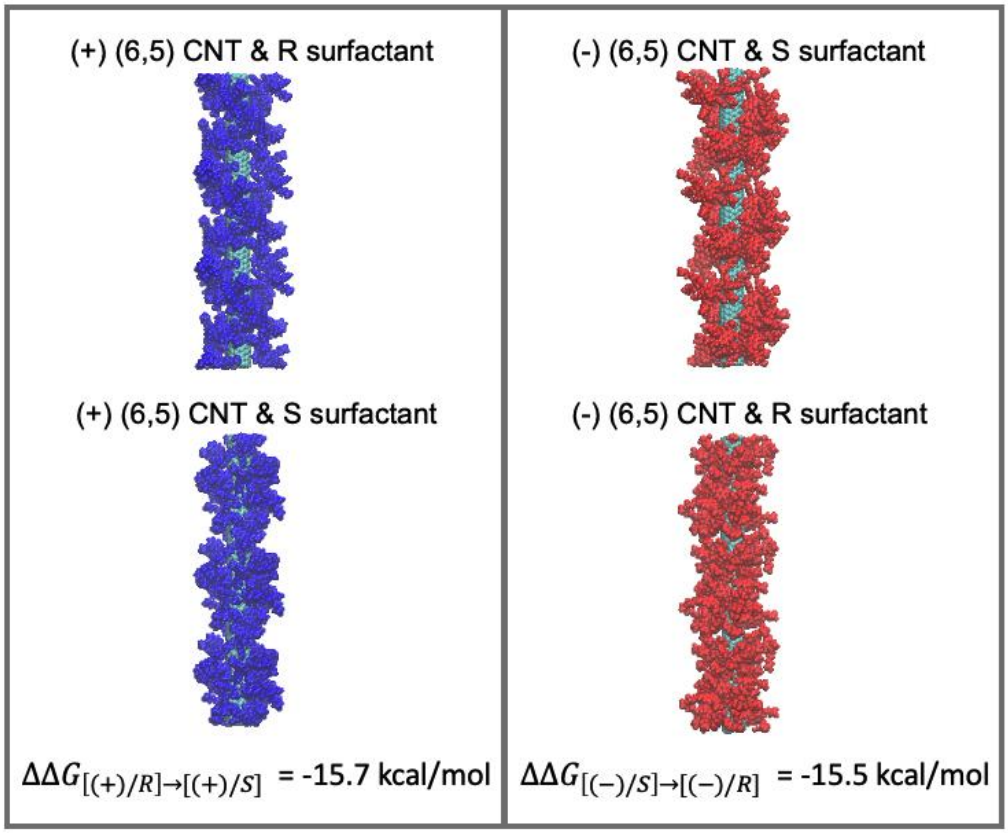

Figure 48: Final snapshots of solvated carbon nanotubes simulated for 3 ns using the CHARMM36 force field. Three periodic cells are shown. The values of $\Delta\Delta G$ correspond to one unit cell.

The breakdown of solvation free energies into enthalpic and entropic Contributions for CNTs are reported in Table 12. The enthalpic contributions to the solvation free energy from the strong surfactant-CNT interaction overwhelms the entropic penalty. The selective dispersion is attributed to the stronger van der Waals interactions between the (+)(6,5) CNT/(-)(6,5) CNT and the S/R surfactants facilitated by the chiral geometries.

Table 12: Enthalpic and Entropic contributions to the Solvation Free energies.

SWCNT	SUR	ΔG_{solv} (kJ/mol)	ΔH_{solv} (kJ/mol)	$-T\Delta S_{solv}$(kJ/mol)
(+) (6,5)	R	-444.1 ± 7.7	-1166.8 ± 8.7	722.7 ± 8.7
(+) (6,5)	S	-510.1 ± 3.2	-1614.3 ± 6.3	1104.2 ± 6.3
(-) (6,5)	R	-508.5 ± 6.2	-1619.1 ± 7.6	1110.6 ± 7.6
(-) (6,5)	S	-443.3 ± 5.2	-1169.0 ± 6.4	725.7 ± 6.4

6.5 Conclusions

We report a facile aqueous two-pase separation protocol for obtaining single-chirality, enantioenriched SWCNTs from commercially-available nanotube samples using chiral binol-based surfactants. The enantioselectivity is attributed to the tubes and surfactant geometries that enable high surface coverage thanks to the strong attractive Van der Waals forces. This enthalpic contribution overcomes the entropic penalty for dispersing the nanotubes. The findings of this work promise to open new opportunities for CNTs in spintronics.

7. Conclusions

This work presents collaborative theoretical and experimental efforts to design, synthesize and characterize the electronic properties of chemical systems for charge and energy transport applications. The studies presented in Chapters 2-6 have contributed towards fundamental insights required for developing more efficient electronic devices at the nano- and larger scales. Below we summarize major findings.

7.1 Chapter 2: Excited-state dynamics of molecular targets for IR-perturbed electron transfer

I employed density functional theory and time-dependent density functional theory to investigate the excited state dynamics of acetylene-bridged organic and organometallic D-B-A complexes. The computational studies supported the conclusions derived from transient absorption spectroscopy in the UV and mid-IR region. 3-pulse experiments could reveal electron transfer modulation thanks to the fast formation of charge separation states.

The utilization of IR pulses to activate symmetry-forbidden charge separation and charge recombination processes in highly conjugated double-slit style molecules is another exciting venue to explore. The asymmetric stretching of the bridge vibrational modes caused by IR pulses can remove the symmetry constraints and substantially increase the Donor-Acceptor electronic coupling and overall electron transfer rate.

7.2 Chapter 3: Exploiting molecular coherences for directed energy flow

We studied covalently linked, strongly coupled light-harvesting complexes based on porphyrin arrays to demonstrate quantum-ratcheted energy transfer and unmask the impact of symmetry-breaking on coherent energy transfer processes in cofacial porphiryn motifs.

The quantum ratchet design would benefit from 2DES and 2DEV studies to show the formation of charge separation states and quantum simulations to compute spectra. Since topology plays the predominant role on forming strong electronic interaction between porphyrin units, new designs should focus on structural connectivities that ensure strong π-overlap between monomers to sustain coherence in this family of compounds.

7.3 Chapter 4: Delocalization-assisted transport through nucleic acids in molecular junctions

Conductance measurements and molecular dynamics was combined to study nucleic acid-based molecular wires for biocompatible electronics. We examined the single-molecule conductance of peptide nucleic acid (PNA) duplexes, molecules analogous to DNA with a peptide backbone, and compared the results with DNA duplexes with a similar base-pair sequence. We analyzed the relative contributions of coherent and incoherent transport on the conductance of these compounds. We provided PNA sequences of several nanometers in length with conductance values

comparable to highly-conductive small molecules. In addition, we emphasize the importance of forming strong molecule-lead interactions to construct efficient nucleic acid-based molecular wires.

7.4 Chapter 5: Electron ratcheting in self-assembled soft matter

The content of this chapter presents two mechanisms for ratcheting employing external electric fields. We analyzed how nucleic acids could be used for electron ratchet devices. These devices rectify electric current over long distances using energy sources different from a net applied bias along the transport direction. We proposed experimental designs to build DNA-based electron ratchet devices to motivate the utilization of organic polymers for charge transport over several micrometers.

7.5 Chapter 6: Enantiomeric separation of semiconducting nanotubes

Cost-efficient synthesis and scalable separation methods of chemical systems are a major step toward future electronics. In this chapter, we used molecular dynamics simulations to understand the action mechanism of small-molecule surfactants to separate chiral semiconductive nanotubes. Structural changes that could enhance the enthalpic contribution to the solvation free energy of the carbon nanotubes could allow separation of other nanotubes of different diameters.

Appendix A

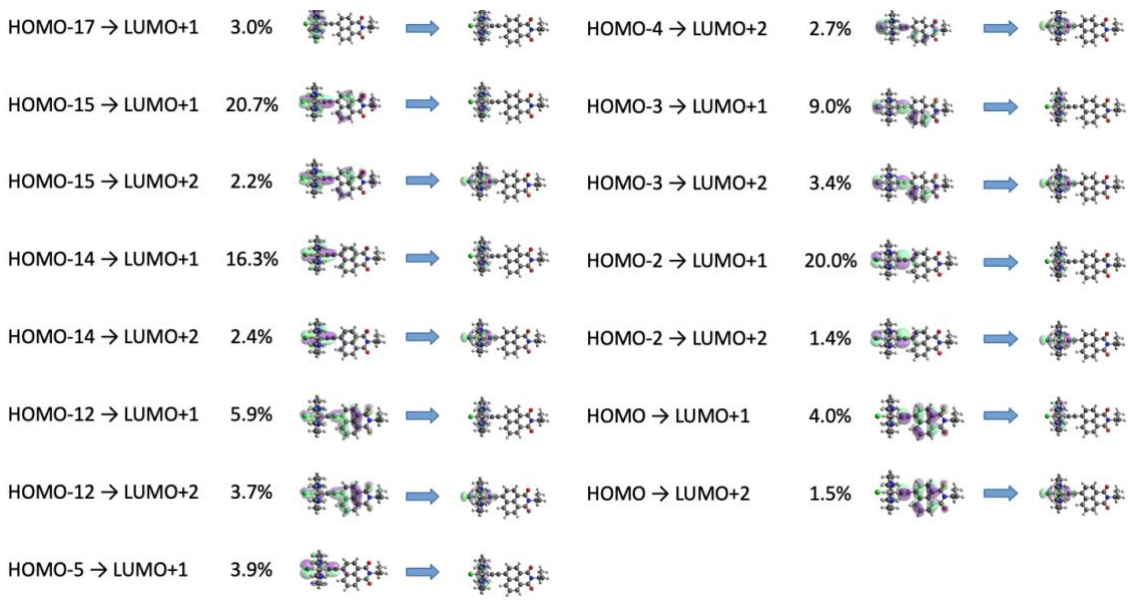

Figure 49: TD-DFT results showing all sizable contributions for the lowest energy triplet state of compound 1.

Table 13: Coordinates of ground state optimized structure of 1 in CH_3CN.

Atom	X	Y	Z
Co	-3.40265	-0.03545	0.04988
N	-3.51322	-0.33856	1.99578
H	-4.51582	-0.15387	2.14735
N	-3.51306	-2.00454	-0.14308
H	-2.52933	-2.28113	-0.26160
N	-3.30809	0.28289	-1.90406
H	-2.31338	0.13236	-2.11908
N	-3.31150	1.92518	0.25428
H	-4.31185	2.13496	0.38762
C	-3.26545	-1.77055	2.23304
H	-3.60042	-2.06743	3.23843
H	-2.17790	-1.93475	2.16861
C	-3.98524	-2.53070	1.14978
H	-3.81471	-3.61547	1.22100

H	-5.06894	-2.34263	1.20314
C	-4.28761	-2.56407	-1.26483
H	-5.33976	-2.28844	-1.10001
H	-4.21013	-3.66264	-1.22417
C	-3.81126	-2.04493	-2.60604
H	-2.73242	-2.24252	-2.73564
H	-4.32411	-2.60833	-3.39810
C	-4.10809	-0.57187	-2.79945
H	-5.16637	-0.36419	-2.58243
H	-3.90502	-0.26803	-3.83916
C	-3.61174	1.70913	-2.11421
H	-4.70098	1.82949	-2.00824
H	-3.31950	2.03089	-3.12517
C	-2.89169	2.48364	-1.04156
H	-3.10466	3.56185	-1.09598
H	-1.80182	2.34410	-1.12787
C	-2.54853	2.50444	1.37148
H	-2.64712	3.60120	1.32930
H	-1.48765	2.25482	1.21182
C	-3.01690	1.98218	2.71440
H	-4.09489	2.18156	2.84679
H	-2.50101	2.54433	3.50518
C	-2.72681	0.50758	2.90777
H	-1.66310	0.29598	2.71744
H	-2.95117	0.20414	3.94318
C	-1.54567	-0.18019	0.09280
C	-0.32938	-0.35293	0.07460
C	1.08958	-0.55190	0.08214
C	1.98138	0.55598	-0.12850
C	1.62103	-1.82073	0.30025
C	1.52314	1.87922	-0.35857
C	3.38334	0.32036	-0.10530
C	3.01118	-2.03520	0.31969
H	0.94105	-2.65912	0.45980
C	2.41324	2.91636	-0.55407

H	0.44638	2.06097	-0.37989
C	4.28245	1.39586	-0.30854
C	3.88688	-0.98287	0.12087
H	3.42015	-3.03237	0.49222
C	3.80359	2.67447	-0.52906
H	2.04329	3.92777	-0.72959
H	4.52044	3.48309	-0.68226
C	5.74883	1.16576	-0.28839
C	5.34754	-1.23439	0.14853
O	6.53516	2.08218	-0.46257
O	5.79756	-2.35175	0.34707
N	6.19347	-0.14359	-0.06164
C	7.66073	-0.36442	-0.04274
H	8.06648	0.63498	-0.23620
C	8.15204	-0.81090	1.33032
H	9.25175	-0.80441	1.33925
H	7.80228	-0.12236	2.11343
H	7.80745	-1.82520	1.56812
C	8.11598	-1.28078	-1.17386
H	7.77950	-2.31297	-1.01425
H	7.73306	-0.92643	-2.14211
H	9.21473	-1.27479	-1.22117
Cl	-5.68960	0.15515	0.03148

Table 14: Coordinates of ground state optimized structure of 2a in CH_3CN.

Co	1.52821	-0.21350	0.02942
N	1.71700	-1.87372	-1.03638
H	2.73149	-1.90125	-1.20506
N	1.49339	-1.38813	1.62804
H	0.48800	-1.46974	1.82770
N	1.35148	1.45093	1.09458
H	0.33968	1.50009	1.27096
N	1.57629	0.95685	-1.56879
H	2.58629	1.01841	-1.75509

C	1.36744	-2.99475	-0.14952
H	1.71348	-3.95329	-0.56589
H	0.26843	-3.02609	-0.07368
C	1.98091	-2.70823	1.19653
H	1.73412	-3.48418	1.93724
H	3.07752	-2.64208	1.11340
C	2.17562	-0.93639	2.85142
H	3.25092	-0.88397	2.62169
H	2.02936	-1.69812	3.63468
C	1.67377	0.41303	3.32363
H	0.57933	0.38608	3.47054
H	2.11087	0.62030	4.31049
C	2.05278	1.54086	2.38534
H	3.13188	1.51083	2.16986
H	1.82121	2.51702	2.84207
C	1.71650	2.56549	0.20514
H	2.81571	2.58034	0.13162
H	1.38207	3.52968	0.61783
C	1.10557	2.28376	-1.14297
H	1.36563	3.05500	-1.88405
H	0.00695	2.23534	-1.06818
C	0.89684	0.50964	-2.79477
H	1.04811	1.27158	-3.57684
H	-0.18050	0.46170	-2.57146
C	1.39739	-0.84017	-3.26737
H	2.49169	-0.81201	-3.41452
H	0.95984	-1.04740	-4.25399
C	1.02138	-1.96922	-2.32919
H	-0.05957	-1.94878	-2.12040
H	1.26121	-2.94391	-2.78478
C	-0.38830	-0.33375	-0.04981
C	-1.61591	-0.43189	-0.01438
C	-3.04069	-0.56969	0.00472
C	-3.88885	0.59195	-0.02773
C	-3.62623	-1.83381	0.05243

C	-3.37602	1.91412	-0.07814
C	-5.29940	0.41358	-0.00922
C	-5.02332	-1.99143	0.06960
H	-2.98083	-2.71368	0.07646
C	-4.22234	3.00487	-0.10790
H	-2.29228	2.05061	-0.09376
C	-6.15300	1.54374	-0.04026
C	-5.85652	-0.88664	0.03970
H	-5.47279	-2.98551	0.10667
C	-5.62131	2.81986	-0.08861
H	-3.81094	4.01481	-0.14653
H	-6.30417	3.67102	-0.11156
C	-7.62721	1.37431	-0.02185
C	-7.32496	-1.07887	0.05879
O	-8.37574	2.33778	-0.04777
O	-7.82264	-2.19333	0.10125
N	-8.12527	0.06556	0.02623
C	-9.60028	-0.09453	0.04264
H	-9.96434	0.93859	0.01005
C	-10.11043	-0.80977	-1.20418
H	-11.20894	-0.76015	-1.22403
H	-9.73250	-0.32370	-2.11557
H	-9.80852	-1.86474	-1.21229
C	-10.09198	-0.72292	1.34254
H	-9.79163	-1.77572	1.41711
H	-9.69927	-0.17747	2.21318
H	-11.18997	-0.66923	1.37589
C	3.43950	-0.10306	0.10108
C	4.66840	-0.04341	0.04374
C	6.10333	0.03460	-0.00153
C	6.76650	1.26003	-0.20457
C	6.90907	-1.10912	0.15691
C	8.15264	1.34531	-0.24846
H	6.17364	2.16950	-0.33099
C	8.29629	-1.04027	0.11548

H	6.42958	-2.07810	0.31710
C	8.96300	0.19347	-0.08967
H	8.61053	2.32144	-0.40865
H	8.86845	-1.95905	0.24470
N	10.33453	0.26962	-0.13266
C	10.97891	1.54664	-0.34065
H	10.73248	2.27093	0.45538
H	12.06616	1.40717	-0.34338
H	10.69381	2.00387	-1.30430
C	11.12775	-0.92731	0.03273
H	10.91271	-1.67889	-0.74689
H	12.19096	-0.66893	-0.03355
H	10.95632	-1.40755	1.01201

Table 15: Coordinates of ground state optimized structure of 2d in CH_3CN.

Co	1.181	-0.22395	-0.1299
N	1.01721	-2.07231	0.56617
H	0.00604	-2.14736	0.7396
N	1.20821	-1.03554	-1.93902
H	2.21263	-1.06418	-2.15742
N	1.33418	1.62875	-0.82196
H	2.34432	1.7271	-0.98754
N	1.14113	0.58171	1.67975
H	0.13422	0.58726	1.89007
C	1.36157	-2.97955	-0.54055
H	1.02388	-4.00612	-0.33157
H	2.45979	-2.98789	-0.63125
C	0.73336	-2.42098	-1.79086
H	0.97871	-3.02092	-2.68055
H	-0.36284	-2.38374	-1.68735
C	0.51318	-0.34373	-3.03646
H	-0.56095	-0.35097	-2.79553
H	0.65983	-0.92371	-3.96241
C	1.00044	1.07947	-3.21891

H	2.09315	1.09505	-3.37902
H	0.55049	1.48539	-4.13584
C	0.62313	1.98179	-2.06153
H	-0.45433	1.90059	-1.85093
H	0.84572	3.03395	-2.30371
C	0.9622	2.52629	0.2839
H	-0.13649	2.51111	0.36434
H	1.28184	3.55989	0.08139
C	1.58824	1.97612	1.5387
H	1.3257	2.56955	2.42769
H	2.68628	1.96261	1.44675
C	1.84684	-0.10279	2.77468
H	1.7002	0.47662	3.70097
H	2.92073	-0.08646	2.53053
C	1.36987	-1.52898	2.96179
H	0.27937	-1.54892	3.13545
H	1.83275	-1.93305	3.87305
C	1.73463	-2.43108	1.80007
H	2.81172	-2.35866	1.58347
H	1.50716	-3.48198	2.04316
C	3.09793	-0.3411	-0.09657
C	4.32542	-0.418	-0.16781
C	5.75157	-0.52589	-0.2334
C	6.58706	0.52626	0.28122
C	6.35107	-1.65227	-0.79442
C	6.05957	1.70363	0.87191
C	7.99945	0.38558	0.19757
C	7.74998	-1.77598	-0.86594
H	5.71596	-2.44994	-1.18356
C	6.89363	2.69314	1.35366
H	4.97442	1.80866	0.93775
C	8.84038	1.41136	0.69486
C	8.5709	-0.77371	-0.37914
H	8.21046	-2.66242	-1.3062
C	8.29458	2.54777	1.26407

H	6.47115	3.59211	1.80544
H	8.96815	3.32065	1.63863
C	10.31644	1.28138	0.61116
C	10.04147	-0.92731	-0.46675
O	11.05391	2.15817	1.03131
O	10.55131	-1.92338	-0.9559
N	10.82905	0.1132	0.03172
C	12.30564	-0.00961	-0.04553
H	12.65827	0.92624	0.40256
C	12.82745	-1.16196	0.80652
H	13.9253	-1.11143	0.84776
H	12.44565	-1.09115	1.83557
H	12.53845	-2.13327	0.38567
C	12.80068	-0.05354	-1.4875
H	12.51352	-0.99065	-1.98104
H	12.39803	0.79165	-2.06479
H	13.89778	0.02336	-1.49399
C	-0.73139	-0.11999	-0.16605
C	-1.96104	-0.0947	-0.10822
C	-3.39736	-0.0572	-0.06645
C	-4.08612	1.07092	0.42001
C	-4.1696	-1.14614	-0.51562
C	-5.47512	1.10908	0.46174
H	-3.51427	1.92838	0.78232
C	-5.55888	-1.10947	-0.48713
H	-3.66368	-2.03216	-0.90625
C	-6.24174	0.01937	0.00556
H	-5.98064	1.99268	0.85648
H	-6.13054	-1.96385	-0.85503
N	-7.64434	0.05679	0.0408
C	-8.34212	1.28921	-0.0752
C	-9.3988	1.59297	0.78813
C	-10.11297	2.78804	0.66678
C	-9.75964	3.71583	-0.32172
C	-8.69408	3.41819	-1.18753
C	-8.00402	2.21875	-1.07357

H	-9.67301	0.87652	1.56628
H	-10.93412	2.98669	1.35617
H	-8.43452	4.14568	-1.95923
H	-7.18574	1.99179	-1.76127
C	-8.39953	-1.13721	0.19365
C	-9.51201	-1.38469	-0.61587
C	-10.28077	-2.54084	-0.45695
C	-9.92797	-3.48638	0.51478
C	-8.80699	-3.24537	1.32653
C	-8.06165	-2.08361	1.17612
H	-9.78648	-0.65443	-1.38099
H	-11.14428	-2.69599	-1.10449
H	-8.54806	-3.98596	2.08588
H	-7.19957	-1.9001	1.822
O	-10.3838	4.90062	-0.50991
C	-11.4545	5.24243	0.3347
H	-11.81469	6.22842	0.0192
H	-12.28181	4.51725	0.2546
H	-11.13727	5.29847	1.38963
O	-10.60303	-4.63715	0.73558
C	-11.7296	-4.92249	-0.05563
H	-12.12465	-5.88873	0.27866
H	-12.5134	-4.15549	0.06307
H	-11.46705	-4.99402	-1.12455

Appendix B

Table 16: TD-DFT computed vibrational frequencies and IR intensities (*I*) for Ph-C4-NAP in toluene and DCM in the ground and excited states at θ = 0.

States	$\nu_{C=O,as}$ / cm^{-1} (*I* / km/mol)	$\nu_{C=O,ss}$ / cm^{-1} (*I* / km/mol)	$\nu_{C\equiv C,as}$ / cm^{-1} (*I* / km/mol)	$\nu_{C\equiv C,ss}$ / cm^{-1} (*I* / km/mol)
In toluene				
S_0	1795.2 (592)	1833.7 (507)	2266.0 (0)	2349.2 (189)
S_4(TD-DFT)	1736.9 (787)	1773.7 (2787)	2147.5 (295)	2313.0 (31540)
S_1(TD-DFT)	1752.3 (735)	1791.6 (2063)	2120.5 (447)	2144.8 (957)
T_1 (variational)	1732.6 (513)	1794.7 (812)	1970.2 (525)	2157.8 (369)
In DCM				
S_0	1782.8 (807)	1825.5 (622)	2264.4 (1)	2347.6 (244)
S_4(TD-DFT)	1720.8 (1234)	1761.7 (3335)	2148.3 (149)	2321.9 (33594)
S_1(TD-DFT)	1735.7 (1067)	1778.3 (2921)	2119.1 (788)	2144.7 (375)
T_1 (variational)	1723.7 (736)	1783.4 (1156)	1971.7 (825)	2155.4 (681)

Table 17: TD-DFT computed vibrational frequencies and IR intensities (*I*) for D-C4-NAP in toluene and DCM in the ground and excited states at θ = 0.

States	$\nu_{C=O,as}$ / cm^{-1} (*I* / km/mol)	$\nu_{C=O,ss}$ / cm^{-1} (*I* / km/mol)	$\nu_{C\equiv C,as}$ / cm^{-1} (*I* / km/mol)	$\nu_{C\equiv C,ss}$ / cm^{-1} (*I* / km/mol)
In toluene				
S_0	1793.6	1831.5	2257.7	2328.4
	(594)	(571)	(45)	(1602)
S_3(TD-DFT)	1740.5	1780.1	2129.8	2197.5
	(776)	(878)	(514)	(3077)
S_1(TD-DFT)	1750.1	1784.5	2139.2	2187.7
	(825)	(2941)	(2387)	(19729)
T_1 (variational)	1738.9	1789.3	2020.5	2129.1
	(671)	(1257)	(108)	(3361)
In DCM				
S_0	1781.2	1823.5	2254.1	2322.3
	(812)	(693)	(101)	(2152)
S_3(TD-DFT)	1724.2	1768.8	2124.3	2191.4
	(1110)	(1326)	(1051)	(4112)
S_1(TD-DFT)	1731.2	1771.0	2136.1	2188.3
	(1309)	(3690)	(1744)	(16318)
T_1 (variational)	1728.1	1776.2	2065.0	2119.2
	(1114)	(2524)	(3209)	(6840)

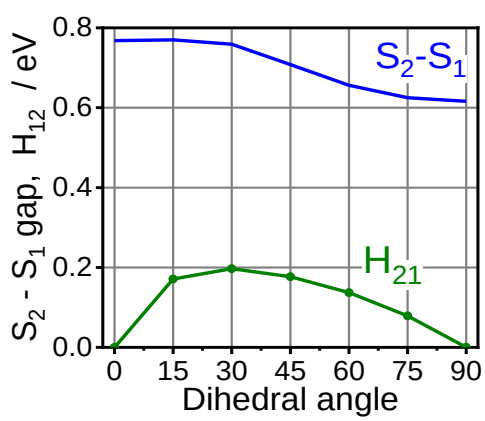

Figure 50: Computed S2-S1 energy gap and the H_{DA} (H_{12}) coupling dependences on torsional angle θ.

Appendix C

Table 18: Coordinates of the D_1-D_2-A optimized structure at the MN15/def2-SVP level of theory in toluene.

C	17.26240	2.78837	-1.77268
C	16.23820	2.04202	-1.27101
C	16.84096	0.97369	-0.50686
N	18.19744	1.07209	-0.55749
C	18.49057	2.16860	-1.32628
C	16.10723	-0.02146	0.18421
C	16.80574	-2.91282	2.23719
C	15.90768	-2.07270	1.64950
C	16.67691	-1.07589	0.93997
N	18.00737	-1.30712	1.10851
C	18.12301	-2.42316	1.89633
C	19.32084	-3.02085	2.32209
C	21.84196	-3.16204	2.44952
C	22.86116	-2.42110	1.92658
C	22.25077	-1.35973	1.16035
N	20.89046	-1.46679	1.22112
C	20.60968	-2.55367	1.99669
C	22.95830	-0.37209	0.46883
C	22.29853	2.51182	-1.58074
C	23.19047	1.67057	-0.98248
C	22.41431	0.68135	-0.27180
N	21.08157	0.92962	-0.43909
C	20.97756	2.03722	-1.22911
C	19.77439	2.63597	-1.65294
C	19.22394	-4.23662	3.18160
C	19.87456	3.84778	-2.51773
C	14.68234	0.03448	0.10876
C	6.11723	3.62912	-0.53121
C	5.13937	2.67937	-0.49274
C	5.80691	1.40475	-0.37043
N	7.15651	1.58489	-0.34305
C	7.37974	2.93228	-0.44045

C	5.13537	0.16023	-0.29699
C	6.01995	-3.33396	-0.04544
C	5.06830	-2.36083	-0.12853
C	5.77121	-1.10079	-0.19128
N	7.11498	-1.31225	-0.13468
C	7.30094	-2.66551	-0.04239
C	8.53852	-3.32680	0.04955
C	11.05425	-3.38710	0.16173
C	12.03196	-2.43706	0.13141
C	11.36438	-1.16074	0.02678
N	10.01529	-1.34160	-0.01374
C	9.79244	-2.69046	0.06426
C	12.03594	0.08526	-0.02994
C	11.15342	3.57421	-0.35029
C	12.10327	2.60458	-0.21952
C	11.40062	1.34464	-0.15486
N	10.05759	1.55435	-0.23373
C	9.87224	2.90579	-0.35109
C	8.63497	3.56662	-0.45159
C	8.52083	-4.81658	0.13551
C	8.65367	5.05334	-0.58050
C	13.46159	0.06578	0.04237
C	-4.92169	3.11087	1.49686
C	-5.88676	2.26397	1.03767
C	-5.20734	1.20376	0.32429
N	-3.85603	1.41366	0.37117
C	-3.65348	2.56692	1.07341
C	-5.85410	0.11417	-0.29430
C	-4.89878	-2.84515	-2.13393
C	-5.87099	-2.02862	-1.63632
C	-5.19750	-0.95360	-0.93985
N	-3.84338	-1.12566	-1.03266
C	-3.63263	-2.27033	-1.74648
C	-2.38033	-2.82807	-2.07765
C	0.13767	-2.85514	-2.08500
C	1.09843	-2.01203	-1.61299
C	0.40743	-0.91147	-0.97976

N	-0.93833	-1.08736	-1.07544
C	-1.13884	-2.26482	-1.74794
C	1.05789	0.18355	-0.36141
C	0.11085	3.22289	1.34593
C	1.07894	2.38867	0.87334
C	0.39765	1.27467	0.25323
N	-0.94963	1.43364	0.35780
C	-1.16041	2.61198	1.02560
C	-2.40650	3.15404	1.37262
C	-2.37889	-4.11224	-2.83742
C	-2.41681	4.44151	2.12667
C	3.70821	0.17630	-0.33066
C	2.48559	0.18329	-0.35056
C	18.80485	-4.13492	4.52080
C	18.71088	-5.27805	5.32963
C	19.04362	-6.51862	4.78852
C	19.46447	-6.65001	3.46624
C	19.55173	-5.50260	2.66288
C	20.29173	5.07696	-1.97539
C	20.39113	6.21965	-2.78396
C	20.06748	6.12069	-4.13608
C	19.65124	4.91675	-4.70161
C	19.55808	3.77773	-3.88692
C	8.09966	-5.45938	1.31370
C	8.08026	-6.86024	1.39621
C	8.48980	-7.60799	0.29352
C	8.91475	-6.99879	-0.88591
C	8.92700	-5.59755	-0.96194
C	8.98415	5.86325	0.52114
C	9.00251	7.26139	0.40071
C	8.68312	7.83848	-0.82714
C	8.34889	7.06161	-1.93509
C	8.33711	5.66411	-1.80767
C	-2.75897	-5.31162	-2.20757
C	-2.76397	-6.52245	-2.91684
C	-2.38209	-6.52182	-4.25738
C	-1.99856	-5.35012	-4.90744

C	-2.00030	-4.14254	-4.19222
C	-2.01579	4.48565	3.47459
C	-2.02552	5.69650	4.18420
C	-2.44375	6.85717	3.53573
C	-2.84945	6.84369	2.20227
C	-2.83278	5.62971	1.49855
O	19.94489	-5.52779	1.37147
O	18.50732	-2.89201	4.95489
O	9.31923	-4.91615	-2.05911
O	7.72615	-4.64979	2.32703
O	-1.64899	-2.95784	-4.73537
O	-3.10792	-5.21113	-0.90724
O	20.58174	5.07224	-0.65680
O	19.16918	2.56845	-4.34339
O	9.27427	5.21247	1.66749
O	8.02886	4.82801	-2.82155
O	-1.63230	3.31062	4.01692
O	-3.20329	5.51534	0.20538
C	20.30294	-6.75176	0.78621
C	18.04854	-2.71434	6.26917
C	21.02046	6.25668	-0.04571
C	18.80560	2.42700	-5.69141
C	9.76931	-5.62430	-3.18399
C	7.26486	-5.21615	3.52529
C	9.63567	5.95116	2.80463
C	7.67038	5.36281	-4.06850
C	-1.23039	-2.91217	-6.07402
C	-3.51921	-6.36064	-0.21561
C	-1.18627	3.28015	5.34713
C	-3.64789	6.65325	-0.48483
C	-7.34537	0.08435	-0.25495
C	-8.10604	1.07357	-0.89640
C	-9.49935	1.04670	-0.84919
C	-10.17625	0.03197	-0.15578
C	-9.41574	-0.95907	0.48303
C	-8.02282	-0.93429	0.43256
C	-17.78513	-0.49373	-3.29153

C	-18.70540	-0.38926	-2.29264
C	-17.95869	-0.23600	-1.06306
N	-16.62179	-0.25081	-1.32065
C	-16.47905	-0.40970	-2.67176
C	-18.53297	-0.08983	0.20552
C	-17.49632	0.34791	3.62424
C	-18.49656	0.21099	2.70972
C	-17.85548	0.07594	1.41968
N	-16.50238	0.13185	1.55991
C	-16.24745	0.30074	2.89300
C	-14.97947	0.41689	3.48145
C	-12.46481	0.53275	3.39176
C	-11.53768	0.42155	2.39844
C	-12.26624	0.17120	1.17281
N	-13.60859	0.14581	1.43589
C	-13.75931	0.35767	2.77637
C	-11.66714	0.00996	-0.09356
C	-12.74850	-0.53281	-3.49826
C	-11.74200	-0.39631	-2.58879
C	-12.36826	-0.16846	-1.30374
N	-13.72851	-0.18134	-1.44917
C	-13.98926	-0.39535	-2.77210
C	-15.26412	-0.48704	-3.36879
C	-14.91527	0.62683	4.95697
C	-15.32150	-0.68691	-4.84616
C	-15.29975	1.85723	5.52113
C	-15.23961	2.05766	6.90894
C	-14.78857	1.02009	7.72304
C	-14.39893	-0.20862	7.19270
C	-14.46539	-0.40233	5.80438
C	-14.97547	0.36017	-5.72013
C	-15.02296	0.17706	-7.11068
C	-15.42093	-1.05932	-7.61643
C	-15.76987	-2.11483	-6.77573
C	-15.71661	-1.92471	-5.38618
O	-14.11321	-1.55544	5.19756
O	-15.71828	2.80132	4.65196

O	-14.60518	1.51920	-5.13586
O	-16.03103	-2.88644	-4.49282
C	-13.63559	-2.62236	5.97398
C	-16.14103	4.04720	5.14008
C	-14.22885	2.60532	-5.94083
C	-16.45638	-4.14159	-4.95411
H	17.20338	3.67916	-2.39504
H	15.16751	2.18512	-1.40377
H	16.60483	-3.78763	2.85250
H	14.82090	-2.10647	1.69314
H	21.90487	-4.04116	3.08817
H	23.93401	-2.56667	2.04563
H	24.04852	-0.42933	0.51194
H	22.50302	3.37741	-2.20809
H	24.27868	1.70321	-1.01597
H	6.00418	4.70814	-0.61587
H	4.06084	2.81406	-0.55013
H	5.87708	-4.41108	0.01418
H	3.98568	-2.47130	-0.14094
H	11.16763	-4.46666	0.23812
H	13.11082	-2.57522	0.16420
H	11.29702	4.64956	-0.43481
H	13.18418	2.71814	-0.16306
H	-5.04790	4.01799	2.08466
H	-6.96225	2.33831	1.18168
H	-5.01939	-3.75201	-2.72331
H	-6.94845	-2.13181	-1.74386
Zn	-2.39839	0.15933	-0.34574
H	0.26964	-3.79460	-2.61814
H	2.18002	-2.10739	-1.68792
H	0.23442	4.16840	1.87031
H	2.15979	2.49942	0.93755
H	18.38752	-5.20535	6.36755
H	18.97263	-7.40994	5.41610
H	19.71506	-7.63324	3.06925
H	20.71145	7.17469	-2.36865
H	20.14207	7.00855	-4.76815

H	19.40796	4.86846	-5.76255
H	7.75594	-7.36393	2.30631
H	8.47752	-8.69858	0.35524
H	9.22703	-7.60890	-1.73289
H	9.25713	7.89387	1.25056
H	8.69495	8.92656	-0.92345
H	8.10604	7.54023	-2.88327
H	-3.05603	-7.45450	-2.43398
H	-2.38324	-7.46288	-4.81212
H	-1.70753	-5.37952	-5.95700
H	-1.71692	5.73670	5.22837
H	-2.45389	7.80071	4.08615
H	-3.16893	7.76733	1.72061
H	20.59254	-6.54041	-0.24965
H	19.46001	-7.46354	0.78363
H	21.15617	-7.21748	1.30809
H	18.80107	-3.03452	7.00967
H	17.11417	-3.27180	6.45148
H	17.85436	-1.64353	6.39982
H	20.26079	7.05400	-0.11141
H	21.95741	6.62405	-0.49784
H	21.20233	6.02554	1.01023
H	18.51241	1.38096	-5.83719
H	19.64657	2.66040	-6.36632
H	17.95300	3.07679	-5.95197
H	10.04908	-4.88187	-3.94028
H	8.98066	-6.27601	-3.59685
H	10.65125	-6.24338	-2.94739
H	8.03991	-5.83618	4.00694
H	6.36739	-5.83653	3.36170
H	7.00641	-4.38710	4.19406
H	8.82418	6.62598	3.12601
H	10.54432	6.55104	2.62699
H	9.83698	5.23034	3.60546
H	7.44967	4.51690	-4.72965
H	8.49051	5.95579	-4.50771
H	6.77384	6.00128	-3.99341

H	-0.98110	-1.86840	-6.29727
H	-2.02705	-3.24466	-6.76100
H	-0.33648	-3.53669	-6.24116
H	-2.72051	-7.12080	-0.17890
H	-4.41525	-6.81190	-0.67455
H	-3.76183	-6.05075	0.80744
H	-1.97547	3.60037	6.04839
H	-0.30177	3.92308	5.49322
H	-0.91190	2.24268	5.57030
H	-3.90226	6.33340	-1.50194
H	-2.86429	7.42795	-0.53915
H	-4.54420	7.09022	-0.01278
H	-7.59192	1.87271	-1.43657
H	-10.07944	1.82401	-1.35322
H	-9.92996	-1.75594	1.02648
H	-7.44270	-1.71250	0.93516
H	-17.96191	-0.61465	-4.35855
H	-19.79083	-0.40983	-2.37609
H	-17.58291	0.46772	4.70245
H	-19.57046	0.19815	2.88889
H	-12.29689	0.73067	4.44860
H	-10.45737	0.51679	2.48108
H	-12.66762	-0.72398	-4.56655
H	-10.67055	-0.45994	-2.76490
H	-15.53417	3.00879	7.35138
H	-14.73903	1.17375	8.80345
H	-14.05304	-1.00271	7.85372
H	-14.75814	0.98495	-7.79209
H	-15.45992	-1.20474	-8.69841
H	-16.07336	-3.07168	-7.19946
H	-13.40407	-3.44288	5.28506
H	-14.39141	-2.96735	6.69977
H	-12.71919	-2.34662	6.52288
H	-15.32918	4.57282	5.67087
H	-17.00102	3.94477	5.82355
H	-16.44525	4.64531	4.27342
H	-13.96365	3.42814	-5.26695

H	-15.05463	2.93148	-6.59563
H	-13.35531	2.36167	-6.56906
H	-16.66653	-4.75449	-4.07002
H	-15.67778	-4.63836	-5.55749
H	-17.37472	-4.06134	-5.56026
Zn	8.58606	0.12143	-0.18023
Zn	19.54732	-0.19348	0.33298
Zn	-15.11452	-0.04145	0.05693
N	-19.97294	-0.10944	0.26965
C	-20.63116	1.12496	0.15144
C	-22.11722	1.09037	0.22679
C	-22.78740	-0.14316	0.41262
C	-22.07242	-1.35992	0.52743
C	-20.58582	-1.35905	0.45317
C	-22.83548	2.26789	0.11676
C	-24.24477	2.25050	0.18898
C	-24.91742	1.05534	0.37124
C	-24.20127	-0.15988	0.48620
C	-24.87448	-1.39082	0.67399
C	-24.15729	-2.56912	0.78373
C	-22.74807	-2.55349	0.70979
O	-19.92812	-2.37272	0.54615
O	-20.01029	2.15431	-0.00219
C	-26.40163	1.04363	0.44823
N	-27.01743	-0.19490	0.63576
C	-26.36066	-1.42328	0.75537
O	-26.97237	-2.46093	0.91706
O	-27.07014	2.05479	0.35524
C	-28.47447	-0.16978	0.70837
H	-22.28689	3.20085	-0.02551
H	-24.82762	3.16958	0.10418
H	-24.70584	-3.50174	0.92796
H	-22.16634	-3.47326	0.79456
H	-28.88855	0.24425	-0.22037
H	-28.79658	0.47162	1.53917
H	-28.82437	-1.19469	0.85898

Table 19: Coordinates of the D_1-D_2-A optimized structure at the MN15/def2-SVP level of theory in toluene.

C	-17.25437	2.81760	1.77867
C	-16.23341	2.06399	1.28011
C	-16.84148	0.98560	0.53296
N	-18.19677	1.08600	0.59186
C	-18.48615	2.19246	1.34770
C	-16.11291	-0.01905	-0.15246
C	-16.82553	-2.93384	-2.17253
C	-15.92286	-2.08684	-1.60090
C	-16.68689	-1.08327	-0.89360
N	-18.01744	-1.31827	-1.04858
C	-18.14072	-2.44194	-1.82401
C	-19.34295	-3.04429	-2.23325
C	-21.86740	-3.18953	-2.33729
C	-22.88295	-2.44322	-1.81371
C	-22.26608	-1.37181	-1.06542
N	-20.90665	-1.47956	-1.13740
C	-20.63097	-2.57453	-1.90245
C	-22.96848	-0.37510	-0.37970
C	-22.29582	2.53919	1.62552
C	-23.19227	1.68870	1.04634
C	-22.42029	0.68960	0.34327
N	-21.08703	0.94190	0.49719
C	-20.97657	2.05989	1.27025
C	-19.76866	2.66479	1.67610
C	-19.25257	-4.26889	-3.08136
C	-19.86346	3.89097	2.52146
C	-14.68741	0.03780	-0.08787
C	-6.11445	3.63289	0.49834
C	-5.13665	2.68340	0.44297
C	-5.80556	1.40874	0.31835
N	-7.15466	1.58964	0.30670
C	-7.37822	2.93574	0.41587
C	-5.13513	0.16350	0.22855
C	-6.01939	-3.33092	-0.05485
C	-5.06715	-2.35821	0.03321

C	-5.77031	-1.09824	0.11319
N	-7.11341	-1.31037	0.06194
C	-7.30097	-2.66208	-0.04183
C	-8.54052	-3.32242	-0.12756
C	-11.05883	-3.38355	-0.20774
C	-12.03664	-2.43398	-0.15615
C	-11.36822	-1.15749	-0.04882
N	-10.01940	-1.33887	-0.02788
C	-9.79579	-2.68636	-0.12091
C	-12.03932	0.08917	0.02770
C	-11.15550	3.57865	0.36745
C	-12.10654	2.60941	0.23811
C	-11.40407	1.34931	0.15867
N	-10.06136	1.55964	0.22867
C	-9.87385	2.90968	0.35299
C	-8.63437	3.56987	0.44480
C	-8.52322	-4.81138	-0.22713
C	-8.65206	5.05614	0.58056
C	-13.46570	0.06947	-0.03168
C	4.93826	3.08344	-1.57083
C	5.90014	2.24073	-1.09629
C	5.21515	1.18798	-0.37587
N	3.86493	1.39905	-0.43399
C	3.66653	2.54441	-1.14901
C	5.85677	0.10379	0.25927
C	4.88994	-2.83879	2.12326
C	5.86570	-2.02754	1.62282
C	5.19639	-0.95802	0.91266
N	3.84225	-1.12889	1.00062
C	3.62581	-2.26591	1.72374
C	2.36973	-2.82024	2.05203
C	-0.14982	-2.84714	2.04421
C	-1.10754	-2.00731	1.55918
C	-0.41177	-0.91121	0.92133
N	0.93232	-1.08778	1.02700
C	1.12957	-2.25964	1.70992
C	-1.05681	0.18176	0.29123

C	-0.09848	3.20759	-1.43874
C	-1.07019	2.38018	-0.96050
C	-0.39300	1.26819	-0.33028
N	0.95403	1.42311	-0.43409
C	1.17095	2.59514	-1.11070
C	2.42031	3.13091	-1.45890
C	2.36356	-4.09855	2.82183
C	2.43656	4.41243	-2.22320
C	-3.70761	0.17903	0.25731
C	-2.48470	0.18450	0.27678
C	-18.85110	-4.17883	-4.42716
C	-18.76478	-5.32962	-5.22573
C	-19.08699	-6.56570	-4.66741
C	-19.49012	-6.68553	-3.33822
C	-19.57014	-5.53060	-2.54509
C	-20.28278	5.11125	1.95973
C	-20.37930	6.26681	2.74995
C	-20.05072	6.18956	4.10260
C	-19.63238	4.99500	4.68695
C	-19.54205	3.84281	3.89083
C	-8.12062	-5.44238	-1.41848
C	-8.10053	-6.84231	-1.51359
C	-8.48978	-7.60009	-0.40997
C	-8.89526	-7.00242	0.78254
C	-8.90893	-5.60205	0.87118
C	-8.98792	5.86986	-0.51713
C	-9.00628	7.26736	-0.39093
C	-8.68190	7.83928	0.83840
C	-8.34222	7.05844	1.94230
C	-8.32991	5.66155	1.80931
C	2.74205	-5.30339	2.20066
C	2.74330	-6.50868	2.91911
C	2.35973	-6.49643	4.25945
C	1.97814	-5.31898	4.90093
C	1.98320	-4.11691	4.17669
C	2.04372	4.44630	-3.57420
C	2.06006	5.65168	-4.29278

C	2.47630	6.81656	-3.64992
C	2.87405	6.81308	-2.31367
C	2.85117	5.60466	-1.60084
O	-19.94524	-5.54470	-1.24778
O	-18.56353	-2.93903	-4.87824
O	-9.28179	-4.93097	1.98204
O	-7.76598	-4.62294	-2.43133
O	1.63513	-2.92669	4.71110
O	3.09209	-5.21376	0.89944
O	-20.57658	5.08606	0.64180
O	-19.15289	2.64047	4.36663
O	-9.28177	5.22353	-1.66559
O	-8.01720	4.82150	2.81916
O	1.66274	3.26730	-4.11099
O	3.21311	5.49999	-0.30402
C	-20.29697	-6.76696	-0.64844
C	-18.12807	-2.77519	-6.20511
C	-21.02172	6.26334	0.01519
C	-18.79076	2.52245	5.72012
C	-9.70306	-5.65448	3.11182
C	-7.32375	-5.18177	-3.64354
C	-9.64743	5.97063	-2.79936
C	-7.65760	5.35533	4.06936
C	1.21987	-2.87179	6.05333
C	3.50268	-6.37302	0.21795
C	1.23081	3.22932	-5.44853
C	3.65757	6.64588	0.37883
C	7.34851	0.07383	0.23031
C	8.10364	1.06818	0.87056
C	9.49734	1.04139	0.83361
C	10.17887	0.02277	0.15037
C	9.42383	-0.97300	-0.48772
C	8.03049	-0.94941	-0.44589
C	17.77331	-0.49926	3.33078
C	18.69955	-0.39445	2.33668
C	17.95874	-0.23818	1.10303
N	16.62079	-0.25278	1.35411

C	16.46984	-0.41343	2.70399
C	18.53977	-0.08769	-0.16300
C	17.52321	0.35944	-3.58847
C	18.51893	0.22312	-2.66803
C	17.86962	0.08225	-1.38186
N	16.51754	0.13526	-1.53090
C	16.26937	0.30646	-2.86476
C	15.00331	0.42057	-3.46019
C	12.48598	0.52947	-3.38534
C	11.55326	0.41421	-2.39719
C	12.27591	0.16557	-1.16691
N	13.61919	0.14457	-1.42317
C	13.77808	0.35800	-2.76213
C	11.67041	0.00229	0.09710
C	12.73154	-0.53788	3.51052
C	11.73001	-0.40180	2.59492
C	12.36400	-0.17569	1.31256
N	13.72281	-0.18893	1.46674
C	13.97708	-0.40163	2.79067
C	15.24994	-0.49173	3.39434
C	14.94719	0.63010	-4.93630
C	15.29903	-0.68935	4.87247
C	15.32717	1.86335	-5.49814
C	15.27493	2.06248	-6.88637
C	14.83674	1.02080	-7.70272
C	14.45222	-0.21087	-7.17473
C	14.51055	-0.40346	-5.78598
C	14.95064	0.36113	5.74210
C	14.98912	0.18050	7.13315
C	15.38094	-1.05636	7.64332
C	15.73252	-2.11485	6.80699
C	15.68807	-1.92755	5.41683
O	14.16410	-1.56004	-5.18137
O	15.73257	2.81197	-4.62679
O	14.58848	1.52118	5.15364
O	16.00440	-2.89312	4.52742
C	13.69941	-2.63144	-5.96443

C	16.15141	4.06127	-5.11743
C	14.20787	2.60969	5.95816
C	16.42605	-4.14902	4.99836
H	-17.18966	3.71585	2.38979
H	-15.16228	2.21065	1.40526
H	-16.62795	-3.81359	-2.78201
H	-14.83664	-2.12199	-1.65563
H	-21.93664	-4.07691	-2.96390
H	-23.95667	-2.59151	-1.92095
H	-24.05893	-0.43411	-0.41337
H	-22.49734	3.41415	2.24090
H	-24.28019	1.72175	1.08769
H	-5.99960	4.71124	0.58990
H	-4.05776	2.82042	0.48799
H	-5.87561	-4.40723	-0.12729
H	-3.98463	-2.47096	0.03951
H	-11.17394	-4.46248	-0.29107
H	-13.11543	-2.57478	-0.17600
H	-11.29966	4.65343	0.45901
H	-13.18767	2.72552	0.19194
H	5.07005	3.98502	-2.16602
H	6.97658	2.31500	-1.23356
H	5.00795	-3.74110	2.72022
H	6.94241	-2.13271	1.73623
Zn	2.40041	0.15208	0.29077
H	-0.28668	-3.78185	2.58461
H	-2.18947	-2.10455	1.62782
H	-0.21946	4.14882	-1.97157
H	-2.15042	2.49668	-1.02670
H	-18.45520	-5.26699	-6.26846
H	-19.02185	-7.46299	-5.28695
H	-19.73285	-7.66553	-2.92870
H	-20.70141	7.21499	2.32071
H	-20.12321	7.08759	4.72024
H	-19.38549	4.96475	5.74769
H	-7.79098	-7.33797	-2.43312
H	-8.47671	-8.69000	-0.48143

H	-9.19167	-7.62101	1.62900
H	-9.26488	7.90355	-1.23673
H	-8.69393	8.92689	0.93915
H	-8.09540	7.53399	2.89095
H	3.03385	-7.44520	2.44414
H	2.35809	-7.43320	4.82128
H	1.68593	-5.34053	5.95032
H	1.75802	5.68519	-5.33907
H	2.49137	7.75581	-4.20740
H	3.19221	7.73998	-1.83756
H	-20.57437	-6.54817	0.38906
H	-19.45374	-7.47750	-0.65109
H	-21.15567	-7.23511	-1.15779
H	-18.89263	-3.10749	-6.92686
H	-17.19537	-3.33141	-6.39617
H	-17.94102	-1.70535	-6.35210
H	-20.26322	7.06207	0.06683
H	-21.95682	6.63361	0.46734
H	-21.20779	6.01712	-1.03645
H	-18.50014	1.47869	5.88516
H	-19.63248	2.76979	6.38816
H	-17.93777	3.17542	5.96891
H	-9.96711	-4.92148	3.88261
H	-8.90199	-6.30681	3.49736
H	-10.58748	-6.27393	2.88850
H	-8.10622	-5.79974	-4.11438
H	-6.42306	-5.80103	-3.49826
H	-7.07885	-4.34800	-4.31131
H	-8.83689	6.64710	-3.11769
H	-10.55530	6.56837	-2.61419
H	-9.85037	5.25478	-3.60403
H	-7.43559	4.50844	4.72858
H	-8.47836	5.94595	4.50912
H	-6.76245	5.99467	3.99349
H	0.97569	-1.82588	6.27153
H	2.01758	-3.20372	6.73843
H	0.32458	-3.49202	6.22535

H	2.70215	-7.13075	0.18832
H	4.39671	-6.82047	0.68309
H	3.74694	-6.07342	-0.80761
H	2.02815	3.54586	-6.14130
H	0.34854	3.87148	-5.60691
H	0.95938	2.19064	-5.66906
H	3.90521	6.33543	1.40035
H	2.87527	7.42189	0.42034
H	4.55703	7.07477	-0.09327
H	7.58685	1.87130	1.40213
H	10.07217	1.82272	1.33737
H	9.94071	-1.77320	-1.02362
H	7.45567	-1.73207	-0.94759
H	17.94584	-0.62311	4.39826
H	19.78453	-0.41698	2.42639
H	17.61766	0.48385	-4.66560
H	19.59393	0.21524	-2.84149
H	12.32233	0.72600	-4.44320
H	10.47308	0.50450	-2.48764
H	12.64326	-0.72612	4.57883
H	10.65764	-0.46322	2.76665
H	15.56599	3.01503	-7.32795
H	14.79359	1.17351	-8.78347
H	14.11673	-1.00741	-7.83807
H	14.72230	0.99004	7.81175
H	15.41307	-1.19977	8.72572
H	16.03139	-3.07120	7.23497
H	13.46972	-3.45485	-5.27856
H	14.46328	-2.96811	-6.68486
H	12.78529	-2.36091	-6.51855
H	15.33981	4.57836	-5.65574
H	17.01659	3.96075	-5.79365
H	16.44484	4.66473	-4.25091
H	13.94909	3.43329	5.28296
H	15.02987	2.93284	6.61829
H	13.32998	2.36618	6.57934
H	16.63927	-4.76701	4.11873

H	15.64329	-4.64018	5.59995
H	17.34092	-4.06584	5.60830
Zn	-8.58721	0.12523	0.14129
Zn	-19.55579	-0.19330	-0.27345
Zn	15.11893	-0.04483	-0.03411
N	19.97967	-0.10783	-0.21939
C	20.63927	1.12058	-0.05978
C	22.12342	1.08771	-0.13432
C	22.79159	-0.14097	-0.35669
C	22.07610	-1.35345	-0.50895
C	20.59136	-1.35178	-0.43803
C	22.84327	2.26041	0.01167
C	24.25240	2.24326	-0.06063
C	24.92303	1.05305	-0.27830
C	24.20522	-0.15713	-0.42958
C	24.87769	-1.38239	-0.65321
C	24.16008	-2.55643	-0.79857
C	22.75096	-2.54172	-0.72592
O	19.92723	-2.35974	-0.56311
O	20.01392	2.14366	0.12677
C	26.40690	1.04094	-0.35572
N	27.02210	-0.19061	-0.57904
C	26.36367	-1.41274	-0.73440
O	26.97483	-2.44684	-0.92607
O	27.07681	2.04930	-0.23314
C	28.47946	-0.16446	-0.65033
H	22.29978	3.19141	0.18181
H	24.83327	3.16028	0.05219
H	24.70470	-3.48645	-0.96995
H	22.17225	-3.46002	-0.83954
H	28.89338	0.22082	0.29062
H	28.80227	0.49814	-1.46387
H	28.82981	-1.18425	-0.82971

Table 20: Coordinates of the D_1'-D_2-A optimized structure at the MN15/def2-SVP level of theory in toluene.

H	23.02704	0.30014	-2.04984
H	22.59867	-0.83899	-3.33886
H	22.56279	2.33947	-1.04652
H	23.02365	1.36205	0.36534
H	22.66697	-1.39097	-1.65115
C	22.37259	-0.55000	-2.29881
H	22.68947	3.09956	0.54986
C	22.36906	2.18288	0.02775
H	21.09579	1.83273	-2.94482
H	20.62372	0.62510	-4.15513
H	22.13674	-1.11577	0.76123
C	20.89286	-0.18651	-2.14160
C	20.48296	0.93004	-3.10500
C	20.88592	1.89143	0.27651
H	20.98633	-2.75828	-0.75364
H	20.29259	-1.08327	-2.38820
H	20.08706	3.15227	-1.32825
C	21.03155	-1.17860	0.78222
H	20.28470	3.98927	0.22279
Si	20.38545	0.18163	-0.35809
H	20.72896	1.81827	1.36916
H	19.42583	1.21701	-2.97716
H	20.95784	-3.36151	0.91969
C	19.99759	3.02872	-0.23704
C	20.60366	-2.55346	0.25837
H	20.90318	-0.03639	2.66032
H	20.90367	-1.80057	2.87373
C	20.55166	-0.98314	2.22277
H	18.93536	2.85006	-0.00956
H	19.50264	-2.62254	0.21219
H	19.44857	-0.97749	2.26621
C	18.54815	0.09725	-0.29370
C	17.32376	0.06124	-0.24127
H	17.10609	-2.12256	1.27533
H	16.92271	2.23852	-1.72079

C	16.02036	-2.05030	1.23537
C	15.84586	2.12835	-1.60200
C	15.89470	0.03534	-0.18545
C	15.28830	-1.01691	0.53861
C	15.20211	1.06871	-0.85842
H	15.25641	-3.75198	2.41770
H	14.93944	3.80593	-2.71618
C	15.09052	-2.86659	1.80708
C	14.84909	2.91384	-2.09949
H	14.32523	6.96611	-0.86312
H	14.63332	-6.92201	0.59032
N	13.94915	-1.20996	0.68848
N	13.85005	1.21723	-0.90733
H	13.74492	6.27737	0.68322
H	13.91580	-6.25209	-0.90587
C	13.79290	-2.33407	1.45483
C	13.59980	2.33647	-1.65552
C	13.45781	6.52202	-0.34594
C	13.71393	-6.51103	0.13989
O	13.05058	5.32517	-0.95521
O	13.30549	-5.33306	0.78408
H	12.89009	7.47367	-2.60635
H	13.34655	-7.49150	2.42917
C	13.05496	-6.53959	2.87188
C	13.00302	-5.36933	2.09913
H	12.64225	7.26460	-0.32294
C	12.65299	5.34205	-2.24508
C	12.60391	6.50872	-3.02356
H	12.92857	-7.28519	0.17152
H	12.75949	-7.38179	4.82746
C	12.72143	-6.47230	4.22356
C	12.62350	-4.14449	2.67777
C	12.57109	-2.90247	1.85228
Zn	12.45092	-0.02013	-0.05349
C	12.33298	2.86153	-1.96033
C	12.27953	4.10040	-2.79053
C	12.17568	6.42064	-4.34706

H	12.13493	7.32726	-4.95510
H	12.39850	-3.06861	6.55802
C	12.34087	-5.27337	4.82394
C	12.29501	-4.10677	4.04526
C	11.85362	4.04199	-4.13007
C	11.79814	5.20461	-4.91402
H	11.80739	2.99312	-6.64034
H	12.08882	-5.25034	5.88368
O	11.94268	-2.89950	4.53517
H	11.47032	5.16572	-5.95236
O	11.51177	2.81940	-4.58830
C	11.57190	-2.78651	5.88408
C	11.30111	-2.38647	1.53163
C	11.04515	2.68432	-5.90504
H	11.31300	-1.73595	6.05926
C	11.10902	2.30381	-1.54463
N	11.05081	-1.25769	0.80001
N	10.95174	1.17060	-0.79370
H	10.81388	1.62372	-6.05678
H	10.69551	-3.41450	6.11771
H	10.13040	3.27738	-6.07386
C	10.05301	-2.98466	1.94630
C	9.81453	2.85973	-1.86399
H	9.96205	-3.89408	2.53696
H	9.64929	3.76261	-2.44851
C	9.69728	-1.11613	0.74174
C	9.61189	0.98719	-0.63041
C	9.00216	-0.07347	0.08303
C	9.05557	-2.19090	1.46121
C	8.88304	2.03759	-1.30124
H	7.97963	-2.30663	1.57832
H	7.79830	2.11862	-1.33729
C	7.57559	-0.08944	0.14139
C	6.35378	-0.09259	0.18630
H	6.05797	2.55682	0.29394
H	6.02177	-2.74337	0.14825
C	4.97590	2.44005	0.30355

C	4.94143	-2.61322	0.17513
C	4.92659	-0.08626	0.22812
C	4.28057	1.17272	0.27710
C	4.26354	-1.33684	0.21351
H	4.15414	4.48763	0.38454
H	4.09139	-4.65072	0.14882
C	4.01861	3.40827	0.35502
C	3.97084	-3.56939	0.17025
H	3.49875	-6.12261	-3.15305
H	3.65866	5.92850	3.73375
H	2.87818	-4.67106	-3.99552
N	2.93611	1.37643	0.31633
N	2.91600	-1.52337	0.22500
H	3.03418	4.47731	4.57392
C	2.61300	-5.48389	-3.30967
C	2.74008	2.73216	0.36837
C	2.70112	-2.87674	0.19289
C	2.76692	5.30126	3.90230
O	2.18726	-4.88919	-2.11199
H	2.09358	-7.59999	-2.05116
O	2.30739	4.72577	2.70771
H	2.25363	7.43820	2.67701
H	1.81507	-6.09264	-3.76778
C	1.81661	-5.67436	-1.07859
C	1.80003	-7.07630	-1.14190
C	1.92558	5.52743	1.69117
C	1.93216	6.92870	1.76915
H	1.98792	5.91675	4.38341
C	1.50147	3.38660	0.43505
C	1.50792	4.87649	0.51566
C	1.45246	-3.51463	0.16532
Zn	1.47187	-0.06391	0.28922
C	1.43549	-5.00514	0.09909
C	1.51322	7.66944	0.66537
H	1.51564	8.76027	0.72381
C	1.39388	-7.79917	-0.02161
H	1.37834	-8.89045	-0.06865

H	1.03292	6.32315	-3.21798
C	1.09173	5.65118	-0.58273
C	1.09113	7.05264	-0.51113
C	1.03019	-5.76203	1.21385
C	1.00657	-7.16398	1.15707
H	1.01730	-6.40537	3.85667
H	0.77152	7.65741	-1.35920
O	0.70415	4.96351	-1.67796
H	0.69573	-7.75511	2.01793
O	0.67596	-5.05713	2.30942
C	0.24951	5.66541	-2.80471
C	0.24716	2.74128	0.43609
C	0.20715	-2.85191	0.18161
C	0.23507	-5.74031	3.45302
H	-0.02255	4.91920	-3.56016
N	0.03075	1.39700	0.33700
N	0.00948	-1.50435	0.27477
H	-0.00978	-4.98225	4.20597
H	-0.63801	6.27756	-2.57077
H	-0.66617	-6.34148	3.24449
C	-1.06475	-3.52685	0.08037
C	-1.01482	3.43273	0.54932
H	-1.19552	-4.60258	-0.01953
H	-1.13027	4.50939	0.65771
C	-1.32332	1.20444	0.36873
C	-1.34217	-1.29308	0.24432
C	-1.98464	-0.03924	0.30289
C	-2.02708	-2.56123	0.11377
C	-1.99057	2.48088	0.50895
H	-3.10436	-2.69109	0.03958
H	-3.06608	2.62431	0.58507
C	-3.47638	-0.02584	0.28022
H	-3.59920	1.02966	-1.59741
H	-3.69794	-1.07586	2.15208
C	-4.16841	0.56885	-0.78600
C	-4.22332	-0.61015	1.31433
C	-5.56180	0.57198	-0.82107

C	-5.61744	-0.60380	1.28112
H	-6.08744	1.03389	-1.66075
H	-6.18646	-1.06416	2.09295
C	-6.30878	-0.01625	0.21088
H	-6.61374	-1.65914	-1.90295
H	-6.78172	1.60120	2.32505
C	-7.69280	-1.52749	-1.86782
C	-7.80026	-0.02240	0.16222
C	-7.85458	1.46878	2.20451
H	-8.47028	-2.73395	-3.54568
C	-8.41016	-0.73894	-0.88831
C	-8.49123	0.68723	1.16565
C	-8.62856	-2.07322	-2.69556
H	-8.85906	-0.94074	-6.78080
H	-8.76386	2.65849	3.82726
C	-8.85360	2.00532	2.96145
H	-9.52042	0.60924	-6.17816
H	-9.43215	0.82850	7.01098
C	-9.76829	-0.43078	-6.41980
N	-9.75422	-0.82554	-1.12753
C	-9.91712	-1.62448	-2.22280
N	-9.85033	0.77004	1.29921
H	-10.22275	-2.72005	-7.35998
O	-10.25892	-1.02059	-5.24480
C	-10.10037	1.56016	2.38430
H	-10.04623	-0.71212	6.33834
H	-10.52206	-0.44061	-7.22529
C	-10.57640	-3.12170	-6.41091
C	-10.30941	0.32675	6.56848
C	-10.63171	-2.31774	-5.26204
H	-10.94707	-5.07890	-7.21905
C	-10.98762	-4.45078	-6.32621
O	-10.69550	0.93045	5.36191
C	-11.09143	-2.84253	-4.04003
H	-10.82927	2.61037	7.48889
C	-11.14301	-1.98463	-2.82059
C	-11.06244	2.22939	5.36031

Zn	-11.24901	-0.02247	0.02508
C	-11.44896	-4.99820	-5.13037
C	-11.09975	3.02268	6.51734
H	-11.12915	0.33254	7.30676
C	-11.49745	-4.18879	-3.98487
H	-11.56394	-6.67577	-2.88706
C	-11.37031	1.91985	2.88233
C	-11.41604	2.76760	4.10918
H	-11.76059	-6.04156	-5.09309
C	-11.49539	4.35492	6.41100
H	-11.52665	4.97477	7.30997
O	-11.92394	-4.62949	-2.78247
H	-11.77318	6.61440	2.95668
C	-11.80849	4.11681	4.03282
C	-11.85177	4.91577	5.18586
C	-12.36565	-5.95509	-2.65251
O	-12.13080	4.57070	2.80321
H	-12.15331	5.96140	5.13236
C	-12.40570	-1.59829	-2.34688
H	-12.67197	-6.09075	-1.60888
N	-12.64963	-0.84267	-1.23334
C	-12.55514	5.89943	2.64942
C	-12.59124	1.54726	2.30022
N	-12.74566	0.79926	1.16564
H	-12.77286	6.04594	1.58521
H	-13.22854	-6.16150	-3.30825
C	-13.66004	-1.95065	-2.97892
H	-13.46900	6.10369	3.23280
H	-13.75548	-2.54269	-3.88710
C	-14.00080	-0.70792	-1.13438
C	-13.89211	1.91570	2.81909
C	-14.08422	0.68882	0.94277
H	-14.06027	2.50400	3.71910
C	-14.65210	-1.39907	-2.22581
C	-14.66811	-0.00208	-0.12599
C	-14.82052	1.38698	1.97403
H	-15.72689	-1.45057	-2.39204

H	-15.90497	1.45694	2.04182
O	-15.99471	1.89115	-1.50508
N	-16.10746	0.02362	-0.20115
O	-16.21288	-1.84612	1.10033
C	-16.68309	1.06208	-0.95043
C	-16.80245	-0.98930	0.47822
C	-18.16949	1.07992	-1.02028
C	-18.28762	-0.94429	0.38849
H	-18.19918	2.82714	-2.24172
H	-18.52115	-2.68620	1.59560
C	-18.80906	2.07414	-1.73914
C	-18.92090	0.08267	-0.35294
C	-19.04166	-1.90919	1.03266
C	-20.21798	2.10372	-1.81359
C	-20.33443	0.11287	-0.42872
C	-20.45058	-1.87896	0.95639
H	-20.73877	2.88089	-2.37593
H	-21.06137	-2.63199	1.45787
C	-20.97069	1.13823	-1.16860
C	-21.08729	-0.88342	0.23697
C	-22.45615	1.18284	-1.25657
C	-22.57135	-0.85695	0.16023
O	-23.03648	2.04832	-1.88206
N	-23.15014	0.17487	-0.58058
O	-23.27003	-1.68616	0.71003
C	-24.60825	0.17122	-0.63432
H	-24.96416	-0.76685	-1.08015
H	-24.92777	1.02565	-1.23713
H	-25.02024	0.24236	0.38084

Table 21: Coordinates of the D_1'-D_2-A optimized structure at the MN15/def2-SVP level of theory in dichloromethane.

H	23.06631	0.24552	-1.82850
H	22.64215	-0.76761	-3.22045
H	22.63194	2.20024	-0.64822
H	23.02844	1.10849	0.69844
H	22.67184	-1.46798	-1.58750
C	22.40311	-0.56789	-2.16258
H	22.71669	2.83276	1.00580
C	22.39970	1.96522	0.40392
H	21.17961	1.87964	-2.63011
H	20.70156	0.78484	-3.94131
H	22.11853	-1.37375	0.82883
C	20.92670	-0.19352	-1.99827
C	20.55156	1.00615	-2.87177
C	20.90435	1.68341	0.58193
H	20.94774	-2.87184	-0.81568
H	20.31727	-1.05696	-2.32756
H	20.19146	3.09211	-0.93780
C	21.01246	-1.41846	0.83917
H	20.33075	3.78635	0.68788
Si	20.40157	0.03642	-0.19746
H	20.71074	1.52702	1.65992
H	19.49857	1.30446	-2.73444
H	20.90535	-3.60362	0.80526
C	20.05253	2.87468	0.13312
C	20.56508	-2.74126	0.20857
H	20.89552	-0.42224	2.79900
H	20.86031	-2.19737	2.87525
C	20.52786	-1.32519	2.28834
H	18.97890	2.69429	0.29818
H	19.46318	-2.79005	0.15613
H	19.42462	-1.30247	2.32788
C	18.55911	-0.02912	-0.16703
C	17.33326	-0.04897	-0.14150
H	17.04533	-2.31229	1.25066
H	17.00321	2.21643	-1.50725

C	15.96223	-2.21563	1.19163
C	15.92224	2.11485	-1.42177
C	15.90275	-0.05347	-0.11861
C	15.26318	-1.13297	0.53530
C	15.24355	1.02693	-0.75230
H	15.14412	-3.96286	2.26615
H	15.07094	3.86346	-2.46776
C	15.00577	-3.04325	1.70077
C	14.95009	2.94110	-1.90286
H	14.43514	6.92172	-0.43513
H	14.46601	-7.03285	0.25672
N	13.91863	-1.30961	0.64726
N	13.89619	1.20001	-0.82837
H	13.79396	6.15601	1.04974
H	13.78425	-6.27435	-1.21371
C	13.72517	-2.46784	1.35084
C	13.68084	2.35959	-1.52321
C	13.54557	6.46284	0.02735
C	13.56326	-6.57853	-0.18426
O	13.14353	5.30622	-0.66393
O	13.17514	-5.42093	0.51330
H	13.06719	7.55010	-2.19057
H	13.14449	-7.66003	2.04853
C	12.86875	-6.72471	2.53456
C	12.85490	-5.51610	1.82166
H	12.73872	7.21346	0.06478
C	12.78923	5.40470	-1.96323
C	12.78127	6.61560	-2.67227
H	12.75833	-7.33200	-0.19852
H	12.52599	-7.65670	4.44105
C	12.51760	-6.71726	3.88378
C	12.49565	-4.31349	2.45791
C	12.48359	-3.03093	1.69490
Zn	12.45529	-0.05753	-0.07208
C	12.42880	2.91815	-1.83501
C	12.41684	4.20313	-2.59389
C	12.39492	6.61152	-4.01187

H	12.38632	7.55276	-4.56611
H	12.24896	-3.43220	6.38378
C	12.15612	-5.54152	4.54003
C	12.14820	-4.33627	3.82130
C	12.03333	4.22941	-3.94746
C	12.01926	5.43695	-4.66223
H	12.06630	3.33373	-6.51492
H	11.88911	-5.56697	5.59602
O	11.81671	-3.14691	4.36774
H	11.72447	5.46504	-5.71074
O	11.69038	3.04091	-4.48866
C	11.43537	-3.09511	5.72026
C	11.22929	-2.47568	1.37456
C	11.27207	2.99261	-5.83035
H	11.20052	-2.04911	5.94794
C	11.18505	2.35801	-1.48342
N	11.01273	-1.31223	0.68808
N	10.99010	1.19307	-0.79268
H	11.03340	1.94681	-6.05496
H	10.54250	-3.71285	5.91252
H	10.37286	3.60890	-5.99584
C	9.96233	-3.06597	1.74271
C	9.90728	2.94733	-1.81317
H	9.84168	-3.99670	2.29360
H	9.76938	3.87809	-2.35994
C	9.66430	-1.14077	0.61161
C	9.64469	1.02225	-0.67303
C	9.00153	-0.05796	-0.01834
C	8.98924	-2.23180	1.27542
C	8.94924	2.11317	-1.31556
H	7.90997	-2.33205	1.37255
H	7.86746	2.21309	-1.37969
C	7.57406	-0.05083	0.01461
C	6.35133	-0.03983	0.04968
H	6.07317	2.62026	0.09460
H	5.99867	-2.69283	0.03388
C	4.99088	2.50825	0.11582

C	4.92094	-2.55156	0.08851
C	4.92438	-0.02138	0.09574
C	4.28744	1.24437	0.12403
C	4.25272	-1.26898	0.11707
H	4.18391	4.56271	0.15767
H	4.05860	-4.58345	0.12876
C	4.04005	3.48395	0.15319
C	3.94430	-3.50116	0.13074
H	3.31414	-6.15182	-3.12954
H	3.69606	6.10179	3.49086
H	2.66989	-4.71944	-3.98698
N	2.94566	1.45845	0.17116
N	2.90555	-1.44674	0.16538
H	3.06203	4.67978	4.37288
C	2.42912	-5.50828	-3.26525
C	2.75709	2.81595	0.19430
C	2.67987	-2.79867	0.17267
C	2.80121	5.48485	3.67649
O	2.06509	-4.87204	-2.06536
H	1.95681	-7.57987	-1.92132
O	2.34095	4.87557	2.49581
H	2.30534	7.58740	2.38854
H	1.60416	-6.12057	-3.66584
C	1.72971	-5.62462	-0.99554
C	1.70134	-7.02758	-1.01756
C	1.96353	5.65151	1.45719
C	1.97923	7.05428	1.49606
H	2.02379	6.11772	4.13580
C	1.52271	3.47991	0.26096
C	1.53989	4.97166	0.30009
C	1.42622	-3.42814	0.19981
Zn	1.46880	0.02576	0.22362
C	1.39803	-4.91988	0.17669
C	1.56387	7.76638	0.37182
H	1.57361	8.85831	0.39984
C	1.33389	-7.71471	0.13845
H	1.30979	-8.80668	0.12359

H	1.07577	6.31840	-3.47091
C	1.12720	5.71744	-0.81967
C	1.13624	7.12027	-0.78721
C	1.02993	-5.64083	1.32796
C	0.99575	-7.04356	1.31272
H	1.12332	-6.21011	3.98416
H	0.81947	7.70377	-1.65104
O	0.73442	5.00160	-1.89528
H	0.71395	-7.60799	2.20101
O	0.72199	-4.90196	2.41560
C	0.28621	5.67831	-3.04340
C	0.26290	2.84383	0.30182
C	0.18419	-2.75732	0.23153
C	0.32689	-5.55261	3.59776
H	0.01014	4.91457	-3.77940
N	0.03537	1.49925	0.25120
N	-0.00491	-1.40719	0.29152
H	0.11817	-4.77306	4.33932
H	-0.59652	6.30242	-2.82628
H	-0.58459	-6.15367	3.44355
C	-1.09368	-3.42764	0.17723
C	-0.99300	3.54795	0.41273
H	-1.23385	-4.50496	0.11267
H	-1.10110	4.62849	0.48490
C	-1.31852	1.31596	0.31424
C	-1.35502	-1.18718	0.27908
C	-1.98825	0.07385	0.30498
C	-2.04982	-2.45514	0.20019
C	-1.97546	2.60159	0.42207
H	-3.12873	-2.58279	0.15044
H	-3.04838	2.75653	0.51153
C	-3.48009	0.09426	0.29974
H	-3.61923	1.10757	-1.60150
H	-3.68892	-0.91143	2.19884
C	-4.18032	0.66402	-0.77504
C	-4.21892	-0.46671	1.35273
C	-5.57374	0.65979	-0.80283

C	-5.61324	-0.46830	1.32630
H	-6.10405	1.09993	-1.65113
H	-6.17408	-0.91473	2.15143
C	-6.31276	0.08835	0.24458
H	-6.58810	-1.58604	-1.85223
H	-6.81656	1.72059	2.35041
C	-7.66854	-1.46508	-1.82153
C	-7.80396	0.06061	0.19501
C	-7.88647	1.56739	2.22792
H	-8.42262	-2.69559	-3.49223
C	-8.39979	-0.67467	-0.85251
C	-8.50794	0.76676	1.19340
C	-8.59413	-2.02962	-2.64869
H	-8.82489	-0.92286	-6.74575
H	-8.81753	2.75054	3.84288
C	-8.89603	2.09110	2.98062
H	-9.51074	0.62423	-6.16358
H	-9.47685	0.91253	7.04113
C	-9.74267	-0.42129	-6.39652
N	-9.74077	-0.78010	-1.09823
C	-9.89057	-1.59069	-2.18631
N	-9.86788	0.82676	1.32626
H	-10.16206	-2.72273	-7.31836
O	-10.23339	-1.00752	-5.21646
C	-10.13464	1.61950	2.40496
H	-10.06782	-0.64122	6.37829
H	-10.49148	-0.44998	-7.20544
C	-10.51322	-3.12242	-6.36759
C	-10.34547	0.39542	6.60070
C	-10.58539	-2.31110	-5.22497
H	-10.85083	-5.09110	-7.16228
C	-10.90440	-4.45728	-6.27424
O	-10.73680	0.98699	5.38663
C	-11.04209	-2.83474	-4.00087
H	-10.89969	2.67506	7.50544
C	-11.11049	-1.96870	-2.78781
C	-11.11917	2.28197	5.37745

Zn	-11.25297	0.00501	0.05059
C	-11.36179	-5.00373	-5.07610
C	-11.17154	3.07938	6.53097
H	-11.16762	0.39580	7.33554
C	-11.42724	-4.18714	-3.93664
H	-11.45403	-6.66885	-2.82662
C	-11.41282	1.95910	2.89932
C	-11.47469	2.81129	4.12264
H	-11.65728	-6.05150	-5.03302
C	-11.58436	4.40611	6.41717
H	-11.62759	5.02898	7.31348
O	-11.84937	-4.62739	-2.73192
H	-11.87577	6.65096	2.95828
C	-11.88441	4.15528	4.03862
C	-11.94296	4.95799	5.18828
C	-12.26903	-5.96251	-2.59688
O	-12.20596	4.60137	2.80542
H	-12.25817	5.99927	5.13000
C	-12.38143	-1.59448	-2.32336
H	-12.57497	-6.09905	-1.55339
N	-12.64086	-0.83734	-1.21468
C	-12.64733	5.92699	2.64778
C	-12.62796	1.56355	2.31746
N	-12.76925	0.80916	1.18571
H	-12.86127	6.06972	1.58243
H	-13.12620	-6.18555	-3.25372
C	-13.62913	-1.96700	-2.95858
H	-13.56607	6.11887	3.22659
H	-13.71468	-2.56507	-3.86391
C	-13.99385	-0.72194	-1.11921
C	-13.93646	1.91305	2.83241
C	-14.10491	0.67599	0.95956
H	-14.11757	2.50317	3.72883
C	-14.63219	-1.42661	-2.21084
C	-14.67442	-0.02567	-0.11148
C	-14.85522	1.36590	1.98752
H	-15.70545	-1.49534	-2.38144

H	-15.94079	1.42018	2.05377
O	-16.03424	1.87073	-1.44590
N	-16.11356	-0.02721	-0.18788
O	-16.17418	-1.93063	1.06300
C	-16.71057	1.01582	-0.91255
C	-16.78717	-1.07146	0.46406
C	-18.19504	1.00526	-0.98326
C	-18.27099	-1.05626	0.37540
H	-18.26556	2.78288	-2.16254
H	-18.47252	-2.83393	1.53947
C	-18.85556	2.00314	-1.67779
C	-18.92475	-0.02423	-0.34101
C	-19.00504	-2.05237	0.99481
C	-20.26461	2.00448	-1.75248
C	-20.33829	-0.02194	-0.41710
C	-20.41409	-2.04935	0.91834
H	-20.79850	2.78538	-2.29659
H	-21.00609	-2.82841	1.40175
C	-20.99622	1.00745	-1.13193
C	-21.07062	-1.04964	0.22316
C	-22.48205	1.02175	-1.21942
C	-22.55456	-1.05121	0.14558
O	-23.08077	1.89078	-1.82436
N	-23.15523	-0.01580	-0.57016
O	-23.23641	-1.90834	0.67567
C	-24.61317	-0.04926	-0.62512
H	-24.94862	-0.98565	-1.08958
H	-24.95140	0.80829	-1.21256
H	-25.02726	-0.00247	0.39049

Appendix D

Table 22: Electronic couplings of cofacial porphyrin systems calculated using the Edmiston-Ruedenbeg localization scheme. The geometry used corresponds to the ground state minimum.

States		Dimer 3 coupling/eV	Dimer 1 β-β coupling/eV	Dimer 1 meso-β coupling/eV
1	2	0.000	0.066	0.004
1	3	0.021	0.002	0.029
1	4	0.010	0.026	0.007
2	2	0.004	0.026	0.010
2	3	0.020	0.002	0.030
3	4	0.004	0.056	0.001

Table 23: Electronic couplings of cofacial porphyrin systems without the bridge unit calculated using the Edmiston-Ruedenbeg localization scheme. The geometry used corresponds to the ground state minimum.

States		Dimer 3 coupling/eV	Dimer 1 β-β coupling/eV	Dimer 1 meso-β coupling/eV
1	2	0.001	0.097	0.003
1	3	0.017	0.011	0.017
1	4	0.029	0.023	0.040
2	2	0.029	0.023	0.038
2	3	0.016	0.011	0.015
3	4	0.003	0.080	0.002

Table 24: Ground-state optimized geometry of monomer 8 at the CAM-B3LYP-D3BJ/def2-SVP level of theory in THF.

C	0.44889	4.05057	0.83670
C	0.01901	3.37285	-0.32318
C	0.55205	5.44867	0.81423
C	-0.31246	4.10306	-1.47080
C	0.22458	6.16020	-0.33066
H	0.88314	5.97111	1.71482

C	-0.21139	5.48700	-1.47526
H	-0.63469	3.56540	-2.36560
C	0.19184	7.75220	-2.10756
H	1.22217	7.75096	-2.49663
H	-0.29281	8.67133	-2.46462
C	0.23384	7.65002	-0.57056
H	-0.66499	8.10575	-0.11933
H	1.10364	8.15529	-0.12576
C	-0.52489	6.47077	-2.57565
H	-0.19793	6.12909	-3.56865
H	-1.61622	6.62778	-2.63576
C	-0.04756	1.87809	-0.36018
C	1.16997	1.18366	-0.39710
C	-1.31738	1.28351	-0.31626
N	1.33067	-0.17184	-0.34649
C	2.46646	1.81835	-0.47740
N	-1.58019	-0.05645	-0.28570
C	-2.56087	2.01822	-0.24675
C	2.67253	-0.42561	-0.37617
C	3.39428	0.82671	-0.46029
H	2.63834	2.88970	-0.53376
C	-2.93544	-0.20614	-0.20325
C	-3.56000	1.09894	-0.18052
H	-2.65169	3.10095	-0.23850
C	3.28374	-1.68976	-0.30397
H	4.47529	0.92840	-0.49159
C	-3.63633	-1.42224	-0.10945
H	-4.62772	1.28394	-0.10400
C	2.59046	-2.90230	-0.16742
C	-3.03018	-2.68519	-0.02420
N	1.23554	-3.04061	-0.07701
C	3.21020	-4.21257	-0.12389
N	-1.68599	-2.92592	-0.00034
C	-3.74380	-3.94556	0.04036
C	0.96994	-4.37396	0.02240
C	2.20618	-5.12043	-0.00018
H	4.27772	-4.40433	-0.18954

C	-1.51787	-4.27653	0.08120
C	-2.80644	-4.92722	0.11302
H	-4.82441	-4.05705	0.02250
C	-0.29670	-4.94616	0.10484
H	2.28280	-6.20476	0.06025
H	-2.96212	-6.00312	0.17168
H	-0.33775	-6.03446	0.17526
Zn	-0.17466	-1.54774	-0.16932
C	4.77413	-1.74506	-0.36696
C	5.53047	-2.11737	0.75358
C	5.45899	-1.42602	-1.53923
C	6.91399	-2.16624	0.70090
H	5.01886	-2.36645	1.68553
C	6.85097	-1.47057	-1.60988
H	4.89270	-1.13708	-2.42709
C	7.58841	-1.84256	-0.48327
H	7.50418	-2.45049	1.57359
H	7.34447	-1.21693	-2.54695
C	-5.12717	-1.36292	-0.08866
C	-5.84513	-0.93875	-1.20695
C	-5.85206	-1.73067	1.05422
C	-7.23812	-0.87883	-1.20444
H	-5.30450	-0.65087	-2.11096
C	-7.23615	-1.67570	1.07430
H	-5.31463	-2.05998	1.94583
C	-7.94356	-1.24957	-0.05709
H	-7.75800	-0.54649	-2.10175
H	-7.80109	-1.95670	1.96454
O	8.93627	-1.91601	-0.44502
O	-9.28933	-1.22844	0.04966
C	-10.05504	-0.80939	-1.05421
H	-11.10676	-0.87021	-0.75005
H	-9.82387	0.23071	-1.33844
H	-9.89712	-1.46085	-1.92983
C	9.67033	-1.59513	-1.60186
H	9.49598	-0.55320	-1.91826
H	10.72987	-1.71760	-1.34742

H	9.42344	-2.26748	-2.44032
C	0.82408	3.31883	2.07889
C	2.07681	3.53092	2.66528
C	2.44972	2.84989	3.82119
C	1.57164	1.94634	4.41401
C	0.31606	1.73618	3.84687
C	-0.05469	2.41684	2.69135
H	2.77629	4.22524	2.19481
H	3.43651	3.02150	4.25655
H	1.86379	1.40765	5.31788
H	-0.38414	1.03735	4.30973
H	-1.04272	2.25152	2.26070

Table 25: Ground-state optimized geometry of monomer 9 at the CAM-B3LYP-D3BJ/def2-SVP level of theory in THF.

C	2.75986	-0.87771	-0.27435
C	1.60779	0.01225	-0.42800
C	2.26061	-2.14502	-0.29755
N	0.46267	-0.74037	-0.43688
C	1.64419	1.40641	-0.61580
C	0.82673	-2.05272	-0.38556
H	2.83118	-3.06176	-0.17703
C	0.50884	2.24011	-0.65317
C	-0.02855	-3.16763	-0.37517
N	-0.78558	1.86624	-0.42768
C	0.55024	3.66196	-0.92691
C	-1.42707	-3.11030	-0.30155
C	-1.55742	2.99123	-0.50447
C	-0.72171	4.12562	-0.82288
H	1.43799	4.23271	-1.17928
N	-2.17910	-1.97515	-0.19615
C	-2.29806	-4.26574	-0.31455
C	-2.94866	3.06189	-0.32621
H	-1.07011	5.14396	-0.97017
C	-3.48711	-2.36057	-0.11303
C	-3.56899	-3.80311	-0.19357

H	-1.97397	-5.29789	-0.41321
C	-3.79162	1.95544	-0.14528
C	-4.59581	-1.51104	0.01780
H	-4.48746	-4.38300	-0.17380
N	-3.41162	0.64438	-0.18125
C	-5.21443	2.03811	0.10448
C	-4.53400	-0.10867	0.00839
C	-5.67291	0.76309	0.19979
H	-5.78425	2.95747	0.20577
H	-6.69081	0.43632	0.39310
C	2.95524	2.07256	-0.87409
C	3.70409	1.73528	-2.00551
C	3.43755	3.07794	-0.02973
C	4.91296	2.36832	-2.27550
H	3.33234	0.96067	-2.67874
C	4.64719	3.71143	-0.29517
H	2.85952	3.35384	0.85203
C	5.39158	3.35592	-1.41791
H	5.48627	2.08599	-3.16096
H	5.01300	4.48586	0.38259
H	6.34296	3.85011	-1.62578
C	-5.93898	-2.14529	0.17467
C	-6.25895	-2.85736	1.33580
C	-6.90171	-2.04049	-0.83511
C	-7.51023	-3.44938	1.48466
H	-5.51627	-2.94166	2.13179
C	-8.15289	-2.63340	-0.68853
H	-6.66077	-1.49106	-1.74742
C	-8.46094	-3.33937	0.47234
H	-7.74461	-3.99814	2.39929
H	-8.89109	-2.54545	-1.48847
H	-9.44229	-3.80409	0.58808
C	-3.57655	4.41673	-0.33658
C	-4.45136	4.79330	-1.36159
C	-3.30055	5.33599	0.68170
C	-5.03569	6.05699	-1.36886
H	-4.66922	4.08599	-2.16433

C	-3.88593	6.59905	0.67710
H	-2.62220	5.05084	1.48837
C	-4.75522	6.96343	-0.34880
H	-5.71267	6.33603	-2.17905
H	-3.66320	7.30227	1.48238
H	-5.21408	7.95431	-0.35346
C	0.61123	-4.51640	-0.42652
C	1.28855	-4.93767	-1.57599
C	0.55623	-5.37846	0.67404
C	1.89392	-6.19032	-1.62556
H	1.33630	-4.27280	-2.44082
C	1.16281	-6.63081	0.62680
H	0.03675	-5.05667	1.57892
C	1.83301	-7.04066	-0.52371
H	2.41525	-6.50468	-2.53220
H	1.11450	-7.28924	1.49669
H	2.30886	-8.02278	-0.56130
Zn	-1.47587	-0.05351	-0.30200
C	4.18670	-0.58234	-0.00274
C	4.61314	0.04142	1.19055
C	5.13545	-0.99304	-0.94806
C	5.98405	0.27739	1.37675
C	6.48373	-0.74593	-0.74832
H	4.78845	-1.47463	-1.86497
C	6.90811	-0.10012	0.41534
H	6.32014	0.75287	2.30064
C	8.76731	-0.14705	-1.07552
H	8.71658	0.82396	-1.59308
H	9.77979	-0.54727	-1.22431
C	7.66413	-1.06892	-1.63042
H	7.94161	-2.13148	-1.51497
H	7.46176	-0.90697	-2.69946
C	8.40896	0.05715	0.40929
H	8.74409	1.02682	0.80589
H	8.87230	-0.72320	1.03838
C	3.66823	0.46567	2.26126
C	2.62073	-0.35631	2.69959

H	2.48770	-1.34225	2.25714
C	1.75161	0.06361	3.70178
H	0.94223	-0.59579	4.02277
C	1.91348	1.31257	4.29698
H	1.22733	1.64400	5.07917
C	2.96419	2.13086	3.88987
H	3.10725	3.11037	4.35142
C	3.83151	1.70900	2.88658
H	4.63867	2.36682	2.56233

Table 26: Ground-state optimized geometry of dimer 1 at the CAM-B3LYP-D3BJ/def2-SVP level of theory in THF.

C	-1.93195	2.22420	1.64956
C	-0.55437	1.79767	1.58565
C	-2.68126	1.11711	1.88682
N	-0.48572	0.45149	1.80202
C	0.52061	2.65421	1.30337
C	-1.76638	-0.00338	1.96967
H	-3.76220	1.05844	1.96631
C	1.87478	2.30073	1.40356
C	-2.15515	-1.34665	2.12130
N	2.35810	1.04863	1.64976
C	2.98154	3.21471	1.21646
C	-1.26742	-2.43876	2.07875
C	3.72253	1.12114	1.60484
C	4.12076	2.49037	1.35676
H	2.89277	4.27496	0.99838
N	0.08742	-2.35858	1.92570
C	-1.64764	-3.83009	2.22522
C	4.61886	0.04666	1.71052
H	5.14574	2.84096	1.27444
C	0.57851	-3.63138	1.97008
C	-0.50728	-4.56532	2.13789
H	-2.65708	-4.19535	2.38733
C	4.23661	-1.29992	1.82909
C	1.92384	-3.98931	1.94888

H	-0.39757	-5.64613	2.20760
N	2.95467	-1.76841	1.81553
C	5.15172	-2.41356	1.96800
C	3.01732	-3.12799	1.91689
C	4.39603	-3.54425	2.01226
H	6.23374	-2.33180	2.02291
H	4.73239	-4.57505	2.10957
C	6.07881	0.34592	1.62519
C	6.80896	-0.04504	0.50362
C	6.75810	1.02000	2.64877
C	8.17474	0.20634	0.39087
H	6.29888	-0.56581	-0.30587
C	8.11600	1.28278	2.55147
H	6.21099	1.33724	3.53911
C	8.83828	0.87599	1.42186
H	8.70053	-0.13142	-0.50123
H	8.65006	1.80222	3.34881
O	10.15702	1.16861	1.41434
C	-3.60485	-1.62951	2.32307
C	-4.30654	-1.08238	3.39920
C	-4.31610	-2.44298	1.43005
C	-5.67180	-1.30430	3.57583
H	-3.77662	-0.45928	4.12203
C	-5.66849	-2.68622	1.59912
H	-3.80127	-2.87494	0.57334
C	-6.36541	-2.10223	2.66312
H	-6.17904	-0.84726	4.42417
H	-6.21993	-3.30072	0.88643
O	-7.69453	-2.34457	2.71576
Zn	1.23068	-0.66199	1.74750
H	2.14477	-5.05620	2.01049
C	10.93292	0.77777	0.30755
C	-8.44969	-1.77356	3.75744
H	11.95897	1.10849	0.50826
H	10.57987	1.25039	-0.62423
H	10.92863	-0.31684	0.17378
H	-9.48684	-2.09701	3.60893

H	-8.40989	-0.67183	3.73009
H	-8.10497	-2.11864	4.74616
H	-2.27605	3.24590	1.51918
C	0.21086	3.97462	0.66430
C	-0.22945	3.98163	-0.68307
C	0.40065	5.18580	1.33522
C	-0.44207	5.20030	-1.33346
C	0.16858	6.38906	0.68039
H	0.72900	5.17239	2.37704
C	-0.24224	6.39643	-0.65517
H	-0.77522	5.19848	-2.37382
C	-0.46741	8.62871	0.15685
H	-0.08796	9.65392	0.04700
H	-1.51856	8.69946	0.47786
C	0.32022	7.80107	1.19071
H	-0.04552	7.93083	2.21982
H	1.38757	8.08387	1.19381
C	-0.39343	7.81436	-1.14914
H	0.49301	8.09870	-1.74292
H	-1.26963	7.95565	-1.79867
C	-0.53038	2.66528	-1.33470
C	0.55100	1.81723	-1.61882
C	-1.88193	2.30114	-1.43331
N	0.49319	0.46956	-1.82943
C	1.92518	2.25415	-1.68291
N	-2.35552	1.04541	-1.68080
C	-2.99574	3.20505	-1.23957
C	1.77777	0.02336	-1.98877
C	2.68346	1.15176	-1.91380
H	2.26120	3.27899	-1.55566
C	-3.72030	1.10598	-1.62969
C	-4.12921	2.47129	-1.37729
H	-2.91558	4.26524	-1.01805
C	2.17872	-1.31910	-2.11673
H	3.76505	1.10092	-1.98989
C	-4.60772	0.02310	-1.72945
H	-5.15657	2.81311	-1.28866

C	1.30153	-2.41844	-2.04631
C	-4.21335	-1.32090	-1.84009
N	-0.05329	-2.34717	-1.88651
C	1.69244	-3.80871	-2.17375
N	-2.92761	-1.77815	-1.81590
C	-5.11786	-2.44383	-1.97454
C	-0.53464	-3.62419	-1.91698
C	0.55831	-4.55173	-2.07283
H	2.70387	-4.16852	-2.33520
C	-2.97802	-3.13932	-1.90037
C	-4.35228	-3.56830	-2.00255
H	-6.20012	-2.37234	-2.03770
C	-1.87744	-3.99216	-1.90508
H	0.45698	-5.63416	-2.12852
H	-4.67924	-4.60292	-2.09094
H	-2.08933	-5.06151	-1.95470
Zn	-1.21309	-0.65673	-1.76886
C	3.62902	-1.59146	-2.32619
C	4.35487	-2.39269	-1.43373
C	4.31682	-1.04710	-3.41283
C	5.70732	-2.62740	-1.61400
H	3.85162	-2.82173	-0.56882
C	5.68184	-1.26029	-3.60083
H	3.77546	-0.43373	-4.13549
C	6.38984	-2.04671	-2.68915
H	6.26999	-3.23257	-0.90208
H	6.17750	-0.80613	-4.45753
C	-6.06954	0.30873	-1.63612
C	-6.79210	-0.10743	-0.51845
C	-6.75855	0.99603	-2.64441
C	-8.15888	0.13223	-0.39471
H	-6.27454	-0.63830	0.27960
C	-8.11776	1.24748	-2.53598
H	-6.21816	1.33297	-3.53159
C	-8.83185	0.81582	-1.41035
H	-8.67757	-0.22517	0.49391
H	-8.65927	1.77727	-3.32140

O	7.71976	-2.28088	-2.75368
O	-10.15236	1.09952	-1.39116
C	-10.91997	0.68470	-0.28729
H	-11.94904	1.01260	-0.47680
H	-10.90838	-0.41203	-0.17269
H	-10.56477	1.14313	0.65075
C	8.46086	-1.71078	-3.80593
H	8.41292	-0.60923	-3.78520
H	9.50178	-2.02540	-3.66512
H	8.10962	-2.06463	-4.78924

Table 27: Ground-state optimized geometry of dimer 3 at the CAM-B3LYP-D3BJ/def2-SVP level of theory in THF.

C	1.11970	2.73796	-1.54348
C	-0.30898	2.41342	-1.55617
C	1.76230	1.60768	-1.94660
N	-0.46633	1.08845	-1.86026
C	-1.36314	3.30438	-1.28779
C	0.77039	0.57695	-2.12586
H	2.83720	1.45683	-1.98556
C	-2.69427	2.92565	-1.05301
C	1.08664	-0.75992	-2.41929
N	-3.18985	1.65359	-1.03338
C	-3.76216	3.85883	-0.75653
C	0.18666	-1.83588	-2.32675
C	-4.51816	1.73690	-0.72230
C	-4.88203	3.12416	-0.53641
H	-3.66584	4.93976	-0.72723
N	-1.12494	-1.75444	-1.95296
C	0.51296	-3.21164	-2.63360
C	-5.42608	0.67189	-0.64918
H	-5.87704	3.48626	-0.29352
C	-1.64089	-3.02004	-2.00113
C	-0.61136	-3.94262	-2.42083
H	1.47529	-3.57200	-2.98261
C	-5.11837	-0.66404	-0.94855

C	-2.97138	-3.38902	-1.75352
H	-0.74197	-5.01208	-2.55817
N	-3.89754	-1.13963	-1.33280
C	-6.04715	-1.76484	-0.82349
C	-4.00806	-2.49765	-1.44233
C	-5.36106	-2.89786	-1.12589
H	-7.08672	-1.68092	-0.52015
H	-5.73054	-3.91927	-1.11838
C	-1.10150	4.77710	-1.31724
C	-0.89419	5.40219	-2.55079
C	-1.13070	5.56794	-0.16501
C	-0.70670	6.77914	-2.63105
H	-0.88318	4.79523	-3.45851
C	-0.92456	6.94195	-0.23926
H	-1.32043	5.10472	0.80349
C	-0.71304	7.55273	-1.47326
H	-0.55039	7.24945	-3.60420
H	-0.93531	7.54055	0.67393
H	-0.55812	8.63210	-1.53198
C	-3.31140	-4.84145	-1.83357
C	-2.82163	-5.73662	-0.87724
C	-4.12309	-5.33190	-2.86174
C	-3.13719	-7.09080	-0.94553
H	-2.19169	-5.35764	-0.07171
C	-4.43811	-6.68644	-2.93194
H	-4.50639	-4.64157	-3.61597
C	-3.94646	-7.56998	-1.97337
H	-2.74974	-7.77580	-0.18818
H	-5.07000	-7.05430	-3.74313
H	-4.19403	-8.63217	-2.02790
C	-6.81118	0.97487	-0.18113
C	-7.91231	0.85077	-1.03466
C	-7.02815	1.37280	1.14271
C	-9.19992	1.11343	-0.57403
H	-7.75394	0.54666	-2.07136
C	-8.31480	1.63062	1.60592
H	-6.17515	1.46582	1.81610

C	-9.40510	1.50120	0.74856
H	-10.04896	1.01487	-1.25378
H	-8.46561	1.92852	2.64551
H	-10.41551	1.70247	1.11059
C	2.48519	-1.05491	-2.84497
C	3.28716	-1.95003	-2.12947
C	3.01982	-0.44533	-3.98706
C	4.57754	-2.24522	-2.55626
H	2.90433	-2.41132	-1.22028
C	4.31672	-0.72861	-4.40562
H	2.40397	0.25312	-4.55686
C	5.09956	-1.63541	-3.69397
H	5.17279	-2.96128	-1.98813
H	4.71467	-0.24434	-5.29986
H	6.11449	-1.86493	-4.02530
Zn	-2.16930	-0.03656	-1.55700
C	1.77979	3.84854	-0.80563
C	2.04762	5.10009	-1.36278
C	2.58992	6.10812	-0.57883
H	1.80062	5.28383	-2.40776
C	3.01397	8.23119	0.41313
H	2.00965	8.59507	0.68245
H	3.69144	9.09635	0.41809
C	2.93789	7.52701	-0.95412
H	3.91577	7.55176	-1.46656
H	2.20480	7.98138	-1.63541
C	2.69113	4.61490	1.31687
C	2.88132	5.87706	0.76799
H	2.96862	4.40782	2.35312
C	3.43113	7.12943	1.40655
H	3.05169	7.29783	2.42517
H	4.53071	7.06184	1.48275
C	2.15822	3.58755	0.53363
C	2.10670	2.17272	1.03182
C	0.87674	1.63182	1.43122
C	3.30505	1.44976	0.93548
N	0.60131	0.30981	1.63883

C	-0.31307	2.40967	1.66508
N	3.45528	0.10722	1.14565
C	4.58622	2.02669	0.59262
C	-0.71829	0.21322	1.97882
C	-1.29986	1.53982	2.00561
H	-0.37084	3.48824	1.57197
C	4.77555	-0.18941	0.96848
C	5.49761	1.01905	0.63541
H	4.76188	3.07161	0.35335
C	-1.43151	-0.98007	2.21872
H	-2.33827	1.77066	2.22208
C	5.36103	-1.46788	1.01942
H	6.56323	1.07739	0.43183
C	-0.89862	-2.26878	2.03605
C	4.63436	-2.66333	1.11058
N	0.38034	-2.55394	1.64277
C	-1.60935	-3.51142	2.26736
N	3.27388	-2.76156	1.20973
C	5.20639	-3.99429	1.07236
C	0.50756	-3.91098	1.61509
C	-0.74517	-4.52294	1.98574
H	-2.63444	-3.59863	2.61398
C	2.96119	-4.08958	1.22237
C	4.16959	-4.87339	1.12094
H	6.26782	-4.21998	1.01634
C	1.68350	-4.62004	1.37569
H	-0.91971	-5.59510	2.05808
H	4.20962	-5.96123	1.10933
H	1.60451	-5.70843	1.37976
Zn	1.92378	-1.22754	1.40137
C	-2.82990	-0.85494	2.71881
C	-3.91450	-1.43532	2.04517
C	-3.10247	-0.14482	3.89096
C	-5.20814	-1.30326	2.51917
H	-3.74020	-1.98237	1.12019
C	-4.40068	0.00742	4.37531
H	-2.27765	0.30392	4.44745

C	-5.46669	-0.57189	3.68323
H	-6.04883	-1.73978	1.98072
H	-4.56358	0.57340	5.29136
C	6.85132	-1.53790	0.95856
C	7.61745	-1.03639	2.01187
C	7.53149	-2.08467	-0.13850
C	9.01078	-1.07505	1.99137
H	7.11300	-0.60396	2.87846
C	8.91573	-2.12985	-0.17664
H	6.96325	-2.46742	-0.98581
C	9.67026	-1.62607	0.89003
H	9.56664	-0.67570	2.83837
H	9.44370	-2.54932	-1.03446
O	-6.76255	-0.46868	4.05058
O	11.01232	-1.71082	0.76919
C	11.82365	-1.21269	1.80560
H	12.86349	-1.37922	1.50004
H	11.66507	-0.13281	1.96301
H	11.64052	-1.74142	2.75579
C	-7.09329	0.31443	5.17108
H	-6.77311	1.36203	5.04217
H	-8.18534	0.28425	5.26579
H	-6.64268	-0.08357	6.09542

Appendix E

Analysis of MD structural ensembles

Figure 51 shows the root-mean-square deviation (RMSD) maps for the nucleic acid duplexes generated using MDAnalysis.[327, 328] Each frame is compared and color-coded according to the RMSD. Both DNA structures have somewhat higher RMSD values than PNA, in contrast to previous studies.[162] Figure 52 includes the percent change in flexibility, $\Delta\sigma$, of helical parameters related to nucleic acid flexibility (rise, roll, shift, slide, tilt, twist). $\Delta\sigma = {\sigma_r - \sigma_d}/{\sigma_r} \cdot 100$, where σ_r is the standard deviation of the reference (DNA 5′) and σ_d is the standard deviation of the nucleic acid duplex (DNA 3′ or PNA N-end). Negative values show a decrease in flexibility.

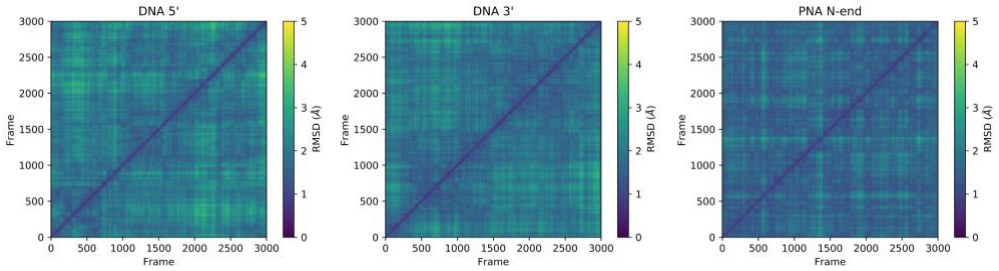

Figure 51: RMSD maps for the MD production simulations of the nucleic acid duplexes.

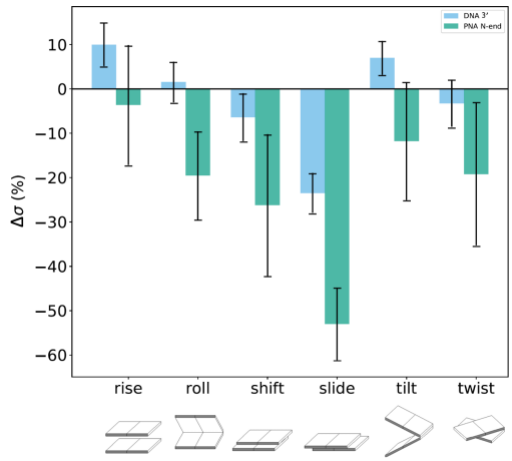

Figure 52: Comparisons between the standard deviations of several parameters between duplexes (using 5′ DNA as the reference). All base pairs were considered. Structural parameters are defined and calculated with the 3DNA software package.[263]

HOMO energies

Table 28 shows the HOMO energies and standard deviations of all of the base pairs of the $n = 5$ duplexes.

Table 28: HOMO energies and standard deviations (σ) in eV for each base pair of the n = 5 duplexes.

	DNA 5′		DNA 3′		PNA N-end	
Base pair	E_{HOMO}	σ	E_{HOMO}	σ	E_{HOMO}	σ
A1-T1	7.45	0.21	7.57	0.23	7.39	0.19
G1-C1	6.61	0.23	6.73	0.22	6.56	0.18
G2-C1	6.45	0.22	6.43	0.21	6.45	0.19
G3-C1	6.31	0.19	6.34	0.19	6.49	0.17
G4-C1	6.31	0.20	6.38	0.21	6.70	0.18
G5-C1	6.56	0.22	6.52	0.20	6.99	0.19
G6-C1	6.55	0.23	6.56	0.21	6.97	0.19
G7-C1	6.34	0.22	6.52	0.21	6.70	0.19
G8-C1	6.40	0.20	6.41	0.22	6.51	0.18
G9-C1	6.48	0.21	6.47	0.21	6.43	0.17
G10-C10	6.68	0.21	6.62	0.22	6.51	0.18
A2-T2	7.54	0.20	7.44	0.22	7.31	0.17

Average structures

The average structures over the 3000 coordinate snapshots for each duplex were obtained from VMD.[186] Figure 53 shows the average structures of the duplexes and Figure 54 shows the four nucleotides at the cross-strand section. The RMSDs of the four nucleobases at the cross-strand section are in Figure 55 and the calculated electronic couplings for the average structures are in Table 29. The base pair electronic couplings are consistent with previous results.[258]

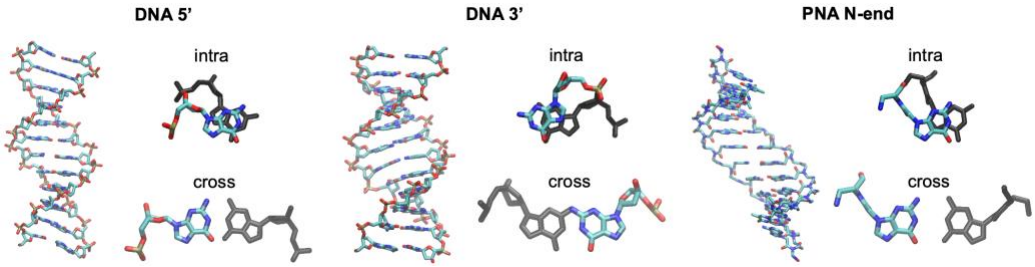

Figure 53: Average structures from the 3000 MD snapshots. The intra-strand and cross-strand G-G overlaps are shown for each duplex.

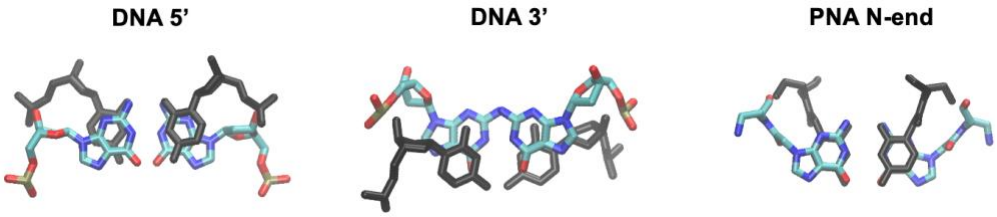

Figure 54: Average structures from the 3000 MD snapshots for the four nucleobases at the cross-strand section.

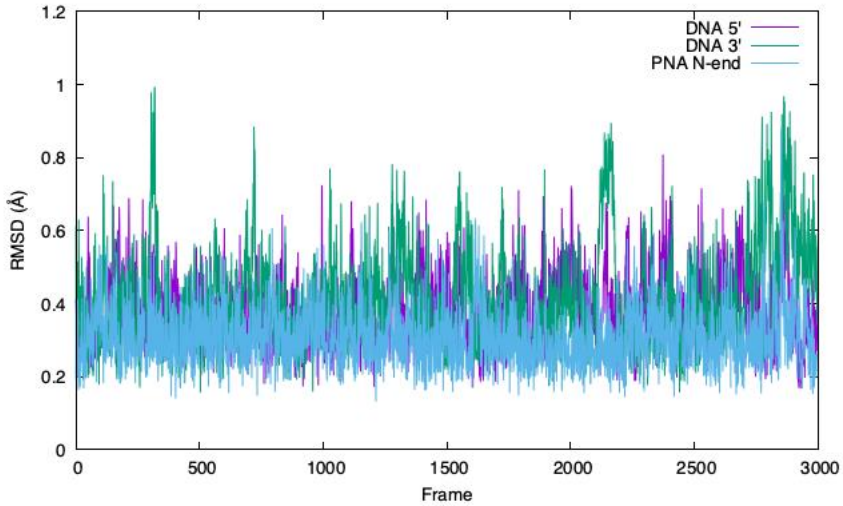

Figure 55: RMSDs (excluding H atoms) from its average structure along the MD production runs for the four nucleobases at the cross-strand section.

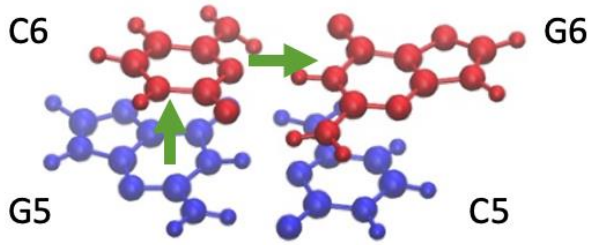

Figure 56: Nucleobase labeling for the calculation of the superexchange contribution to the coupling, V_C^{SE}.

Table 29: V_{RMS} **values of the electronic couplings in eV of the four nucleotides at the cross-strand section (Figure 56) calculated at the M11/ma-def2TZVPP level of theory[184, 185] using single snapshots taken every 5 ns. The superexchange cross-strand coupling, $V_C^{SE} = {V_{G5-C6}V_{G6-C6}}/{\Delta E}$. ΔE is approx. 0.7 eV[190, 191] The V_C^{SE} value calculated with the alternative pathway ($V_{G5-C5}V_{C5-G6}$) gives similar results. (i.e. $V_{G5-C6} \approx V_{C5-G6}$ and $V_{C6-C6} \approx V_{G5-C5}$)**

DNA 5′			DNA 3′			PNA N-end		
G5-C6	G6-C6	V_C^{SE}	G5-C6	G6-C6	V_C^{SE}	G5-C6	G6-C6	V_C^{SE}
0.015	0.052	0.001	0.069	0.046	0.005	0.250	0.040	0.014

Double-Barrier Model

The DNA conductance data were fit using a double-barrier transmission model that includes coherent and incoherent transport,[152] where the conductance (G) and the effective resistance (R_{tot}) are given by

$$\frac{1}{G} = R_{tot} = R_0 + \frac{h}{e^2 T_{GG}} \frac{2n+1}{1 - 2e^{-B(2n+1)} \cos\big(C(2n+1)\big)} \tag{23}$$

This model was used earlier to describe the measured resistance in G-block DNA duplexes.[150, 329, 330] R_0 is the effective resistance of the molecule-electrode contacts, and it includes the resistance between the electrodes and the AT base pairs. The second term on the right side of Equation 23 describes mixed coherent and incoherent transport from the AT base pair through the G-blocks; it includes a coherent transport correction that produces conductance oscillations. T_{GG} is the probability of incoherent transmission through the π-stack. The double barrier model includes coherence effects through a 'correction' term, associated with parameters B and C. The parameter $B = {w_0}/{(v\,\tau_i)}$ describes the decrease in the coherent mechanism with distance, where w_0 is the inter-base pair distance, v is the velocity of the charge carrier, and τ_i is the scattering time. The C parameter represents the change in phase of the charge carrier for coherent transport, and $C = {2w_0\sqrt{2mE}}/{\hbar}$ where m is the effective mass of the charge carrier and E is its energy. Fits of the experimental data using Equation 23 are shown in Figure 36 and the fitted parameters appear in Table 30. The presence of oscillations has been interpreted as a

signature that reflects a coherent-resonant (ballistic) mechanism,[159, 197, 198] and the smaller amplitude of oscillations for PNA indicates a smaller relative contribution from the fully delocalized G-blocks to the overall conductance.

The data were fit by this model in a two-step process. In the first step, we estimated the contact resistance (between the molecule and the electrode), the PNA data were fit by a sequential hopping model based on the steady-state flux method.[271, 272] The model is given by

$$\frac{1}{G} = R_{tot} = R_0 + \frac{2n+1}{e^2\rho(E_F)} k^{-1} e^{E_a/k_B T} \tag{24}$$

where R_0 is the effective resistance of the molecule-electrode contact, e is the electron charge, $\rho(E_F)$ is the density of states at the Fermi level, k is the hole transfer rate constant between hopping sites, E_a is the activation energy, k_B is Boltzmann's constant, and T is the temperature. In the second step we used the contact resistance R_0 from step 1 as an initial guess for R_0 and we assumed similar carrier energies for PNA and DNA (i.e., similar C values) to constrain the fit by Equation 23. The fitting parameters are shown in Table 30.

Table 30: Best fit parameters for the data in Figure 36 using Equation 23.

	DNA 5′	DNA 3′	PNA N-end
R_0 /MΩ	1.26	0.65	0.15
B	0.11	0.19	0.32
C	1.38	1.40	1.40
T_{GG}	0.03	0.19	1.23
Slope/MΩ	-	-	0.02

The parameters found in the fitting indicate that the contact resistance R_0 is larger for DNA than for N-linked PNA. 5′ DNA has a larger resistance than 3′ DNA. The decrease in molecule-lead coupling for DNA compared to PNA is attributed to the structural fluctuations of the duplex ends that manifested in the MD simulations.

The single barrier transmission factor T_{GG} is determined by the cross-strand, intra-strand, and AT-GC couplings (Table 29). Given the similar HOMO energies and intra-strand couplings for 3′-DNA and 5′-DNA, the small T_{GG} value found for 5′-DNA is believed to arise from its much smaller 5′ cross-strand coupling. Figure 57 shows contour plots that indicate the correlation among the fitting parameters. The parameters used in Table 30 guarantee a good fit as described by the parameter χ^2. Although the R_0 and T_{GG} parameters in Equation 23 are coupled in the fitting, the uncertainty in the best fit parameters is small enough that it does not change the above interpretations. The large T_{GG} value for PNA arises from the strong coupling among G base pairs and between AT and GC pairs.

The effects of coherent transport through the cross-strand junction (i.e., the even-odd effect) manifest in the B and C parameters of Equation 23. The B parameter reflects the strength of the dephasing as a function of distance and affects the magnitude of this coherent correction to the transmission. The small value of B for 5′ DNA indicates that the duplex has a larger coherent contribution to the overall conductance, which accounts for the larger amplitude of the even-odd effect that is seen experimentally. As the value of B

increases, the coherent contribution becomes less important and T_{GG} dominates, which leads to a dampening of the conductance oscillations. For 3′-DNA, the coherent contribution decreases and seems to arise from the increase in the cross-strand coupling, which is the only significant difference between the 3′ and 5′ G-block DNAs.[159] The *C* parameter is similar in 5′-DNA and 3′-DNA, which indicates that the hole energies are not too different among the species. For N-linked PNA, the strong cross-strand coupling and the molecule-lead coupling reduces the relative importance of the coherent correction, resulting in the largest *B* value among the structures.[159, 197, 198]

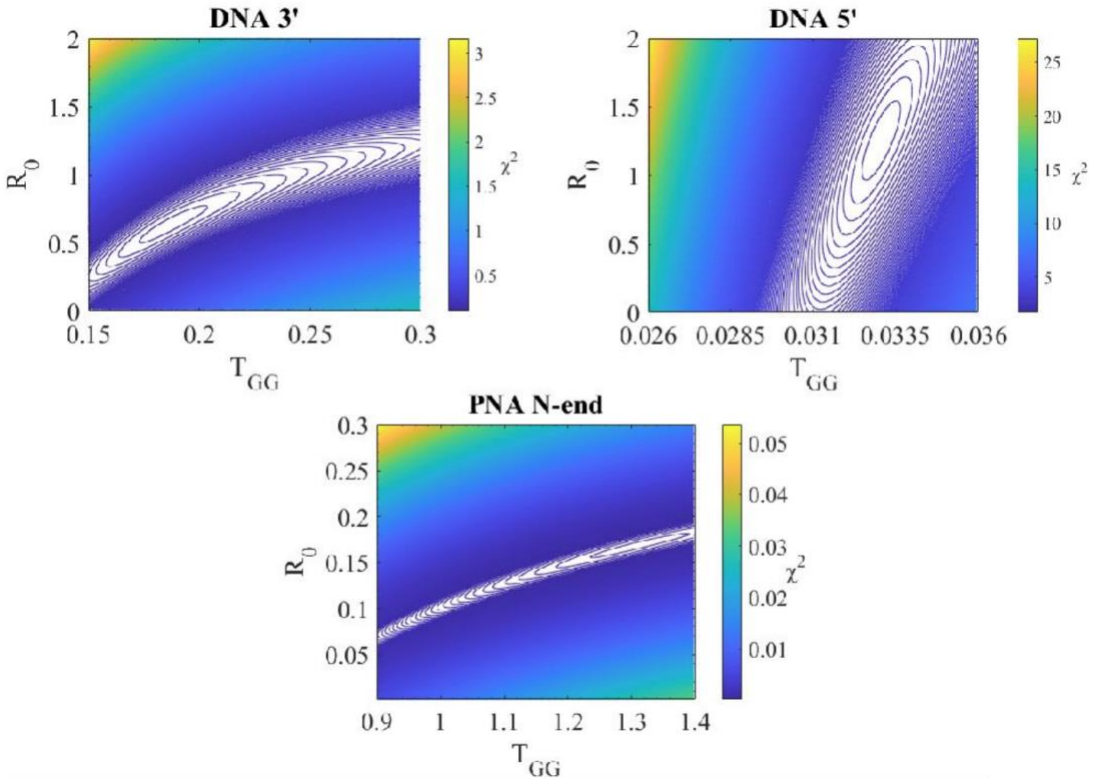

Figure 57: Contour plots of fitting parameters R_0 and T_{GG}. B and C are fixed at the values given in Table 30.

Appendix F

Table 31: XYZ coordinates of the anionic surfactant in R configuration optimized in water at the wB97-XD/def2-SVP level of theory.

S	5.08432	-1.77372	-0.16251
O	5.42378	-1.20511	1.16280
O	6.10823	-1.49297	-1.19784
O	4.69530	-3.20314	-0.10118
C	3.60616	-0.89428	-0.69730
H	3.86805	0.17505	-0.70594
H	2.84977	-1.04950	0.08543
C	3.10726	-1.36376	-2.05471
H	3.89591	-1.20829	-2.80695
H	2.91146	-2.44678	-2.01338
C	1.85603	-0.64345	-2.51410
H	1.57565	-0.97368	-3.53013
H	2.03052	0.44662	-2.54748
O	0.80644	-0.92609	-1.59772
C	-0.27024	-0.09380	-1.62868
C	-1.18059	-0.15242	-2.71507
H	-0.98472	-0.85349	-3.52884
C	-2.29849	0.64095	-2.72015
H	-3.01160	0.58215	-3.54564
C	-2.55990	1.53357	-1.64497
C	-3.73673	2.33033	-1.60674
H	-4.44595	2.25801	-2.43496
C	-3.98832	3.16545	-0.54510
H	-4.89902	3.76757	-0.52271
C	-3.06171	3.25145	0.52289
H	-3.26213	3.92457	1.35929
C	-1.91521	2.49331	0.51366
H	-1.20527	2.56303	1.34043
C	-1.63774	1.60228	-0.56071
C	-0.48084	0.76431	-0.56793
C	0.48089	0.76438	0.56786
C	1.63779	1.60235	0.56058

C	1.91529	2.49326	-0.51388
H	1.20536	2.56290	-1.34068
C	3.06180	3.25138	-0.52319
H	3.26224	3.92440	-1.35966
C	3.98839	3.16548	0.54483
H	4.89910	3.76759	0.52238
C	3.73677	2.33050	1.60656
H	4.44597	2.25826	2.43480
C	2.55992	1.53376	1.64486
C	2.29848	0.64128	2.72015
H	3.01158	0.58256	3.54565
C	1.18057	-0.15207	2.71514
H	0.98467	-0.85304	3.52900
C	0.27025	-0.09358	1.62871
O	-0.80644	-0.92585	1.59782
C	-1.85607	-0.64311	2.51413
H	-2.03057	0.44696	2.54740
H	-1.57572	-0.97325	3.53020
C	-3.10727	-1.36351	2.05477
H	-2.91143	-2.44652	2.01354
H	-3.89593	-1.20800	2.80699
C	-3.60619	-0.89416	0.69732
H	-2.84982	-1.04943	-0.08542
H	-3.86809	0.17517	0.70587
S	-5.08436	-1.77366	0.16265
O	-4.69537	-3.20310	0.10157
O	-6.10829	-1.49273	1.19792
O	-5.42380	-1.20528	-1.16276

Table 32: XYZ coordinates of the anionic surfactant in S configuration optimized in water at the wB97-XD/def2-SVP level of theory.

S	-5.08485	-1.77316	-0.16247
O	-4.69635	-3.20273	-0.10131
O	-6.10874	-1.49198	-1.19770
O	-5.42404	-1.20457	1.16292
C	-3.60640	-0.89420	-0.69726
H	-3.86803	0.17520	-0.70618
H	-2.85016	-1.04944	0.08561
C	-3.10743	-1.36412	-2.05450
H	-3.89604	-1.20888	-2.80682
H	-2.91166	-2.44713	-2.01280
C	-1.85616	-0.64397	-2.51406
H	-1.57563	-0.97472	-3.52989
H	-2.03066	0.44608	-2.54803
O	-0.80671	-0.92613	-1.59739
C	0.27006	-0.09400	-1.62859
C	1.18023	-0.15268	-2.71513
H	0.98421	-0.85372	-3.52888
C	2.29820	0.64060	-2.72036
H	3.01119	0.58174	-3.54595
C	2.55983	1.53321	-1.64523
C	3.73673	2.32988	-1.60718
H	4.44583	2.25747	-2.43549
C	3.98852	3.16502	-0.54560
H	4.89927	3.76708	-0.52335
C	3.06205	3.25113	0.52250
H	3.26262	3.92428	1.35885
C	1.91550	2.49306	0.51345
H	1.20567	2.56287	1.34031
C	1.63784	1.60199	-0.56083
C	0.48090	0.76408	-0.56786
C	-0.48072	0.76422	0.56801
C	-1.63769	1.60210	0.56064
C	-1.91527	2.49287	-0.51392
H	-1.20536	2.56246	-1.34073
C	-3.06184	3.25090	-0.52329

H	-3.26234	3.92381	-1.35984
C	-3.98840	3.16507	0.54475
H	-4.89916	3.76710	0.52225
C	-3.73670	2.33024	1.60658
H	-4.44588	2.25803	2.43484
C	-2.55980	1.53358	1.64496
C	-2.29828	0.64123	2.72033
H	-3.01136	0.58258	3.54586
C	-1.18032	-0.15206	2.71539
H	-0.98435	-0.85293	3.52931
C	-0.27002	-0.09363	1.62893
O	0.80671	-0.92586	1.59813
C	1.85644	-0.64282	2.51423
H	2.03082	0.44728	2.54724
H	1.57626	-0.97275	3.53041
C	3.10768	-1.36316	2.05487
H	2.91197	-2.44621	2.01390
H	3.89643	-1.20739	2.80694
C	3.60635	-0.89406	0.69725
H	2.84992	-1.04972	-0.08536
H	3.86802	0.17534	0.70548
S	5.08465	-1.77337	0.16264
O	5.42368	-1.20539	-1.16305
O	6.10867	-1.49178	1.19762
O	4.69601	-3.20294	0.10217

References

1. Albinsson, B.; Mårtensson, J., Long-range electron and excitation energy transfer in donor–bridge–acceptor systems. *J. Photochem. Photobiol. C* **2008,** *9*, 138-155.

2. Barbara, P. F.; Meyer, T. J.; Ratner, M. A., Contemporary Issues in Electron Transfer Research. *J. Phys. Chem.* **1996,** *100*, 13148-13168.

3. Lin, Z. W.; Lawrence, C. M.; Xiao, D. Q.; Kireev, V. V.; Skourtis, S. S.; Sessler, J. L.; Beratan, D. N.; Rubtsov, I. V., Modulating Unimolecular Charge Transfer by Exciting Bridge Vibrations. *J. Am. Chem. Soc.* **2009,** *131* (50), 18060-18062.

4. Ma, Z.; Lin, Z. W.; Lawrence, C.; Rubtsov, I. V.; Antoniou, P.; Skourtis, S. S.; Zhang, P.; Beratan, D. N., How can infra-red excitation both accelerate and slow charge transfer in the same molecule? *Chem. Sci.* **2018,** *9* (30), 6395-6405.

5. Yue, Y. K.; Grusenmeyer, T.; Ma, Z.; Zhang, P.; Schmehl, R. H.; Beratan, D. N.; Rubtsov, I. V., Electron transfer rate modulation in a compact Re(I) donor-acceptor complex. *Dalton Trans.* **2015,** *44* (18), 8609-8616.

6. Delor, M.; Scattergood, P. A.; Sazanovich, I. V.; Parker, A. W.; Greetham, G. M.; Meijer, A. J. H. M.; Towrie, M.; Weinstein, J. A., Toward control of electron transfer in donor-acceptor molecules by bond-specific infrared excitation. *Science* **2014,** *346*, 1492-1495.

7. Delor, M.; Keane, T.; Scattergood, P. A.; Sazanovich, I. V.; Greetham, G. M.; Towrie, M.; Meijer, A. J. H. M.; Weinstein, J. A., On the mechanism of vibrational control of light-induced charge transfer in donor–bridge–acceptor assemblies. *Nat. Chem.* **2015,** *7*, 689-695.

8. Scattergood, P. A.; Delor, M.; Sazanovich, I. V.; Bouganov, O. V.; Tikhomirov, S. A.; Stasheuski, A. S.; Parker, A. W.; Greetham, G. M.; Towrie, M.; Davies, E. S.; Meijer, A. J. H. M.; Weinstein, J. A., Electron transfer dynamics and excited state branching in a charge-transfer platinum(II) donor-bridge-acceptor assembly. *Dalton Trans.* **2014,** *43* (47), 17677-17693.

9. Rubtsov, I. V., Shake it off. *Nat. Chem.* **2015,** *7* (9), 683-684.

10. Haque, A.; Al-Balushi, R. A.; Al-Busaidi, I. J.; Muhammad S. Khan; Raithby, P. R., Rise of Conjugated Poly-ynes and Poly(Metalla-ynes): From Design Through

Synthesis to Structure–Property Relationships and Applications. *Chem. Rev.* **2018,** *118*, 8474-8597.

11. Bruce, M. I., Transition Metal Complexes Containing Allenylidene, Cumulenylidene, and Related Ligands. *Chem. Rev.* **1998,** *98* (8), 2797-858.

12. Szafert, S.; Gladysz, J. A., Update 1 of: Carbon in One Dimension: Structural Analysis of the Higher Conjugated Polyynes. *Chem. Rev.* **2006,** *106*, 1-33.

13. Pigulski, B.; Gulia, N.; Szafert, S., Reactivity of Polyynes: Complex Molecules from Simple Carbon Rods. *Eur. J. Org. Chem.* **2019,** (7), 1420-1445.

14. Schull, T. L.; Kushmerick, J. G.; Patterson, C. H.; George, C.; Moore, M. H.; Pollack, S. K.; Shashidhar, R., Ligand Effects on Charge Transport in Platinum(II) Acetylides. *J. Am. Chem. Soc.* **2003,** *125* (11), 3202-3203.

15. Blum, A. S.; Ren, T.; Parish, D. A.; Trammell, S. A.; Moore, M. H.; Kushmerick, J. G.; Xu, G.-L.; Deschamps, J. R.; Pollack, S. K.; Shashidhar, R., $Ru_2(ap)_4$(s-oligo(phenyleneethynyl)) Molecular Wires: Synthesis and Electronic Characterization. *J. Am. Chem. Soc.* **2005,** *127*, 10010-10011.

16. Meng, F. B.; Hervault, Y. M.; Norel, L.; Costuas, K.; Van Dyck, C.; Geskin, V.; Cornil, J.; Hng, H. H.; Rigaut, S.; Chen, X. D., Photo-modulable molecular transport junctions based on organometallic molecular wires. *Chem. Sci.* **2012,** *3* (10), 3113-3118.

17. Tanaka, Y.; Kato, Y.; Tada, T.; Fujii, S.; Kiguchi, M.; Akita, M., "Doping" of Polyyne with an Organometallic Fragment Leads to Highly Conductive Metallapolyyne Molecular Wire. *J. Am. Chem. Soc.* **2018,** *140* (32), 10080-10084.

18. Meng, F. B.; Hervault, Y. M.; Shao, Q.; Hu, B. H.; Norel, L.; Rigaut, S.; Chen, X. D., Orthogonally modulated molecular transport junctions for resettable electronic logic gates. *Nat. Commun.* **2014,** *5*, Art. 3023.

19. Zhu, H.; Pookpanratana, S. J.; Bonevich, J. E.; Natoli, S. N.; Hacker, C. A.; Ren, T.; Suehle, J. S.; Richter, C. A.; Li, Q., Redox-Active Molecular Nanowire Flash Memory for High-Endurance and High-Density Non-Volatile Memory Applications. *ACS Appl. Mater. Interfaces* **2015,** *7*, 27306-27313.

20. Wong, W.-Y.; Ho, C.-L., Organometallic Photovoltaics: A New and Versatile Approach for Harvesting Solar Energy Using Conjugated Polymetallaynes. *Acc. Chem. Res.* **2010,** *43*, 1246-1256.

21. Ho, C.-L.; Yu, Z.-Q.; Wong, W.-Y., Multifunctional polymetallaynes: properties, functions and applications. *Chem. Soc. Rev.* **2016,** *45*, 5264-5295.

22. Bhaskar, A.; Ramakrishna, G.; Lu, Z. K.; Twieg, R.; Hales, J. M.; Hagan, D. J.; Van Stryland, E.; Goodson, T., Investigation of two-photon absorption properties in branched alkene and alkyne chromophores. *J. Am. Chem. Soc.* **2006,** *128* (36), 11840-11849.

23. Williams-Harry, M.; Bhaskar, A.; Rarnakrishna, G.; Goodson, T.; Imamura, M.; Mawatari, A.; Nakao, K.; Enozawa, H.; Nishinaga, T.; Iyoda, M., Giant thienylene-acetylene-ethylene macrocycles with large two-photon absorption cross section and semishape-persistence. *J. Am. Chem. Soc.* **2008,** *130* (11), 3252-3253.

24. Ren, T., A Sustainable Metal Alkynyl Chemistry: 3d Metals and Polyaza Macrocyclic Ligands. *Chem. Commun.* **2016,** *52*, 3271-3279.

25. Banziger, S. D.; Ren, T., Syntheses, Structures and Bonding of 3d Metal Alkynyl Complexes of Cyclam and Its Derivatives. *J. Organomet. Chem.* **2019,** *885*, 39-48.

26. Hoffert, W. A.; Kabir, M. K.; Hill, E. A.; Mueller, S. M.; Shores, M. P., Stepwise acetylide ligand substitution for the assembly of ethynylbenzene-linked Co(III) complexes. *Inorg. Chim. Acta* **2012,** *380*, 174-180.

27. Cook, T. D.; Natoli, S. N.; Fanwick, P. E.; Ren, T., Dimeric Complexes of CoIII(cyclam) with a Polyynediyl Bridge. *Organometallics* **2015,** *34* (4), 686-689.

28. Cook, T. D.; Natoli, S. N.; Fanwick, P. E.; Ren, T., CoIII(cyclam) Oligoynyls: Monomeric Oligoynyl Complexes and Dimeric Complexes with an Oligoyn-diyl Bridge. *Organometallics* **2016,** *35* (9), 1329-1338.

29. Natoli, S. N.; Zeller, M.; Ren, T., Stepwise Synthesis of Bis-Alkynyl CoIII(cyclam) Complexes under Ambient Conditions. *Inorg. Chem.* **2016,** *55*, 5756-5758.

30. Natoli, S. N.; Zeller, M.; Ren, T., An Aerobic Synthetic Approach Toward Bis-Alkynyl Cobalt(III) Compounds. *Inorg. Chem.* **2017,** *56*, 10021-10031.

31. Banziger, S. D.; Cook, T. D.; Natoli, S. N.; Fanwick, P. E.; Ren, T., Synthetic and Structural Studies of Mono-acetylide and Unsymmetric Bis-acetylide Complexes based on CoIII-cyclam. *J. Organomet. Chem.* **2015,** *799-800*, 1-6.

32. Rury, A. S.; Wiley, T. E.; Sension, R. J., Energy Cascades, Excited State Dynamics, and Photochemistry in Cob(III)alamins and Ferric Porphyrins. *Acc. Chem. Res.* **2015,** *48* (3), 860-867.

33. Miller, N. A.; Wiley, T. E.; Spears, K. G.; Ruetz, M.; Kieninger, C.; Krautler, B.; Sension, R. J., Toward the Design of Photoresponsive Conditional Antivitamins B-12: A Transient Absorption Study of an Arylcobalamin and an Alkynylcobalamin. *J. Am. Chem. Soc.* **2016,** *138* (43), 14250-14256.

34. McCusker, J. K.; Walda, K. N.; Magde, D.; Hendrickson, D. N., Picosecond Excited-State Dynamics in Octahedral Cobalt(Iii) Complexes - Intersystem Crossing Versus Internal-Conversion. *Inorg. Chem.* **1993,** *32* (4), 394-399.

35. Pal, A. K.; Li, C. F.; Hanan, G. S.; Zysman-Colman, E., Blue-Emissive Cobalt(III) Complexes and Their Use in the Photocatalytic Trifluoromethylation of Polycyclic Aromatic Hydrocarbons. *Angew. Chem. Int. Ed.* **2018,** *57* (27), 8027-8031.

36. Langford, C. H.; Malkhasian, A. Y. S.; Sharma, D. K., Subnanosecond Transients in the Spectra of Cobalt(Iii) Amine Complexes. *J. Am. Chem. Soc.* **1984,** *106* (9), 2727-2728.

37. Banziger, S. D.; Li, X.; Valdiviezo, J.; Zeller, M.; Zhang, P.; Beratan, D. N.; Rubtsov, I. V.; Ren, T., Unsymmetrical Bis-Alkynyl Complexes Based on Co (III)(cyclam): Synthesis, Ultrafast Charge Separation, and Analysis. *Inorg. Chem.* **2019,** *58* (22), 15487-15497.

38. Yu, H. S.; He, X.; Li, S. L.; Truhlar, D. G., MN15: A Kohn–Sham global-hybrid exchange–correlation density functional with broad accuracy for multi-reference and single-reference systems and noncovalent interactions. *Chem. Sci.* **2016,** *7* (8), 5032-5051.

39. Weigend, F.; Ahlrichs, R., Balanced basis sets of split valence, triple zeta valence and quadruple zeta valence quality for H to Rn: Design and assessment of accuracy. *Phys. Chem. Chem. Phys.* **2005,** *7* (18), 3297-3305.

40. Frisch, M. J.; Trucks, G. W.; Schlegel, H. B.; Scuseria, G. E.; Robb, M. A.; Cheeseman, J. R.; Scalmani, G.; Barone, V.; Petersson, G. A.; Nakatsuji, H.; Li, X.; Caricato, M.; Marenich, A. V.; Bloino, J.; Janesko, B. G.; Gomperts, R.; Mennucci, B.; Hratchian, H. P.; Ortiz, J. V.; Izmaylov, A. F.; Sonnenberg, J. L.; Williams; Ding, F.; Lipparini, F.; Egidi, F.; Goings, J.; Peng, B.; Petrone, A.; Henderson, T.; Ranasinghe, D.; Zakrzewski, V. G.; Gao, J.; Rega, N.; Zheng, G.; Liang, W.; Hada, M.; Ehara, M.; Toyota, K.; Fukuda, R.; Hasegawa, J.; Ishida, M.; Nakajima, T.; Honda, Y.; Kitao, O.; Nakai, H.; Vreven, T.; Throssell, K.; Montgomery Jr., J. A.; Peralta, J. E.; Ogliaro, F.; Bearpark, M. J.; Heyd, J. J.; Brothers, E. N.; Kudin, K. N.; Staroverov, V. N.; Keith, T. A.; Kobayashi, R.; Normand, J.; Raghavachari, K.; Rendell, A. P.; Burant, J. C.; Iyengar, S. S.; Tomasi, J.; Cossi, M.; Millam, J. M.; Klene, M.; Adamo, C.; Cammi, R.;

Ochterski, J. W.; Martin, R. L.; Morokuma, K.; Farkas, O.; Foresman, J. B.; Fox, D. J. *Gaussian 16* Rev. A.03; Gaussian, Inc.: Wallingford, CT, 2016.

41. Scalmani, G.; Frisch, M. J., Continuous surface charge polarizable continuum models of solvation. I. General formalism. *J. Chem. Phys.* **2010,** *132* (11), 114110.

42. Becke, A. D., Density-functional thermochemistry. III. The role of exact exchange. *J. Chem. Phys.* **1993,** *98* (7), 5648-5652.

43. Yanai, T.; Tew, D. P.; Handy, N. C., A new hybrid exchange–correlation functional using the Coulomb-attenuating method (CAM-B3LYP). *Chem. Phys. Lett.* **2004,** *393* (1-3), 51-57.

44. Chai, J.-D.; Head-Gordon, M., Long-range corrected hybrid density functionals with damped atom–atom dispersion corrections. *Phys. Chem. Chem. Phys.* **2008,** *10* (44), 6615-6620.

45. Zhao, Y.; Truhlar, D. G., The M06 suite of density functionals for main group thermochemistry, thermochemical kinetics, noncovalent interactions, excited states, and transition elements: two new functionals and systematic testing of four M06-class functionals and 12 other functionals. *Theor. Chem. Acc.* **2008,** *120* (1), 215-241.

46. Thakker, P. U.; Aru, R. G.; Sun, C.; Pennington, W. T.; Siegfried, A. M.; Marder, E. C.; Wagenknecht, P. S., Synthesis of trans bis-alkynyl complexes of Co(III) supported by a tetradentate macrocyclic amine: A spectroscopic, structural, and electrochemical analysis of pi-interactions and electronic communication in the C equivalent to C-M-C equivalent to C structural unit. *Inorg. Chim. Acta* **2014,** *411*, 158-164.

47. Knutson, J. R.; Walbridge, D. G.; Brand, L., Decay-Associated Fluorescence-Spectra and the Heterogeneous Emission of Alcohol-Dehydrogenase. *Biochemistry* **1982,** *21* (19), 4671-4679.

48. van Stokkum, I. H. M.; Larsen, D. S.; van Grondelle, R., Global and target analysis of time-resolved spectra. *Biochim. Biophys. Acta Bioenergetics* **2004,** *1657* (2-3), 82-104.

49. Sazanovich, I. V.; Best, J.; Scattergood, P. A.; Towrie, M.; Tikhomirov, S. A.; Bouganov, O. V.; Meijer, A.; Weinstein, J. A., Ultrafast photoinduced charge transport in Pt(II) donor-acceptor assembly bearing naphthalimide electron acceptor and phenothiazine electron donor. *Phys. Chem. Chem. Phys.* **2014,** *16* (47), 25775-25788.

50. Castellano, F. N., Transition metal complexes meet the rylenes. *Dalton Trans.* **2012,** *41* (28), 8493-8501.

51. Dixon, D. W.; Thornton, N. B.; Steullet, V.; Netzel, T., Effect of DNA scaffolding on intramolecular electron transfer quenching of a photoexcited ruthenium(II) polypyridine naphthalene diimide. *Inorg. Chem.* **1999,** *38* (24), 5526-5534.

52. Johansson, O.; Wolpher, H.; Borgstrom, M.; Hammarstrom, L.; Bergquist, J.; Sun, L. C.; Akermark, B., Intramolecular charge separation in a hydrogen bonded tyrosine-ruthenium(II)-naphthalene diimide triad. *Chem. Commun.* **2004,** (2), 194-195.

53. McAdam, C. J.; Manning, A. R.; Robinson, B. H.; Simpson, J., Group 8 and 10 metal acetylide naphthalimide dyads. *Inorg. Chim. Acta* **2005,** *358* (5), 1673-1682.

54. Prodi, A.; Chiorboli, C.; Scandola, F.; Iengo, E.; Alessio, E.; Dobrawa, R.; Wurthner, F., Wavelength-dependent electron and energy transfer pathways in a side-to-face ruthenium porphyrin/perylene bisimide assembly. *J. Am. Chem. Soc.* **2005,** *127* (5), 1454-1462.

55. Sazanovich, I. V.; Alamiry, M. A. H.; Best, J.; Bennett, R. D.; Bouganov, O. V.; Davies, E. S.; Grivin, V. P.; Meijer, A.; Plyusnin, V. F.; Ronayne, K. L.; Shelton, A. H.; Tikhomirov, S. A.; Towrie, M.; Weinstein, J. A., Excited State Dynamics of a Pt-II Diimine Complex bearing a Naphthalene-Diimide Electron Acceptor. *Inorg. Chem.* **2008,** *47* (22), 10432-10445.

56. Sazanovich, I. V.; Alamiry, M. A. H.; Meijer, A.; Towrie, M.; Davies, E. S.; Bennett, R. D.; Weinstein, J. A., Photoinduced charge separation in a Pt-II acetylide donor-acceptor triad based on 2-(1-pyrazole)-pyridine modified with naphthalene mono-imide electron acceptor. *Pure Appl. Chem.* **2013,** *85* (7), 1331-1348.

57. Duncan, T. V.; Ghoroghchian, P. P.; Rubtsov, I. V.; Hammer, D. A.; Therien, M. J., Ultrafast excited-state dynamics of nanoscale near-infrared emissive polymersomes. *J. Am. Chem. Soc.* **2008,** *130* (30), 9773-9784.

58. Shan, B.; Nayak, A.; Williams, O. F.; Yost, D. C.; Polizzi, N. F.; Liu, Y.; Zhou, N.; Kanai, Y.; Moran, A. M.; Therien, M. J.; Meyer, T. J., Excitation energy-dependent photocurrent switching in a single-molecule photodiode. *Proc. Natl. Acad. Sci. U.S.A.* **2019,** *116* (33), 16198-16203.

59. Shi, Y.; Frattarelli, D.; Watanabe, N.; Facchetti, A.; Cariati, E.; Righetto, S.; Tordin, E.; Zuccaccia, C.; Macchioni, A.; Wegener, S. L.; Stern, C. L.; Ratner, M. A.; Marks, T. J., Ultra-High-Response, Multiply Twisted Electro-optic Chromophores:

Influence of π-System Elongation and Interplanar Torsion on Hyperpolarizability. *J. Am. Chem. Soc.* **2015,** *137* (39), 12521-12538.

60. Bai, Y. S.; Rawson, J.; Roget, S. A.; Olivier, J. H.; Lin, J. X.; Zhang, P.; Beratan, D. N.; Therien, M. J., Controlling the excited-state dynamics of low band gap, near-infrared absorbers via proquinoidal unit electronic structural modulation. *Chem. Sci.* **2017,** *8* (9), 5889-5901.

61. Fenenko, L.; Shao, G.; Orita, A.; Yahiro, M.; Otera, J.; Svechnikov, S.; Adachi, C., Electrical properties of 1,4-bis(4-(phenylethynyl)phenylethynyl)benzene and its application for organic light emitting diodes. *Chem. Commun.* **2007,** (22), 2278-2280.

62. Nayak, A.; Park, J.; De Mey, K.; Hu, X. Q.; Duncan, T. V.; Beratan, D. N.; Clays, K.; Therien, M. J., Large Hyperpolarizabilities at Telecommunication-Relevant Wavelengths in Donor-Acceptor-Donor Nonlinear Optical Chromophores. *ACS Cent. Sci.* **2016,** *2* (12), 954-966.

63. Kang, Y. K.; Zhang, P.; Rubtsov, I. V.; Zheng, J. R.; Bullard, G.; Beratan, D. N.; Therien, M. J., Orientational Dependence of Cofacial Porphyrin-Quinone Electronic Interactions within the Strong Coupling Regime. *J. Phys. Chem. B* **2019,** *123* (49), 10456-10462.

64. Polizzi, N. F.; Jiang, T.; Beratan, D. N.; Therien, M. J., Engineering opposite electronic polarization of singlet and triplet states increases the yield of high-energy photoproducts. *Proc. Natl. Acad. Sci. U.S.A.* **2019,** *116* (29), 14465-14470.

65. Dumur, F.; Gautier, N.; Gallego-Planas, N.; Şahin, Y.; Levillain, E.; Mercier, N.; Hudhomme, P.; Masino, M.; Girlando, A.; Lloveras, V.; Vidal-Gancedo, J.; Veciana, J.; Rovira, C., Novel Fused D−A Dyad and A−D−A Triad Incorporating Tetrathiafulvalene and p-Benzoquinone. *J. Org. Chem.* **2004,** *69* (6), 2164-2177.

66. Heitzer, H. M.; Marks, T. J.; Ratner, M. A., Molecular Donor–Bridge–Acceptor Strategies for High-Capacitance Organic Dielectric Materials. *J. Am. Chem. Soc.* **2015,** *137* (22), 7189-7196.

67. Kandhadi, J.; Yeduru, V.; Bangal, P. R.; Giribabu, L., Corrole–ferrocene and corrole–anthraquinone dyads: synthesis, spectroscopy and photochemistry. *Phys. Chem. Chem. Phys.* **2015,** *17* (40), 26607-26620.

68. Kirketerp, M.-B. S.; Petersen, M. Å.; Wanko, M.; Zettergren, H.; Rubio, A.; Nielsen, M. B.; Nielsen, S. B., Double-Bond versus Triple-Bond Bridges: Does it Matter

for the Charge-Transfer Absorption by Donor–Acceptor Chromophores? *ChemPhysChem* **2010,** *11* (12), 2495-2498.

69. Van Dyck, C.; Ratner, M. A., Molecular Rectifiers: A New Design Based on Asymmetric Anchoring Moieties. *Nano Lett.* **2015,** *15* (3), 1577-1584.

70. Yamazaki, Y.; Umemoto, A.; Ishitani, O., Photochemical hydrogenation of π-conjugated bridging ligands in photofunctional multinuclear complexes. *Inorg. Chem.* **2016,** *55* (21), 11110-11124.

71. Dickson-Karn, N. M.; Olson, C. M.; Leu, W. C. W.; Hartley, C. S., Intramolecular charge transfer in donor-bridge-acceptor compounds with paired linearly conjugated or cross-conjugated pathways. *J. Phys. Org. Chem.* **2014,** *27* (8), 661-669.

72. Hoffman, D. P.; Lee, O. P.; Millstone, J. E.; Chen, M. S.; Su, T. A.; Creelman, M.; Fréchet, J. M. J.; Mathies, R. A., Electron Transfer Dynamics of Triphenylamine Dyes Bound to TiO2 Nanoparticles from Femtosecond Stimulated Raman Spectroscopy. *J. Phys. Chem. C* **2013,** *117* (14), 6990-6997.

73. Ricks, A. B.; Brown, K. E.; Wenninger, M.; Karlen, S. D.; Berlin, Y. A.; Co, D. T.; Wasielewski, M. R., Exponential Distance Dependence of Photoinitiated Stepwise Electron Transfer in Donor–Bridge–Acceptor Molecules: Implications for Wirelike Behavior. *J. Am. Chem. Soc.* **2012,** *134* (10), 4581-4588.

74. Ricks, A. B.; Solomon, G. C.; Colvin, M. T.; Scott, A. M.; Chen, K.; Ratner, M. A.; Wasielewski, M. R., Controlling Electron Transfer in Donor−Bridge−Acceptor Molecules Using Cross-Conjugated Bridges. *J. Am. Chem. Soc.* **2010,** *132* (43), 15427-15434.

75. Kivala, M.; Diederich, F., Acetylene-Derived Strong Organic Acceptors for Planar and Nonplanar Push−Pull Chromophores. *Acc. Chem. Res.* **2009,** *42* (2), 235-248.

76. Priyadarshy, S.; Therien, M. J.; Beratan, D. N., Acetylenyl-linked, porphyrin-bridged, donor-acceptor molecules: A theoretical analysis of the molecular first hyperpolarizability in highly conjugated push-pull chromophore structures. *J. Am. Chem. Soc.* **1996,** *118* (6), 1504-1510.

77. Rizzuto, F. J.; Hua, C.; Chan, B.; Faust, T. B.; Rawal, A.; Leong, C. F.; Hook, J. M.; Kepert, C. J.; D'Alessandro, D. M., The electronic, optical and magnetic consequences of delocalization in multifunctional donor–acceptor organic polymers. *Phys. Chem. Chem. Phys.* **2015,** *17* (17), 11252-11259.

78. Van Dyck, C.; Marks, T. J.; Ratner, M. A., Chain Length Dependence of the Dielectric Constant and Polarizability in Conjugated Organic Thin Films. *ACS Nano* **2017,** *11* (6), 5970-5981.

79. Wang, R. B.; Brugh, A. M.; Rawson, J.; Therien, M. J.; Forbes, M. D. E., Alkyne-Bridged Multi Copper(II) Porphyrin Structures: Nuances of Orbital Symmetry in Long-Range, Through-Bond Mediated, Isotropic Spin Exchange Interactions. *J. Am. Chem. Soc.* **2017,** *139* (29), 9759-9762.

80. Smith, M. E.; Flynn, E. L.; Fox, M. A.; Trottier, A.; Wrede, E.; Yufit, D. S.; Howard, J. A. K.; Ronayne, K. L.; Towrie, M.; Parker, A. W.; Hartl, F.; Low, P. J., Facile photoinduced charge separation through a cyanoacetylide bridge in a heterobimetallic Fe(ii)–Re(i) complex. *Chem. Commun.* **2008,** (44), 5845-5847.

81. Hoffmann, M.; Karnbratt, J.; Chang, M. H.; Herz, L. M.; Albinsson, B.; Anderson, H. L., Enhanced pi conjugation around a porphyrin 6 nanoring. *Angew. Chem. Int. Ed.* **2008,** *47* (27), 4993-4996.

82. Leu, W. C. W.; Fritz, A. E.; Digianantonio, K. M.; Hartley, C. S., Push–Pull Macrocycles: Donor–Acceptor Compounds with Paired Linearly Conjugated or Cross-Conjugated Pathways. *J. Org. Chem.* **2012,** *77* (5), 2285-2298.

83. Leu, W. C. W.; Hartley, C. S., A Push–Pull Macrocycle With Both Linearly Conjugated and Cross-Conjugated Bridges. *Org. Lett.* **2013,** *15* (14), 3762-3765.

84. Nilsson, D.; Watcharinyanon, S.; Eng, M.; Li, L.; Moons, E.; Johansson, L. S. O.; Zharnikov, M.; Shaporenko, A.; Albinsson, B.; Mårtensson, J., Characterization of Self-Assembled Monolayers of Oligo(phenyleneethynylene) Derivatives of Varying Shapes on Gold: Effect of Laterally Extended π-Systems. *Langmuir* **2007,** *23* (11), 6170-6181.

85. Heckmann, A.; Lambert, C., Organic Mixed-Valence Compounds: A Playground for Electrons and Holes. *Angew. Chem. Int. Ed.* **2012,** *51* (2), 326-392.

86. Göransson, E.; Emanuelsson, R.; Jorner, K.; Markle, T. F.; Hammarström, L.; Ottosson, H., Charge transfer through cross-hyperconjugated versus cross-π-conjugated bridges: an intervalence charge transfer study. *Chem. Sci.* **2013,** *4* (9), 3522-3532.

87. Winters, M. U.; Kärnbratt, J.; Eng, M.; Wilson, C. J.; Anderson, H. L.; Albinsson, B., Photophysics of a Butadiyne-Linked Porphyrin Dimer: Influence of Conformational Flexibility in the Ground and First Singlet Excited State. *J. Phys. Chem. C* **2007,** *111* (19), 7192-7199.

88. Pati, A. K.; Gharpure, S. J.; Mishra, A. K., White Light Emission in Butadiyne Bridged Pyrene–Phenyl Hybrid Fluorophore: Understanding the Photophysical Importance of Diyne Spacer and Utilizing the Excited-State Photophysics for Vapor Detection. *J. Phys. Chem. A* **2016,** *120* (29), 5838-5847.

89. Pati, A. K.; Mohapatra, M.; Ghosh, P.; Gharpure, S. J.; Mishra, A. K., Deciphering the Photophysical Role of Conjugated Diyne in Butadiynyl Fluorophores: Synthesis, Photophysical and Theoretical Study. *J. Phys. Chem. A* **2013,** *117* (30), 6548-6560.

90. Pati, A. K.; Gharpure, S. J.; Mishra, A. K., Substituted diphenyl butadiynes: a computational study of geometries and electronic transitions using DFT/TD-DFT. *Phys. Chem. Chem. Phys.* **2014,** *16* (27), 14015-14028.

91. Tait, C. E.; Neuhaus, P.; Peeks, M. D.; Anderson, H. L.; Timmel, C. R., Excitation wavelength-dependent EPR study on the influence of the conformation of multiporphyrin arrays on triplet state delocalization. *Phys. Chem. Chem. Phys.* **2016,** *18* (7), 5275-5280.

92. Winters, M. U.; Karnbratt, J.; Blades, H. E.; Wilson, C. J.; Frampton, M. J.; Anderson, H. L.; Albinsson, B., Control of electron transfer in a conjugated porphyrin dimer by selective excitation of planar and perpendicular conformers. *Chem. Eur. J.* **2007,** *13* (26), 7385-7394.

93. Albinsson, B.; Eng, M. P.; Pettersson, K.; Winters, M. U., Electron and energy transfer in donor–acceptor systems with conjugated molecular bridges. *Phys. Chem. Chem. Phys.* **2007,** *9* (44), 5847-5864.

94. Daub, J.; Engl, R.; Kurzawa, J.; Miller, S. E.; Schneider, S.; Stockmann, A.; Wasielewski, M. R., Competition between Conformational Relaxation and Intramolecular Electron Transfer within Phenothiazine−Pyrene Dyads. *J. Phys. Chem. A* **2001,** *105* (23), 5655-5665.

95. Davis, W. B.; Ratner, M. A.; Wasielewski, M. R., Conformational Gating of Long Distance Electron Transfer through Wire-like Bridges in Donor−Bridge−Acceptor Molecules. *J. Am. Chem. Soc.* **2001,** *123* (32), 7877-7886.

96. Wenger, O. S., Photoinduced electron and energy transfer in phenylene oligomers. *Chem. Soc. Rev.* **2011,** *40* (7), 3538-3550.

97. Valdiviezo, J.; Palma, J. L., Molecular Rectification Enhancement Based On Conformational and Chemical Modifications. *J. Phys. Chem. C* **2018,** *122* (4), 2053-2063.

98. Rubtsov, I. V.; Redmore, N. P.; Hochstrasser, R. M.; Therien, M. J., Interrogating conformationally dependent electron transfer dynamics via ultrafast visible pump / IR probe spectroscopy. *J. Am. Chem. Soc.* **2004,** *126* (9), 2684-2685.

99. Benniston, A. C.; Harriman, A.; Li, P.; Patel, P. V.; Sams, C. A., The effect of torsion angle on the rate of intramolecular triplet energy transfer. *Phys. Chem. Chem. Phys.* **2005,** *7* (21), 3677-3679.

100. Marcus, R. A.; Sutin, N., Electron transfers in chemistry and biology. *Biochim. Biophys. Acta* **1985,** *811* (3), 265-322.

101. Beratan, D. N.; Skourtis, S. S.; Balabin, I. A.; Balaeff, A.; Keinan, S.; Venkatramani, R.; Xiao, D., Steering electrons on moving pathways. *Acc. Chem. Res.* **2009,** *42*, 1669-1678.

102. Beratan, D. N.; Liu, C.; Migliore, A.; Polizzi, N. F.; Skourtis, S. S.; Zhang, P.; Zhang, Y., Charge transfer in dynamical biosystems, or the treachery of (static) images. *Acc. Chem. Res.* **2015,** *48* (2), 474-481.

103. Skourtis, S. S.; Waldeck, D. H.; Beratan, D. N., Fluctuations in Biological and Bioinspired Electron-Transfer Reactions. *Ann. Rev. Phys. Chem.* **2010,** *61*, 461-485.

104. Eng, M. P.; Albinsson, B., The dependence of the electronic coupling on energy gap and bridge conformation – Towards prediction of the distance dependence of electron transfer reactions. *Chem. Phys.* **2009,** *357* (1), 132-139.

105. Blumberger, J., Recent advances in the theory and molecular simulation of biological electron transfer reactions. *Chem. Rev.* **2015,** *115* (20), 11191-11238.

106. Oberhofer, H.; Reuter, K.; Blumberger, J., Charge Transport in Molecular Materials: An Assessment of Computational Methods. *Chem. Rev.* **2017,** *117* (15), 10319-10357.

107. Jiang, F.; Trupp, D. I.; Algethami, N.; Zheng, H.; He, W.; Alqorashi, A.; Zhu, C.; Tang, C.; Li, R.; Liu, J.; Sadeghi, H.; Shi, J.; Davidson, R.; Korb, M.; Sobolev, A. N.; Naher, M.; Sangtarash, S.; Low, P. J.; Hong, W.; Lambert, C. J., Turning the Tap: Conformational Control of Quantum Interference to Modulate Single-Molecule Conductance. *Angew. Chem. Int. Ed.* **2019,** *58* (52), 18987-18993.

108. Lin, Z.; Lawrence, C. M.; Xiao, D.; Kireev, V. V.; Skourtis, S. S.; Sessler, J. L.; Beratan, D. N.; Rubtsov, I. V., Modulating unimolecular charge transfer by exciting bridge vibrations. *J. Am. Chem. Soc.* **2009,** *131* (50), 18060-2.

109. Rubtsov, I. V.; Kang, Y. K.; Redmore, N. P.; Allen, R. M.; Zheng, J. R.; Beratan, D. N.; Therien, M. J., The degree of charge transfer in ground and charge-separated states revealed by ultrafast visible pump/mid-IR probe spectroscopy. *J. Am. Chem. Soc.* **2004,** *126* (16), 5022-5023.

110. Fayer, M. D., *Elements of quantum mechanics*. Oxford University Press: 2001; p 356.

111. Li, X.; Valdiviezo, J.; Banziger, S. D.; Zhang, P.; Ren, T.; Beratan, D. N.; Rubtsov, I. V., Symmetry controlled photo-selection and charge separation in butadiyne-bridged donor–bridge–acceptor compounds. *Phys. Chem. Chem. Phys.* **2020,** *22* (17), 9664-9676.

112. Baboul, A. G.; Schlegel, H. B., Improved method for calculating projected frequencies along a reaction path. *J. Chem. Phys.* **1997,** *107* (22), 9413-9417.

113. Cave, R. J.; Newton, M. D., Generalization of the Mulliken-Hush treatment for the calculation of electron transfer matrix elements. *Chem. Phys. Lett.* **1996,** *249* (1), 15-19.

114. Aidas, K.; Angeli, C.; Bak, K. L.; Bakken, V.; Bast, R.; Boman, L.; Christiansen, O.; Cimiraglia, R.; Coriani, S.; Dahle, P.; Dalskov, E. K.; Ekström, U.; Enevoldsen, T.; Eriksen, J. J.; Ettenhuber, P.; Fernández, B.; Ferrighi, L.; Fliegl, H.; Frediani, L.; Hald, K.; Halkier, A.; Hättig, C.; Heiberg, H.; Helgaker, T.; Hennum, A. C.; Hettema, H.; Hjertenæs, E.; Høst, S.; Høyvik, I.-M.; Iozzi, M. F.; Jansík, B.; Jensen, H. J. A.; Jonsson, D.; Jørgensen, P.; Kauczor, J.; Kirpekar, S.; Kjærgaard, T.; Klopper, W.; Knecht, S.; Kobayashi, R.; Koch, H.; Kongsted, J.; Krapp, A.; Kristensen, K.; Ligabue, A.; Lutnæs, O. B.; Melo, J. I.; Mikkelsen, K. V.; Myhre, R. H.; Neiss, C.; Nielsen, C. B.; Norman, P.; Olsen, J.; Olsen, J. M. H.; Osted, A.; Packer, M. J.; Pawlowski, F.; Pedersen, T. B.; Provasi, P. F.; Reine, S.; Rinkevicius, Z.; Ruden, T. A.; Ruud, K.; Rybkin, V. V.; Sałek, P.; Samson, C. C. M.; de Merás, A. S.; Saue, T.; Sauer, S. P. A.; Schimmelpfennig, B.; Sneskov, K.; Steindal, A. H.; Sylvester-Hvid, K. O.; Taylor, P. R.; Teale, A. M.; Tellgren, E. I.; Tew, D. P.; Thorvaldsen, A. J.; Thøgersen, L.; Vahtras, O.; Watson, M. A.; Wilson, D. J. D.; Ziolkowski, M.; Ågren, H., The Dalton quantum chemistry program system. *WIREs Comput. Mol. Sci.* **2014,** *4* (3), 269-284.

115. Peeks, M. D.; Neuhaus, P.; Anderson, H. L., Experimental and computational evaluation of the barrier to torsional rotation in a butadiyne-linked porphyrin dimer. *Phys. Chem. Chem. Phys.* **2016,** *18*, 5264-5274.

116. Martin, R. L., Natural transition orbitals. *J. Chem. Phys.* **2003,** *118* (11), 4775-4777.

117. Xiao, D. Q.; Skourtis, S. S.; Rubtsov, I. V.; Beratan, D. N., Turning Charge Transfer On and Off in a Molecular Interferometer with Vibronic Pathways. *Nano Lett.* **2009,** *9* (5), 1818-1823.

118. Delor, M.; Archer, S. A.; Keane, T.; Meijer, A.; Sazanovich, I. V.; Greetham, G. M.; Towrie, M.; Weinstein, J. A., Directing the path of light-induced electron transfer at a molecular fork using vibrational excitation. *Nat. Chem.* **2017,** *9* (11), 1099-1104.

119. Delor, M.; Scattergood, P. A.; Sazanovich, I. V.; Parker, A. W.; Greetham, G. M.; Meijer, A.; Towrie, M.; Weinstein, J. A., Toward control of electron transfer in donor-acceptor molecules by bond-specific infrared excitation. *Science* **2014,** *346* (6216), 1492-1495.

120. Bhattacharyya, P.; Fleming, G. R., Quantum Ratcheted Photophysics in Energy Transport. *J. Phys. Chem. Lett.* **2020**.

121. Fletcher, J. T.; Therien, M. J., Extreme electronic modulation of the cofacial porphyrin structural motif. *J. Am. Chem. Soc.* **2002,** *124* (16), 4298-4311.

122. Christiansen, O.; Koch, H.; Jørgensen, P., The second-order approximate coupled cluster singles and doubles model CC2. *Chem. Phys. Lett.* **1995,** *243* (5-6), 409-418.

123. TURBOMOLE V7.5.1 2021, a development of University of Karlsruhe and Forschungszentrum Karlsruhe GmbH, 1989-2007, TURBOMOLE GmbH, since 2007; available from https://www.turbomole.org.

124. Balasubramani, S. G.; Chen, G. P.; Coriani, S.; Diedenhofen, M.; Frank, M. S.; Franzke, Y. J.; Furche, F.; Grotjahn, R.; Harding, M. E.; Hättig, C., TURBOMOLE: Modular program suite for ab initio quantum-chemical and condensed-matter simulations. *J. Chem. Phys.* **2020,** *152* (18), 184107.

125. Grimme, S.; Ehrlich, S.; Goerigk, L., Effect of the damping function in dispersion corrected density functional theory. *J. Comput. Chem.* **2011,** *32* (7), 1456-1465.

126. Shao, Y.; Gan, Z.; Epifanovsky, E.; Gilbert, A. T.; Wormit, M.; Kussmann, J.; Lange, A. W.; Behn, A.; Deng, J.; Feng, X., Advances in molecular quantum chemistry contained in the Q-Chem 4 program package. *Mol. Phys.* **2015,** *113* (2), 184-215.

127. Subotnik, J. E.; Cave, R. J.; Steele, R. P.; Shenvi, N., The initial and final states of electron and energy transfer processes: Diabatization as motivated by system-solvent interactions. *J. Chem. Phys.* **2009,** *130* (23), 234102.

128. Hsu, C.-P.; You, Z.-Q.; Chen, H.-C., Characterization of the short-range couplings in excitation energy transfer. *J. Phys. Chem. C* **2008,** *112* (4), 1204-1212.

129. Giovanelli, L.; Lee, H.-L.; Lacaze-Dufaure, C.; Koudia, M.; Clair, S.; Lin, Y.-P.; Ksari, Y.; Themlin, J.-M.; Abel, M.; Cafolla, A. A., Electronic structure of tetra (4-aminophenyl) porphyrin studied by photoemission, UV–Vis spectroscopy and density functional theory. *J. Electron Spectrosc. Relat. Phenom.* **2017,** *218*, 40-45.

130. Roy, P. P.; Shee, J.; Arsenault, E. A.; Yoneda, Y.; Feuling, K.; Head-Gordon, M.; Fleming, G. R., Solvent mediated excited state proton transfer in Indigo Carmine. *J. Phys. Chem. Lett.* **2020,** *11* (10), 4156-4162.

131. Genereux, J. C.; Barton, J. K., Mechanisms for DNA charge transport. *Chem. Rev.* **2010,** *110* (3), 1642-1662.

132. Lewis, F. D.; Young, R. M.; Wasielewski, M. R., Tracking photoinduced charge separation in DNA: from start to finish. *Acc. Chem. Res.* **2018,** *51* (8), 1746-1754.

133. Lewis, F. D.; Wu, T.; Zhang, Y.; Letsinger, R. L.; Greenfield, S. R.; Wasielewski, M. R., Distance-dependent electron transfer in DNA hairpins. *Science* **1997,** *277* (5326), 673-676.

134. Fink, H.-W.; Schönenberger, C., Electrical conduction through DNA molecules. *Nature* **1999,** *398* (6726), 407-410.

135. Kelley, S. O.; Jackson, N. M.; Hill, M. G.; Barton, J. K., Long-range electron transfer through DNA films. *Angew. Chem. Int. Ed.* **1999,** *38* (7), 941-945.

136. Giese, B.; Amaudrut, J.; Köhler, A.-K.; Spormann, M.; Wessely, S., Direct observation of hole transfer through DNA by hopping between adenine bases and by tunnelling. *Nature* **2001,** *412* (6844), 318-320.

137. Xu, B.; Zhang, P.; Li, X.; Tao, N., Direct conductance measurement of single DNA molecules in aqueous solution. *Nano Lett.* **2004,** *4* (6), 1105-1108.

138. Risser, S. M.; Beratan, D. N.; Meade, T. J., Electron transfer in DNA: predictions of exponential growth and decay of coupling with donor-acceptor distance. *J. Am. Chem. Soc.* **1993,** *115* (6), 2508-2510.

139. Jortner, J.; Bixon, M.; Langenbacher, T.; Michel-Beyerle, M. E., Charge transfer and transport in DNA. *Proc. Natl. Acad. Sci. U.S.A.* **1998,** *95* (22), 12759-12765.

140. Renaud, N.; Berlin, Y. A.; Lewis, F. D.; Ratner, M. A., Between superexchange and hopping: An intermediate charge-transfer mechanism in poly (A)-poly (T) DNA hairpins. *J. Am. Chem. Soc.* **2013,** *135* (10), 3953-3963.

141. Beratan, D. N., Why are DNA and protein electron transfer so different? *Annu. Rev. Phys. Chem.* **2019,** *70*, 71-97.

142. Korol, R.; Segal, D., From exhaustive simulations to key principles in DNA nanoelectronics. *J. Phys. Chem. C* **2018,** *122* (8), 4206-4216.

143. Beratan, D. N.; Priyadarshy, S.; Risser, S. M., DNA: insulator or wire? *Chem. Biol.* **1997,** *4* (1), 3-8.

144. Priyadarshy, S.; Risser, S.; Beratan, D., DNA is not a molecular wire: protein-like electron-transfer predicted for an extended π-electron system. *J. Phys. Chem.* **1996,** *100* (44), 17678-17682.

145. Teo, R. D.; Rousseau, B. J.; Smithwick, E. R.; Di Felice, R.; Beratan, D. N.; Migliore, A., Charge transfer between [4Fe4S] proteins and DNA is unidirectional: Implications for biomolecular signaling. *Chem* **2019,** *5* (1), 122-137.

146. Kilgour, M.; Segal, D., Charge transport in molecular junctions: From tunneling to hopping with the probe technique. *J. Chem. Phys.* **2015,** *143* (2), 024111.

147. Berlin, Y. A.; Burin, A. L.; Ratner, M. A., Charge hopping in DNA. *J. Am. Chem. Soc.* **2001,** *123* (2), 260-268.

148. Berlin, Y. A.; Kurnikov, I. V.; Beratan, D.; Ratner, M. A.; Burin, A. L., DNA electron transfer processes: Some theoretical notions. In *Long-Range Charge Transfer in DNA II*, Schuster, G. B., Ed. Springer: Berlin, 2004; pp 1-36.

149. Venkatramani, R.; Davis, K. L.; Wierzbinski, E.; Bezer, S.; Balaeff, A.; Keinan, S.; Paul, A.; Kocsis, L.; Beratan, D. N.; Achim, C., Evidence for a near-resonant charge transfer mechanism for double-stranded peptide nucleic acid. *J. Am. Chem. Soc.* **2011,** *133* (1), 62-72.

150. Xiang, L.; Palma, J. L.; Bruot, C.; Mujica, V.; Ratner, M. A.; Tao, N., Intermediate tunnelling–hopping regime in DNA charge transport. *Nat. Chem.* **2015,** *7* (3), 221.

151. Michaeli, K.; Beratan, D. N.; Waldeck, D. H.; Naaman, R., Voltage-induced long-range coherent electron transfer through organic molecules. *Proc. Natl. Acad. Sci. U.S.A.* **2019,** *116* (13), 5931-5936.

152. Buttiker, M., Coherent and sequential tunneling in series barriers. *IBM J. Res. Dev.* **1988,** *32* (1), 63-75.

153. Di Felice, R.; Calzolari, A.; Molinari, E.; Garbesi, A., Ab initio study of model guanine assemblies: The role of $\pi-\pi$ coupling and band transport. *Phys. Rev. B* **2001,** *65* (4), 045104.

154. Livshits, G. I.; Stern, A.; Rotem, D.; Borovok, N.; Eidelshtein, G.; Migliore, A.; Penzo, E.; Wind, S. J.; Di Felice, R.; Skourtis, S. S., Long-range charge transport in single G-quadruplex DNA molecules. *Nat. Nanotechnol.* **2014,** *9* (12), 1040.

155. Wierzbinski, E.; Venkatramani, R.; Davis, K. L.; Bezer, S.; Kong, J.; Xing, Y.; Borguet, E.; Achim, C.; Beratan, D. N.; Waldeck, D. H., The single-molecule conductance and electrochemical electron-transfer rate are related by a power law. *ACS Nano* **2013,** *7* (6), 5391-5401.

156. Wolak, M. A.; Balaeff, A.; Gutmann, S.; Helmrich, H. J.; Vosloo, R.; Beerbom, M. M.; Wierzbinski, E.; Waldeck, D. H.; Bezer, S.; Achim, C., Electronic structure of self-assembled peptide nucleic acid thin films. *J. Phys. Chem. C* **2011,** *115* (34), 17123-17135.

157. Paul, A.; Bezer, S.; Venkatramani, R.; Kocsis, L.; Wierzbinski, E.; Balaeff, A.; Keinan, S.; Beratan, D. N.; Achim, C.; Waldeck, D. H., Role of nucleobase energetics and nucleobase interactions in single-stranded peptide nucleic acid charge transfer. *J. Am. Chem. Soc.* **2009,** *131* (18), 6498-6507.

158. Beall, E.; Sargun, A.; Ulku, S.; Bae, Y.; Wierzbinski, E.; Clever, C.; Waldeck, D. H.; Achim, C., Molecular conductance of nicked nucleic acid duplexes. *J. Phys. Chem. C* **2018,** *122* (13), 7533-7540.

159. Liu, C.; Xiang, L.; Zhang, Y.; Zhang, P.; Beratan, D. N.; Li, Y.; Tao, N., Engineering nanometre-scale coherence in soft matter. *Nat. Chem.* **2016,** *8* (10), 941-945.

160. Šponer, J.; Leszczyński, J.; Hobza, P., Nature of nucleic acid− base stacking: nonempirical ab initio and empirical potential characterization of 10 stacked base dimers. Comparison of stacked and H-bonded base pairs. *J. Phys. Chem.* **1996,** *100* (13), 5590-5596.

161. Voityuk, A. A., Electronic couplings and on-site energies for hole transfer in DNA: Systematic quantum mechanical/molecular dynamic study. *J. Chem. Phys.* **2008,** *128* (11), 03B608.

162. Hatcher, E.; Balaeff, A.; Keinan, S.; Venkatramani, R.; Beratan, D. N., PNA versus DNA: Effects of structural fluctuations on electronic structure and hole-transport mechanisms. *J. Am. Chem. Soc.* **2008,** *130* (35), 11752-11761.

163. Venkatramani, R.; Keinan, S.; Balaeff, A.; Beratan, D. N., Nucleic acid charge transfer: black, white and gray. *Coord. Chem. Rev.* **2011,** *255* (7-8), 635-648.

164. Wierzbinski, E.; de Leon, A.; Yin, X.; Balaeff, A.; Davis, K. L.; Reppireddy, S.; Venkatramani, R.; Keinan, S.; Ly, D. H.; Madrid, M., Effect of backbone flexibility on charge transfer rates in peptide nucleic acid duplexes. *J. Am. Chem. Soc.* **2012,** *134* (22), 9335-9342.

165. Beall, E.; Ulku, S.; Liu, C.; Wierzbinski, E.; Zhang, Y.; Bae, Y.; Zhang, P.; Achim, C.; Beratan, D. N.; Waldeck, D. H., Effects of the backbone and chemical linker on the molecular conductance of nucleic acid duplexes. *J. Am. Chem. Soc.* **2017,** *139* (19), 6726-6735.

166. Zhang, Y.; Liu, C.; Balaeff, A.; Skourtis, S. S.; Beratan, D. N., Biological charge transfer via flickering resonance. *Proc. Natl. Acad. Sci. U.S.A.* **2014,** *111* (28), 10049-10054.

167. Egholm, M.; Buchardt, O.; Christensen, L.; Behrens, C.; Freier, S. M.; Driver, D. A.; Berg, R. H.; Kim, S. K.; Norden, B.; Nielsen, P. E., PNA hybridizes to complementary oligonucleotides obeying the Watson–Crick hydrogen-bonding rules. *Nature* **1993,** *365* (6446), 566-568.

168. Valdiviezo, J.; Clever, C.; Beall, E.; Pearse, A.; Bae, Y.; Zhang, P.; Achim, C.; Beratan, D. N.; Waldeck, D. H., Delocalization-Assisted Transport through Nucleic Acids in Molecular Junctions. *Biochemistry* **2021,** *60* (17), 1368-1378.

169. Jorgensen, W. L.; Chandrasekhar, J.; Madura, J. D.; Impey, R. W.; Klein, M. L., Comparison of simple potential functions for simulating liquid water. *J. Chem. Phys.* **1983,** *79* (2), 926-935.

170. Huang, J.; MacKerell Jr, A. D., CHARMM36 all-atom additive protein force field: Validation based on comparison to NMR data. *J. Comput. Chem.* **2013,** *34* (25), 2135-2145.

171. Hart, K.; Foloppe, N.; Baker, C. M.; Denning, E. J.; Nilsson, L.; MacKerell Jr, A. D., Optimization of the CHARMM additive force field for DNA: Improved treatment of the BI/BII conformational equilibrium. *J. Chem. Theory Comput.* **2012,** *8* (1), 348-362.

172. Jasiński, M.; Feig, M.; Trylska, J., Improved force fields for peptide nucleic acids with optimized backbone torsion parameters. *J. Chem. Theory Comput.* **2018,** *14* (7), 3603-3620.

173. Darden, T.; York, D.; Pedersen, L., Particle mesh Ewald: An N· log (N) method for Ewald sums in large systems. *J. Chem. Phys.* **1993,** *98* (12), 10089-10092.

174. Phillips, J. C.; Braun, R.; Wang, W.; Gumbart, J.; Tajkhorshid, E.; Villa, E.; Chipot, C.; Skeel, R. D.; Kale, L.; Schulten, K., Scalable molecular dynamics with NAMD. *J. Comput. Chem.* **2005,** *26* (16), 1781-1802.

175. Martyna, G. J.; Tobias, D. J.; Klein, M. L., Constant pressure molecular dynamics algorithms. *J. Chem. Phys.* **1994,** *101* (5), 4177-4189.

176. Feller, S. E.; Zhang, Y.; Pastor, R. W.; Brooks, B. R., Constant pressure molecular dynamics simulation: the Langevin piston method. *J. Chem. Phys.* **1995,** *103* (11), 4613-4621.

177. Pacher, T.; Cederbaum, L.; Köppel, H., Approximately diabatic states from block diagonalization of the electronic Hamiltonian. *J. Chem. Phys.* **1988,** *89* (12), 7367-7381.

178. Ridley, J.; Zerner, M., An intermediate neglect of differential overlap technique for spectroscopy: pyrrole and the azines. *Theoret. Chim. Acta* **1973,** *32* (2), 111-134.

179. Zeng, J.; Hush, N.; Reimers, J., Solvent effects on molecular and ionic spectra. 7. Modeling the absorption and electroabsorption spectra of pentaammine-ruthenium (II) pyrazine and its conjugate acid in water. *J. Am. Chem. Soc.* **1996,** *118* (8), 2059-2068.

180. Voityuk, A. A., Assessment of semiempirical methods for the computation of charge transfer in DNA π-stacks. *Chem. Phys. Lett.* **2006,** *427* (1-3), 177-180.

181. Kubař, T.; Elstner, M., What governs the charge transfer in DNA? The role of DNA conformation and environment. *J. Phys. Chem. B* **2008,** *112* (29), 8788-8798.

182. Kubař, T.; Kleinekathöfer, U.; Elstner, M., Solvent fluctuations drive the hole transfer in DNA: a mixed quantum− classical study. *J. Phys. Chem. B* **2009,** *113* (39), 13107-13117.

183. Boese, A. D., Density functional theory and hydrogen bonds: are we there yet? *ChemPhysChem* **2015,** *16* (5), 978-985.

184. Peverati, R.; Truhlar, D. G., Improving the accuracy of hybrid meta-GGA density functionals by range separation. *J. Phys. Chem. Lett.* **2011,** *2* (21), 2810-2817.

185. Zheng, J.; Xu, X.; Truhlar, D. G., Minimally augmented Karlsruhe basis sets. *Theor. Chem. Acc.* **2011,** *128* (3), 295-305.

186. Humphrey, W.; Dalke, A.; Schulten, K., VMD: visual molecular dynamics. *J. Mol. Graphics* **1996,** *14* (1), 33-38.

187. Tan, B.; Hodak, M.; Lu, W.; Bernholc, J., Charge transport in DNA nanowires connected to carbon nanotubes. *Phys. Rev. B* **2015,** *92* (7), 075429.

188. Neaton, J. B.; Hybertsen, M. S.; Louie, S. G., Renormalization of molecular electronic levels at metal-molecule interfaces. *Phys. Rev. Lett.* **2006,** *97* (21), 216405.

189. Teo, R. D.; Terai, K.; Migliore, A.; Beratan, D. N., Electron transfer characteristics of 2′-deoxy-2′-fluoro-arabinonucleic acid, a nucleic acid with enhanced chemical stability. *Phys. Chem. Chem. Phys.* **2018,** *20* (41), 26063-26067.

190. Roca-Sanjuán, D.; Rubio, M.; Merchán, M.; Serrano-Andrés, L., Ab initio determination of the ionization potentials of DNA and RNA nucleobases. *J. Chem. Phys.* **2006,** *125* (8), 084302.

191. Kawai, K.; Majima, T., Hole transfer kinetics of DNA. *Acc. Chem. Res.* **2013,** *46* (11), 2616-2625.

192. Evers, F.; Korytár, R.; Tewari, S.; van Ruitenbeek, J. M., Advances and challenges in single-molecule electron transport. *Rev. Mod. Phys.* **2020,** *92* (3), 035001.

193. Tivanski, A. V.; He, Y.; Borguet, E.; Liu, H.; Walker, G. C.; Waldeck, D. H., Conjugated thiol linker for enhanced electrical conduction of gold− molecule contacts. *J. Phys. Chem. B* **2005,** *109* (12), 5398-5402.

194. Bruot, C.; Xiang, L.; Palma, J. L.; Tao, N., Effect of mechanical stretching on DNA conductance. *ACS Nano* **2015,** *9* (1), 88-94.

195. Frisenda, R.; Stefani, D.; van der Zant, H. S., Quantum transport through a single conjugated rigid molecule, a mechanical break junction study. *Acc. Chem. Res.* **2018,** *51* (6), 1359-1367.

196. Valdiviezo, J.; Rocha, P.; Polakovsky, A.; Palma, J. L., Nonexponential Length Dependence of Molecular Conductance in Acene-Based Molecular Wires. *ACS Sens.* **2021,** *6* (2), 477-484.

197. Kim, H.; Kilgour, M.; Segal, D., Intermediate Coherent–Incoherent Charge Transport: DNA as a Case Study. *J. Phys. Chem. C* **2016,** *120* (42), 23951-23962.

198. Karasch, P.; Ryndyk, D. A.; Frauenheim, T., Vibronic dephasing model for coherent-to-incoherent crossover in DNA. *Phys. Rev. B* **2018,** *97* (19), 195401.

199. Carey, R.; Chen, L.; Gu, B.; Franco, I., When can time-dependent currents be reproduced by the Landauer steady-state approximation? *J. Chem. Phys.* **2017,** *146* (17), 174101.

200. Jin, Y.; Ru, X.; Su, N. Q.; Mei, Y.; Beratan, D. N.; Zhang, P.; Yang, W., Revisiting the Hole Size in Double Helical DNA with Localized Orbital Scaling Corrections. *J. Phys. Chem. B* **2020,** *124* (16), 3428-3435.

201. Bag, S.; Biswas, T.; Jain, M.; Maiti, P. K., Anisotropic Charge Transport in Nanoscale DNA Wire. *J. Phys. Chem. C* **2020,** *124* (31), 16763-16772.

202. Astumian, R. D., Thermodynamics and kinetics of a Brownian motor. *Science* **1997,** *276* (5314), 917-922.

203. Kitamura, K.; Tokunaga, M.; Iwane, A. H.; Yanagida, T., A single myosin head moves along an actin filament with regular steps of 5.3 nanometres. *Nature* **1999,** *397* (6715), 129-134.

204. Stock, D.; Leslie, A. G.; Walker, J. E., Molecular architecture of the rotary motor in ATP synthase. *Science* **1999,** *286* (5445), 1700-1705.

205. Rice, S.; Lin, A. W.; Safer, D.; Hart, C. L.; Naber, N.; Carragher, B. O.; Cain, S. M.; Pechatnikova, E.; Wilson-Kubalek, E. M.; Whittaker, M., A structural change in the kinesin motor protein that drives motility. *Nature* **1999,** *402* (6763), 778-784.

206. Carter, N. J.; Cross, R., Mechanics of the kinesin step. *Nature* **2005,** *435* (7040), 308-312.

207. Kinbara, K.; Aida, T., Toward intelligent molecular machines: directed motions of biological and artificial molecules and assemblies. *Chem. Rev.* **2005,** *105* (4), 1377-1400.

208. Brown, A. I.; Sivak, D. A., Theory of nonequilibrium free energy transduction by molecular machines. *Chem. Rev.* **2019,** *120* (1), 434-459.

209. Lau, B.; Kedem, O., Electron ratchets: State of the field and future challenges. *J. Chem. Phys.* **2020,** *152* (20), 200901.

210. Zhang, Y.; Zhang, W. B.; Liu, C.; Zhang, P.; Balaeff, A.; Beratan, D. N., DNA charge transport: Moving beyond 1D. *Surf. Sci.* **2016,** *652*, 33-38.

211. Ru, X.; Zhang, P.; Beratan, D. N., Assessing Possible Mechanisms of Micrometer-Scale Electron Transfer in Heme-Free Geobacter sulfurreducens Pili. *J. Phys. Chem. B* **2019,** *123* (24), 5035-5047.

212. Slinker, J. D.; Muren, N. B.; Renfrew, S. E.; Barton, J. K., DNA charge transport over 34 nm. *Nat. Chem.* **2011,** *3* (3), 228-233.

213. Livshits, G. I.; Stern, A.; Rotem, D.; Borovok, N.; Eidelshtein, G.; Migliore, A.; Penzo, E.; Wind, S. J.; Di Felice, R.; Skourtis, S. S., Long-range charge transport in single G-quadruplex DNA molecules. *Nat. Nanotechnol.* **2014,** *9* (12), 1040-1046.

214. Tuccitto, N.; Ferri, V.; Cavazzini, M.; Quici, S.; Zhavnerko, G.; Licciardello, A.; Rampi, M. A., Highly conductive~ 40-nm-long molecular wires assembled by stepwise incorporation of metal centres. *Nat. Mater.* **2009,** *8* (1), 41-46.

215. Jiménez-Monroy, K. L.; Renaud, N.; Drijkoningen, J.; Cortens, D.; Schouteden, K.; Van Haesendonck, C.; Guedens, W. J.; Manca, J. V.; Siebbeles, L. D.; Grozema, F. C., High electronic conductance through double-helix DNA molecules with fullerene anchoring groups. *J. Phys. Chem. A* **2017,** *121* (6), 1182-1188.

216. Lau, B.; Kedem, O.; Ratner, M. A.; Weiss, E. A., Identification of two mechanisms for current production in a biharmonic flashing electron ratchet. *Phys. Rev. E* **2016,** *93* (6), 062128.

217. Valdiviezo, J. s.; Palma, J. L., Molecular rectification enhancement based on conformational and chemical modifications. *J. Phys. Chem. C* **2018,** *122* (4), 2053-2063.

218. Lorke, A.; Wimmer, S.; Jager, B.; Kotthaus, J.; Wegscheider, W.; Bichler, M., Far-infrared and transport properties of antidot arrays with broken symmetry. *Phys. B* **1998,** *249*, 312-316.

219. Song, A.; Omling, P.; Samuelson, L.; Seifert, W.; Shorubalko, I.; Zirath, H., Room-temperature and 50 GHz operation of a functional nanomaterial. *Appl. Phys. Lett.* **2001,** *79* (9), 1357-1359.

220. Linke, H.; Humphrey, T.; Löfgren, A.; Sushkov, A.; Newbury, R.; Taylor, R.; Omling, P., Experimental tunneling ratchets. *Science* **1999,** *286* (5448), 2314-2317.

221. Müller, T.; Würtz, A.; Lorke, A.; Reuter, D.; Wieck, A., Wave-form sampling using a driven electron ratchet in a two-dimensional electron system. *Appl. Phys. Lett.* **2005,** *87* (4), 042104.

222. Tanaka, T.; Nakano, Y.; Kasai, S., GaAs-based nanowire devices with multiple asymmetric gates for electrical Brownian ratchets. *Jpn. J. Appl. Phys.* **2013,** *52* (6S), 06GE07.

223. Roeling, E. M.; Germs, W. C.; Smalbrugge, B.; Geluk, E. J.; De Vries, T.; Janssen, R. A.; Kemerink, M., Organic electronic ratchets doing work. *Nat. Mater.* **2011,** *10* (1), 51-55.

224. Kedem, O.; Lau, B.; Weiss, E. A., Mechanisms of Symmetry Breaking in a Multidimensional Flashing Particle Ratchet. *ACS Nano* **2017,** *11* (7), 7148-7155.

225. Kedem, O.; Lau, B.; Ratner, M. A.; Weiss, E. A., Light-responsive organic flashing electron ratchet. *Proc. Natl. Acad. Sci. U.S.A.* **2017,** *114* (33), 8698-8703.

226. Kedem, O.; Lau, B.; Weiss, E. A., How to drive a flashing electron ratchet to maximize current. *Nano Lett.* **2017,** *17* (9), 5848-5854.

227. Drexler, C.; Tarasenko, S.; Olbrich, P.; Karch, J.; Hirmer, M.; Müller, F.; Gmitra, M.; Fabian, J.; Yakimova, R.; Lara-Avila, S., Magnetic quantum ratchet effect in graphene. *Nat. Nanotechnol.* **2013,** *8* (2), 104-107.

228. Custer, J. P.; Low, J. D.; Hill, D. J.; Teitsworth, T. S.; Christesen, J. D.; McKinney, C. J.; McBride, J. R.; Brooke, M. A.; Warren, S. C.; Cahoon, J. F., Ratcheting quasi-ballistic electrons in silicon geometric diodes at room temperature. *Science* **2020,** *368* (6487), 177-180.

229. Rothemund, P. W., Folding DNA to create nanoscale shapes and patterns. *Nature* **2006,** *440* (7082), 297-302.

230. Ke, Y.; Ong, L. L.; Shih, W. M.; Yin, P., Three-dimensional structures self-assembled from DNA bricks. *Science* **2012,** *338* (6111), 1177-1183.

231. Conron, S. M. M.; Thazhathveetil, A. K.; Wasielewski, M. R.; Burin, A. L.; Lewis, F. D., Direct measurement of the dynamics of hole hopping in extended DNA G-tracts. An unbiased random walk. *J. Am. Chem. Soc.* **2010,** *132* (41), 14388-14390.

232. Fujitsuka, M.; Majima, T., Charge transfer dynamics in DNA revealed by time-resolved spectroscopy. *Chem. Sci.* **2017,** *8* (3), 1752-1762.

233. Seeman, N. C., DNA in a material world. *Nature* **2003,** *421* (6921), 427-431.

234. Seeman, N. C., Nanomaterials based on DNA. *Annu. Rev. Biochem.* **2010,** *79*, 65-87.

235. Wood, B. R., The importance of hydration and DNA conformation in interpreting infrared spectra of cells and tissues. *Chem. Soc. Rev.* **2016,** *45* (7), 1980-1998.

236. Lau, B.; Kedem, O.; Schwabacher, J.; Kwasnieski, D.; Weiss, E. A., An introduction to ratchets in chemistry and biology. *Mater. Horiz.* **2017,** *4* (3), 310-318.

237. Giese, B., Long-distance electron transfer through DNA. *Annu. Rev. Biochem.* **2002,** *71* (1), 51-70.

238. Beratan, D.; Betts, J.; Onuchic, J., Protein electron transfer rates set by the bridging secondary and tertiary structure. *Science* **1991,** *252* (5010), 1285-1288.

239. Prytkova, T. R.; Kurnikov, I. V.; Beratan, D. N., Coupling coherence distinguishes structure sensitivity in protein electron transfer. *Science* **2007,** *315* (5812), 622-625.

240. Zhang, N.; Samanta, S. R.; Rosen, B. M.; Percec, V., Single electron transfer in radical ion and radical-mediated organic, materials and polymer synthesis. *Chem. Rev.* **2014,** *114* (11), 5848-5958.

241. Okada, Y.; Chiba, K., Redox-tag processes: Intramolecular electron transfer and its broad relationship to redox reactions in general. *Chem. Rev.* **2017,** *118* (9), 4592-4630.

242. Balabin, I. A.; Onuchic, J. N., Dynamically controlled protein tunneling paths in photosynthetic reaction centers. *Science* **2000,** *290* (5489), 114-117.

243. Nitzan, A., *Chemical dynamics in condensed phases: relaxation, transfer and reactions in condensed molecular systems*. Oxford University Press: Oxford, U.K., 2006.

244. May, V.; Kühn, O., *Charge and energy transfer dynamics in molecular systems*. 3rd ed.; Wiley-VCH Verlag GmbH & Co. KGaA: Weinheim, Germany, 2011.

245. Malak, R. A.; Gao, Z.; Wishart, J. F.; Isied, S. S., Long-range electron transfer across peptide bridges: The transition from electron superexchange to hopping. *J. Am. Chem. Soc.* **2004,** *126* (43), 13888-13889.

246. Moser, C. C.; Keske, J. M.; Warncke, K.; Farid, R. S.; Dutton, P. L., Nature of biological electron transfer. *Nature* **1992,** *355* (6363), 796-802.

247. Migliore, A.; Polizzi, N. F.; Therien, M. J.; Beratan, D. N., Biochemistry and theory of proton-coupled electron transfer. *Chem. Rev.* **2014,** *114* (7), 3381-3465.

248. Seki, K.; Traytak, S.; Tachiya, M., Rigorous calculation of electric field effects on the free energy change of the electron transfer reaction. *J. Chem. Phys.* **2003,** *118* (2), 669-679.

249. Kim, W. Y.; Kim, K. S., Tuning molecular orbitals in molecular electronics and spintronics. *Acc. Chem. Res.* **2010,** *43* (1), 111-120.

250. Šponer, J.; Leszczynski, J.; Hobza, P., Electronic properties, hydrogen bonding, stacking, and cation binding of DNA and RNA bases. *Biopolymers* **2001,** *61* (1), 3-31.

251. Nelson, R. D.; Standards, U. S. N. B. o.; Lide, D. R.; Maryott, A. A., *Selected Values of Electric Dipole Moments for Molecules in the Gas Phase*. U.S. Government Printing Office: Washington, DC, 1967.

252. Kubař, T. s.; Elstner, M., Solvent reorganization energy of hole transfer in DNA. *J. Phys. Chem. B* **2009,** *113* (16), 5653-5656.

253. Wolfram Research, Inc. *Mathematica*, Version 11.0; Mathematica, Version 12.0, Champaign, IL, 2019.

254. Curtiss, C. F.; Hirschfelder, J. O., Integration of stiff equations. *Proc. Natl. Acad. Sci. U.S.A.* **1952,** *38* (3), 235.

255. Henrici, P., *Discrete variable methods in ordinary differential equations*. John Wiley & Sons: New York, U.S.A., 1962.

256. Hush, N.; Cheung, A. S., Ionization potentials and donor properties of nucleic acid bases and related compounds. *Chem. Phys. Lett.* **1975,** *34* (1), 11-13.

257. Thazhathveetil, A. K.; Trifonov, A.; Wasielewski, M. R.; Lewis, F. D., Increasing the speed limit for hole transport in DNA. *J. Am. Chem. Soc.* **2011,** *133* (30), 11485-11487.

258. Senthilkumar, K.; Grozema, F. C.; Guerra, C. F.; Bickelhaupt, F. M.; Lewis, F. D.; Berlin, Y. A.; Ratner, M. A.; Siebbeles, L. D., Absolute rates of hole transfer in DNA. *J. Am. Chem. Soc.* **2005,** *127* (42), 14894-14903.

259. LeBard, D. N.; Lilichenko, M.; Matyushov, D. V.; Berlin, Y. A.; Ratner, M. A., Solvent reorganization energy of charge transfer in DNA hairpins. *J. Phys. Chem. B* **2003,** *107* (51), 14509-14520.

260. Siriwong, K.; Voityuk, A. A.; Newton, M. D.; Rösch, N., Estimate of the reorganization energy for charge transfer in DNA. *J. Phys. Chem. B* **2003,** *107* (11), 2595-2601.

261. Krishnan, R.; Binkley, J. S.; Seeger, R.; Pople, J. A., Self-consistent molecular orbital methods. XX. A basis set for correlated wave functions. *J. Chem. Phys.* **1980,** *72* (1), 650-654.

262. Clark, T.; Chandrasekhar, J.; Spitznagel, G. W.; Schleyer, P. V. R., Efficient diffuse function-augmented basis sets for anion calculations. III. The 3-21+ G basis set for first-row elements, Li–F. *J. Comput. Chem.* **1983,** *4* (3), 294-301.

263. Lu, X. J.; Olson, W. K., 3DNA: a software package for the analysis, rebuilding and visualization of three-dimensional nucleic acid structures. *Nucleic Acids Res.* **2003,** *31* (17), 5108-5121.

264. Levitt, M., How many base-pairs per turn does DNA have in solution and in chromatin? Some theoretical calculations. *Proc. Natl. Acad. Sci. U.S.A.* **1978,** *75* (2), 640-644.

265. Srinivasan, A.; Sauers, R. R.; Fenley, M. O.; Boschitsch, A. H.; Matsumoto, A.; Colasanti, A. V.; Olson, W. K., Properties of the nucleic-acid bases in free and Watson-Crick hydrogen-bonded states: computational insights into the sequence-dependent features of double-helical DNA. *Biophys. Rev.* **2009,** *1* (1), 13.

266. Hanwell, M. D.; Curtis, D. E.; Lonie, D. C.; Vandermeersch, T.; Zurek, E.; Hutchison, G. R., Avogadro: an advanced semantic chemical editor, visualization, and analysis platform. *J. Cheminformatics* **2012,** *4* (1), 1-17.

267. Arabi, A. A.; Matta, C. F., Effects of external electric fields on double proton transfer kinetics in the formic acid dimer. *Phys. Chem. Chem. Phys.* **2011,** *13* (30), 13738-13748.

268. Cerón-Carrasco, J. P.; Jacquemin, D., Electric field induced DNA damage: an open door for selective mutations. *Chem. Commun.* **2013,** *49* (69), 7578-7580.

269. Cerón-Carrasco, J. P.; Cerezo, J.; Jacquemin, D., How DNA is damaged by external electric fields: selective mutation vs. random degradation. *Phys. Chem. Chem. Phys.* **2014,** *16* (18), 8243-8246.

270. Cerón-Carrasco, J. P.; Jacquemin, D., Exposing the G-quadruplex to electric fields: the role played by telomeres in the propagation of DNA errors. *Phys. Chem. Chem. Phys.* **2017,** *19* (14), 9358-9365.

271. Segal, D.; Nitzan, A.; Ratner, M.; Davis, W. B., Activated conduction in microscopic molecular junctions. *J. Phys. Chem. B* **2000,** *104* (13), 2790-2793.

272. Nitzan, A., The relationship between electron transfer rate and molecular conduction 2. The sequential hopping case. *Isr. J. Chem.* **2002,** *42* (2-3), 163-166.

273. Sisido, M.; Tanaka, R.; Inai, Y.; Imanishi, Y., Photoinduced electron transfer on a single. alpha.-helical polypeptide chain. *J. Am. Chem. Soc.* **1989,** *111* (17), 6790-6796.

274. Zheng, M.; Rostovtsev, V. V., Photoinduced charge transfer mediated by DNA-wrapped carbon nanotubes. *J. Am. Chem. Soc.* **2006,** *128* (24), 7702-7703.

275. Bloom, B. P.; Graff, B. M.; Ghosh, S.; Beratan, D. N.; Waldeck, D. H., Chirality control of electron transfer in quantum dot assemblies. *J. Am. Chem. Soc.* **2017,** *139* (26), 9038-9043.

276. Hughes, M. P., AC electrokinetics: applications for nanotechnology. *Nanotechnology* **2000,** *11* (2), 124.

277. Venkata Kamalakar, M.; Raychaudhuri, A. K., A novel method of synthesis of dense arrays of aligned single crystalline copper nanotubes using electrodeposition in the presence of a rotating electric field. *Adv. Mater.* **2008,** *20* (1), 149-154.

278. Ayub, M.; Ivanov, A.; Hong, J.; Kuhn, P.; Instuli, E.; Edel, J. B.; Albrecht, T., Precise electrochemical fabrication of sub-20 nm solid-state nanopores for single-molecule biosensing. *J. Phys.: Condens. Matter* **2010,** *22* (45), 454128.

279. Yokota, K.; Tsutsui, M.; Taniguchi, M., Electrode-embedded nanopores for label-free single-molecule sequencing by electric currents. *RSC Adv.* **2014,** *4* (31), 15886-15899.

280. Xiang, L.; Palma, J. L.; Li, Y.; Mujica, V.; Ratner, M. A.; Tao, N., Gate-controlled conductance switching in DNA. *Nat. Commun.* **2017,** *8*, 14471.

281. Song, H.; Kim, Y.; Jang, Y. H.; Jeong, H.; Reed, M. A.; Lee, T., Observation of molecular orbital gating. *Nature* **2009,** *462* (7276), 1039-1043.

282. Li, Y.; Buerkle, M.; Li, G.; Rostamian, A.; Wang, H.; Wang, Z.; Bowler, D. R.; Miyazaki, T.; Xiang, L.; Asai, Y.; Zhou, G.; Tao, N., Gate controlling of quantum interference and direct observation of anti-resonances in single molecule charge transport. *Nat. Mater.* **2019,** *18* (4), 357-363.

283. West, R. M., Electrical Manipulation of DNA Self-Assembled Monolayers: Electrochemical Melting of Surface-Bound DNA. *J. Electrochem. Soc.* **2020,** *167* (3), 037544.

284. Phillips, R.; Kondev, J.; Theriot, J.; Garcia, H., *Physical biology of the cell*. 2nd ed.; Garland Science: New York, U.S.A., 2012.

285. Di Muccio, G.; della Rocca, B. M.; Chinappi, M., Geometrically Induced Selectivity and Unidirectional Electroosmosis in Uncharged Nanopores. *arXiv preprint arXiv:2104.03390* **2021**.

286. Allen, J. B.; Larry, R. F., *Electrochemical methods: fundamentals and applications*. 2nd ed.; John Wiley & Sons: New York, U.S.A., 2001.

287. Israelachvili, J. N., *Intermolecular and surface forces*. 3rd ed.; Academic Press: Burlington, MA, 2011.

288. Tan, Z.-J.; Chen, S.-J., Nucleic acid helix stability: effects of salt concentration, cation valence and size, and chain length. *Biophys. J.* **2006,** *90* (4), 1175-1190.

289. Kohagen, M.; Uhlig, F.; Smiatek, J., On the nature of ion-stabilized cytosine pairs in DNA i-motifs: The importance of charge transfer processes. *Int. J. Quantum Chem.* **2019,** *119* (14), e25933.

290. Morais, P.; Qu, F., A quantum dot model for the surface charge density in ferrite-based ionic magnetic fluids. *J. Magn. Magn. Mater.* **2002,** *252*, 117-119.

291. Bagchi, D.; Nguyen, T. D.; de la Cruz, M. O., Surface polarization effects in confined polyelectrolyte solutions. *Proc. Natl. Acad. Sci. U.S.A.* **2020,** *117* (33), 19677-19684.

292. Yuly, J. L.; Lubner, C. E.; Zhang, P.; Beratan, D. N.; Peters, J. W., Electron bifurcation: progress and grand challenges. *Chem. Commun.* **2019,** *55* (79), 11823-11832.

293. Ishizaki, A.; Fleming, G. R., Theoretical examination of quantum coherence in a photosynthetic system at physiological temperature. *Proc. Natl. Acad. Sci. U.S.A.* **2009,** *106* (41), 17255-17260.

294. Ao, G.; Streit, J. K.; Fagan, J. A.; Zheng, M., Differentiating left-and right-handed carbon nanotubes by DNA. *J. Am. Chem. Soc.* **2016,** *138* (51), 16677-16685.

295. Tanaka, T.; Urabe, Y.; Hirakawa, T.; Kataura, H., Simultaneous chirality and enantiomer separation of metallic single-wall carbon nanotubes by gel column chromatography. *Anal. Chem.* **2015,** *87* (18), 9467-9472.

296. Green, A. A.; Duch, M. C.; Hersam, M. C., Isolation of single-walled carbon nanotube enantiomers by density differentiation. *Nano Res.* **2009,** *2* (1), 69-77.

297. Ghosh, S.; Bachilo, S. M.; Weisman, R. B., Advanced sorting of single-walled carbon nanotubes by nonlinear density-gradient ultracentrifugation. *Nat. Nanotechnol.* **2010,** *5* (6), 443-450.

298. Zheng, M.; Jagota, A.; Semke, E. D.; Diner, B. A.; McLean, R. S.; Lustig, S. R.; Richardson, R. E.; Tassi, N. G., DNA-assisted dispersion and separation of carbon nanotubes. *Nat. Mater.* **2003,** *2* (5), 338-342.

299. Xu, L.; Valášek, M.; Hennrich, F.; Sedghamiz, E.; Penaloza-Amion, M.; Häussinger, D.; Wenzel, W.; Kappes, M. M.; Mayor, M., Enantiomeric Separation of Semiconducting Single-Walled Carbon Nanotubes by Acid Cleavable Chiral Polyfluorene. *ACS Nano* **2021,** *15* (3), 4699-4709.

300. Li, H.; Gordeev, G.; Garrity, O.; Reich, S.; Flavel, B. S., Separation of small-diameter single-walled carbon nanotubes in one to three steps with aqueous two-phase extraction. *ACS Nano* **2019,** *13* (2), 2567-2578.

301. Olivier, J. H.; Park, J.; Deria, P.; Rawson, J.; Bai, Y.; Kumbhar, A. S.; Therien, M. J., Unambiguous diagnosis of photoinduced charge carrier signatures in a stoichiometrically controlled semiconducting polymer-wrapped carbon nanotube assembly. *Angew. Chem. Int. Ed.* **2015,** *127* (28), 8251-8256.

302. Naaman, R.; Paltiel, Y.; Waldeck, D. H., Chiral molecules and the electron spin. *Nat. Rev. Chem.* **2019,** *3* (4), 250-260.

303. Martínez, J. M.; Martínez, L., Packing optimization for automated generation of complex system's initial configurations for molecular dynamics and docking. *J. Comput. Chem.* **2003,** *24* (7), 819-825.

304. Martínez, L.; Andrade, R.; Birgin, E. G.; Martínez, J. M., PACKMOL: a package for building initial configurations for molecular dynamics simulations. *J. Comput. Chem.* **2009,** *30* (13), 2157-2164.

305. Bekker, H.; Berendsen, H.; Dijkstra, E.; Achterop, S.; Van Drunen, R.; Van der Spoel, D.; Sijbers, A.; Keegstra, H.; Reitsma, B.; Renardus, M. In *Gromacs: A parallel computer for molecular dynamics simulations*, Physics computing, World Scientific Singapore: 1993; pp 252-256.

306. Berendsen, H. J.; van der Spoel, D.; van Drunen, R., GROMACS: a message-passing parallel molecular dynamics implementation. *Comput. Phys. Commun.* **1995,** *91* (1-3), 43-56.

307. Lindahl, E.; Hess, B.; Van Der Spoel, D., GROMACS 3.0: a package for molecular simulation and trajectory analysis. *J. Mol. Model.* **2001,** *7* (8), 306-317.

308. Van Der Spoel, D.; Lindahl, E.; Hess, B.; Groenhof, G.; Mark, A. E.; Berendsen, H. J., GROMACS: fast, flexible, and free. *J. Comput. Chem.* **2005,** *26* (16), 1701-1718.

309. Hess, B.; Kutzner, C.; Van Der Spoel, D.; Lindahl, E., GROMACS 4: algorithms for highly efficient, load-balanced, and scalable molecular simulation. *J. Chem. Theory Comput.* **2008,** *4* (3), 435-447.

310. Pronk, S.; Páll, S.; Schulz, R.; Larsson, P.; Bjelkmar, P.; Apostolov, R.; Shirts, M. R.; Smith, J. C.; Kasson, P. M.; van der Spoel, D., GROMACS 4.5: a high-throughput and highly parallel open source molecular simulation toolkit. *Bioinformatics* **2013,** *29* (7), 845-854.

311. Páll, S.; Abraham, M. J.; Kutzner, C.; Hess, B.; Lindahl, E. In *Tackling exascale software challenges in molecular dynamics simulations with GROMACS*, International conference on exascale applications and software, Springer: 2014; pp 3-27.

312. Abraham, M. J.; Murtola, T.; Schulz, R.; Páll, S.; Smith, J. C.; Hess, B.; Lindahl, E., GROMACS: High performance molecular simulations through multi-level parallelism from laptops to supercomputers. *SoftwareX* **2015,** *1*, 19-25.

313. Berendsen, H. J.; Postma, J. P.; van Gunsteren, W. F.; Hermans, J., Interaction models for water in relation to protein hydration. In *Intermolecular forces*, Springer: 1981; pp 331-342.

314. Jo, S.; Kim, T.; Iyer, V. G.; Im, W., CHARMM-GUI: a web-based graphical user interface for CHARMM. *J. Comput. Chem.* **2008,** *29* (11), 1859-1865.

315. Hinkle, K. R.; Phelan Jr, F. R., Solvation Free Energy of Self-Assembled Complexes: Using Molecular Dynamics to Understand the Separation of ssDNA-Wrapped Single-Walled Carbon Nanotubes. *J. Phys. Chem. C* **2020,** *124* (24), 13127-13140.

316. Hinkle, K. R.; Phelan Jr, F. R., Solvation of carbon nanoparticles in water/alcohol mixtures: using molecular simulation to probe energetics, structure, and dynamics. *J. Phys. Chem. C* **2017,** *121* (41), 22926-22938.

317. Van Gunsteren, W. F.; Berendsen, H. J., A leap-frog algorithm for stochastic dynamics. *Mol. Simul.* **1988,** *1* (3), 173-185.

318. Martoňák, R.; Laio, A.; Parrinello, M., Predicting crystal structures: the Parrinello-Rahman method revisited. *Phys. Rev. Lett.* **2003,** *90* (7), 075503.

319. Hess, B.; Bekker, H.; Berendsen, H. J.; Fraaije, J. G., LINCS: a linear constraint solver for molecular simulations. *J. Comput. Chem.* **1997,** *18* (12), 1463-1472.

320. Bennett, C. H., Efficient estimation of free energy differences from Monte Carlo data. *J. Comput. Phys.* **1976,** *22* (2), 245-268.

321. Pohorille, A.; Jarzynski, C.; Chipot, C., Good practices in free-energy calculations. *J. Phys. Chem. B* **2010,** *114* (32), 10235-10253.

322. Shirts, M. R.; Pitera, J. W.; Swope, W. C.; Pande, V. S., Extremely precise free energy calculations of amino acid side chain analogs: Comparison of common molecular mechanics force fields for proteins. *J. Chem. Phys.* **2003,** *119* (11), 5740-5761.

323. Christ, C. D.; Mark, A. E.; Van Gunsteren, W. F., Basic ingredients of free energy calculations: a review. *J. Comput. Chem.* **2010,** *31* (8), 1569-1582.

324. Klimovich, P. V.; Shirts, M. R.; Mobley, D. L., Guidelines for the analysis of free energy calculations. *J. Comput.-Aided Mol. Des.* **2015,** *29* (5), 397-411.

325. Lemkul, J., From proteins to perturbed Hamiltonians: A suite of tutorials for the GROMACS-2018 molecular simulation package [article v1. 0]. *Living J. Comp. Mol. Sci.* **2019,** *1* (1), 5068.

326. Smith, D. E.; Haymet, A., Free energy, entropy, and internal energy of hydrophobic interactions: Computer simulations. *J. Chem. Phys.* **1993,** *98* (8), 6445-6454.

327. Michaud-Agrawal, N.; Denning, E. J.; Woolf, T. B.; Beckstein, O., MDAnalysis: a toolkit for the analysis of molecular dynamics simulations. *J Comput Chem* **2011,** *32* (10), 2319-27.

328. Gowers, R. J.; Linke, M.; Barnoud, J.; Reddy, T.; Melo, M. N.; Seyler, S.; DombDski, J.; Dotson, D.; Buchoux, S.; Kenney, I. M.; Beckstein, O. In *MDAnalysis: A Python Package for the Rapid Analysis of Molecular Dynamics Simulations*, Benthall, S.; Rostrup, S., Eds. Proc. of the 15th Python in Science Conf.: 2016; pp 98 - 105.

329. Artés, J. M.; Li, Y.; Qi, J.; Anantram, M.; Hihath, J., Conformational gating of DNA conductance. *Nat. Commun.* **2015,** *6* (1), 1-8.

330. Bruot, C.; Palma, J. L.; Xiang, L.; Mujica, V.; Ratner, M. A.; Tao, N., Piezoresistivity in single DNA molecules. *Nat. Commun.* **2015,** *6* (1), 1-8.

Biography

Jesús del Carmen Valdiviezo Mora graduated cum laude with a B.S. in Chemistry from Tecnologico de Monterrey, Campus Monterrey, in May 2016 and was the recipient of a Fulbright Fellowship to support his graduate studies. At Duke University, he received a Ph.D. in Chemistry and an M.S. in Electrical in Computer Engineering in Summer 2021. He will continue his scientific training at UC Berkeley as a Computing Innovation Postdoctoral Fellow.

Selected awards:

- Fulbright-Garcia Robles Scholarship.
- CONACYT-Nuevo Leon Fellowship (declined).
- Graduate Program in Nanoscience (GPNANO) Fellowship.
- Duke Support for Interdisciplinary Graduate Networks (D-SIGN) Grant.
- NSF/DOE Quantum Science Summer School Award.
- Telluride School on Theoretical Chemistry Award.
- Duke Incubation Fund.
- Anne T. and Robert M. Bass Instructional Fellowship.
- Kathleen Zielik Fellowship.
- Fitzpatrick Institute for Photonics Special Student Seminar Award.
- Rice Academy Postdoctoral Fellowship (declined).
- CRA/CCC Computing Innovation Fellowship.

Publications (in chronological order):

1. J. Valdiviezo and J. L. Palma. Molecular Rectification Enhancement Based on Conformational and Chemical Modifications. *J. Phys. Chem. C.*, **2018**, 122(4), pp.2053–2063.
2. S. D. Banziger, X. Li, J. Valdiviezo, M. Zeller, P. Zhang, D. N. Beratan, I. V. Rubtsov and T. Ren. Unsymmetrical Bis–Alkynyl Complexes Based on Co(III)(cyclam): Synthesis, Ultrafast Charge Separation and Analysis. *Inorg. Chem.*, **2019**, 58(22), pp.15487-15497.
3. X. Li, J. Valdiviezo, S. D. Banziger, P. Zhang, T. Ren, D. N. Beratan and I. V. Rubtsov. Symmetry Controlled Photo-Selection and Charge Separation in Butadiyne-Bridged Donor–Bridge–Acceptor Compounds. *Phys. Chem. Chem. Phys.*, **2020**, 22(17), pp.9664-9676.
4. Polakovsky, J. Showman, J. Valdiviezo and J. L. Palma. Quantum Interference Enhances Rectification Behavior of Molecular Devices. *Phys. Chem. Chem. Phys.*, **2021**, 23(2), pp.1550-1557.
5. J. Valdiviezo, P. Rocha, A. Polakovsky and J. L. Palma. Nonexponential Length Dependence of Molecular Conductance in Acene-Based Molecular Wires. *ACS Sens.*, **2021**, 6(2), pp.477-484.
6. J. Valdiviezo, C. Clever, E. Beall, A. Pearse, Y. Bae, P. Zhang, C. Achim, D. N. Beratan and D. H. Waldeck. Delocalization-Assisted Transport

through Nucleic Acids in Molecular Junctions. *Biochemistry*, **2021**, 60(17), pp.1368-1378.

7. J. Valdiviezo, P. Zhang and D. N. Beratan. Electron Ratcheting in Self-Assembled Soft Matter. *J. Chem. Phys*, **2021**, DOI: 10.1063/5.0044420.
8. F. Mastrocinque, J. Valdiviezo G. Bullard, A. Nayak, P. Zhang, D. N. Beratan and M. J. Therien. Enantiomeric Separation of Carbon Nanotubes with Binaphthol-based Surfactants. *In preparation.*
9. M. Kang, J. Valdiviezo, K. Su, J. Whitlow, Z. Zhang, T. Hurant, S. Bai, J. Yuly, P. Zhang, K. N. Brown and D. N. Beratan. Quantum Simulators and Condensed Phase Chemical Dynamics. *In preparation.*
10. D. N. Beratan., J. Valdiviezo, J. Yuly and P. Zhang. Dynamical Chemistry: A Hands-on Guidebook for Understanding Coherence Phenomena in Chemistry. *In preparation.*